Development and Testing of Self-Powered Detectors for Nuclear Measurements in Fusion Reactors
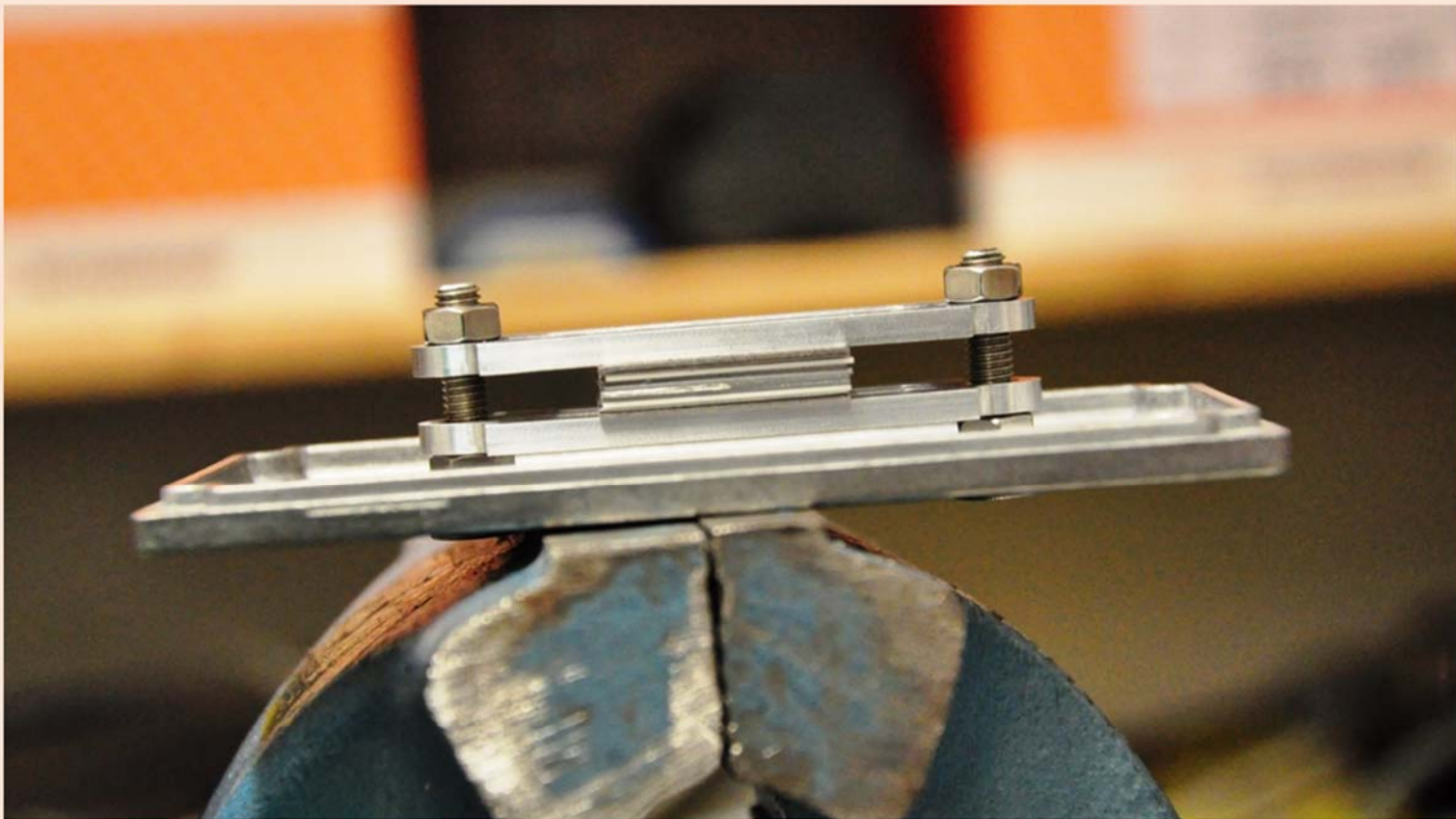
Prasoon Raj

Department of Mechanical Engineering
Karlsruhe Institute of Technology

Development and Testing of Self–Powered Detectors for Nuclear Measurements in Fusion Reactors

Zur Erlangung des akademischen Grades

Doktor der Ingenieurwissenschaften (Dr.-Ing.)

von der KIT-Fakultät für Maschinenbau des

Karlsruher Instituts für Technologie (KIT)

angenommene

Dissertation

von

M.S.-M.Tech. Prasoon Raj

Erklärung

Hiermit erkläre ich, dass ich die vorliegende Arbeit selbständig angefertigt und keine anderen als die angegebenen Quellen und Hilfsmittel benutzt sowie die wörtlich und inhaltlich übernommenen Stellen als solche kenntlich gemacht und die Satzung des KIT zur Sicherung guter wissenschaftlicher Praxis in der jeweils gültigen Fassung beachtet habe.

Karlsruhe, den 02.05.2019   Prasoon Raj

ABSTRACT

Robust technologies for radiation detection and measurement are quintessential for safe and reliable operation of a fusion power plant. Diverse detector-types sensitive to high-energy neutrons, photons, and various charged particles must be integrated into the reactor designs. The applied devices and electronics should sustain high fluxes of energetic particles, intense electromagnetic fields, and high temperatures. Therefore, the traditional detection technologies need to be adapted accordingly and novel methods and instruments should be developed.

This thesis presents a comprehensive investigation of self-powered detectors (SPD), a class of common neutron and photon flux monitors used in fission reactors, for application in fusion reactors. An SPD is an electrical device with two conducting layers: emitter and collector, isolated with an intermediate ceramic layer. The emitter, the central element, preferentially interacts with the incident particles (neutrons and photons) leading to the release of electrons. Creation of small charges in such a process produces the direct current (DC) signal of the SPD, proportional to the incident particles' fluxes. Due to the unique simplicity of an SPD's engineering design, its high reliability, robustness, compactness and low-price, SPD is of high interest for use as an online detector in fusion reactors. However, SPDs are tailored for fission reactor radiation conditions, mainly the neutron and photon energies, which are significantly different from those in fusion systems. Also, the overall structure of a fusion reactor brings a number of new technical constraints on the SPDs. A detailed study of the nuclear performance of this detector type for fusion applications has not been performed earlier and is the subject matter of this work. Experimental and computational studies have been conducted to check the feasibility of implementing SPDs in the European test blanket modules (TBM) of the ITER reactor, and to pave an optimum path for development and testing of prototype SPDs for fusion reactors.

Using the basic operating principles of the device, test SPDs have been chosen for their high responses to neutrons of energies up to 14 MeV and high-energy photons, as present in fusion reactors. A new, flat sandwich-like SPD with flexible design has been conceptualized and developed in this work. It allows testing of multiple material combinations and provides higher sensitivity under laboratory radiation sources. At first, detailed reference experiments have been done using a flat SPD and a commercial cylindrical SPD, both with vanadium emitters. Then, several other materials have been selected for comparative studies, as the nature of an SPD's signal is known to depend on the layer-materials. Vanadium, silver and beryllium have been picked for the emitters, and niobium, graphite and Inconel-600 for collectors.

Extensive irradiation tests under representative neutron and photon fields have been conducted for various test-SPDs. The scope of experiments gets limited as no available radiation source has wide-energy and intense fields like those in the TBMs. The utilized sources include the 14 MeV neutron generator of the Technical University of Dresden, the bremsstrahlung photon source of the ELBE accelerator at Helmholtz-Zentrum Dresden-Rossendorf and the TRIGA Mark-II fission reactor of Johannes

Gutenberg-University of Mainz. The signals of different detectors in different radiation fields have been compared and conclusions about their sensitivities, neutron-photon discrimination capabilities and susceptibilities to changes in the detector and/or the surroundings have been made.

Through tests over wide ranges of particle flux intensities, the SPDs have been proven to produce good proportionality between signal and incident flux, as demanded for the reactor flux monitors. Measured currents lie in the range of 100 fA to 100 pA. A flat design has been shown to exhibit a higher response, with signals improved by around 100 times as compared to the traditional cylindrical SPDs. Compact flat SPDs have been deemed favourable for possible use in reactor fields. The high-energy bremsstrahlung photon responses have been found to be higher for all detectors when compared with their fast 14 MeV neutron responses. An SPD, preferably with high atomic number emitter, is thus, concluded as a good choice for high-accuracy photon measurements in TBMs. For neutron measurements, an SPD with suitable materials shall have relatively stronger neutron signal in TBMs than that in the pure 14 MeV field because the spectrum of neutrons in the TBM is much wider. So, SPDs for the neutron flux monitoring have also been established as valid options.

To better understand the experiments and ultimately, for extrapolation to the real fusion reactor environment, a Monte-Carlo model for electrical sensitivity of an SPD has been developed and implemented. Questions regarding the discrimination of different signal forming processes are answered by scrutinizing various physical processes through the modelling. Computational studies of selected coaxial SPDs show that reliable signals, of the orders of nA to mA, can be produced by SPDs in the TBMs. A clear proportionality to the neutron or photon flux depending upon the choice of materials is expected from them.

In the end, a set of parametric computational studies on the materials, dimensions and overall geometric designs of the SPD have been proposed to be conducted. Several constructional aspects have been identified and reported, to eliminate the secondary effects from different events of nuclear, mechanical and electrical nature in the detector and in its vicinity.

ZUSAMMENFASSUNG

Robuste Technologien zur Strahlungserkennung und -messung sind von zentraler Bedeutung für den sicheren und zuverlässigen Betrieb eines Fusionskraftwerks. Vielfältige Arten von Detektoren, die auf hochenergetische Neutronen, Photonen und verschiedene geladene Teilchen reagieren, müssen in das Design des Reaktors integriert werden. Die eingesetzten Geräte und die Elektronik sollten hohe Ströme aus energiereichen Teilchen, intensive elektromagnetische Felder und hohe Temperaturen aushalten. Die herkömmlichen Detektionstechnologien müssen entsprechend angepasst und neue Methoden und Instrumente entwickelt werden.

Diese Doktorarbeit befasst sich mit einer umfassenden Untersuchung von Selbst Angetriebenen Detektoren (*Self-Powered Detectors, SPD*), einer gängigen Klasse zur Neutronen- und Photonenflussüberwachung in Kernreaktoren, welche in Fusionsreaktoren eingesetzt werden sollen. Ein SPD ist ein elektrisches Gerät mit zwei leitenden Schichten: Emitter und Kollektor, isoliert durch eine keramischen Zwischenschicht. Der Emitter ist das zentrale Element, welches bevorzugt mit den einfallenden Teilchen (Neutronen und Photonen) interagiert wodurch Elektronen freigesetzt werden. Die Erzeugung kleiner Ladungen in einem solchen Prozess führt zu einem Gleichstrom (DC) SPD-Signal, das proportional zu den einfallenden Teilchenflüssen ist. Aufgrund seiner einzigartig einfachen Konstruktion, seiner hohen Zuverlässigkeit, Robustheit, Kompaktheit und seines niedrigen Preises, ist der SPD von großem Interesse für den Einsatz als online Detektor in Fusionsreaktoren. Allerdings sind die SPDs auf die Strahlungsbedingungen im Kernspaltungsreaktor zugeschnitten, vor allem auf die Neutronen- und Photonenenergien, die sich deutlich von denen in Fusionsanlagen unterscheiden. Darüber hinaus bringt die Gesamtstruktur eines Fusionsreaktors eine Reihe neuer technischer Einschränkungen für SPDs mit sich. Eine detaillierte Untersuchung der nuklearen Leistungsfähigkeit dieses Detektortyps für Fusionsanwendungen wurde noch nie zuvor durchgeführt und ist Gegenstand dieser Arbeit. Im Rahmen der Entwicklung von kerntechnischen Instrumenten für die Europäischen Testblanketmodule (TBM) des ITER-Reaktors wurden experimentelle und rechnerische Studien durchgeführt, um die Machbarkeit der Implementierung von SPDs in Fusionsblankets zu prüfen und einen optimalen Weg für die Entwicklung und Erprobung von Prototypen von SPDs für Fusionsreaktoren zu ebnen.

Es wurden Test-SPDs mit einer starken Reaktion auf Neutronen mit Energien bis zu 14 MeV und hochenergetischen Photonen, wie sie in Fusionsreaktoren vorhanden sind, gewählt. In dieser Arbeit wurde ein neues, flaches, sandwichartiges SPD mit flexiblem Design konzipiert und entwickelt. Dieses ermöglicht die Untersuchung mehrerer Materialkombinationen und bietet eine höhere Empfindlichkeit bei Strahlungsquellen unter Laborbedingungen. Für genaue Referenzexperimente wurden ein flacher SPD und eine kommerzielle zylindrische SPD-Einheit – beide mit V Emitter – getestet. Die Art des Signals eines SPDs hängt vom Material ab, welches für den Schichtaufbau verwendet wird. Darum wurden mehrere Materialien ausgewählt, um sie in verschiedenen Kombinationen miteinander zu vergleichen: V, Ag und Be für die Emitter und Nb, Graphit und Inconel-600 für die Kollektoren.

Umfangreiche Bestrahlungstests unter repräsentativen Neutronen- und Photonenfeldern wurden durchgeführt, um deren Signale zu messen und zu vergleichen. Keine der verfügbaren Strahlungsquellen verfügt über so energiereiche und intensive Felder wie innerhalb der TBMs, was den Umfang der experimentellen Analysen einschränkt. So werden für die Detektorentests nur repräsentative Strahlungsquellen verwendet: der 14 MeV Neutronengenerator der Technischen Universität Dresden, die Bremsstrahlungs-Photonenquelle des ELBE-Beschleunigers am Helmholtz-Zentrum Dresden-Rossendorf und der TRIGA Mark-II-Spaltreaktor der Johannes Gutenberg-Universität Mainz. Die Signale verschiedener Detektoren in verschiedenen Strahlungsfeldern wurden verglichen und Rückschlüsse auf ihre Empfindlichkeit, Neutronen-Photonen-Diskriminierungsfähigkeiten und Anfälligkeit für Veränderungen im Detektor und/oder in der Umgebung gezogen.

Durch Tests unter Neutronen- und Photonenfeldern über große Intensitätsbereiche hinweg wird nachgewiesen, dass die SPDs eine gute Proportionalität zwischen Signal und einfallendem Strahlungsfluss erzeugen, wie es für die Reaktorflussüberwachung gefordert wird. Die gemessenen Ströme liegen im Bereich von 100 fA bis 100 pA. Ein flaches Design zeigt ein höheres Ansprechverhalten, wobei sich die Signale im Vergleich zu den herkömmlichen koaxialen SPDs um das etwa 100-fache verbessern. Kompakte flache SPDs werden für den möglichen Einsatz im Reaktor als vorteilhaft erwiesen. Die hochenergetischen Bremsstrahlungs-Photonensignale sind für alle Detektoren höher, verglichen mit den Signalen für schnelle 14 MeV Neutronen. Ein SPD, vorzugsweise mit hoch-Z Emitter, ist somit eine gute Wahl für hochpräzise Photonenmessungen in den TBMs. Durch das breite Neutronenspektrum im TBM erzeugt ein SPD mit geeigneter Materialzusammensetzung ein höheres Neutronensignal als in einem reinen 14 MeV-Feld. Dadurch sind SPDs weiterhin geeignet für die Neutronenflussmessungen.

Zum besseren Verständnis der Experimente und letztlich zur Extrapolation auf die reale Fusionsreaktorumgebung wurde ein Monte-Carlo-Modell für die elektrische Empfindlichkeit eines SPDs entwickelt und implementiert. Fragen zur Unterscheidung verschiedener Signalbildungsprozesse werden durch die Untersuchung verschiedener physikalischer Prozesse und die Durchführung von Monte-Carlo-Simulationen beantwortet. Berechnungen an ausgewählten koaxialen SPDs zeigen, dass verlässliche Signale in der Größenordnungen nA bis mA von SPDs in den TBMs erzeugt werden können. Von diesen wird eine klare Proportionalität zum Neutronen- oder Photonenfluss in Abhängigkeit von der Materialauswahl erwartet.

Abschließend werden eine Reihe von parametrischen Berechnungsstudien über die Materialien, deren Abmessungen und das gesamte geometrische Design der SPDs, vorgeschlagen. Mehrere konstruktive Aspekte werden identifiziert und berichtet, um die sekundären Auswirkungen von verschiedenen Ereignissen nuklearer, mechanischer und elektrischer Natur im Detektor und in seiner Umgebung zu beseitigen.

*In memory of my foster-father **Mr. Shiwa Kant Das**.*

आच्छादने दोषवृध्दिः ख्यापने तु लयो भवेत्।

[ācchādane doṣavṛdhdiḥ khyāpane tu layo bhavet]

ACKNOWLEDGEMENTS

TABLE OF CONTENTS

1. NUCLEAR FUSION AND INSTRUMENTATION FOR FUSION REACTORS

1.1 Nuclear Fusion: Introduction and State of its Development

Energy is the cornerstone of the human civilization and search for sustainable sources of energy for the future is one of the prime quests of the 21st century world. Enhancement of the living standards of the rapidly growing population will require consumption of enormous amounts of energy, primarily in the form of electrical power, and especially in the developing nations. Fossil fuels are projected to fulfill a major part of this demand in this century [1]. But, for the coming generations, innovative solutions with alternative sources are required, owing to the disadvantages of the fossil fuels which are: scarce reserves and damage to the natural environment.

For long-term and large-scale electricity production, strategies characterized by larger outputs, higher efficiencies and decreased ecological impacts are needed. Nuclear energy, inevitably, is at the center stage of the envisaged solutions to this global challenge [2]. With its generation IV fission-based reactor systems and the planned establishment of fusion-based power plants by mid-century, the nuclear energy sector has a prominent position in the roadmap for sustainable development.

Hans Alexander Bethe, recipient of the 1967 Nobel Prize in Physics is credited for the theories of nuclear reactions forming the stellar energy [3]. He described nuclear fusion as the main process behind the energy of the sun and the stars. In fusion, two light nuclei combine to form a bigger and more stable nucleus. The corresponding mass-defect is released as the kinetic energies of the emitted particles and radiation.

An example of a fusion reaction is the so-called *D-T reaction.* In this, two heavier isotopes of hydrogen: deuterium (^{2}H or D) and tritium (^{3}H or T) fuse to produce helium nucleus (^{4}He or α-particle) and neutron (n). Energy of around 17 MeV is released in total per reaction, most of which is carried out by the 14 MeV neutrons.

$$^2_1D + ^3_1T \rightarrow ^4_2He\ (3.5\ MeV) + ^1_0n\ (14.1\ MeV)\ .$$
(Eq. 1.1)
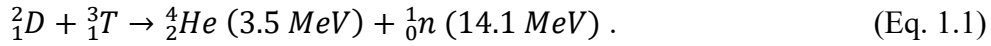
To harness fusion energy for generation of electricity, ventures into a fusion reactor began soon after Bethe's discovery. Fusion does not occur spontaneously as the reactant nuclei are positively charged and repel each other. Nuclei should be able to overcome the electrostatic potential barrier between them and come close enough for the strong nuclear force to take over. When thermal energy is used to facilitate this, the process is called *thermonuclear fusion.* In this type of fusion reaction, the nuclei are combined in a plasma state at very high temperatures. Creating suitable conditions for such a process in the laboratory is extremely difficult. Compared to other common reactions like D-D, D-^{3}He etc., D-T is one of the most favorable fusion reactions feasible on earth and is considered as the basis for the first generation of fusion power plants. Temperatures between 10-20 keV (equivalent to approx. 100 million˚C), and densities of 10^{20} nuclei per m^3 are required for D-T fusion to take place in a plasma device. No material walls can face such high temperatures. Moreover, the plasma is a very fragile state of matter, as it is easily contaminated, destabilised and lost. Production, confinement and conservation of a stable plasma state at high temperatures, with sufficient particle densities, and for sufficiently long time periods pose a major set of physics and engineering challenges.

Even with the difficulties, fusion is a potential long-term solution to the energy crisis. Its primary fuel: deuterium, and lithium (which is used to breed tritium) are abundant and accessible, and it is one of the cleanest and safest choices among all the alternative sources of energy. In the past decades, research in fusion science and technology aimed at developing a power plant has made considerable progress.

There are two major physical approaches to realize the conditions for fusion on earth: inertial confinement (ICF) [4] and magnetic confinement (MCF) [5]. In the former approach, high-density pellets containing fuel mixture are heated to stellar temperatures using highly focused beams of lasers, electrons or ions. On the other hand, MCF utilizes strong magnetic fields to trap the ionized particles of the fuel mixture in a plasma state and externally heats it for fusion to occur. Whereas theoretical bases for both are reasonably well-understood, ways of practically achieving them make a rich subject of research in laboratories across the world. At present, the magnetic confinement is a more developed approach and seems a more promising choice for fusion reactors [6].

In what follows, the physical principle and the state-of-art of the so-called *tokamak*-type reactor, which is a variant of MCF, are briefly elaborated.

1.1.1 Tokamak and its Breeding Blanket

The term tokamak, first coined in 1957, is derived from a Russian word (токамáк) meaning toroidal chamber with magnetic coils [7]. A tokamak is an evacuated donut-shaped vessel (known as vacuum vessel) to generate, contain and heat the plasma for the fusion reaction. A specific arrangement of superconducting coils around the torus produces nested magnetic field lines along which the ions and electrons gyrate according to their electric charge, and get confined. A set of D-shaped toroidal field (TF) coils generates a field component in the toroidal direction (φ). A perpendicular field component is produced by the plasma current, which is generated by a transformer action between the central solenoid (CS) and the plasma. A set of poloidal field (PF) coils concentric to the torus, produces a *pinching effect*, pushing the plasma away from the chamber walls. A stable configuration of plasma can be maintained only for short time duration until the maximum driving current for the CS which induces the plasma current, has been achieved, ultimately making a tokamak a *pulsed power device*.

The plasma current supplies a fraction of the energy required for fusion conditions through Ohmic heating. Further heating is done using additional means namely the neutral beam injection (NBI) and radiofrequency (RF) heating. The reaction products and the electromagnetic radiation are dumped on the plasma-facing components: the divertor and the breeding blanket (BB). A simplified model of a tokamak-type reactor with its important components is shown in Figure 1-1.
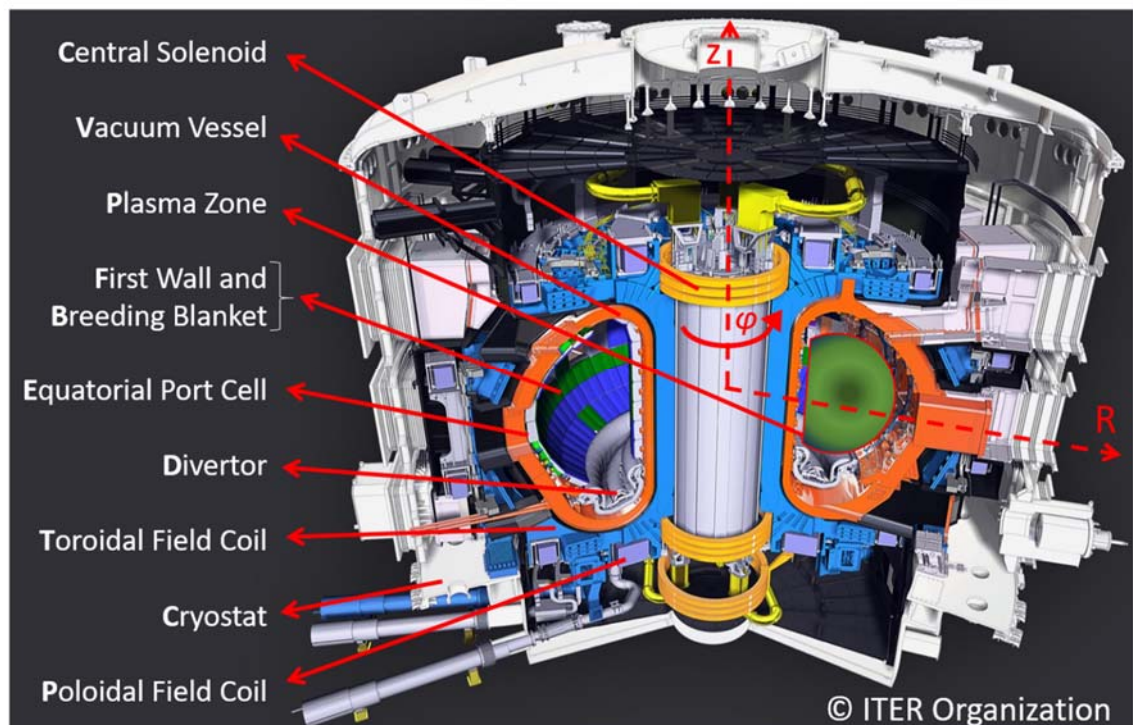
Figure 1-1: A simplified schematic view of a tokamak-type fusion reactor depicting the D-shaped plasma and the important components of the reactor design. The standard coordinate system with radial (R), toroidal (φ) and vertical (z) axes, followed for a tokamak's geometry is indicated through dashed red arrows. Image source: [8].

Tokamak is the leading confinement strategy for application in power plants. Multiple experimental devices have been constructed and utilized for experimentation worldwide. Majority of the research has been focussed on the physics of confinement in tokamaks, but also substantial knowledge in the fields of plasma-wall interactions, fusion materials, plasma diagnostics etc. have been achieved through these experiments.

An important parameter for a fusion power reactor is its *gain factor (Q)*, which is the ratio of net power produced (P_{out}) in fusion reactions to the total input power (P_{in}). The power input is mainly the external heating required to equate various power losses, which if not done can rapidly cool down the plasma and impede the fusion reactions. The losses are mainly due to thermal conduction, convection, impurities and bremsstrahlung and synchrotron radiations. A reactor regime with *Q* = 1 is classically called as the *breakeven condition*, while for efficient power production, it is crucial to have *Q* ≫ 1.

As pointed out earlier, the reaction of interest for fusion plants is the D-T reaction. Deuterium, a primary fuel for this reaction is abundantly and freely available in the seawater. The tritium, however, is a radioactive isotope and cannot be stored in large amounts for fuelling the reactors. An alternative way is to breed tritium in the fuel cycle of the reactor, using the neutron absorption reactions on ^{6}Li nuclei (and also on ^{7}Li, see Eq. 1.2 and Eq. 1.3 below) which is contained in the plasma facing component designated as the *breeding blanket*. Lithium being the second raw material, which is also available in large amounts in the seawater for consumption in reactors for millions of years, the reserve for fusion fuels is often claimed to be virtually limitless [9].

$$^6Li + {}^1n \rightarrow {}^4He + {}^3T + 4.8\ MeV\ .$$ (Eq. 1.2)

$$^7Li + {}^1n \rightarrow {}^4He + {}^3T + {}^1n - 2.5\ MeV\ .$$ (Eq. 1.3)
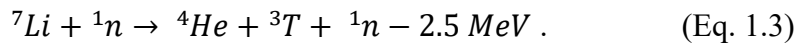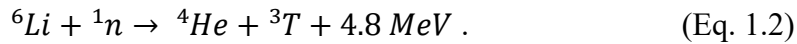
A tritium breeding blanket (TBB) will be a key component for the power reactors. As shown in Figure 1-1, the blanket surrounds the plasma and is attached to the interior walls of the vacuum vessel. It is made of Li compounds for tritium breeding and neutron multiplier materials like Be or Pb for production of further neutrons through the (n, 2n) reactions. Because most of the fusion energy is carried by the neutrons and they will be stopped in the blanket, a TBB will also serve as the energy conversion unit of the reactor. Therefore, the power deposited in the blanket needs to be extracted using an efficient and safe coolant for which He, H_2O etc. are being considered. A third crucial function of the blanket is the shielding of the vacuum vessel, magnetic coils and other components from the dangerous radiations emitted from the plasma chamber.

The TBB is arguably the most challenging component to design and deploy in a fusion reactor. It sits at an interface between multiple important systems in the power plant. On one side, it complies with the constraints dictated by the physics of fusion plasma and its interaction with the blanket walls. On the other side, it has to ensure stringent radiation shielding requirements for the outlying components. A TBB is designed to guarantee the *tritium self-sufficiency*, which means that it must produce enough tritium for the fuel cycle of the reactor. For this, it accounts for the losses incurred

in tritium reprocessing: its extraction, transport, and refueling processes, and tritium's radioactive decay. Tritium is a hazardous element, and its confinement within the permissible boundaries is also essential to incorporate while designing blankets. TBB's design and operation closely influence the performance of the heat transfer system. Last but not the least, blanket partakes important position in the plant safety as it has roles in various accident scenarios. To combat these issues, multiple design concepts for the TBB have been proposed [10], mainly categorized into the liquid metal and the solid breeder concepts. In the former, the breeder (Li) alone or in a eutectic mixture with multipliers (e.g. Pb-Li) flows in a liquid state for breeding and extraction of tritium. In the latter, layers with a breeder in the form of ceramic pebbles are placed between alternate solid neutron-multiplier (e.g. Be) layers. In both cases, the coolant (e.g. He) flows through channels in the liquid container or the solid breeder layers.

1.1.2 ITER and its Test Blanket Modules (TBM)

Of the two important conditions for a fusion reactor explained earlier, so far, no fusion device has either achieved the breakeven condition or demonstrated any of the tritium breeding concepts. Similar open issues like, plasma regimes suitable for power plants, the efficiency of the heat and particle exhaust systems, radiation-resistant and low-activation materials (specifically for the plasma-facing components), reactor safety etc., must be addressed before the feasibility of fusion power plants can be established. To do this, with the limited resources and time, a three-stage experimental approach has been devised in the European Union (EU) [11]. Under this approach, the first stage is to achieve a net energy production, and test and validate the performance of key technologies and methodologies in an experimental device known as *ITER*. In the intermediate stage, a full-size reactor called *DEMO*, a short form for demonstration power plant, will be constructed. DEMO will close the remaining gaps, practically establishing a fully-integrated fusion power plant design with all essential components for large-scale electricity production, thereby paving the path to the final stage, i.e. the commercial power stations based on nuclear fusion.

Lynchpin of the global plan for fusion power is the ITER project [8]. Proclaimed as the biggest ever energy experiment on the earth, with contribution from over 35 participating nations, ITER is a culmination of the decades of experience in the MCF. A key milestone in "the way" (*iter* in Latin means *the way*) towards incorporation of fusion in the energy portfolio for future generations, ITER is a tokamak-type reactor under construction in St. Paul-lez-Durance (France) (see Figure 1-1 for a reference artistic rendition of a tokamak). The main goals to be achieved in this project are:

1. Physics goals:
    a. A ten-folds steady-state power gain, i.e. $Q = 10$ ($P_{out} = 500$ MW, for $P_{in} = 50$ MW) for longer pulse durations (400 s – 600 s).
    b. A *burning plasma* regime with D-T fuel mixture, in which the reaction products self-heat the plasma sustaining it for longer durations.

2. Technological goals:
   a. The combined operation of various components and systems, e.g. plasma heating, diagnostics, control, cryogenics, remote handling etc., thereby validating their suitability for future power plants (e.g. DEMO).
   b. Demonstration of the feasibility of tritium breeding in a fusion reactor.
   c. Establishing through operation, that the fusion reactors are safe and incur minimal effects on the environment.

A particulary interesting detail of the ITER machine is that its blanket will not have fully-integrated tritium breeding capabilities. However, to test the concept(s) of TBB designs, an important goal of the project, the so-called *test blanket modules* (TBM) will be installed in the ITER [12]. A TBM is a prototype of a sector of a reactor breeding blanket, whose performance needs to be experimentally validated in a real fusion environment. It is a box-like structure containing breeding units with Li, neutron moderator and multiplier materials, and channels for tritium purge gas and coolant (He or water) flow systems. Several different design-proposals for a TBB will be tested through their respective TBM systems (*TBS*) integrated in the dedicated side ports of ITER. For this, a series of measurements will be done during different phases of ITER's operation. The phases vary in the fuel mixture (H-H, D-D, D-T etc.), plasma regimes, and pulse characteristics (duration, power etc.). For each kind of TBS, TBMs with integrated equipment specific to the goals of the particular ITER phase will be dedicated to measurements related to one or more of the electromagnetic, thermal-hydraulic, thermo-mechanical, magnetohydrodynamic, neutronic, tritium-control and integrational properties of the blanket. The obtained data will be used to validate and improve the design and analysis tools, like algorithms, hypotheses, computational codes etc. used for the design of fusion blankets.

The EU, a partner of the ITER project, has proposed two TBMs for testing in ITER: the Helium Cooled Lithium-Lead (HCLL) and the Helium Cooled Pebble-Bed (HCPB) TBMs. Figure 1-2 shows their overall views and a detailed schematic picture of HCPB showing the essential components of a TBM. Recently, Water Cooled Lithium Lead (WCLL) TBM concept has been proposed in place of the HCLL. The construction, installation and operation of TBMs are demanding tasks. The TBMs with their supporting systems and the instrumentation for measurements are being developed under partnership agreements between various European laboratories, overseen by the central organization of EU domestic agency for ITER, *Fusion for Energy* (F4E) [13].

Among other challenges in the development of TBMs, the high radiation, electromagnetic, and temperature fields in the TBMs severely constrain the choices available for TBM instrumentation. High energy neutron and gamma exposure (flux densities in the range of 10^9 to 10^{14} cm^{-2} s^{-1}) can damage or change the properties of the sensors and their signal processing and transmission devices. Furthermore, up to 4 T of magnetic field and temperatures between 300 to 550 °C expected in the TBMs could be detrimental for sensitive measurements. This forms the background for the tasks undertaken and presented in this thesis.
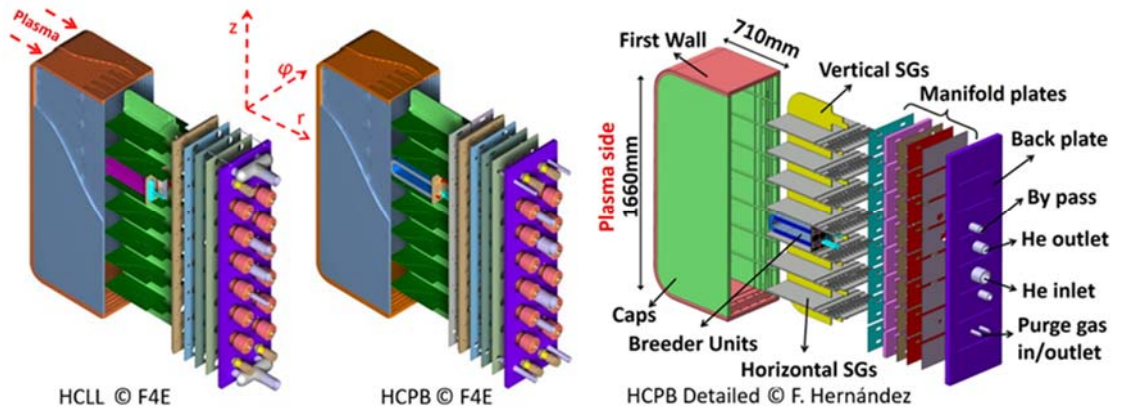
Figure 1-2: Overall views of the EU ITER TBMs: (left) the HCLL and HCPB TBM designs where the internal structures has been expanded out, and (right) details of the structure of HCPB TBM showing its essential components like breeder units, stiffening grids (SG), coolant and purge gas routes etc. Left image also provides a label to show the plasma facing side of the TBM and axes showing the orientation of the tokamak's (r, φ, z) coordinate system. Left image source: [13]. Right image source: [14].

1.2 Neutron and Photon Flux Measurements in Fusion Reactors

Instrumentation and control systems are central elements for nuclear reactors. In a fusion machine, they are required to monitor, configure and optimize the plasma conditions, for machine protection, and for achieving the expected thermonuclear reaction efficiency. Fusion diagnostics need to be non-perturbative and should rely on measurements of electromagnetic and nuclear emissions from the plasma. Multiple different types of instruments with their supporting systems need to be integrated, which must function in the harsh environment of the fusion device.

In the plan for implementation of ITER TBM program, a class of experiments is of interest from the nuclear instrumentalist's point of view. ITER being a large tokamak device with physical characteristics like those of a fusion power reactor, it will provide a unique opportunity for the validation of the computational tools and methods employed in the neutronic design and analysis of fusion reactor components. To this end, during the later D-T phases of ITER's campaigns, *nuclear experiments* will be performed in a set of specialized *neutronic (NT) TBMs*. Time-resolved nuclear responses related to blanket performance will be measured at various pre-decided locations in the TBMs. The measured data will be compared with respective calculations for their validation.

Development of reliable and well-qualified nuclear instrumentation for a fusion reactor is a complex and time-consuming task. To illustrate this, and as a basis for the rest of the thesis, this section sheds light on the measurements of the nuclear responses in fusion reactors and more specifically, the detector development project for EU TBMs. With ITER TBM being an experimental unit, some requirements for reactor instrumentation are relaxed, while newer constraints appear. Overall, the design philosophy adopted in this project is representative for the future reactors.

1.2.1 Distinguishing Features of Fusion Neutronics Measurements

1.2.1.1 Neutron and Photon Fields in Fusion Reactors

The radiation field of a fusion reactor is primarily comprised of neutrons and photons (mainly the prompt and decay gammas), the byproducts of fusion reactions, in combination with the tritium, present as a fuel element, and high-energy electrons emitted from the plasma. The fusion neutrons, mainly emitted in the D-T reaction, have energies around 14 MeV. Neutrons usually encountered in the physics of the thermal and fast fission reactors, in contrast to this, range between thermal energies (25 meV) to a few MeV. For an example to illustrate this, Figure 1-3 shows flux-spectra of neutrons in fusion (here for EU's ITER TBMs) and for fission (here, that in an experimental position in the core of the High Flux Reactor (HFR) of Petten, Netherlands [15]) cases. Considering this, fusion neutrons are "fast" neutrons. The overall reaction cross-section of fast neutrons is relatively lower but they also open up more reaction channels as compared to the thermal neutrons.
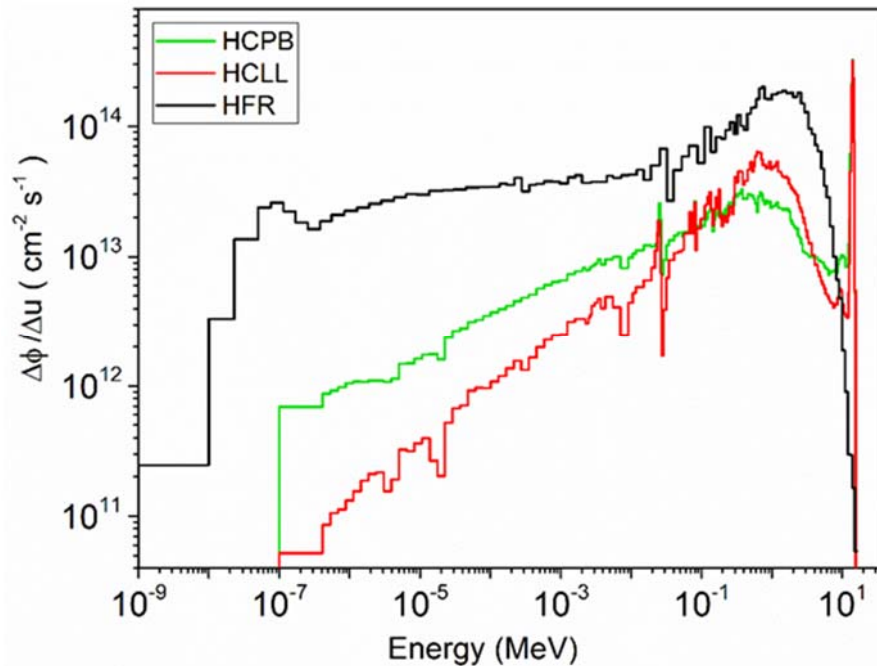
Figure 1-3: Calculated normalized neutron fluxes and energy spectra at the centre of the plasma-facing front walls of the HCPB and HCLL TBMs of ITER. These calculations are presented in Chapter 8. For a comparison with a typical fission reactor, the estimated neutron flux-spectra at a core position in the High Flux Reactor (HFR) Petten, Netherlands is reproduced [15]. Ordinates show the group neutron fluxes ($\Delta\varphi n$) per lethargy interval (Δu).

The neutrons and photons in TBMs lie over a wide energy range (see Figure 1-3 for calculated neutron flux-spectra in HCLL and HCPB TBMs). Neutrons go from thermal energy to 14 MeV D-T neutron energy. Near to the plasma-facing edge, there is also a strong photon field. Figure 1-4 shows the calculated photon flux-spectra, estimated near the centers of the plasma-facing front walls (see Figure 1-2) of the HCLL and HCPB

TBMs of EU. For the 500 MW operation of ITER in the D-T phase, the estimated flux density of neutrons in front of the TBMs is of the order of 2×10^{14} cm^{-2} s^{-1} and photons of 7×10^{13} cm^{-2} s^{-1}. The flux densities expected close to the plasma facing walls in a DEMO-like reactor, in contrast to TBMs, are much higher, of the orders of 10^{15} cm^{-2} s^{-1}.
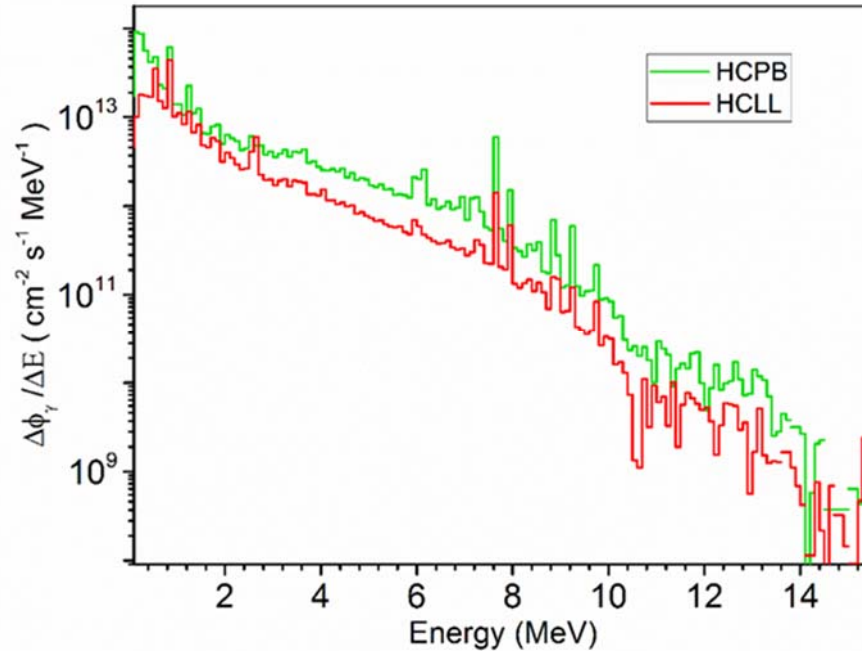
Figure 1-4: Calculated normalized fluxes and energy spectra of photons in the center of the plasma-facing front walls of the HCPB and HCLL TBMs of ITER. Details of the calculation are presented in Chapter 8. The ordinates show the group flux ($\Delta\varphi\gamma$) per unit of the bin size (ΔE).

Major impacts of the presence of fast neutrons at higher fluxes in a fusion reactor are the need of thicker and more complex shielding, and the heavy radiation damage sustained on the components and systems. Of rather high importance from the point of view of radiation measurements is the fact that these lead to reduce the detection efficiency of the classical nuclear reactor instrumentation, from which most fusion neutron diagnostics are chosen (except for a few alternative ideas). Therefore, there appears a specific need for development, testing and qualification of the radiation detectors for application in fusion reactors. Finally, this also poses a challenge for research activities in fusion technology as no currently available neutron or photon sources provide comparable fluxes and such wide energy-distributions, severely limiting the possibilities to test the detectors for fusion applications, or to determine the radiation hardness of materials for building the reactors.

Presence of large quantities of tritium in a fusion plant brings with itself another unique set of challenges. Due to the danger of its radioactive contamination, it is necessary to confine tritium within the boundaries of its flow circuits in the breeding blankets and in its purification and recovery systems. This adds to the complexity of the mechanical design of TBMs and its associated auxiliary systems in ITER, for example.

1.2.1.2 Essentials of Nuclear Measurements in Reactors

Fusion neutronics is a core area of research on the roadmap to develop power plants. At the stage of the designing of a fusion reactor, it is required to preconceive the radiation environment and, analyze and optimize the architecture, materials and dimensions of the components, shielding etc. to have a safe and functional reactor unit. Computational tools like deterministic and Monte-Carlo radiation transport codes, activation and inventory calculation codes, nuclear cross-section data etc. find immense use serving this process.

On the experimental side of fusion neutronics, the development of adequate and sensitive nuclear instruments and measurement methodologies for the reactor, to feed in real-time information are critical for the stage of reactor operation. The main quantities to be measured are the neutron and photon fluxes and their energy-spectra and if the focus is upon a breeding blanket area, then also the tritium production rate. While *flux* (unit: $cm^{-2} s^{-1}$) gives the time rate of particles crossing a unit surface area in the region of interest, a similar quantity called as *dose rate* (unit: $Gy h^{-1}$) is a measure of the time rate of mean energy imparted by the particles in a unit mass of the matter in the region. These quantities carry information on the basic plasma properties, viz. the fusion power (and so, the Q value), alpha particle production (thereby the departure from burning plasma condition), ion temperature profiles, fuel ratio etc. Fluxes are indirect measures of several other operating parameters, namely the tritium production rate (relevant for self-sufficiency and tritium accountancy), material damage and nuclear heating. Although the derived quantities like tritium production rate can be monitored by monitoring neutron flux, their direct measurement is also critical many a times.

When ionizing radiations interact with materials, (directly or indirectly) electrons or other charged particles (e.g. interstitial holes, nuclides, α-particles, positrons etc.) are produced. For example, neutron interacts through an absorption or scattering reaction producing positively charged nuclides, photons and secondary electrons. Essential idea of a wide variety of nuclear detectors is a purposeful creation of charges by a reaction of the detector's material with the radiation to be measured. To generate an electrical signal varying in proportion to the rate of the charge deposition, an electric field (commonly known as the *bias voltage*) is applied across the ends (electrodes) of the detector volume. Signal is subsequently acquired and transmitted using a series of adequate electronic equipment. The rate of charge creation is proportional to the rate of the corresponding reaction, and in turn, to the count rate of interacting particles entering the volume of the detector. Numerous physical devices are capable of serving this purpose, categorized on the basis of the type of detection material, e.g. *gaseous*, *semiconductors* etc.

A class of nuclear detectors known as *flux* or *dose rate monitors,* are frequently applied for measurements in reactors. A monitor can either provide an energy-integrated value of flux or a coarse energy-spectrum of the flux. The latter variant is called as a *spectrometer*. With regard to the temporal variation of quantities, a detector can be *active* or *passive*. The former have short response times and give real-time flux signals. Whereas, passive detectors show time-integrated flux signals.

1.2.2 Development of Candidate Detectors for EU TBMs

1.2.2.1 Design Constraints for TBM Instruments

For the aforementioned nuclear experiments in the ITER TBM, the fundamental parameters of interest are the neutron and photon fluxes (or dose rates) and their variations dependent on position, time and energy. In addition to this, count rate measurement of tritium is also necessary to judge the breeding performance of TBM. While the high radiation, thermal and electromagnetic fields in ITER make the environment for instruments very harsh, TBMs also have scarce space for integration of diagnostics. Overall, the nuclear detectors for TBM are faced by physical and technical constraints and must fulfil important requirements as, but not limited to, the following.

1. High sensitivity: of one or a group of similar detectors, to the complete range of particle fluxes and energies possible in the TBM.
2. Good neutron-gamma discrimination: as the TBM has a mixed radiation field and many applicable detector types are responsive to both neutrons and gamma.
3. Low response times: needed for operation in tokamaks, which are pulsed devices with high field intensities.
4. Tolerance towards disturbances: major effects are expected due to detector's sensitivity to a magnetic field, noises from EM fields, noises from high temperature and thermal gradients, mechanical vibrations etc. Sensor, cables and processing circuits must be able to withstand these effects.
5. Radiation hardness: this decides the operational life of the equipment.
6. Compactness and invasiveness: essential because TBM has limited space for positioning, and constricted routes (e.g. diameter of some channels is 5 mm) and stringent conditions (e.g. relevant for safety) for integration of diagnostics.
7. Accessibility and lifetime: are important concerns, as once installed the detector will not be accessible during the ITER runs. Online systems, incurring minimal degradation (like, burn up of detection material) in performance over the period of operation are essential, to avoid or minimize maintenance or replacement.

Keeping in view the above necessities, a broad class of detectors are to be studied. Additionally, the reliability of the TBM instrumentation requires fulfillment of the following two points also.

1. Redundancy and diversity: which entail implementation of multiple independent and if possible, physically separated measurement channels with same or different physical principles/methods to measure each parameter of interest. Cross-examination of channels provides a safeguard for the experimentalist against making a wrong judgement based on a faulty signal in one channel.
2. Low margin of uncertainty: requiring a pre-decided range of uncertainties for all quantities of interest. Considering the acceptable limit of the impact of the uncertainties on the measurement of tritium production rate, ± 5% to 10% is the range adopted for neutron and gamma flux measurements in ITER TBMs [16].

1.2.2.2 Candidate Nuclear Detectors

A series of studies to develop, test and qualify reliable and complementary detectors for neutron and photon fields in the European HCLL and HCPB TBMs have been undertaken in a project supported by F4E [16, 17]. Several detection techniques, out of the standard commercial reactor instrumentation [18], have been selected as candidates. For complementarity and diversity, both active and passive detectors have been selected. Responsive to limited ranges of neutron and photon energies, susceptibility to thermal and EM noise, and integrational issues affect most of them.

For active detectors, *diamond detector, silicon-carbide detector, ionization chamber, micro-fission chamber* and *self-powered detector* have been shortlisted [17].

First two of these are semiconductor diode detectors for neutron flux measurements, and within some bounds also the energy-spectra measurements. In a semiconductor detector, nuclear reactions ultimately lead to formation of electron-hole pairs. Under the influence of an externally applied electric field, they drift and form the signal. Single-crystal diamond detectors and variants with artificial diamond have been classically used for neutron and photon measurements in tokamak environment. Using a ^{6}LiF coating, it can also be applied for tritium measurement. Issues with electrical contacts, thermal noise etc. deter the direct use of existing detectors in TBM. Similarly, silicon carbide detectors can operate under TBM-relevant temperatures and provide higher effective radiation hardness than other semiconductor detectors. Efforts are underway to adapt these two concepts for neutron flux measurements in TBM.

An ionization chamber is a gas-filled gamma dose rate monitor, where ion pairs are produced along the track of a gamma-ray. A two-electrode structure in the chamber accelerates the ions to form the signal. An ionization chamber with a coating of fissile material ($^{235/238}$U) can in turn detect neutrons, which is the concept behind a fission chamber. Both these technologies are considered to be relatively mature and are aimed to be applied in TBMs with minor modifications in designs and modes of operation

A self-powered detector (SPD) is a direct current device with two electrodes, one of which releases higher number of electrons due to high cross-section of neutron or photon reactions. The so-created difference of charge between electrodes directly produces the signal. It is a common in-core instrument for fission reactors worldwide, for monitoring of neutron and photon fluxes and reactor power-level. Commercial detectors are tailored for response to thermal neutrons. So, the aim is to develop and test detectors for fusion neutrons and photons.

Among the passive detectors, only the *neutron activation system* is considered for use in TBMs [17]. Selected material samples are irradiated with neutrons to produce activation products (see Appendix 3 for the basic principle). The amount of activation is usually quantified through gamma-ray spectrometry of the activated sample, using semiconductor detectors. Neutron activation is a well-established and highly reliable flux measurement method for reactors. With a set of threshold reactions allowing to work with short irradiation times, it is expected that coarse information on the temporal variation of fluxes and energy spectra can be obtained using this technique also. Studies are underway for integration of the intrusive transport system for samples in the TBM.

1.3 Thesis on Self-Powered Radiation Detectors for Fusion

1.3.1 Objectives of the Thesis and Methodology Adopted

A self-powered detector (SPD) represents a class of neutron and photon flux monitoring instruments used in fission reactor cores worldwide. It is an electrical device with two conducting layers, *emitter* and *collector*, isolated with an *insulator* layer. Emitter, the central element, preferentially interacts with the incident particles, neutrons and photons, leading to release of electrons. Creation of small charges in such a process produces the direct current (DC) SPD signal which is proportional to the incident particles' flux. This detector has inherent advantages of simple measurement scheme, ruggedness, compactness, ease of operation and high reliability. It is less expensive and has a simpler engineering design compared to other in-core detectors. For these reasons, SPDs are desired for use in fusion reactors also.

Commercially available SPDs are tailored for high response to fission reactor radiation fields, mainly thermal neutrons, which makes it difficult to directly use them in fusion reactors. Fusion neutrons have much wider energy-spectra extending to 14 MeV, as well as relatively wider range of photon energies. Additional constraints of the fusion environment, as explained earlier, also demand improvement of the present technology. A detailed study of the detector type for fusion applications has not been done, and is the subject of this thesis.

The main objective is to check SPD's adaptability to fusion environment. For this, the nuclear performance of various types of SPDs are to be evaluated in the radiation fields similar to those in the fusion reactors. This dissertation branched out of the task on the development of candidate detectors for EU ITER TBMs [19]. It is thus, aimed to identify the difficulties in detector design, construction, application and signal interpretation. And further, explore solutions for these problems and recommend method(s) for the design and test of prototype SPDs for use in the TBMs of ITER.

The approach adopted in this thesis is to conduct experimental and computational studies with the currently available and newly-designed SPD varieties. An emphasis has been made on experimental investigations. For a deeper understanding of the signals and predictions for a check of the applicability of SPDs under TBM environment, a Monte-Carlo based modeling scheme has been implemented. The conclusions from irradiation tests and representative simulations have been finally combined to ascertain if the SPDs can be used in fusion conditions or not and if yes, then in what forms.

The starting point of the work is to choose, design and construct test detectors. Some units of commercial *cylindrical SPDs* are procured from the market. To test other layer materials, an openable, *flat sandwich-like SPD* design has been conceptualized and realized in this thesis. Newer test SPDs, with either different geometry, or different material combination, or both, have been constructed. For the testing of these detectors, electronic equipment has been organized, which involves tasks on choice of measurement device(s), establishing signal transmission, acquisition and analyses protocols, and optimization of the method for low-level signal (pA-scale currents, typical of an SPD) measurements.

The irradiation tests of the SPDs have been performed at three facilities, providing thermal neutrons, fast (14 MeV) neutrons and high-energy bremsstrahlung photons. Before the experiments, it is important to have alternative means of measuring or estimating neutron and photon fluxes and energy-spectra in the irradiation positions, as the SPDs are calibrated against them. Therefore, using common experimental and computational techniques, the radiation sources have been characterized, and uncertainty-margins in flux estimations ascertained. These information are useful when analyzing the SPD performance. Then, a series of irradiations of the test detector units have been conducted, and the characteristics of different detector variants and their responses have been determined and compared. At first, a set of reference studies has been performed with chosen detectors, for a complete analysis. The signals from these tests are observed, interpreted and explained. The neutron-photon discrimination, which is an essential characteristic for an SPD to be used in the reactor, has been analyzed for the tested SPDs.

Not all available detectors variants could be tested under all the reference conditions due to unavailability of the irradiation facilities. To compensate for this, they have been tested in the available setups, mainly the laboratory with fast neutrons. These tests give information on the dependence of the SPD's behavior on its various properties, like layer materials, thicknesses, geometry etc. and identifies crucial aspects of SPDs while making conclusions about their applications in TBMs.

The implemented Monte-Carlo model is of immense use in understanding the signals deeply. The results of the modelling, capable of simulating the SPD responses under fusion relevant neutron and photon fields and extended for use with flat geometries, have been compared with the experiments. This establishes the pros, cons and boundary conditions for the usage of this model. Ultimately, the computational studies for predictions of the signals of a set of representative SPD-variants under real ITER TBM conditions have been conducted. This closes the gap for extending the conclusions to reactor scale, demonstrating the capabilities of the modeling tools in feasibility studies, and giving a first impression of the expected SPD signals and their modes of operation.

1.3.2 Structure of the Thesis

The thesis is divided into nine chapters. After an introduction to the field of nuclear fusion and instrumentation development in this chapter, a broad overview of the SPD, its past, present and future are given in the Chapter 2. Starting with the physics of the detector, the chapter gives the background information and insights into its application, its pros and cons, summarizes the long-standing literature on the subject and the focus-areas for current research in this field.

Chapter 3 describes the experimental apparatus for the tasks performed. Here, the design and construction of test-SPDs, considerations for measurement equipment and a concise account of the characteristics of the signal transmission path used in the work are provided. The chapter sets the stage for an understanding of the experimental results discussed in next chapter(s). Chapter 4 presents the details of the three irradiation facilities utilized for the experiments, describing the exercise on and the results of source characterization using nuclear detectors and Monte-Carlo modelling, along with presenting the uncertainty estimates for various setups.

In the next four chapters, the results of different studies performed in this work are presented. The Chapter 5 provides results, conclusions and discussions of the full experimental analyses of two reference SPDs. The chapter is divided based on the radiation source: thermal or fast neutrons, or high-energy photons, under which the responses of SPDs are tested. In it, the signals from different tests are shown, discussed, compared and utilized to understand the neutron-photon shares' ratio in mixed fields.

The theoretical basis of the Monte-Carlo simulations and the computational method utilized in the thesis is presented in Chapter 6. General scheme and the procedure for the further analyses of the results, as developed and implemented in this work are described. Following this, the chapter shows the comparison of reference SPD experimental measurements with the ones calculated using this model, for all three irradiation setups. A concise discussion on the model is also given at the end.

Chapter 7 presents experimental results of comparing SPD's behavior with change of some essential characteristics, namely, the material of emitter and collector, thickness of different layers, and the electronic circuit components in the SPD assembly. The aforementioned computational study of representative cylindrical SPDs under radiation fields expected in the ITER TBMs are shown in the Chapter 8. And finally, Chapter 9 of the thesis summarizes the main aspects of the studies and their conclusions towards the objectives of the thesis while giving an outlook into the possible scientific investigations to further this work.

Parts of the results obtained during this work have been presented internationally through oral contributions to the conferences and publication of papers in renowned peer-reviewed journals [20-24].

2. STATE-OF-THE-ART OF THE SELF-POWERED DETECTORS

A self-powered detector, abbreviated as SPD, is a class of in-core neutron and photon flux measurement devices used in nuclear power reactors [18]. In fission reactor cores, several units of SPDs are installed in the instrumentation channels and at its surrounding locations. They are online detectors whose signals vary in proportion with the incident fluxes of neutron and/or photon. A combination of these signals is used to create a spatial map of the neutron and photon fluxes in the core. A variant of SPD with short response time is commonly used as one of the multiple redundant techniques for monitoring the reactor power level, in normal and emergency situations.

2.1 Physical Operating Principle of an SPD

Certain types of atomic or nuclear processes lead to the emission of charged particles. The beta decay is a fundamental radioactive process of this type, in which an unstable nucleus emits an electron (e⁻), designated as *beta minus (β⁻)* particle accompanied by an anti-neutrino ($\bar{\nu}_e$). An example of this, is the decay of the ^{52}V nucleus to ^{52}Cr nucleus with a half-life of 3.74 min.

$$^{52}_{23}V \rightarrow\ ^{52}_{24}Cr + e^- + \bar{\nu}_e \qquad . \qquad\qquad \text{(Eq. 2.1)}$$

Another such process is the Compton interaction of a high-energy photon leading to the ejection of a loosely-bound or free electron. Irradiation of materials by neutrons or photons can initiate such electron-emission processes.

If the electrons from such a process in a conducting material are stopped in another conducting material, it creates a potential difference. This is the so-called *radioactive charging principle* which has been proposed for production of high voltages [25] since the early days of nuclear physics research. This principle can also be used to measure the flux density of the neutrons or the photons. One of the first devices based on it was constructed and tested by Mitel'man et al [26] in the erstwhile Soviet Union. The device, named as a *converter* consisted of a wire of rhodium as the electron emitter element. The isotope nucleus ^{103}Rh undergoes a radiative capture reaction with thermal neutrons producing unstable nucleus $^{104g/m}$Rh, which then decays by β^- emission. Replicating the device as neutron flux monitor and identifying many new emitters like ^{51}V, ^{115}In, ^{107}Ag/^{109}Ag etc., J. W. Hilborn formally named it a *self-powered neutron detector (SPND)* [27], which also came to be known as *Hilborn detectors*.

An SPD is an electrical device with a multi-layered design, having two conducting electrodes. The active electrode is called *emitter* which emits electrons on neutron or photon exposure and attains high positive charge. Its material is chosen to have a high cross-section of interaction with neutrons or photons depending on the type of radiation intended to be measured. The other electrode is called the *collector* and is designed to stop the electrons coming from the emitter. A layer of dielectric *insulator* is usually placed in between them to provide electrical insulation and slow the electrons down. Inter-electrode separation of charges creates a potential difference. This can be measured as a direct current or a voltage across a load resistance. Traditionally, the components of an SPD are arranged in a coaxial cylindrical fashion. However, they can be organized in a flat geometry as well. Figure 2-1 shows sketches of SPDs in cylindrical and flat geometries with the electrical connection across an ammeter and main interactions leading to the emission of electrons.

There are three main electrical processes in the emitter which lead to the production of electrons and therefore create currents in SPDs, as described in the following.

1. *(n, β⁻) process:* In this process, neutron absorption reaction leads to the formation of a radioactive daughter nuclide in the emitter that undergoes beta minus decay. The signal due to this process does not vary promptly on varying the incident flux as the decay has a half-life. Known as *delayed SPND*, this is the most common type of SPDs used in the fission reactors. The neutron capture (n, γ) reactions in materials like Rh, V, Ag etc. lead to beta decays with half-lives from seconds to minutes. With fast neutrons, threshold reactions like (n, p), (n, α) etc. can also be the primary reaction for this process to occur. Emitted beta particles have high energies (1-10 MeV) leading to a lot of them crossing the insulator layer and making a strong signal. With high and well-known cross-sections of capture reactions with thermal neutrons, delayed SPNDs have negligible interference from secondary processes in such neutron fields.

2. *(n, γ, e⁻) process*: In this process, neutron interaction leads to the emission of high-energy photons in the emitter material. The photons interact through

photoelectric effect, Compton scattering and pair-production routes to produce fast secondary electrons which form the detector signal. This is a two-step emission process unlike (n, β^-) and is relatively less probable and less effective in creating a signal in fission reactors. But, the process is prompt and so, the signal due to it varies instantly with a variation of flux. Based on this process, *prompt SPND*s are constructed. These are good choices for reactor power-level monitoring as they have an instantaneous response. Co, Hf and Pt are common emitters for such an SPND, where capture gammas make the signal.

3. *(γ, e^-) process*: In this process, external photons, e.g. reactor gammas from the surrounding of the detector, are detected through secondary electron emission in the emitter. This process also makes a promptly varying signal. This is the principle at the heart of a *self-powered gamma detector (SPGD)*. Due to their higher interaction probabilities with photons, materials with high atomic numbers (Z) like Bi and Pb are suitable emitters for SPGD.
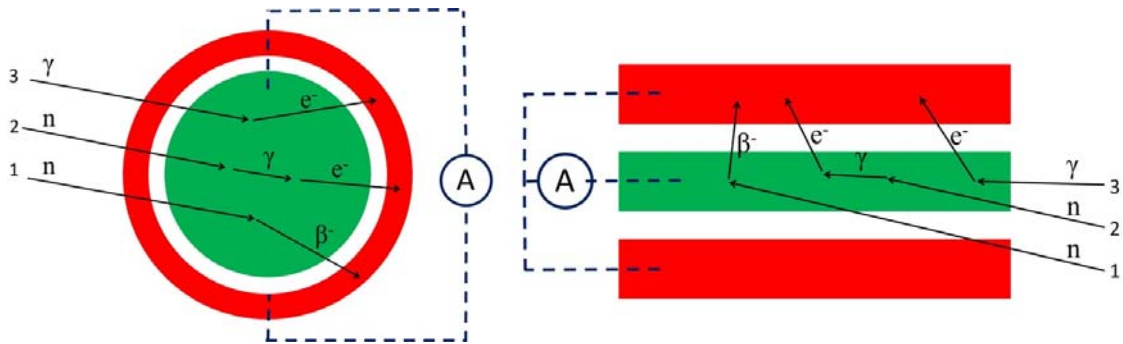
Figure 2-1: Cross-sectional sketches of SPD in (left) cylindrical and (right) flat geometries. The emitter layers are shown in green-coloured central regions, collector layers in red-coloured outer regions and insulation layers in white. Three important electron emission processes in the emitter are depicted: 1– (n, β^-), 2– (n, γ, e^-) and 3– (γ, e^-). Current measurement connection between emitter and collector across an ammeter (A) is shown for both cases.

It is to be noted that in the latter two processes, an electron can be ejected out by any kind of photon. The SPDs are applied in reactors, where the majority of photons are prompt or delayed gamma-rays from the fission products. The traditional nomenclature (SPGD) and depictions of processes using the symbol γ are retained in this thesis.

Any individual unit of SPD must be designed with only one of the three processes in mind to simplify the post-processing of signal, even though smaller contributions from other two processes are always present.

2.2 Application of SPD as an In-Core Device

2.2.1 Characteristics of a Typical in-core SPD

Traditionally, an SPD is constructed in the same way as coaxial cables are made. A thin wire or rod of emitter material is packed in a tube of collector material with tube

or beads of mineral insulation between them. The emitter is directly linked to the central conductor of a mineral-insulated (MI) signal transmission cable. A photograph of a commercial vanadium SPND with its MI cable, is shown in Figure 2-2. The active detector is the part which contains the emitter, usually measuring from 5 cm to 20 cm in length and from 0.1 cm to 0.5 cm in (outer) diameter. The detector is integrated in core and at out of the core locations in most of the power reactors worldwide.
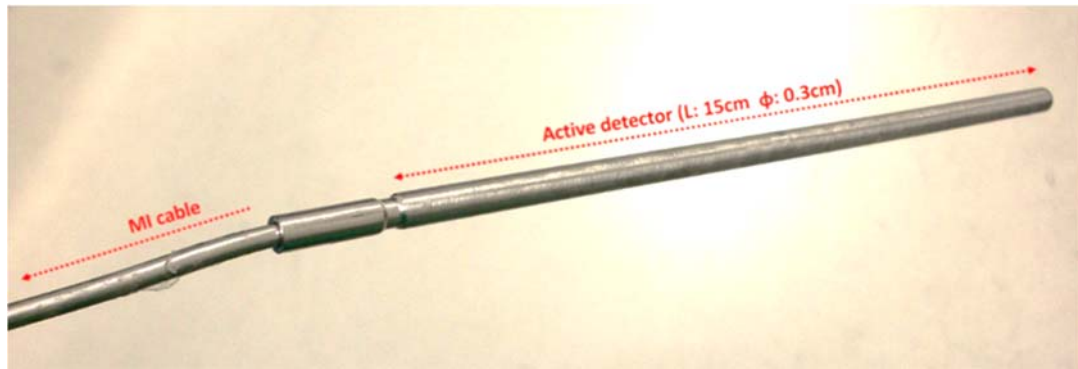
Figure 2-2: Photograph of a commercial SPND unit depicting the active volume containing emitter and the conjoined mineral-insulated (MI) cable. Length (L) and diameter (φ) of the detector are also given.

A list of the common emitter, insulator and collector materials used in commercial SPDs is provided in Table 2-1. Most common emitter material choices for all three variants of SPDs, delayed SPND, prompt SPND and SPGD, are given, with their respective SPD-types indicated in parentheses. These can be combined with several choices of insulators and collectors. Whereas most of the present day SPDs use alumina for insulator and Inconel-600 alloy for the collector, alternative choices are also shown in the table. Plastic (PVC, PMMA, etc.), not suitable for use at high-temperatures in power reactors, is often an easier insulator to use in laboratory-based research with SPDs. Aluminum, mentioned as a collector, is one of the many pure metals which has been tried as both emitter and collector in early SPNDs.

An SPD offers following advantages over other choices of detector technologies for in-core instrumentation:

1. It has a rugged and robust design, and compact shape and size. In addition, it works without a *bias voltage supply*, which is typically a requirement for many common radiation detectors, like proportional chambers, those based on semiconductors etc. It is a high voltage applied across the active detection volume, which facilitates the transport and collection of charges for signal generation. An SPD relies on the inherently-produced charge-separation, leading to drastic simplification in its design and usage. These characteristics make it highly suited for integration in zones with limited access, like reactor core.
2. It is an online detector, giving real-time or nearly real-time information about the radiation field.

3. It usually does not contain materials excluded by the radio-protection, export-control or the non-proliferation guidelines, making it easier to acquire, test and integrate into experimental facilities, unlike for example, fission chambers and gaseous detectors.

4. Due to its simpler engineering design, it is relatively easier to fabricate and therefore cheaper than other common detector classes, namely the semiconductor-based detectors, fission chambers etc.

5. Its signal measurement method and readout electronics are not as cumbersome as other detector choices making it a relatively simpler detector to use.

Table 2-1: List of commonly used layers' materials for the self-powered detectors.

Emitter	Insulator	Collector
Rhodium (Delayed SP<u>N</u>D) Vanadium (Delayed SP<u>N</u>D) Cobalt (Prompt SP<u>N</u>D) Platinum (Prompt SP<u>N</u>D) Bismuth (SP<u>G</u>D)	Alumina (Al_2O_3) Magnesia (MgO) Beryllia (BeO) Silica (SiO_2) Plastic	Inconel-600 Stainless Steel Aluminum

Soon after its invention, SPD was adopted as a part of in-core instrumentation for reactor cores. Many variants of self-powered neutron detectors were constructed and tested worldwide [28, 29]. For a long time, the detector class was applied exclusively as neutron field monitors but similar detectors for gamma (SP<u>G</u>D) and electron fields were also developed in due time and implemented [30, 31]. In more recent years, many new SPD types have been developed and tested for reactor [32-35] and medical [36] applications. SPDs are now considered one of the most robust and reliable choices of in-core flux-detectors owing to their successful performance for decades.

2.2.2 Components of an SPD's Output Signal and their Interpretation

In common application of SPDs, DC signals are measured and the flux intensities are determined by multiplying the SPD current values with their known sensitivity values (defined in the following). The radiation field of a reactor, in which an SPD is applied, is a mixture of neutron and photon fields. Even though an SPD is constructed with one of the three main processes in mind, its signal has contributions from all of them and many other interfering processes. Knowledge of their relative contributions is important for reliable interpretation by the reactor operators.

A significant complexity is introduced in the interpretation of an SPD signal by delays incurred in a change of the signal with a change in the flux. These delays are usually quantified by the *response time (T_R)*, which is defined as the time required for the signal to reach approximately 63% of the saturation signal on a sharp change of flux [37]. Apart from the neutron (or gamma) flux which is intended to be measured, there are various contributing factors with varying response times. If the response times associated with the major factors are different then their effects can be discriminated from each other by evaluating the profile of the signal in time. The quality and

reliability of this discrimination depend strongly upon the magnitude of differences between various response times and magnitudes of the currents. A common procedure to do this starts by recording the detector signal under constant flux condition until equilibrium is achieved between all time-dependent processes and the detector signal becomes constant. Following this, a sharp change in reactor power is made (e.g. scramming of the reactor, which is the automatic shutdown of the reactor by sudden insertion of control rods into the core, often implemented in emergency situations.) and then the approach to a new equilibrium in the detector signal is recorded.

A typical time-profile of a reactor SPD is shown in Figure 2-3. This signal has been measured by irradiating a commercial SPND in a fission reactor, the details of which are postponed for chapters 4 and 5. The components of the signal, as labeled, are divided into two distinctly-visible categories, based on their response times:

1. Prompt component: It is the part of the signal which varies immediately with a change in the incident flux. The (n, γ, e⁻) and (γ, e⁻) are the common processes behind this component. Whereas the signal due to the former process is an indirect measure for the neutron flux, the latter is for the photons. Because these two have no associated time-lags, it is difficult to separate them. A reliable, practical method to separate them is given by Monte-Carlo simulation of the detector response in the mixed neutron-photon field, as explained in Chapter 6.

2. Delayed component: It is the part of the signal which mostly arises due to (n, β⁻) process, which has a characteristic half-life ($T_{1/2}$). The detector shows a signal constant in time only when the radioactive decay process is in equilibrium with the creation of nuclides through neutron reactions. For short-lived nuclides, which are the ones considered for SPNDs, durations equal or more than four to five half-lives are assumed to arrive at an equilibrium state. Decay gammas from activated materials of the detector or its surrounding also contribute to the delayed part which can be eliminated, for the purpose of studying the signal, by extracting the detector out of the core immediately after the shut-down.

Both these components are aggregates of signals originating through multiple routes; they both vary linearly with the incident flux, but they are independent. No hard and fast rules are prescribed for precise separation of prompt and delayed parts in SPDs used in power reactors. For the delayed parts, it is customary to extract the decaying signal part, fit an exponential decay curve to it and extrapolate it to the time of changing of the flux. The difference of the so-obtained delayed current from the total saturated current can be accepted as the prompt component. Very short-lived nuclides, generating quickly-changing (n, β⁻)-type delayed signals can be mixed with the prompt component. Likewise, prompt (γ, e⁻)-type signals coming from decay photons in the SPD's surrounding can be adding to the delayed component. Normally, these two are considered negligible. But, extensive, application-dependent experimental tests and computational simulations are undertaken to reasonably segregate the two components, giving a *prompt to delayed (P/D) ratio* of the signal. In turn, they also resolve the signals into parts due to neutrons and photons. Using the alternative flux measurements in the position of the detector and resolved signal components, neutron and photon sensitivities of the detector are calculated. Their ratio is known as the *neutron to*

gamma/photon (n:γ or N/G) ratio, a frequently reported characteristic of an SPD in a specified mixed-radiation field.
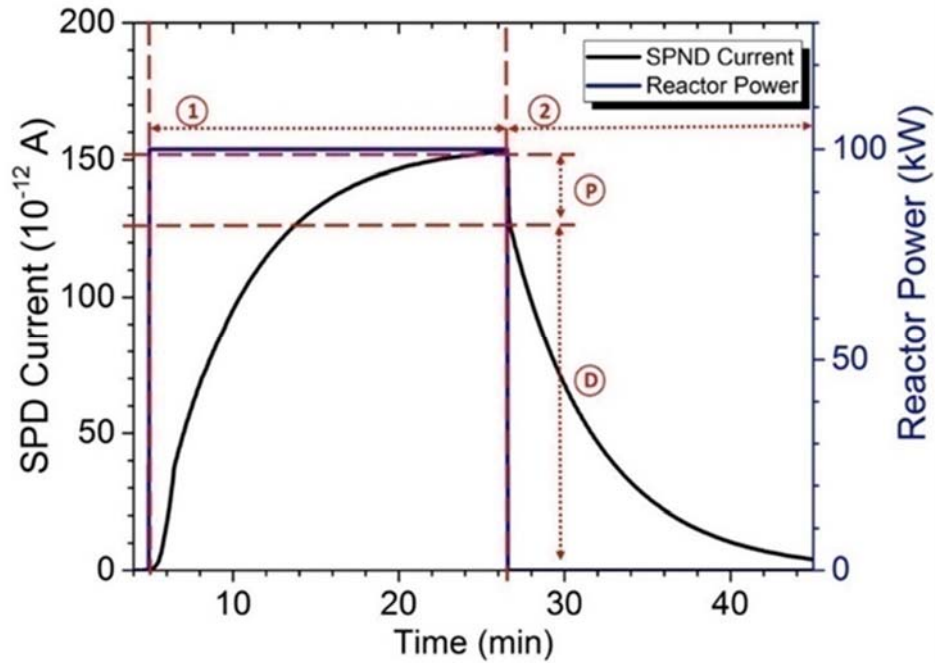
Figure 2-3: Example of a time-dependent measurement of an SP<u>ND</u>-signal, depicting the prompt (P) and the delayed (D) components, as the reactor power is changed from 0 to 100 kW and back (shown on second Y-axis). The region labelled as (1) shows the duration of irradiation when the signal is approaching an equilibrium state and (2) shows the subsequent decay. This is a signal obtained from a real measurement of a commercial SP<u>ND</u> in a thermal reactor (more details in Chapter 5).

The SPDs exhibit excellent signal-flux linearity as deemed after years of experience, making them highly trusted detectors. In practical application, this linearity is given by the *sensitivity* of the SPD.

$$Sensitivity\ (S) = \frac{SPD\ Current\ (I)}{Incident\ Flux\ (\varphi)} \quad , \qquad\qquad (Eq.\ 2.2)$$

with SPD-current in units of Ampere (A) and the flux in particles per cm^2 per second (cm^{-2} s^{-1}), sensitivity is reported in units of A cm^2 s. It is usually determined by cross-calibrating the SPD with other flux detectors. Flux is determined using an alternative detector, like neutron activation foils or gamma dosimeters. So-called *unit sensitivities* reported in units of A cm s are relevant for situations when the same detector is manufactured or used with different lengths. Sensitivity is an invariant attribute if the energy spectrum of incident particles does not change. It changes with a change in the detector position with respect to the neutron or photon source, therefore the complete information about detector's integration must be specified alongside the reported sensitivity. Nevertheless, time-averaged sensitivities over long-term operation(s) of

permanently integrated SPDs in power reactors are often reported for reference (e.g. a typical vanadium SP<u>N</u>D has a sensitivity of the order 10^{-21} A cm^2 s [28]).

2.2.3 Important Practical Issues in the Usage of SPDs

Although SPDs are widely recognized and used detectors, they do suffer certain limitations making them a subject of active research and development globally. In the following, some important practical issues in the application of SPDs in reactors are discussed. Adding to these brief discussions, more details, specification of the origins, scope, and the mitigation techniques for these issues, etc. are discussed in Chapter 3, where the experimental setup involving SPD based measurements are described.

An inherently low-level of DC signals produced by SPDs is arguably its main disadvantage. The SPD currents range from the orders of pA to mA (10^{-12} to 10^{-3} A), which are quite small for the noisy environments they are used in. Low-level measurement becomes a major challenge for SPD applications. These measurements are prone to electromagnetic interferences, radiation-induced effects, temperature changes, mechanical disturbances etc. Spurious currents are produced at various stages of signal creation and propagation (more details in Section 3.3 and Figure 3-7). Often, some of these effects themselves create currents in the range of detector signal and limit the scope of its application. Extreme care needs to be taken in the detector design, manufacture, cabling, fixture-design, integration and choice of instrument and so on, to eliminate or reduce these currents [38]. For the experimental activities undertaken in this thesis work, this aspect has received due attention. Some inevitable issues of the electronics for SPD, and the solutions identified for them, are pointed out in much details in the next chapter, but it should be stressed that it is a much wider field of study and not limited to these, and the solutions are often customized for a particular situation.

A second major difficulty in the usage of an SPD is its high susceptibility to the secondary effects. One of the three main processes: (n, β^-), (n, γ, e$^-$) and (γ, e$^-$) in emitter creates the primary signal of an SPD. While the primary process dominates, several other mechanisms generate similar types of currents in the detector. In one of the early works [39], 76 explicit mechanisms were reported to sophisticate the signal of SPDs, some of which can be studied in the modern day modelling of SPDs [40]

At first, an SPD is designed based on one of the main three, emitted-based processes but smaller contributions from the other two processes are always present. A much-involved problem is with the SPD applied in fast neutrons field, as more than one (n, β^-) and (n, γ, e$^-$) channels come into existence due to similar cross-sections of multiple fast neutron reactions.

Secondly, these three categories of processes also occur in the collector and insulator layers. Depending on where the electrons from these processes stop in the detector (emitter, insulator, collector or outside), their contributions to the net current are either positive, negative or zero. Furthermore, these and other electron-emission phenomena are highly probable in the materials in the surroundings of the detector also, like the mounting arrangements, irradiation channel walls, source components etc. Fast electrons emitted by fission products in a reactor core can also travel and stop in the

emitter layer disturbing the total signal. In previous studies with SPDs in reactors, effect of fission betas emitted within 1 cm distance from SPD have been found to perturb the signal by ±50% or more [40]. Decay of neutron-activated materials can also affect an SPD's signal in a similar manner. Such effects lead to a so-called *extended behaviour* of SPD-type detectors, in which a considerable portion of the signal can arise due to undesired events in its vicinity. While the *active detector* is the part of the multi-layered region with emitter in it, this behaviour leads to an *extended detector* which can respond to events up to a few centimetres around the active detector.

Thirdly, because the signal cable also has a cylindrical multi-layered design with two conductors, the SPD-like effects producing small DC signals can occur in cables as well [41-43]. These can either be radiation-induced electron production processes, or processes of thermo-electrical or electromagnetic origins. Quality of the build of the cables and other circuit elements, and noise-reduction measures like grounding etc. become important in SPD related experiments.

All the secondary processes can sometimes be parasitic in nature, as they can interfere with the primary signal adversely. Generated simultaneously in the detector components or its environment, these mechanisms have varying orders of effect on the ultimate signal measured. Most of them also vary with the incident flux. There are no ways of eliminating them; therefore, one relies largely on experimentally measuring them and subtracting from the signal, and theoretical study of detector's response. Geometrical optimization of the detector design can help in reducing some effects.

The two previously mentioned categories of issues combine to make the processing and interpretation of SPD's signal very tricky and challenging, which is the final major issue in its application. Added to that, over long-term neutron exposure in a reactor, the density of the emitter isotope, originally used in small quantities (volume < 1 cm^3), decreases. Because of such an *emitter burnup*, the sensitivity of detector reduces over time. With the decline in the rate of one process, other competing processes show an enhanced effect on the signal. A material with higher reaction cross-section (e.g. Rh) makes more sensitive detector but the degradation in detector sensitivity is more rapid than the others (e.g. V). Additionally, the delayed SP<u>N</u>D category has high response time and the detector signal in transient conditions is complex to interpret. However, it has highest signal amplitudes and is the most desired one.

To efficiently monitor the reactor flux changes, especially the smaller fluctuations, an online signal processing system is required to bypass the mentioned last category of issues in SPD's application [44]. The burnup, at first, is accounted for, on a routine basis by performing time-dependent inventory calculations and incorporating them in the signal processing algorithms. Secondly, such a system takes the measured delayed signals in real time, correctly applies the characteristic response times of the detector and supplies promptly varying signals for the reactor operators. It is important to point out that there are more than one or two reaction channels which can create currents, most of them contributing varying portions of the net delayed signal. To reliably unfold multiple delayed processes and extract the information on incident flux, especially in a mixed field, is a highly complex job and algorithms are continually evolving with more and more feedback from the experiments.

3. DEVELOPMENT OF TEST DETECTORS AND THE EXPERIMENTAL APPARATUS

The operating conditions for nuclear detectors in the ITER TBMs are highly detrimental and their integration and maintenance are also challenging. Any detector installed in TBM must sustain harsh conditions over the period of ITER's operation while having a high response to the unique neutron or photon spectrum. On one or the other grounds, most of the detectors from the market are unsuitable for direct application in TBM and need adaptations. On these lines, the SPDs have been under investigation in European laboratories in last few years [19-24]. This chapter presents an overview of the development of neutron and photon test SPDs and their measurement setups, as done in this thesis. The broad approach for experimental tests under different irradiation conditions and essential aspects related to them are also briefly described. The contents of the chapter can be broadly divided into two parts. The first two sections talk about the development of test SPDs, and the third is dedicated to elaborating the apparatus and in specific, the characteristics which are important for low-level SPD measurements.

3.1 Selection of Materials for Test Detectors

A principal task in this thesis has been to shortlist candidate SPD materials for higher sensitivity towards the wide spectra of neutrons and photons expected in the TBM.

3.1.1 Emitters for Fusion Neutron and Photon Sensitivity

Usually, the radiative capture (n, γ) reaction is the basis for the (n, β⁻) process in a classical delayed-SPND. This is majorly a slow-neutron reaction and the SPND is tailored for thermal neutron measurements only. In contrast, threshold reactions like the

(n, p), (n, α) and (n, 2n) are feasible with the fast fusion neutrons. An SP<u>N</u>D with such a reaction gives an explicit way, via the half-life of its product, to discriminate the flux of neutrons faster than the threshold energy. This can add a coarse information on the energy-spectrum of neutrons. But, the cross-section of any such reaction is quite low, which is the paramount challenge in the design of a delayed fast neutron SPD.

Most of the fast neutrons (in the MeV range of energies) cross the detector material without interactions. In Figure 3-1, energy-dependent cross-sections of various neutron reactions in vanadium are shown. The cross-sections of usable reactions in high energy (near 14 MeV) region are lower than the ones in thermal-energy (near 25 meV) region by more than two orders of magnitude. This makes a delayed fast neutron SP<u>N</u>D to produce lower signals. Also, multiple channels of reactions are possible at higher energies, leading to many competing routes for current-creation in fast neutron SPDs.
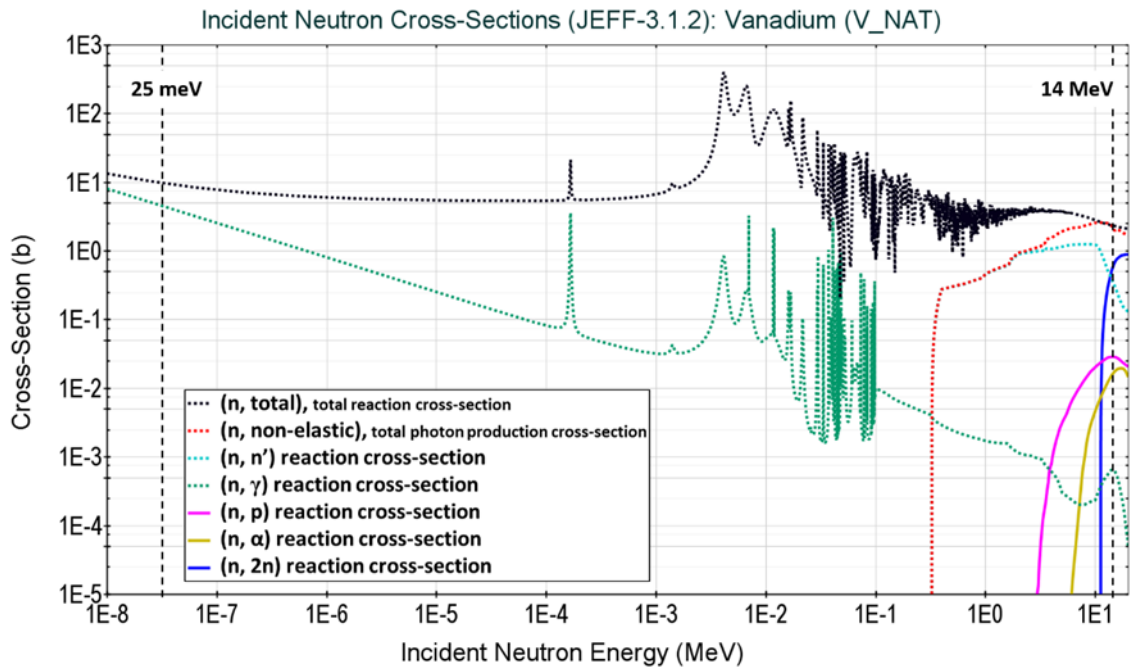
Figure 3-1: Cross-sections vs. energy for neutron-induced reactions in natural vanadium, extracted (using code system JANIS [45]) from the JEFF-3.1.2 evaluated nuclear data library [46]. The total photon production cross-section (dotted red curve) is also shown to present the dominance of prompt route of neutron signals in SPDs for fast neutrons.

The criteria, given in the following, for choosing emitters for high sensitivity to TBM neutron spectrum resulted from the irradiation tests of three standard SP<u>N</u>Ds procured from the market [19]. For obvious reasons, the delayed-SP<u>N</u>D type was deemed favorable for neutron monitoring and was initially proposed for further studies.

1. Conducting materials: electrical conductivity is necessary to make an electrode out of the emitter material, for which stable metals are most suitable.
2. High beta emission probability of neutron-activation products: materials producing nuclides undergoing beta-minus decay with high probability offer

lower interference from competing current-production mechanisms. Greater than 50% intensity for beta-minus channel has been taken as the basic criterion but practically, most of the chosen nuclides decay 100% through this channel.

3. High energy beta electrons: faster electrons have larger chances of crossing the insulator layer to contribute to the current. The mean free path of electrons varies from material to material. A few hundreds of keV, the higher the better, has been taken as enough to allow the electron to reach the collector for signal-creation.

4. Short half-life of emitter nuclide: the response time of a delayed-SPND is determined by the half-life of the beta-emitting product nuclide. Shorter half-life results in a faster detector. ITER is a pulsed device with pulse sizes of 300 s to 3000 s, for which this factor becomes very important. However, there are very few nuclides theoretically capable of providing fast enough response. For preliminary selection of emitters, around 600 s has been taken as a rough limit on half-lives, from which the ones providing a suitable compromise for time-resolved monitoring of flux in TBM are shortlisted for further studies.

5. High saturation activity in TBM neutron spectrum and flux: SPND with rhodium emitter resulted in tens of pA current on irradiation in a fast neutron facility [19]. The specific activity corresponding to the (n, β^-) reaction in this case is of the order of 10^8 Bq g^{-1}. This has been taken as a lower limit for saturation activities of reactions in candidate materials. The effective cross-section of an (n, β^-)-type reaction is a crucial factor for comparison of specific activities.

The selection procedure for emitters starts with tabulating metals undergoing suitable (n, β^-) reactions with fast neutrons. The unfit materials have been sorted out based on the above-mentioned criteria. For the final criterion, the fitting reactions have been analyzed through calculation of their effective cross-sections with *FISPACT* [47]. FISPACT is a multi-physics code system for radioactivity growth and decay calculations, used to determine the inventory and decay radiation source terms in irradiated materials. The complete list of analyzed emitter materials is presented in Appendix 1, with the nuclides produced in various neutron reactions, their half-lives, mean beta energies and effective reaction cross-sections for HCPB TBM and 14 MeV neutron generator spectra. Leaving some exceptions, details of the reactions which do not strictly fulfil one or more of the criteria are crossed out. Some outstanding examples of test emitter materials include: Be, Na, Al, V, Cr and Ag.

Be and Cr have been regarded as main candidate emitters for the purity of their responses to fast fusion neutrons in the preliminary activities for SPD developments for TBMs [16, 19]. Beryllium almost exclusively responds by ^{9}Be (n, α) ^{6}He reaction. With a very short half-life of 0.81 s, this can serve as a *pseudo*-prompt SPND if realized. It has a threshold at the neutron energy of around 0.67 MeV, however, the cross-section is negligible till around 1 MeV. The effective cross-section in 14 MeV neutron spectrum and for ITER TBM is about or below 10 mb. Chromium, on the other hand responds mainly through ^{52}Cr (n, p) ^{52}V reaction in its main isotope, without severe interference from any other reactions. Half-life of ^{52}V is around 224 s and the effective cross-section of this reaction for 14 MeV neutrons is about 70 mb, making it also a good choice for testing in 14 MeV neutron sources in labs.

Both Be and Cr present physical difficulties for use as emitters in SPDs. Be is a hazardous element and can potentially cause respiratory issues if its microparticles are inhaled or ingested [48]. Although it poses little or no specific danger in its solid and clean form, special handling procedures are essential to use Be in labs (and in reactors). At the same time, Cr in its solid and pure form is quite fragile, which makes it difficult to make rugged electrical contacts in a detector with Cr emitter. In old literature, SPNDs with both Be [49] and Cr [50] have been proposed but seldom tested experimentally.

During the deeper examination of relative interaction cross-sections in the selected materials, the (n, γ, e⁻) process based prompt-SPNDs have also been found suitable for fast neutron monitoring. One recognizable reason is that in fast neutron fields materials are expected to emit high-energy photons (from different reaction channels) with comparable or more probability than that of emitting betas. This is clear from the cross-section curve for the total photon production ((n, non-elastic) reactions) shown in Figure 3-1. No special constraints for the emitters of prompt-SPNDs have been identified in this dissertation but the feasibility of their application in TBM is explored, with the same emitter materials as in the case of delayed-SPND.

For photon-detection, using an SPGD, emitters should have high probabilities of (γ, e⁻) interactions. A wide spectrum of gamma rays in TBM field means that all major secondary electron production processes are probable. But, most of the photons lie in intermediate energy range. Compton scattering has more chances of occurrence, compared to pair production and photoelectric effect in this energy region [18, 51]. In this kind of scattering process, atomic electrons act as the scattering targets for the incident gamma ray. With the increase in the number of electrons in atomic shells of the emitter material for an SPD, the probability of the electron-emission process and the SPD response increase. Therefore, high Z materials are well-suited and often used for SPGDs. One of the standard choices, i.e. Bi has been selected through a computational method in Chapter 8, while other test SPDs have been checked for photon responses in experiments.

Besides the electron emission characteristics explained above, practical aspects of detector design, development and operation play a critical role in further constraining the choices of testable materials. Two important factors mentioned in the following points have been considered while choosing the materials for testing in this work.

- Physical and chemical properties have a huge impact on the test detector development. The physical state of the material, its surface properties for stable electrical contact with the lead cable, electrical conductivity, balance of strength and flexibility for compact (sub-millimetre scale) design, ease of handling etc. are crucial. To illustrate this with an example, it can be pointed out that Na and In, among the selection of emitters, are liquid at operating temperatures of TBM, becoming challenging for design of SPDs.
- Material and detector costs restrict the number of experimental tests that can be performed. Material layers in SPD have small dimensions. Expensive mechanical processes are required to get them. Thus, only a few emitters with high electron emission potential and cost-effectiveness have been preferred.

Ultimately, in this work V, Be, Ag and Inconel-600 (Cr-Ni alloy) have been employed as the main SPD emitter materials for different kinds of experimental tests.

3.1.2 Materials for Collectors and Insulators

For the enhanced sensitivity of an SPD, choosing a correct pair of insulator and collector materials is also essential. The process of choice of an apt material combination is long, rigorous and often relies on trial and error techniques with a series of parametric experiments/computations. The basic criterion for both is a lower contribution to the net emitter charge. A wide range of choices could not be probed into in this work, but basic theories for optimum material combination have been practically tested with standard and a few newer materials.

Collector, also known as *sheath*, should be made with a thin layer of metallic material. Lower thickness reduces the reaction rate with neutrons or photons. The metal (or alloys, as often chosen) should show long-term stability under the harsh reactor environment. Cross-sections of neutron and gamma interactions should be low. For the neutrons, the choices are very limited in fusion environment with very small cross-sections of most of the materials, even emitters. The trick is to use a material which has no or negligible probability of emitting electrons through (n, β^-) process. Regarding this, niobium has been found suitable and tested. For low-response to photon through (γ, e^-) process only considerable material property is low Z. Graphite foils have been used in test-detectors to study its effect on reduction of gamma-induced interference from collectors. In harsh media, the fragility of graphite will need to be supported by use of a metallic backing to it. The most common sheath materials in SPNDs, Inconel-600 has also been chosen for test of compatibility with the new emitters.

Insulator materials are also submerged in the environment of SPD application. Low-neutron and gamma activity, high mechanical strength and long-term electrochemical stability are in that context, the key concerns. Insulation's quality changes over time due to various environmental, temperature and radiation-induced damages [52]. Degradation can create leakage currents. In this work, alumina (Al_2O_3) has been chosen as the main insulator in test-detectors. Being the most common SPD insulator in the market, it also proves to be an economical option for use in the laboratory.

3.2 Design and Construction of Test Detectors

Three alternative designs of self-powered detectors (SPD) have been tested and verified in this thesis: commercially-available coaxial cylindrical SPDs and two variants of newly-conceptualized flat sandwich-type SPDs.

3.2.1 Cylindrical Test-SPDs

Three commercial SPNDs were bought from the market by the partners of F4E for preliminary experiments preceding the tasks undertaken in this dissertation [16]. They have been utilized here for further studies.

With the design proposed together by the two partners of F4E, a fourth customized SPND for the test as a fast neutron detector has been produced. Henceforth known as *Cr-SPND*, this is an entirely new detector with chromium emitter and stainless-steel collector. For ease of manufacturing, its dimensions have been kept in the regular SPNDs' ranges. It should be noted that the collector of Cr-SPND is made of steel instead of the

usual Inconel-600 alloy. Inconel-600 is composed of nickel and chromium. High amount of chromium in the collector electrode cancels the effect of emitter made of the same element, reducing the overall current.

The modes of operation, either delayed or prompt SP<u>N</u>D or SP<u>G</u>D, of these detectors in TBM is still unknown but they are used as SP<u>N</u>Ds in fission reactors. Therefore, they are named as SP<u>N</u>D for simplicity and uniqueness of names in this thesis. Figure 3-2 shows a photograph with the four cylindrical SPDs. Table 3-1 summarizes the radial build-up of the four SPDs with the material and approximate sizes of the three layers (from manufacturers' datasheets) in each of the detector units. While an SPD is usually longer, the active length is equal to the length of the emitter wire. For the test SPDs here, this was 10 cm. A delayed-SP<u>N</u>D with rhodium emitter, named as *Rh-SPND*, another delayed-SP<u>N</u>D with vanadium emitter, henceforth known as *V-SPND*, and a prompt-SP<u>N</u>D with cobalt emitter, henceforth designated as *Co-SPND* are among them.
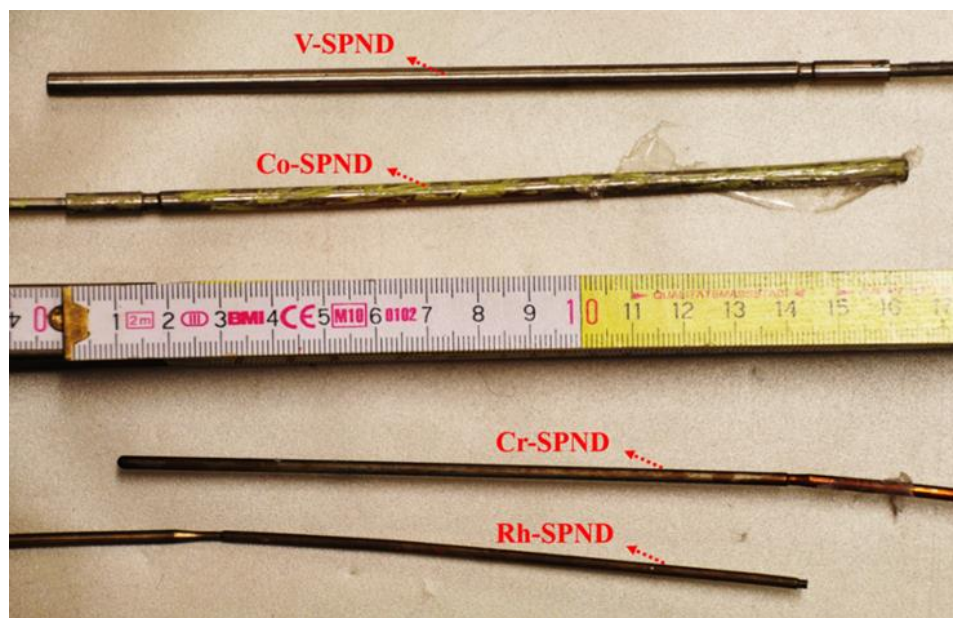
Figure 3-2: Photograph showing the detector sections of four cylindrical SPD variants. For detailed examination in this thesis, only V-SPND has been utilized. Other detectors have been tested in preliminary studies.

Table 3-1: Materials and approximate dimensions (Do: outer diameter, Th: thickness) of different layers in the four cylindrical test SPDs. The active lengths, the lengths of the emitter wires, are also given.

SPD	Emitter (Do)	Insulator (Th)	Collector (Do)	Active Length
Rh-SPND	Rhodium (1.0 mm)	Al_2O_3 (0.53 mm)	Inconel-600 (2.5 mm)	100 mm
V-SPND	Vanadium (3.0 mm)	Al_2O_3 (0.53 mm)	Inconel-600 (5.3 mm)	100 mm
Co-SPND	Cobalt (3.0 mm)	Al_2O_3 (0.53 mm)	Inconel-600 (5.3 mm)	100 mm
Cr-SPND	Chromium (2.0 mm)	Al_2O_3 (0.53 mm)	Steel SS304L (3.0 mm)	100 mm

It is important to reiterate that cylindrical SPDs are tailored in terms of geometry and materials for use as thermal neutron detectors. This feature has been exploited in this work; V-SPND has been tested with a thermal neutron source to verify the Monte-Carlo model developed for SPND simulations. These are reported in forthcoming chapters. All four of them have also been tested under different conditions to assess their limitations and for preliminary assessments. This study, which has not been reported in details in this thesis, led to pursuing of further design studies of the test-SPDs for fast neutrons.

The emitter-materials, reactions, half-lives and cross-sections of the (n, β^-) processes in three delayed-SPNDs chosen for the test are shown in Table 3-2. The effective cross-sections are shown for thermal neutrons (ref. to TRIGA reactor among test setups in Chapter 4) and 14 MeV fast neutrons (ref. to TUD-NG among test setups Chapter 4), which are calculated by collapsing of the corresponding neutron spectra and energy-dependent reaction cross-sections in FISPACT.

Table 3-2: List of neutron-induced reactions in emitter materials of the delayed cylindrical SPNDs; half-lives ($T_{1/2}$) with the effective reaction cross-sections (Σ) in TRIGA (thermal) and 14 MeV (TUD-NG) neutron spectra, and the rough estimates of maximum achievable neutron currents (I) with these detectors under these spectra are also given.

Material	Reaction	$T_{1/2}$ (s)	Σ_{TRIGA} (b)	Σ_{14MeV} (b)	I_{TRIGA} (A)	$I_{14\,MeV}$ (A)
Rhodium	^{103}Rh (n, γ) $^{104g/m}$Rh	42.3	5.6E+01	4.1E-04	5.1E-10	3.8E-15
Rhodium	^{103}Rh (n, α) ^{100}Tc	15.5	2.0E-06	1.0E-02	1.8E-17	9.2E-14
Vanadium	^{51}V (n, γ) ^{52}V	224.6	1.3	6.0E-04	1.1E-10	4.9E-14
Vanadium	^{51}V (n, p) ^{51}Ti	345.6	1.4E-04	2.9E-02	1.1E-14	2.4E-12
Chromium	^{52}Cr (n, p) ^{52}V	224.6	2.2E-04	7.4E-02	7.8E-15	2.6E-12

A good estimate for the comparison of the SPND's responses in two spectra is the so-called *maximum achievable current (I_{MAX})*. It is a predicted value of current due to total activation created in the emitter. This calculation is based on the atomic density of the nuclide in the emitter, calculated effective cross-section and nominal neutron flux (10^{10} cm^{-2} s^{-1}), neglecting all other effects capable of affecting the signal formation. Evidently, the currents due to capture reactions are reduced on going from thermal to fast neutron spectrum, while those due to threshold reactions are increased. Higher currents from the 14 MeV reactions in Cr-SPD is a reassuring fact as it is a design specifically aimed for this purpose.

3.2.2 Motivation for Flat Test-SPDs

The measurement of sub-picoampere level responses, which have been estimated for some cylindrical SPDs (Table 3-2), is a difficult task. Low sensitivity of SPDs can be combatted by geometrical adjustments, mainly increase of the detector's irradiating area and emitter volume. Increasing wire or rod thickness in cylindrical design leads to increase of *self-shielding* of incident particles and self-absorption of emitter photons or electrons, limiting the sensitivity again. The self-shielding (or self-absorption) effect

relates to the phenomenon in which an incident (or an emitted) particle is stopped completely in the emitter volume itself, thereby effectively reducing the incident (or emitted) particle flux, and so reducing the sensitivity. In principle, this can be avoided by using the emitter in a flat geometry. The concept of SPD with flat foil(s) of emitter material has been experimentally examined in this work. Below are the main arguments in favor of flat detectors.

1. With flat design, the active reaction volume of the detector can be narrowed to a closed space, good for irradiation with compact sources. Sources encountered in laboratory tests are often disc- or beam-type in contrast to the extended reactor sources. In such situations, one can attain a higher sensitivity in flat design than a cylindrical one, with the equivalent amount of detector material.

2. Production and handling of thin layers of detector materials are easier and cheaper in flat geometry than in cylindrical one. This is a decisive factor when adjustable designs are required. Openable designs with cylindrical tubes are relatively more difficult to construct. Secondly, they also suffer more wear and tear over multiple uses and are prone to damages.

3. Flat SPD is of interest for TBMs which will have sensors constricted to very small spaces. Compact detectors are preferred for ease of integration. For application in TBM, one can think of a multi-layer strip-like detector or a chip-like compact detector which will be less invasive than long cylindrical detectors.

The idea of flat SPD is per se, not new. In his original work on SPDs, Hilborn [27] had stated that any arrangement of detector elements permitting emitter electrons to travel to the collector through the insulator can be used. Some flat SPDs, mostly for gamma detection have been constructed and tested earlier [53]. They have been found to work satisfactorily, however, information on their wide-spread application or commercialization is not available in the literature. In this work, a renewed look has been given to this idea with a new sandwich-like design.

3.2.3 Sandwich-type Test-SPDs

The *sandwich-type SPD* has been proposed, developed and tested in this work. This design has flat foils of collector, insulator and emitter stacked in correct order and fixed with supporting structures. Figure 3-3 shows a sketch of the basic design (with a five-layer sandwich structure shown as D) and a section of the engineering drawing of a product based on it. The foils are pressed from top and bottom using thin and small metal frames, which are screwed on the two sides. One can employ springs while screwing, when one or more materials may easily damage due to mechanical compression. Together designated as *fixer structures,* they are designed to have a low quantity of materials (F in the figure). They can be easily unscrewed to dis-assemble the detector, making the design openable and adjustable for testing multiple material combinations.

The sandwich is packaged in an aluminum box (E in Figure 3-3 right), which supports the connector for the lead cable and performs as the electromagnetic (EM) shield of the detector. For a more compact design, the lower aluminum frame is removed and the detector sandwich is directly attached to the base of the shield. In this design, it is easy to add more number of layers in the sandwich. For example, two emitters with the

parallel connection results in a nine-layer structure with a common collector in the centre. For signal transmission, a female type coaxial connector is coupled to a side of the shield. Thin wires of copper are soldered to its central conductor and extended to be pressed between emitter and insulator foils in the sandwich. Its outer electrode is coupled to the shield, which is in electrical contact with the collector layers through fixer structures.
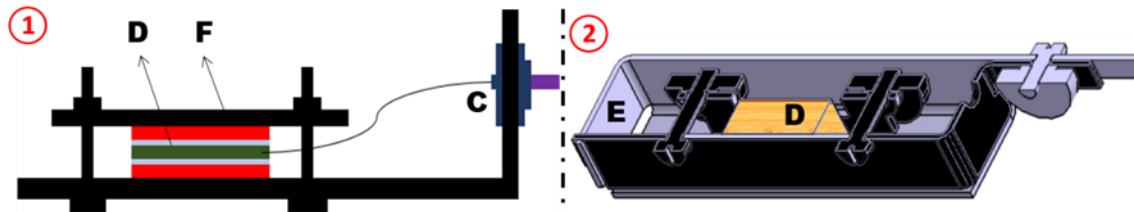
Figure 3-3: (1) Sketch of the structure and assembly of a sandwich-type SPD and (2) cross-sectional engineering drawing of an SPD with detachable parts (flat base darkened). The active sandwich area (D), fixer structures (F), electrical contact (C) and electromagnetic shield (E) made of aluminium are labelled.

First version of this device, henceforth referred to as *edition-1 sandwich-like test-SPD* has been built using a readymade aluminum box (3 mm thick walls) as EM shield. The photographs are given in Figure 3-4, with the outer dimensions of the product and the imapratant components labelled. This detector design is inexpensive and it satisfactorily serves its purpose for a series of experiments.
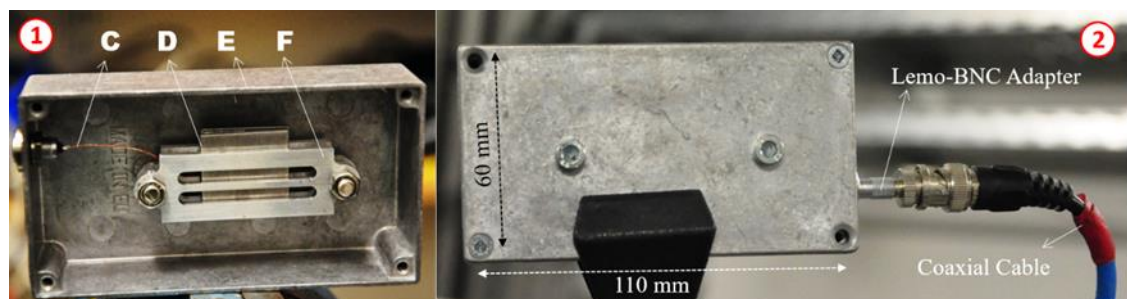
Figure 3-4: Photographs of the (1) inside and (2) outside of the edition-1 of sandwich-type test-SPD, depicting the active sandwich area (D), electrical contact with the cable (C), Al EM shield (E), fixer structures (F) with aluminum plates, and the outer dimensions of the product. Signal cable and connector have been identified in the right picture.

In adjustable designs, manual handling of the assembly is required for changes in the foils of the sandwich between two irradiation tests. With respect to this, edition-1 has some areas of improvements. Sandwich changeover times are longer during irradiation experiments, causing the need of longer cooling periods. Also, it is difficult to quickly re-assemble the detector sandwich in (approx. 50 mm wide) small spaces of this design. For laboratory tests, it is convenient to divide the assembly into two separable parts, as shown in Figure 3-3 (2). The L-shaped flat base (darkened in engineering drawing shown in the figure) holds the detector sandwich with its electrical connection. It is completely

detachable from rest of the shield and offers an open platform for quick adjustment of SPD components. For time-bound irradiation experiments, this is an ergonomic feature but requires more effort in the design of detector parts.

An improved, second edition, named as *edition-2 of sandwich-type SPD* has been developed in-house using aluminium for base material. Its photographs are shown in Figure 3-5. It features a detachable section with the detector sandwich. Essential improvements include a more compact and lighter detector assembly, thinner shield walls (1 mm to 1.5 mm), less material in fixer structures and handy design for material adjustments. This design minimizes the cooling periods and exposure during changeover times as only a smaller part of the irradiated detector needed to be handled. Aspects of SPD design like foil-dimensions, style of electrical connections etc. remain unchanged.
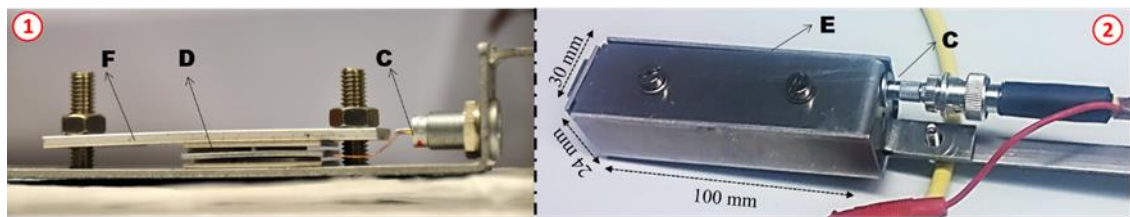
Figure 3-5: Photographs of the edition-2 sandwich-type test-SPD: (1) the detachable section with an active detector sandwich (D) containing material layers in the form of square foils, fixer structures (F) and electrical contacts (C); and (2) the complete packaged detector with its outer dimensions. It also shows the electromagnetic shield (E) and connection to the signal cable (C) from the outside.

The flat SPDs have openable design. In Figure 3-6, the dimensions of a typical test detector are shown using a diagram. The fixer structures are made of a 2 mm thick aluminum plate (50 mm long and 20 mm wide), with slots to reduce the material content. They are fixed using stainless steel screws and nuts to the bottom of the box, with the detector sandwich between them. Bare Cu-wire (0.015 mm diameter) soldered to a standard coaxial jack (Lemo 00) is used for electrical connection with the cable. Square-shaped foils (25 mm by 25 mm, 0.5 to 2 mm thick) of emitter, insulator and collector are utilised for various tests with this adjustable SPD design. For most of the test-SPDs in this thesis, a 1 mm thick layer of emitter, two 1 mm layers of collector and two 0.5 mm layers of insulators have been used. So, the typical height of the SPD sandwich with five layers, is around 4 mm. Appendix 2 shows various test combinations of materials and dimensions of the foils used in this thesis. High-purity foils have been procured from industrial suppliers in appropriate dimensions, for all the selected materials: Be, V, Ag, etc. for emitter, Al_2O_3 for insulator, and Inconel-600, Nb, graphite etc. for collector.

To overcome the hazards from Be, high-purity, clean and sealed foils in exact dimensions as required for tests (25 mm by 25 mm, 0.5 mm thick) have been procured from an industrial supplier, which have been carefully handled, avoiding any kind of scratching, machining, harsh cleaning or any other destructive processes. The copper wire connected to the core of the connector has been pressed mechanically between two foils of Be. As it is a hard material, it has shown to suffer no damage and the way of contacting has functioned efficiently.

3.2.4 Comment on the Extended Behaviour of SPDs

At this juncture, it is critical to address the subject of extended detector behaviour (introduced in Section 2.2.3), while understanding the design(s) of the test-SPDs. In Figure 3-6, with the sketch of the flat SPD mounted in front of a radiation source, two rectangular regions depicting the active and the extended detectors are shown. For a typical flat SPD, the active zone majorly comprises the emitter (typical volume: 25 mm × 25 mm × 1 mm) and the rest of the sandwich (typically, about 4 mm in height). For establishing the extended detector, detailed computational estimates are difficult and beyond the scope of studies in this thesis. Electrons emitted up to distances of the order of a few centimetres have high chances of ending up in the active volume. Based on this, a crude assumption has been taken that the SPD is affected by smaller contributions from events up to about 5 cm away. Electrical signals of different origins can disturb the SPD-current signals, not only those induced by the radiation (which are shown using yellow stars in the figure). For example, a mechanical vibration in the radiation source, passing to the SPD through the mounting structure, can also be part of this behaviour. Considering this, the extended detector zone in Figure 3-6 has been exaggerated to include mounting structure and a part of the radiation source also.
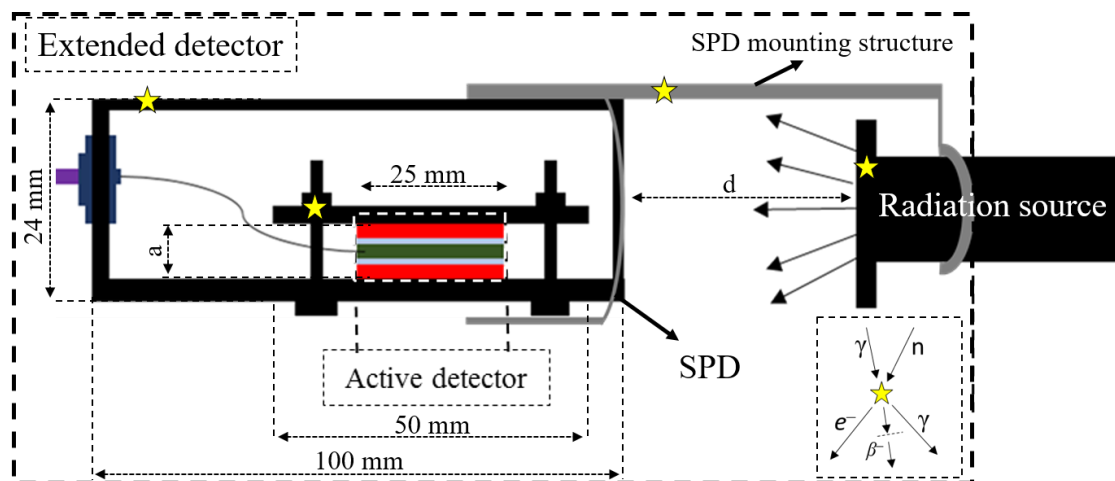
Figure 3-6: A simplified sketch showing a typical flat SPD mounted in front of a radiation source. The active detector (sandwich region) and the extended detector regions are schematically depicted. Commonly, the height (a) of sandwich is 4 mm and distance (d) of the SPD from radiation source is between 5 mm and 50 mm depending on the setup. The most common positions of electron-emitting reactions in extended detector are shown using yellow stars, and the processes in the bottom right corner of the figure.

3.3 Development of Experimental Apparatus for SPD Tests

A typical laboratory setup for SPD measurements comprises of the radiation source, detector, signal transmission cable, current measurement device and a computer with a suitable program to read the signal in real time. Afterwards, for signal processing and analyses, further computational tools are needed. In any such test, the detector is attached to a mounting structure like a long rod, to position it close to the radiation source while the user maintains a safe distance from the source. Standard coaxial cables are used to transmit the electrical signal from the detector to the ammeter. Using appropriate

connector, the cable is coupled to the detector, connecting the emitter to the central conductor of the cable and collector to its sheath. Collector and the cable sheath are usually grounded at the instrument ground of the ammeter circuitry. The ammeter principally measures the DC signal produced due to the positive charge on the emitter with respect to the ground. A complete sketch of the flow of signal in such a setup is outlined in the Figure 3-7. In the figure, the physical processes and parameters originating at each stage of the setup, which can impact the results of the measurements are pointed out. Some descriptions of the apparatus utilized in this thesis are also provided. Finally, the major sources of errors are identified for each stage, which arise due to the physical phenomena at these stages. These errors ultimately affect the measured sensitivity of an SPD in any irradiation test. Salient aspects of the different stages of signal transmission and their importance in the work performed in this thesis have been summarized in the following, for a reference for the future chapters.

3.3.1 Test Detector and the Radiation Source

For the radiation sources, three different test facilities have been utilized in this work. At first, some irradiation tests have been performed in a thermal reactor to obtain the proof of the functioning of newly constructed flat detector design and to verify the computational model for SPD's sensitivity calculation. Then, a series of irradiation tests have been conducted to analyse the responses of two chosen *reference test SPDs* to the neutron and photon radiation fields similar to those expected in the TBM. Fusion neutron source and high-energy photon sources formed the test beds for those tests. The irradiation positions in these facilities, flux-monitoring and the characterisation of the fields for testing of the SPDs are explained in broad details in the next chapter. Here, it is essential to point out in some details, the impacting parameters and their interplay, for the test detectors and the radiation sources.

The incident fluxes of different particles: neutrons, photons and electrons, and their spatial, angular, temporal and energy-dependent distributions are important parameters w.r.t. the radiation source. For this thesis, extensive Monte-Carlo modelling of test facilities have been undertaken to determine the angle- and energy-distributions around the positions of the SPD testing. The temporal variations of fluxes have been recorded in real-time using the flux monitoring systems available at the respective facilities. Computations have also been employed in calibration of these monitors. A brief discussion of the prime effects of these distributions on the analyses of SPDs follows.

In a neutron irradiation experiment, the activation of structural materials leads to prompt and decay gammas, which make the radiation field a *mixed-field* with both neutrons and photons. While, for the photon irradiation tests performed in this thesis, the photonuclear interaction probabilities are very low so that the sources can be considered relatively pure photon sources. Coupled neutron-photon radiation transport simulations have been performed to relate the two kinds of fluxes in these facilities. Electrons, mainly decay products from the activated structure, secondary products of photon scattering, and in the case of thermal reactor, the fission betas, are of negligibly small fluxes. Electron fields estimates are usually difficult to make and not specified for the facilities.

	DAQ & Analysis	Picoammeter	Cable	Detector & Environment	Radiation Source
Impacting processes/ parameters	• Acquisition speed • Signal processing • Sensitivity analysis	• Triggering/synchronizing • Average/median filtering • Compensation methods	• Radio-activation • EM shield/grounding • Heating effects • Mechanical effects	• n or γ induced electrons in emitter (**major effect**) • n or γ induced electrons emitted in active detector • n or γ induced electrons emitted in extended detector • Other non-nuclear electronic effects in extended region	• Incident flux of particles: n, γ and e^- • Energy and angular distributions of flux
Possible sources of error	• Background current subtraction • Time-average calculation • Synchronization with source monitor	• Inaccuracy of ammeter • Current instabilities at level of 100 fA • Background current subtraction	• Thermo-electric current • Radiation-induced current • Pickup A.C. noises • Turbo-electric current	• Change of detector geometry or orientation, thereby a change of the definition of active region (affected by properties of layer-materials and layer-thicknesses) • Manufacturing inaccuracies • Effect of ambient housing on quality of insulation • Extended detector behavior (difficult to quantify)	• Flux oscillations • Changes in energy-spectra • Changes in detector's angular position w.r.t. source beam-axis • Inaccuracy in estimation of source-detector distance

Active detector

Extended detector

Radiation source angular distributions:
Beam-like   Disc-like   Reactor-like

SPD sandwich orientations w.r.t. beam axis:
Across the beam   In the beam

Figure 3-7: The overall signal transmission path in an SPD irradiation experiment. From the irradiation setup, with radiation source and detector, the signal passes through the cable, is recorded in a picoammeter, and is acquired and analysed using a computer system. The physical effects impacting the signal at each stage and the common sources of errors are pointed out.

The angular distributions of the sources encountered in this thesis have been categorized into: *reactor-like, beam-like* and *disc-like* sources. The first one is an extended source, such as one in a research reactor, where the emission surface of incident particles (thermal neutrons in this thesis; see Section 4.1) is large, on orders of 1000 cm^2 or more. Also, the source surrounds the SPD from all sides. The non-uniformity of the field distribution and the difference in the SPD response due to angular orientation of its layers are not much pronounced here. However, some partial directionality may still exist when the test position is radially far from the core.

The other two source types, featuring stronger effects of SPDs relative orientation, are associated with the accelerator-based radiation facilities. Such a source has a *beam axis*, the preferential direction along which the particles are emitted. The *beam-like* source is one in which the particle tracks at the position of SPD testing are confined within a well-defined (usually circular or oval) shape, with uniform distribution of intensity and energy along the beam plane. The high-energy photon source for SPD tests (see Section 4.3) is created, at first, by the bremsstrahlung effect of a high-energy electron beam on a niobium radiator foil, and then a beam of photons is produced by passing them through a long aluminium collimator. In comparison to this, a source is defined to be *disc-like* when the collimation is not done. For fusion neutrons in SPD tests (see Section 4.2), a beam of high-energy ^{2}D ions in bombarded on a disc (target) containing ^{3}T atoms, making a nuclear reaction to produce neutrons. The angular distribution of the released neutrons are guided by the geometrical details of the beam-target interactions and the dynamics of the nuclear reaction. It is non-uniform on a plane perpendicular to the axis of the ^{2}D beam.

Orientation of the layered structure of a cylindrical or a flat sandwich-like SPD with respect to an anisotropic radiation source can affect the measured response. The orientation is called *across the beam* if the cylindrical axis of the SPD is perpendicular to the beam axis. While, if it is parallel to the beam axis then the SPD is *in the beam.* The part on radiation source in Figure 3-7 shows analogous orientations of the stack of layers in a sandwich-like SPD w.r.t. the beam axis of the radiation source. In the former orientation, the part of an outer layer of the SPD design, due to its closeness to the source position, is irradiated with higher fluence as compared to an inner layer. This causes a directional bias of nuclear processes in the detector, and to avoid that the SPDs have been often placed in the beam in experiments in this thesis.

If the lateral dimensions of an SPD does not fit in the well-defined radiation beam, then only a part of the active detector is irradiated and this calls for a correction to determine true SPD response. Similarly, in a disc-like source, correct estimation of SPD to source distance is prone to errors. Only an approximate location of the source is usually known, and due to reaction and beam dynamics, it also changes during the test duration. These factors are of special importance in situations when a mathematical comparison of the SPD responses in two different test facilities is required. While characterizing the test setups and analysing the SPD responses, these and some other sources of errors (see Figure 3-7) due to physical effects at the source and the detector stages of the signal's path have been duly accounted for, as will be explained in chapters 4 and 5. For the inaccuracies due to the manufacturing issues, or quality of materials in the test SPDS, much involved engineering and mathematical treatments are required. This is beyond the scope of this work. Nonetheless, a pragmatic approach is adopted here, and some broad

understanding of these physical factors have been established through parametric experimental tests as shown in Chapter 7.

3.3.2 Choice of Cables and Discussion on their Radiation Behaviour

Choice and qualification of the correct signal transmission cable play vital roles in low-level current measurement setups. For the measurements below 1 nA, shielded cables are needed. A usual cable of this type has a coaxial cylindrical design. There is a *central/core conductor* (typically Cu) wire which connects with the positive terminal (or pole) of the nuclear detector's circuit. In some cables, multiple core conductors are provided, depending on the application. After a thin layer of high-resistance plastic or mineral insulation, an outer *sheath* or *shield* of metal is provided, for electromagnetic shielding of the signal-carrying core(s). The sheath is the circuit low or the negative pole, and often, electrically grounded in SPD circuits. Sheath can be a continuous tube or in the form of a cylindrical net, which makes the cable's build flexible. Some cables have an additional layer of plastic on the outside, known as the *jacket,* for better handling. While details of it depends on the type of detector, electrical contacts between the cable and the detector are made through *connectors* which are directly linked using thin wires/fibres, appropriately welded or soldered with the ends of the detector volume.

Four types of coaxial cables have been used for various tests in this work, whose photographs are shown in Figure 3-8 (left), and explained below. While two of them (1 and 4) were available in the laboratory, the other two have been procured specifically for SPDs. All of them have been historically applied for low current transmissions. To suffice for the cable characterization, their performances have been practically compared, over the course of irradiation tests. Finally, the one providing best measurement capabilities has been chosen for frequent use in SPD's testing as reported in this thesis.

1. RG-58/59 type coaxial cables are readily available for use in the laboratory. These have single cores (Cu alloys), plastic insulation, Cu shields and plastic jackets. BNC type plugs are connected on both ends of the cable. The cable resistance could be 50 or 75 Ω, but mostly, the former is used in this work. There are several 40–50 m long units already installed through labyrinths in some of the test facilities, but their origin and history are unknown.
2. A triaxial-cable has a second shield for grounding. This provides an additional layer of shielding for highly sensitive circuits, reduces the paths of leakage and decreases the noise. Two units of low-noise triaxial cable with BNC connectors and banana cable extensions from the second shield have been procured (Belden 9222 [54]) in lengths of 10 m and 30 m . It has tinned Cu core, net of Cu for shields and plastic insulation. For use with SPDs, both the shields are grounded.
3. A special low-noise (LN) extension cable often used for medical applications has been tested. The cable unit is bought with BNC connectors (PTW T-26059 [55]). Geometrically, this cable has the most compact construction among the four choices, and it has a plastic jacket, while more details of the cable's constructions and materials are not disclosed by the manufacturer. However, it has been validated for high-precision measurements down to 10^{-15} A.
4. Mineral insulated metal cables offer low-noise and long-term advantages of being resistant to mechanical tensions, water, fire etc. and are often used in reactor

environments. They are highly recommended for in-core SPDs. All cylindrical SPDs came pre-linked with MI cable having Inconel-600 cores and sheaths and MgO insulations [56]. A separate 20 m long unit of (BNC) cable has been prepared for use as extension to pre-linked cables or with the flat SPDs.
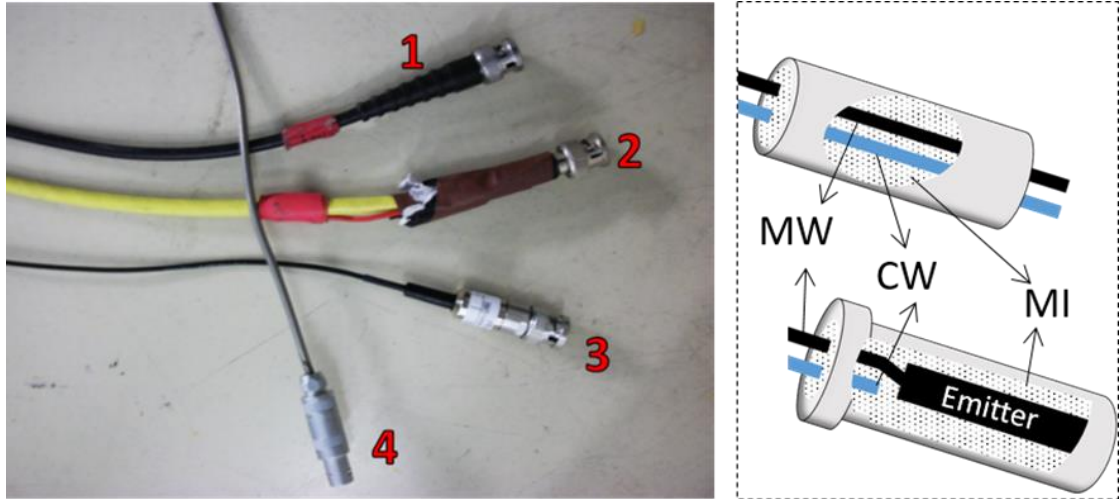
Figure 3-8: (Left) the four types of cables and ends of their connectors on the device terminal as used in this work: (1) RG-59 Coax, (2) Belden 9222 Triax, (3) PTW Low Noise Coax and (4) MI Twin-Core. (Right) schematic sketches of (top) twin-core MI cable and (bottom) a commercial cylindrical SPD. The sketches show the MW: main wire, CW: compensation wire and the MI: mineral insulation in the cable and the detector. For an understanding of the method of contacting cable and the SPD, the wires of the cable and the SPD have been coloured appropriately.

A common concern for coaxial cables comes from the charges produced from nuclear reactions in its layers due to the incident radiation [41, 42]. The cylindrical multi-layered design with two conductors leads to SPD-like effects, leading to a *radiation-induced electromotive force (RIEMF)*. The main effect in cables is the (γ, e^-) from photons (gammas), as the conducting layer materials are usually chosen for low cross-sections of reactions with the thermal neutrons. In long-term operations however, accumulated neutron activation of the core wire can produce betas which can leak to the shield due to their high-energies. In MI cables with Inconel-600 core for example, production of ^{56}Mn or ^{52}V, both beta-emitters can lead to sustained delayed signals.

To reduce the RIEMF effect, the cables of the cylindrical SPDs are constructed so that the electron emission from core and sheath cancel each other [43]. For this, *symmetric conductor combination*, i.e. putting same metal for inner and outer conducting layers, is quite usual. Another method, traditionally called as the *cable compensation*, is to add a second core wire, also known as the *compensation wire (CW)* to the cable, apart from the central conductor (MW: *main wire*) which connects to the emitter of the detector. The internal geometries of a twin-core MI cable and an SPD can be seen in the sketches in Figure 3-8 (right). The CW starts from the end of the active detector region of the SPD. Its geometrical positioning and material mimic the other wire in the cable, essentially making the CW-shield combination a dummy MI cable itself. The signal measured in

MW is a sum of cable's RIEMF and the SPD current. The difference of the currents in the two wires (i.e. MW – CW) therefore, is the net signal of the SPD.

Besides the nuclear effects, cables have numerous other detrimental electronic effects which can generate spurious signals. First of all, a low-quality or degraded insulation can cause large leakage currents. In-core SPDs often fail if the sheath has been breached due to the erosive coolant media of the reactor core. With high quality jacketing of the MI cable and the SPD, ceramics like Al_2O_3 and MgO have proven to show acceptable long-term behaviors. Then, the triboelectric effect due to mechanical stress between layers of the cable is often encountered whenever longer coaxial cables must be used. This can be reduced by dissipative conductive layer on the insulation (usually graphite lubrication) in some cables. Thermomechanical, piezoelectric and thermoelectric effects etc. can introduce noises in the range of fA to nA also. Shielding and secure grounding of the cable (and detector) sheath are of utmost importance to reduce picking up of outside, electromagnetic noises by the measurement setup. Optimization of dimensions and materials also helps in reducing various cable noises.

In a setup with the SPD and the cable, the electrical connections, adapters, soldered joints etc., create varying contact resistances and additional leakage paths for charges in the measurement circuits, further causing systematic electrical noise. The sum of these currents is often called as the *zero* or *background current* in the SPD circuits. Zero currents are normally in the cables, and are below 100 fA, but they could reach up to 10 pA in some cases. From experiences in the SPD industry, zero current has been found to be mainly affected by how the cable is constructed. Long-term use in high-temperature or high-radiation environment also changes the quality of a cable. Treatments like high-temperature heating of MI cable (often done to remove insulation defects), cutting and reconnection of connectors etc. also alter its quality and response.

The zero current and the RIEMF current of the cables used in the SPD tests in this work have been measured before the start of each test. A preliminary measurement with four types of the cables of the apparatus have been performed at the fast neutron facility (see Section 4.3) to compare their behaviors in a representative SPD test. Irradiations have been performed at highest neutron fluxes (2×10^{10} cm^{-2} s^{-1}). Full cables have been placed on a table in front of the radiation source, while 10 cm portions (detector ends with connectors) of the cables are attached directly to the source. Results of the measurements are reported in Figure 3-9.

In the planned SPD tests, currents of the order of few to tens of pA are expected. Around 1 pA of radiation-induced current is quite common in cables, but this remains below 5% of the total signal (except some worse cases) in the SPD test, which has been carefully measured before testing and subtracted from the total signal measured. Simultaneous and real-time cable current subtraction during an irradiation test has not been possible in the setups. By and large, RIEMF currents have not been detrimental because the cables do not see large fluxes over long time-periods in the laboratory based radiation sources. Only a part of the cable stays in the proximity to the source in any test, unlike the ones integrated in reactors. The PTW low-noise cable is proven to show comparably the best behavior, with low zero as well as RIEMF currents, and has been used for most of the tests with flat SPDs which are reported in this thesis.
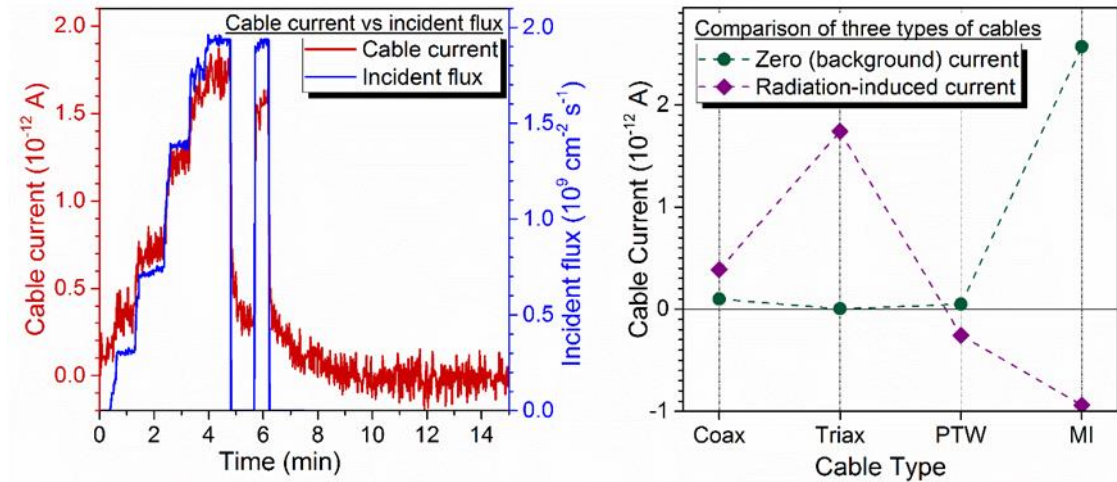
Figure 3-9: (Left) measured radiation-induced (RI) current in the Belden triaxial cable on irradiation with fast neutrons, as an example of the radiation testing of cables. The right Y-axis shows the incident flux of neutrons. (Right) reference zero and radiation-induced currents in the four cables from the SPD apparatus, as measured through irradiation with high fluxes of fast neutrons (lines for guidance only).

3.3.3 Picoammeter and the Data Acquisition System

A *picoammeter*, an advanced ammeter which can measure down to fA levels, is often used for experiments involving SPDs. Such an instrument offers high precision, high speed, and assists in keeping low zero currents in the circuits. In cases where the currents are close to the level of background, solutions for signal amplification are sought (but the choices are severely limited).

The Keithley model number 6485 picoammeter (*KE6485*) [57] has been used as the current meter in all the setups for testing SPDs in this work. It is a feedback-type ammeter offering low-voltage burden to achieve high-accuracy measurements of small currents. With $5\frac{1}{2}$-digit resolution, its lowest and highest measurable currents are 20 fA and 21 mA, respectively. The ammeter has a female BNC-type input terminal. It has a multi-functional front panel for operations and it can be remotely controlled using a computer via a GPIB bus or a serial (RS-232) interface. SCPI (Standard Commands for Programmable Instruments) commands can be used to communicate with it. The device can be employed at high speeds, up to 1000 readings per second. It features a large buffer of 2500 readings for such fast measurements. Easy-to-use standard filters, zero-correction capability and other digital multi-meter features are available in this model.

In its application in this work, KE6485 has been controlled over a serial connection using a Windows PC. ExceLINX, an MS Excel based software provided by Keithley is utilized for fast measurements from KE6485. The software is based on standard drivers and communication protocols coded in Excel, and can make use of the data analysis capabilities of MS Excel. It accumulates readings in the instrument buffer and data can be read out only at the end of the measurement. On one hand, this facilitates readings at the highest possible speeds, while on the other it does not provide an online graphical output, limiting its use to shorter measurements. As an alternative, an interface module has been developed using LabVIEW [58] virtual instrument (VI) to interact with

the KE6485. The VI has been written using the KE6485 driver from Keithley. It initializes and configures the instrument and then, reads, plots and exports the readings to Microsoft (MS) Excel. On the front panel of the VI, the DC signal vs. time is plotted in real-time showing an online output of the measurement. Due to the plotting function requiring the online transfer of data, the measurement speed gets limited as compared to ExceLINX.

Before using, the KE6485 unit has been calibrated using a DC output circuit containing 100 GΩ resistor and a DC milli-voltmeter calibration source. On the left panel of Figure 3-10, the output current (in pA) of KE6485 from this test is plotted against time, along with the input voltage (V) on right Y-axis. The measured current is found directly proportional to the input voltage, establishing that the overall performance of the ammeter is satisfactory in the range of currents expected in the planned measurements.

For small current setups, various random fluctuations in measured currents are normal, arising from circuit imperfections and outside sources of noises. These effects are worse at the lower levels of signals, such as below 1 pA for the KE6485 calibration circuit, as reported in Figure 3-10. This measurement is also affected by (up to 1%) discrepancy between the set voltage and the measured current. This is mainly attributed to the 0.1 mV difference between voltage set and voltage produced by the voltmeter, as verified by direct measurement of the voltage using a standard multi-meter.
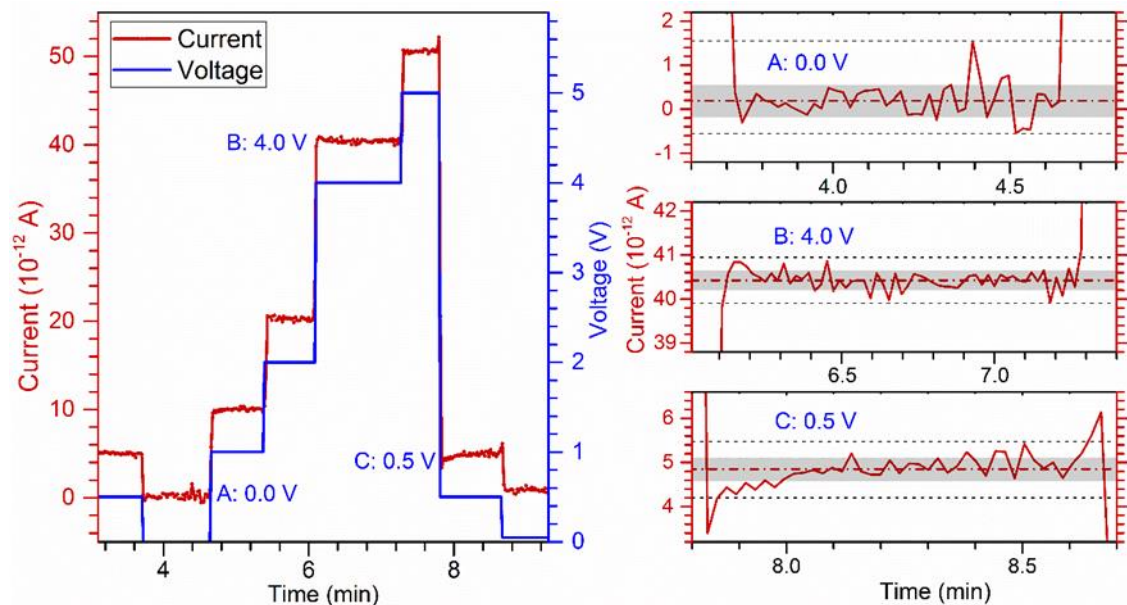
Figure 3-10: (Left) time-dependent plot of the measured output current (in red) of the calibration circuit, along with the corresponding set voltage (in blue) to highlight the proportionality between the two. (Right) three levels (A, B and C in left figure) in the current plot are zoomed-in to show the fluctuations. The approx. mean currents (dashed red lines) are: (A) 0.2 pA, (B) 40.4 pA, (C) 4.8 pA. The dotted black lines are used to show upper and lower limits of the fluctuations (peak-to-peak) at each level, and the grey shaded regions above and below the mean current shows the RMS deviation.

On the right panel of the Figure 3-10, three levels in the SPD-current curve are zoomed into, in order to discuss in detail the typical methods of analysing DC signals in

this thesis. Usually, the DC signal is affected by systematically produced background current (due to circuit imperfections and cables) and also randomly generated noises. Detailed noise-analysis is a complex subject and has not been adopted here. In SPD-related measurements, at any constant level of DC signal, a mean current is obtained. Mean currents in Figure 3-10 (right) are shown using dotted red lines.

The noise content of a DC level is denoted by the *root mean square (RMS)* of the signal at that level, which is physically equivalent to the standard deviation of the mean. One RMS range of the current levels in Figure 3-10 (right) are shown using grey regions about the mean. During the sampling, the KE6485 LabView program does not report RMS, and often the *peak-to-peak fluctuation* has been ascertained for an idea of the noise level. Dotted black lines show the upper and lower peaks of fluctuations of the measured currents in the figure. While discussing currents measured in this thesis, the RMS of the noise is reported either as an absolute value in pA units or as relative (%) value w.r.t. the mean signal. Random fluctuations being the major source of error in SPD signal measurements, often uncertainties in the reported signals are same as the RMS.

At zero voltage (A:0.0V) in Figure 3-10, the mean current is approx. 0.2 pA, with comparatively larger fluctuations than the other two levels. Practically, it corroborates again the previously discussed need for zero current measurement and subtraction from the actual result in an SPD-based experiment. This also means that the net signal, after subtracting the noisier zero signal, also accumulates the uncertainty of the zero current measurement. The undershoots and overshoots (see the end points at the C:0.5V level, for example) in measured current are artefacts of the voltage switching mechanism of the DC power-supply of the input circuit.

4. CHARACTERIZATION OF THE IRRADIATION SETUPS FOR SPD EXPERIMENTS

This chapter deals with the experimental facilities and irradiation setups which have been used for testing of SPDs. The TRIGA Mark II reactor facility of Johannes Gutenberg-University (JGU) Mainz [59] has been chosen for thermal neutron source in this work. Whereas for fast neutron irradiations, the 14 MeV Neutron Generator of Technical University of Dresden (TUD-NG) [60] has been utilized. TUD-NG has also been used for extensive tests with various detectors, equipment etc. Finally, the high-energy photon tests have been conducted at the bremsstrahlung facility of the ELBE accelerator in Helmholtz-Zentrum Dresden-Rossendorf (HZDR) Dresden [61].

A good knowledge of the flux intensities and energy spectra of the neutrons and photons in an irradiation setup is important, as the SPD signals depend strongly on these characteristics of the radiation field. In what follows, the employed facilities and their experimental setups are explained along with the results of the pre-analyses, which involved the flux measurements, Monte-Carlo simulations and uncertainty analyses of the estimated fluxes for different setups.

4.1 Thermal Neutron Test Setup

4.1.1 TRIGA Reactor of Johannes Gutenberg-University Mainz

The Institute of Nuclear Chemistry of the JGU Mainz hosts a TRIGA Mark II fission research reactor [59]. The reactor uses U-Zr-H alloy with 8% U for fuel, demineralized light water for moderator and graphite for reflectors, in a swimming pool

type core. Maximum steady state power is 100 kW$_{thermal}$. Figure 4-1 shows a schematic side-view of a the TRIGA reactor, with some important parts.
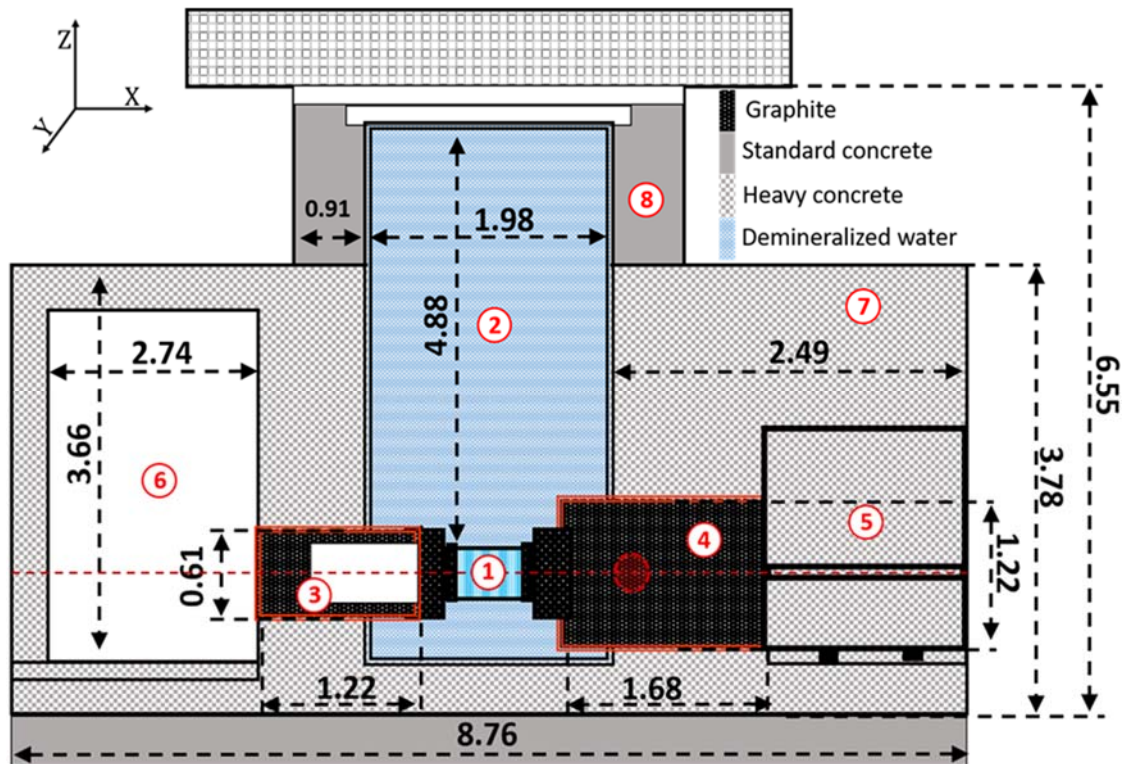
Figure 4-1: A schematic side-view of the built-up of a TRIGA Mark-II reactor with major dimensions (in m) and important parts. The labeled components include: (1) core with graphite reflectors (in aluminum casing), (2) reactor water tank built of aluminum, (3) neutron radiography collimator, (4) graphite thermal column, (5) heavy concrete movable door for accessing irradiation channels of the column in (4), (6) bulk-shielding experimental tank with a direct, shielded link to neutron collimator in (3), (7) dotted-grey parts show heavy-concrete shielding, and (8) grey parts show standard concrete shielding. The vertical level of the core's center is denoted using a dotted red line drawn across the sketch. A dotted red circle in (4) roughly shows the position of the SPDs in a typical thermal neutron test at TRIGA Mainz.

The graphite thermal column (GTC) of TRIGA Mainz is utilized for irradiation of SPDs. Thermal neutron tests are aimed at establishing a proof of principle of working of a flat geometry SPD and the experimental validation of the computational model for detector sensitivity calculation. The thermal column is a large radial channel which is packed with detachable blocks of graphite (approx. 1.2 m long) extending from the core reflectors ((1) in Figure 4-1, details of the reflectors not shown) to the outside of the reactor wall. Graphite slows down the faster neutrons from nuclear fission, rendering mainly thermal and epithermal (main part between energies of 0.005 eV and 0.1 eV) neutrons. The GTC is shown in (4) in Figure 4-1, while its movable gate in (5). A horizontal channel, like GTC, offers flexibility in terms of loading and unloading of the detectors. Blocks of graphite can be removed to have empty irradiation channels in the column, which can be accessed directly from the outer side of the gate.

The available detectors, in both cylindrical and flat geometries, have been loaded into the central irradiation channel of the GTC. A simplified sketch in Figure 4-2 shows the GTC w.r.t. the reactor core and typical positioning of the channel and the SPDs. The detector cable has been extended through a shielded hose of approx. 2 cm diameter in the heavy concrete gate of the GTC. The measurement and acquisition setup has been placed around 4 m away from the reactor's biological shield, making it feasible to use shorter cables. The SPD current signal measurements have been run online, while the times of reactor flux variations have been manually recorded for analysis of the acquired data. With TRIGA, the reactor power can be changed from one constant level to another in a short time (few seconds to 2 min) which is an advantage as the effects of flux transients on the dynamics of detector signals could be largely avoided, simplifying the analysis of the rise and decay parts of the detector signals.
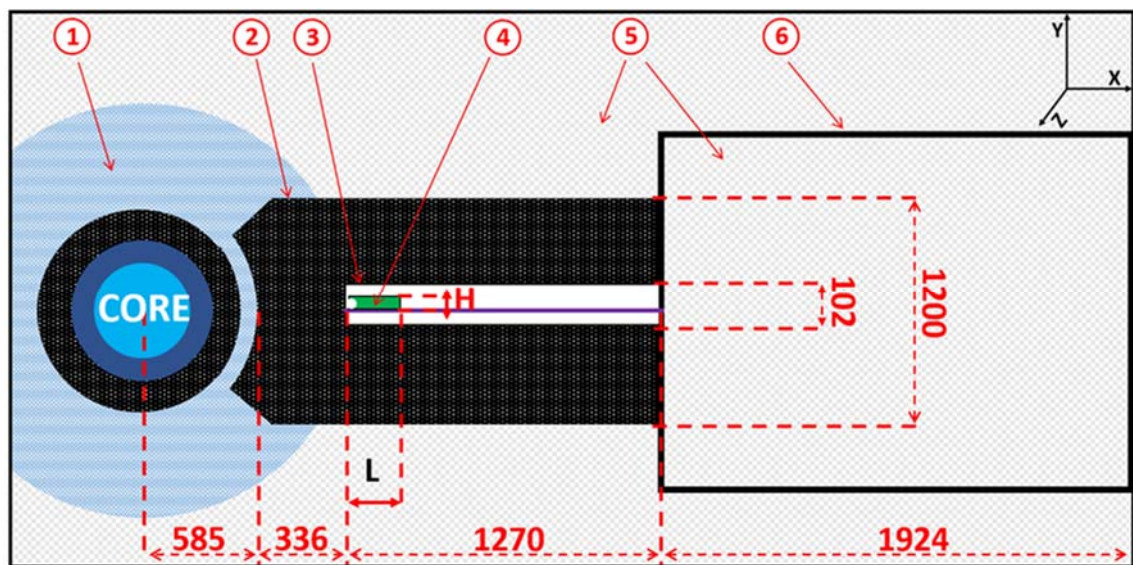
Figure 4-2: A schematic sketch showing the top-view of the TRIGA-GTC and its position w.r.t. the reactor core, with approximate dimensions in mm. Region (1) shows core with its reflector and the water tank, (2) the GTC, (3) the irradiation channel for testing of the SPDs, (5) heavy concrete shielding of the reactor, and (6) the movable door providing access to the outer end of the GTC. The SPD, shown in (4), is inserted in the column horizontally. Typical (L) length of an SPD is from 100 mm to 150 mm, while (H) height can be 3 mm to 35 mm (see Chapter 3). The colours represent different materials, same as in Figure 4-1.

4.1.2 Neutron and Photon Fields in the Experimental Position

It is crucial to have accurate information on the neutron and gamma fields at the experimental position with flux densities and energy spectra. TRIGA Mainz GTC is a proposed facility for radio-therapy treatments of liver cancers. In this context, the radiation field in the column has been previously characterized with computations and experiments [62, 63]. Neutron fluxes have been measured using activation foils at different positions in the column. With the use of cadmium shields, coarse spectral data (integrated thermal and fast neutron flux densities) have also been obtained. Similarly, for the gammas, dose rate measurements have been performed using thermo-

luminescence detectors (TLDs). These values have been compared and found to agree well with the computational values obtained using both Monte-Carlo and deterministic modeling of the reactor. The absolute energy spectra in the central channel of GTC is reproduced here from the work of Wortmann et al [63]. A simplified method for simulation of radiotherapy related measurements in GTC has been proposed by Blaickner et al [62], in which a representative neutron *source plane* is defined. The particle spectra are taken as those estimated close to the surface of the reactor core in front of the column. The neutron and gamma spectra from the two mentioned cases are shown in Figure 4-3. The position of the flux-spectra calculations is at the hot end of the column, roughly indicated by a white circle in front of the SPD (4) in Figure 4-2.
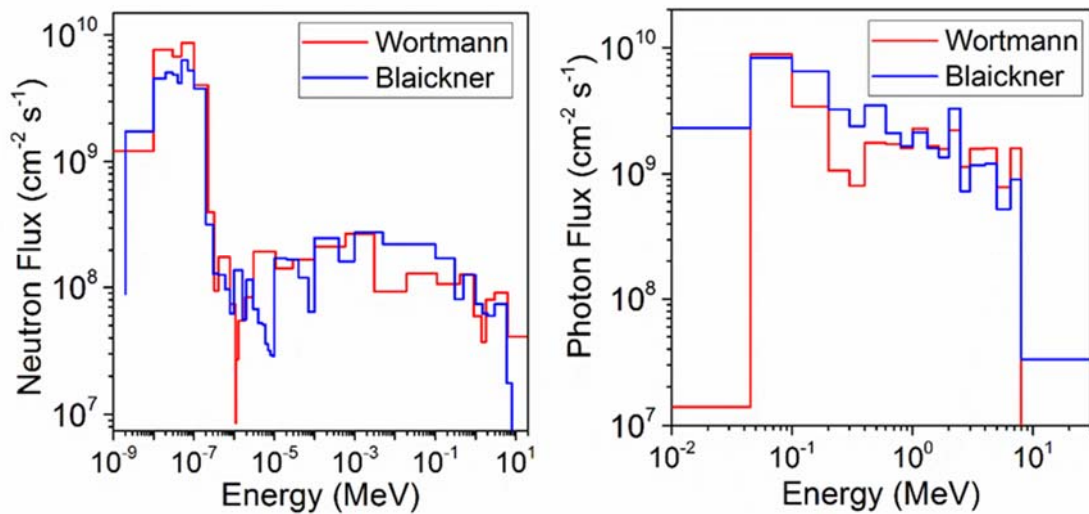
Figure 4-3: Computed flux densities and energy-spectra of (left) neutrons and (right) photons at 1 cm away from the hot-end of TRIGA GTC, from the two sources: Wortmann [63] and Blaickner [62].

Neutron activation analysis is a standard procedure to measure fluxes in reactors. As the sensitivity measurement of the reference SPD, cylindrical V-SPND (as explained later) in TRIGA GTC tests are required for validation of the computational model, ancillary neutron flux measurements have been conducted again, using activation foils. Sets of standard gold and zinc wires have been stuck at three equidistant positions along the length of the SPD, during irradiations at the three different flux levels. The white circle in front of the SPD ((4) in Figure 4-2, roughly the same as the position of calculations) indicates the place of the front most foil set. This is designated as origin for the detector alignment, and two other sets have been placed 7.5 cm and 15 cm away from it along the X-axis (Figure 4-2). The activation reactions with the gamma decay characteristics of the activation products are presented in Table 4-1.

The foils have been irradiated at power levels of 25 kW, 50 kW and 100 kW, alongside the irradiation of the cylindrical V-SPND at these levels. The activities have been measured using a characterized and calibrated HPGe-type gamma-ray spectrometer. Figure 4-4 shows a plot with the distance variation of the measured neutron flux densities at different power levels and using the two different foil types.

Table 4-1: Neutron activation reactions for the two activation foils with their cross-sections (σ) and the product gamma decay characteristics: decay half-life ($T_{1/2}$), energy of the main gamma-ray (E_γ) and relative probability of the decay (I_γ) through emission of the main gamma-ray. Source of nuclear data: [46].

Foil	Reaction	σ (b)	Nuclide	$T_{1/2}$ (s)	E_γ (MeV)	I_γ (%)
Au	$^{197}Au(n,\gamma)^{198}Au$	98.65	^{198}Au	2.33E+05	0.41	95.6
Zn	$^{64}Zn(n,\gamma)^{65}Zn$	0.79	^{65}Zn	2.11E+07	1.12	50.6
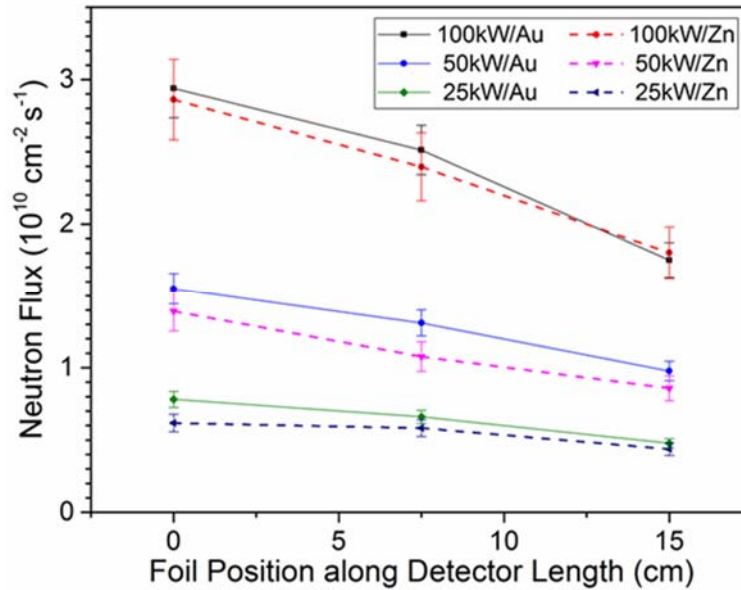
Figure 4-4: Neutron flux densities measured with activation of Au and Zn wires, at different reactor power levels and at different positions along the detector length. The position 0 cm is approximately at the hot-end of the TRIGA GTC experimental position.

In application of the neutron flux values in analyses of SPD measurements, average of multiple flux measurements have been taken. For this, either the results of one type of foils at more than one positions have been combined, or the results from two foil types at multiple positions have been averaged. Such combinations have to be used for two reasons. Firstly, the bias created by large cross-section resonances in one dosimetry reaction of a single foil (like for the ^{197}Au reaction in Au foil) can be partially normalized by taking an average of measurements through two different reactions in two different foils. Secondly, the active area of detector spreads across 5 cm to 10 cm in length, for which any one position of flux measurement is not sufficient. It is required to estimate an average flux either in front of the SPD sandwich (for flat SPDs) or on the lateral surface of the SPD (for cylindrical SPDs), depending upon the case, and also on the available model with the which the experimental results are to be compared.

4.1.3 Uncertainties in flux estimation in TRIGA GTC

As the fluxes have been measured using two neutron activation foil setups, the main sources of uncertainties in the estimation of flux densities in case of TRIGA GTC

are the experimental errors accumulated in gamma spectroscopy and reaction rate calculations. The gamma-ray spectrum analyses are performed using a computational routine developed in the post-analysis software of the HPGe detector. This includes steps like energy and efficiency calibrations, peak-fitting, background subtraction, Compton suppression, peak area determination and activity calculation. It calculates the activity at the end of irradiation employing the cooling and measurement times, and the decay constant of the identified nuclide. Some details have been provided in Appendix 3, including the mathematical equations used in this process. While this is frequently applied, it has amounted to net uncertainties between ±1.4% to ±3.4% in the determined activities in TRIGA GTC neutron flux measurements. A major part of this is due to efficiency calibration, for which a commercially-available radioisotope calibration-solution, irradiated under same conditions as the activation foils, has been used.

The measured activities have later been used to calculate reaction rates, which can be used to obtain flux densities. The uncertainties due to the foil masses (up to ±0.15 %), half-lives (±0.01% for Au and ±0.05% for Zn), gamma ray yields (±0.1% to 0.5%), irradiation and cooling times (±5%) and effective reaction cross-sections (±0.1% for Au and ±2.5% for Zn) lead to total uncertainties in flux density calculated with any individual foil between ±6% and ±10%. As the averaged values of multiple measurements have been used for the SPDs tested in TRIGA, the total uncertainties in fluxes after averaging have been determined to be between ±17% and ±21%.

4.2 Fast Neutron Test Setup

4.2.1 TU-Dresden D-T Neutron Generator

TUD-NG, the neutron generator of Technical University of Dresden (TUD) is an accelerator-based facility for fusion neutrons [60]. It is operated under a collaborative effort by the Institute of Nuclear and Particle Physics of TUD, and the Institute of Neutron Physics and Reactor Technology (INR) of KIT. The facility is situated at the campus of Helmholtz-Zentrum Dresden-Rossendorf (HZDR). It is an intense source of fast neutrons from D-D and D-T reactions. The reaction occurs on bombarding of an energetic beam of deuterons on a target containing tritium or deuterium, depending on the needs of the experiment. A duoplasmatron deuteron ion source, a Cockroft-Walton type accelerator and quadrupole focusing magnets are important components of the assembly, a schematic drawing of which is shown in Figure 4-5.

For the deuteron (^{2}D) beams in TUD-NG, a maximum terminal energy of 320 keV and a maximum current of 10 mA can be achieved. A tritiated titanium (Ti-^{3}T) target, of approx. 6 cm diameter, supported by Cu backing plates and having tritium loads between 3 Ci and 250 Ci, is mounted for D-T neutron generation. It is actively cooled using running water in a cap made from stainless steel. In Figure 4-6, sketches of the tritium target assembly of the TUD-NG are provided from side- and front-views. For the discussions in this thesis, the TUD-NG beam axis has been taken along the Y-axis of a Cartesian coordinate system. Typically an SPD is mounted in front of the water cap, as shown using a black circle on (7) in Figure 4-6.
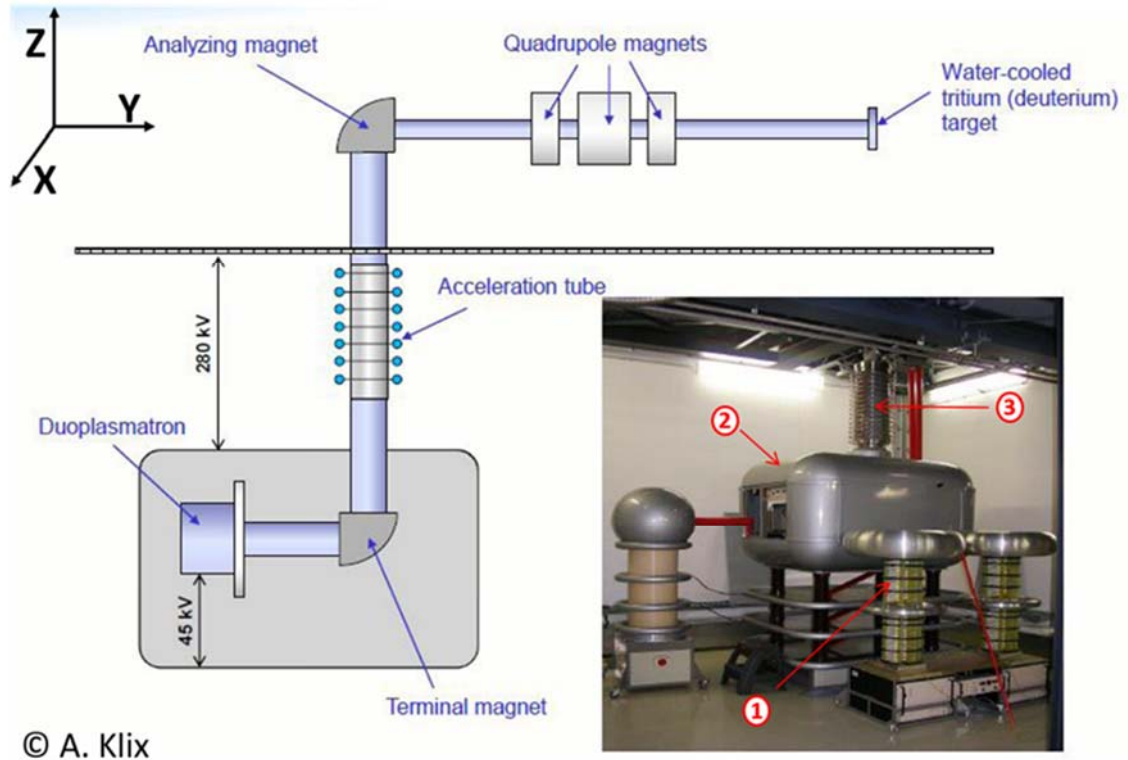
Figure 4-5: Schematic sketch of the TUD-NG showing its main components, and (inset) picture of the setup showing components of (1) Cockroft-Walton type high-voltage generator, (2) duoplasmatron ^{2}D ion-source and (3) acceleration tube leading to the vertically exiting beamline.

The testing of SPDs has been done with continuous ^{2}D beams, typically accelerated across 320 kV, and focused on the target with currents from 0.7 to 1.8 mA. With a 1 mA ^{2}D beam in a typical SPD setup, average yield of D-T neutrons is 10^{11} s^{-1} in 4π. The intensity has been varied from 10^9 to 10^{11} s^{-1}, often by varying the beam current, as per the needs of the experiments.

For this facility, the detailed and precise information on the beam shape, size and its deviations has not been obtained. However, in [64], the beam spot and angular dependence of neutron emission profiles have been experimentally and theoretically understood. The impinging beam creates an oval distribution on the target, whose center may shift between any two irradiations by 1 cm to 1.5 cm, due to the need of manual focusing of the beam. On right image in Figure 4-6, the dotted black circle (10) roughly depicts the area of target within which the beam can be focused in any experiment. The mean energy of emitted neutrons can vary on changing detector's angular position w.r.t. beam axis ((7) in Figure 4-6) due to the D-T reaction kinematics, from 13.4 MeV (at θ = 180°) to 14.9 MeV (at θ = 0°). These factors have been taken care of when characterizing the TUD-NG experimental setup, while it is pointed out that it is a difficult task and does lead to unavoidable errors.
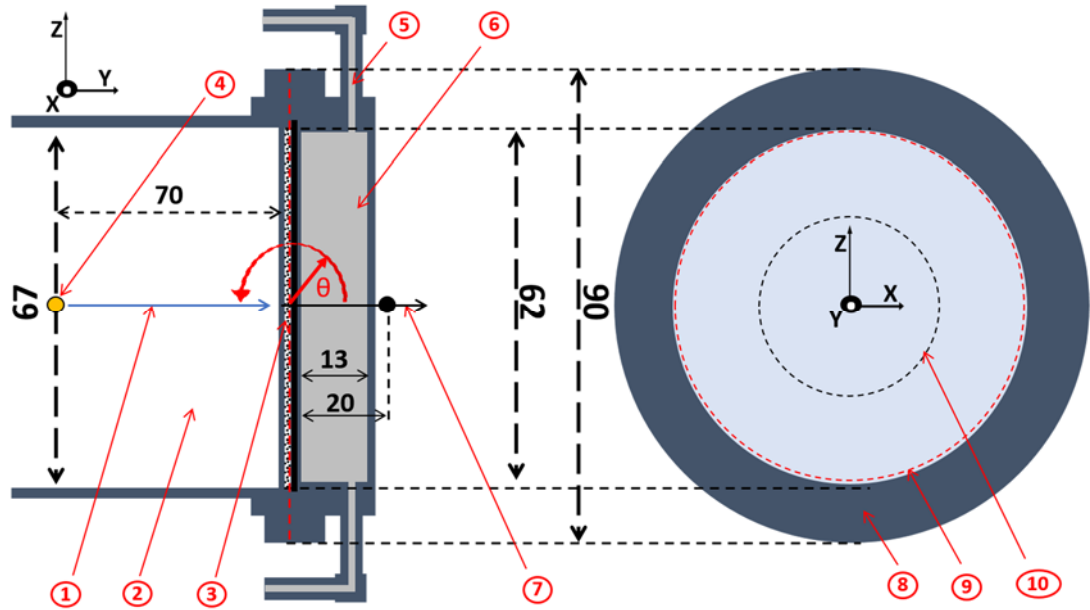
Figure 4-6: Schematic sketches to show the (left) side-view and (right) front-view of the region around the tritium-target assembly of the TUD-NG. The shown dimensions (in mm) are approximate. On the left image, one can identify: (1) the beam-axis of ^{2}D-beam (taken along Y-axis in this coordinate system), (2) the ^{2}D beam-tube, (3) Ti-^{3}T target with Cu backing plates (red dashed line shows the approximate position of the thin target), (5) cooling water tube, (6) water cap for active cooling of the target and (7) primary axis of neutron emission. The relative angle (θ) of neutron emission w.r.t. to the ^{2}D beam axis is depicted. On the right image, (8) outer ring shows the stainless-steel target mounting structure and (9) ring with red border highlights the approximate lateral positioning of the tritium target. Studies in [64] have led to realize that the beam spot on target can shift up to 1.5 cm from the centre, in the region shown through a dotted circle in (10). Typically, an SPD has been placed very close to the target, like shown using a black circle on (7), approx. 2 cm away from the target, however this varies in the real experiments depending on the type of SPD and its mounting structure. Neutron monitor detector is placed behind the target at (4).

The TUD-NG laboratory has been the home laboratory for design, construction, and qualification of SPDs. Furthermore, it has been used for fast neutron experiments in this work. Besides the source for reference studies with SPDs, TUD-NG provides the source for most extensive tests on newer SPDs. In Figure 4-7, three photographs show different SPD-variants mounted in front of the Ti-^{3}T target of the neutron generator. While lighter cylindrical detectors have been stuck directly to the target using cellophane tapes, auxiliary structures like vertical stands, SPD mounting rack have been employed for flat detectors. As the sensitive pico-ammeter cannot be placed in the neutron hall, for the danger of high radiation, long lead cables have been used. The cables run through either the access port on the ceiling of the hall or the underground labyrinth. In some cases, the device has also been placed in a shielded cage in one corner of the hall.

4.2.2 TUD-NG Neutron Monitoring and Flux-Spectra Estimation

At TUD-NG, a Si-diode based α-particle detector (4 in Figure 4-6), placed about 70 cm behind the target, measures the alphas from the D-T reaction in real time. It is used to monitor the 14 MeV neutron generation rate at the target position. The count rate of alphas (unit s^{-1}) is proportional to the neutron intensity. Through a validated

computational model of the TUD-NG target assembly setup, a *calibration factor* between alpha particle rate and neutron emission rate is obtained. This is verified using a neutron activation analysis based upon the standard dosimetry reaction ^{93}Nb (n, 2n) ^{92m}Nb. A ^{238}U fission chamber is used for additional real-time neutron monitoring.
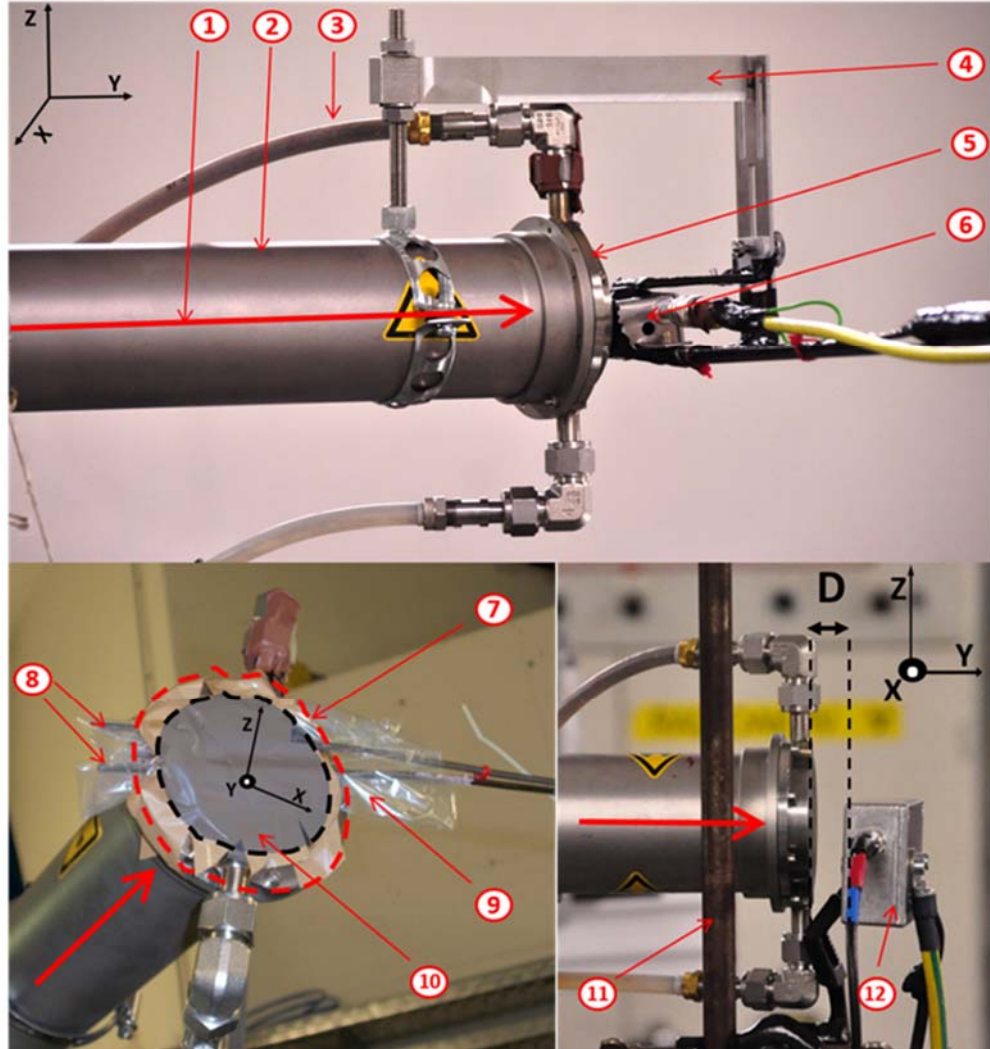
Figure 4-7: Images showing photographs of the TUD-NG SPD test setup with three types of test detectors: (top) sandwich-type edition-2 SPD, (bottom left) two cylindrical SPNDs and (bottom right) sandwich-type edition-1 SPD. The detector is normally mounted close to the target for irradiations. The components are labelled as: (1) arrow showing the ^{2}D beam-axis, (2) ^{2}D beam-tube, (3) cooling water tube, (4) mounting setup for flat SPDs, (5) tritium target assembly, (6) SPD stuck to the target assembly, (7) outline depicting the periphery of the target assembly, (8) cylindrical SPDs stuck to the target assembly, (9) cellophane tapes used for sticking detectors and isolating them from the TUD-NG, (10) grey coloured region depicts the approximate shape of Ti-^{3}T target, (11) metal stand used for mounting SPDs, (12) flat SPD mounted a bit far from the target assembly. The typical distance (exaggerated in this image), D of SPD front from target assembly is between 0.5 cm to 4 cm, depending on the aim of the test.

The only measured quantity in TUD-NG monitoring is the α-particle count rate (in s^{-1}), also known as the *TUD-NG monitor count rate*, proportional to the neutron emission rate at the center of target. The neutron spectra for each kind of SPD have been

determined through Monte-Carlo simulations, with the geometrical description of the individual SPD in the model. The computational model of the setup is thus, a crucial element in flux-spectrum estimation for tests at TUD-NG. This model has been in use at TUD-NG for more than a decade and it defines the tritium-target assembly and its surroundings on the lines of Figure 4-6. The discussion on it is postponed for Chapter 6, and the reader is pointed to Figure 6-6 for a quick view of the renditions of the two geometry plots (one with cylindrical SPD and another with flat SPD) from this model.

The radiation source at irradiation position in TUD-NG is a disc-like source. The neutron flux drops rapidly with an inverse square dependence, with increasing distance from the source. In test of an SPD, high neutron flux is necessary to have stronger signals. Because pA-scale currents are expected, it has been decided to place the detectors within 2 cm distance from the target. This distance also accomodates the cooling water assembly (around 1.5 cm thick), and the cardboard/paper and the cellophane tapes used for sticking and mounting the SPDs and electrically isolating them from the target water cap. In any test, the distance D in Figure 4-7 has been measured before the experiment, which has been added to the approx. thickness of water cap, giving the total distance between assumed neutron emission position and the SPD surface.

Calculated flux-spectra of neutrons and photons in TUD-NG, at a position approx. 2 cm away from the front of the target, and at $\theta = 0˚$, are shown in Figure 4-8. The neutron spectrum has a peak at approx. 14 MeV. The photons have an energy distribution between 10 keV to 10 MeV with some peaks. The real-time α-particle count rate (in s^{-1}) has been recorded on a separate computer in test of an SPD. Its value as high as 2×10^3 s^{-1} can be achieved in a typical run, equivalent to the yield of neutrons of the order of 7×10^{10} s^{-1}, as determined using the calibration factor. The order of the total flux-density of neutrons at the SPD position is then, 10^9 cm^{-2} s^{-1}, and of photons, 10^8 cm^{-2} s^{-1}. Photons, mainly prompt gamma from irradiation of the target assembly and surrounding materials, constitute 17% to 20% of total incident particle flux in the experimental positions.

4.2.3 Uncertainties in flux estimation at TUD-NG

The estimation of the flux densities of neutrons and photons in TUD-NG may incur large uncertainties. Main inputs are the measured count-rates from α-detector, calibration factor and distance of the detector from the tritium target. The calibration factor is available for region around centre of the target, while the beam spot is not at the centre always, which is a source of error. In longer runs of the generator it is also difficult to maintain constant flux due to operational constraints, such as the need to change the beam position to avoid large burning of tritium at the spot. Therefore, the flux may fluctuate and it becomes necessary to obtain an average value over the time of operation for analyses of SPD signals. In the presented results in this dissertation, count rate uncertainties range between ±0.1% and ±7%. The pre-evaluated calibration factor, which is the number of neutrons per α-particle count recorded in the monitor, has a relative uncertainty of approx. ±5%.

A rather large error arises due to the SPD-source distance measurement. Precise positioning of the beam spot is difficult and it varies between two measurements. It is to be noted that the issue of beam positioning is critical only when the test position in very

close to the target. This is not common for other kinds of tests at TUD-NG, and so, no good methodology for monitoring this has been implemented in the lab. The geometrical centre of the target has been assumed for the beam spot for SPD tests. It is not always correct and so an uncertainty value in distance due to this, depending on the type of SPD tested, has been taken. Secondly, an assumption of the point of flux estimation, either geometrical centre of the SPD active region or its front surface, has to be made. Auxiliary components like the mounting setup, insulation, cellophane tapes etc. make additional (up to 1 cm) gaps between SPD and target, each of which incur small shares of uncertainties. With uncertainty of the distance measurement device, uncertainties in the location of beam-spot and that of the flux measurement position, and uncertainty of the thicknesses of components making the gap between Ti-^{3}T target and the SPD, even in the best cases, a ±5% uncertainty in distance can arise. In practical cases however, these factor make the estimated uncertainty in distances as large as ±30%.
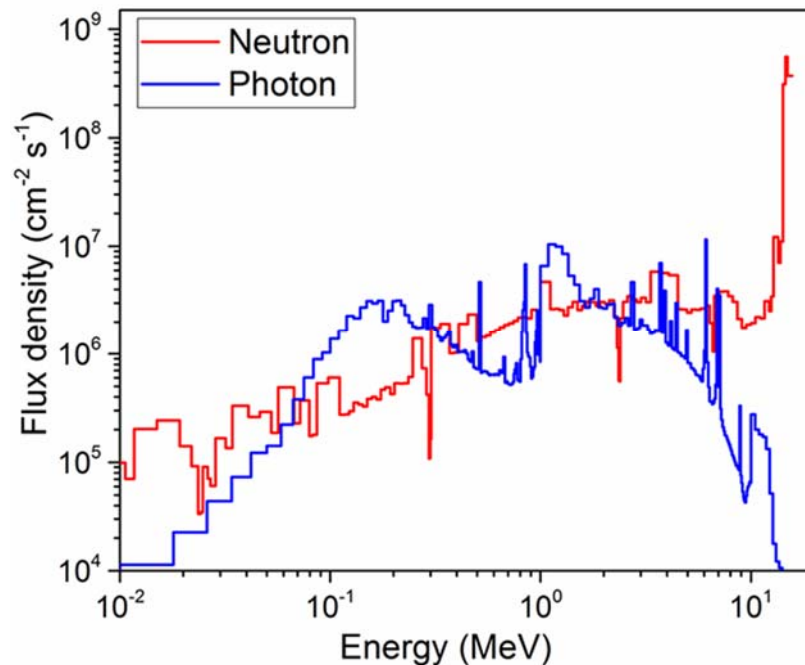
Figure 4-8: MCNP-calculated flux-spectra of neutrons and photons in front of the TUD-NG target. Fusion-relevant 175 energy groups are used for neutrons, while an ad-hoc 100 keV equidistant bin size has been used for photons. A typical position, approx. 2 cm away from the Ti-^{3}T target centre, and along the beam (at angle, $\theta = 0°$) has been chosen for a reference exercise on TUD-NG source characterization. The beam at current of around 1 mA, amounting to a recorded α-particle count of 2000 s^{-1} has been taken here.

Through quadratic propagation of the aforementioned sources of uncertainties, the total uncertainty in measured flux density at the SPD position in TUD-NG lies between ±11% and ±61%. The former value is nominal for experimental setups, while the latter value evidently leads to large uncertainty in estimated SPD sensitivities. For high-precision quantitative analyses in future, many improvements in source characterization approach and devices are desired, but for this thesis, it will suffice for conclusive understanding of the fast neutron response characteristics of SPDs.

4.3 High-Energy Photon Test Setup

4.3.1 ELBE Bremsstrahlung Facility

The superconducting electron accelerator ELBE (**E**lectron **L**inear accelerator for beams with high **B**rilliance and low **E**mittance) hosted by the HZDR Dresden, can deliver electron beams of energies from 6 to 18 MeV and average currents up to 1 mA [65]. With several secondary beamlines like a free-electron laser (FELBE), THz pulses (TELBE), neutrons (nELBE), positrons (pELBE) and bremsstrahlung photons (γELBE or GELBE) etc., the accelerator constitutes an international user-facility for high-power radiation experiments. For studies with photon-induced reactions, there are two associated experimental sites in ELBE: the *electron beam dump (ELBE-BD)* and the *GELBE beamline and cave*. A rough sketch of the bremsstrahlung facility at ELBE HZDR [61] is shown in Figure 4-9. Main components of the beamline are marked using numbers in the figure, which are accordingly quoted in the following description.
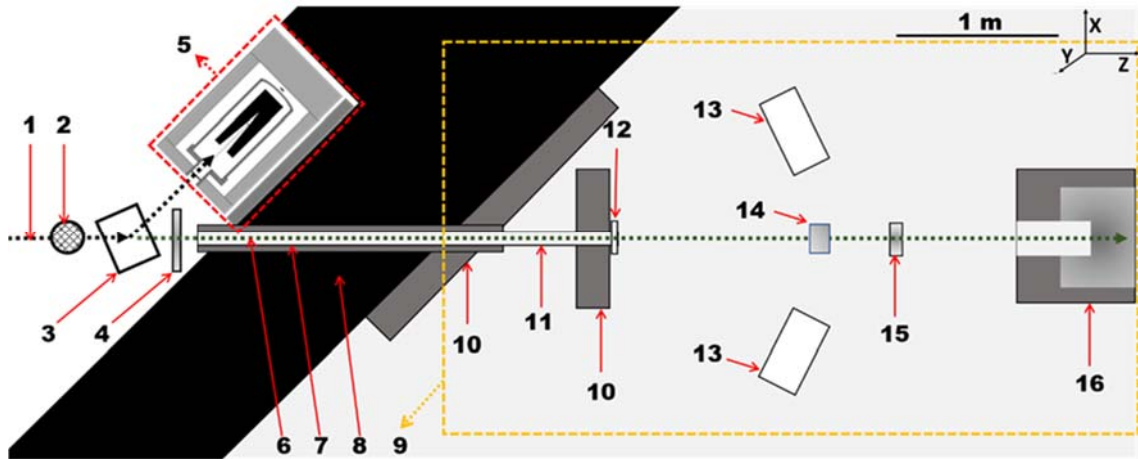
Figure 4-9: An outline of the bremsstrahlung facility at ELBE accelerator showing the two SPD photon irradiation sites: ELBE-BD (in red rectangle) and GELBE cave (in yellow rectangle). Only important elements have been drawn and numbered: (1) electron beam, (2) Nb radiator foil, (3) purging magnet, (4) quartz window, (5) ELBE-BD, (6) photon beam, (7) Al-collimator, (8) heavy concrete walls, (9) GELBE cave, (10) Pb-shielding, (11) collimated beam pipe, (12) beam exit feedthrough, (13) shielded germanium detector setup, (14) scattering target (e.g. ^{11}B) position, (15) SPD position in GELBE, (16) photon beam dump. In GELBE, the photon beam is assumed along the Z-axis of the Cartesian coordinate system.

As seen in Figure 4-9, a high-energy electron beam (1) is bombarded on a radiator foil (2) using focusing magnets to produce photons. For the radiator, one of the multiple Nb foils (varying in thickness) can be selected using a remote-controlled motor drive. The spatially distributed emitted photons are beamed (6) by passing through a 2.6 m long collimator made of high-purity aluminum (7). The Al-collimator is placed around 1 m ahead of the radiator and is made of 13 cylinders with conical drill-holes sequentially varying in diameter (5 mm at the entry of the beam to 25 mm at the exit). The beam exits in a room called as *GELBE cave* (9), separated by a heavy concrete wall (8) from the main accelerator hall. The photon beam exits from the collimator into an evacuated

feedthrough (12) connected to an evacuated polyethylene pipe. It travels in this pipe and is stopped in the photon beam dump (16) made of polyethylene with lead walls. In the cave, in Figure 4-9, a well-shielded germanium detector setup (13) is installed for photon scattering experiments with targets (14) of chosen materials, e.g. Nb, B etc.

For the SPD irradiation experiments in GELBE, the polyethylene beam pipe and the target(s) have been removed. The test-SPD has been placed a few centimeters away (15) from the usual target position.

For the collimated photon beam created in GELBE, the beam spot at the SPD position has a highly homogenous distribution over a circle with 2 cm diameter, as ascertained from experiments and calculations previously [66]. Two labelled and numbered photographs of the SPD mounting in irradiation position in GELBE are shown in Figure 4-10. The images show the exit of the photon beam (2), in the center of the evacuated feedthrough (1) which connects with the Al-collimator in the concrete wall on the back of the room. Yellow parts (German word for yellow is *gelbe*) show concrete and lead shielding. Four symmetrically placed blocks of lead with mounts for HPGe detectors (4) are also seen in the figure. At the center of the four detectors (removed for SPD experiments) is the position of scattering targets in usual bremsstrahlung measurement experiments (14 in Figure 4-9).
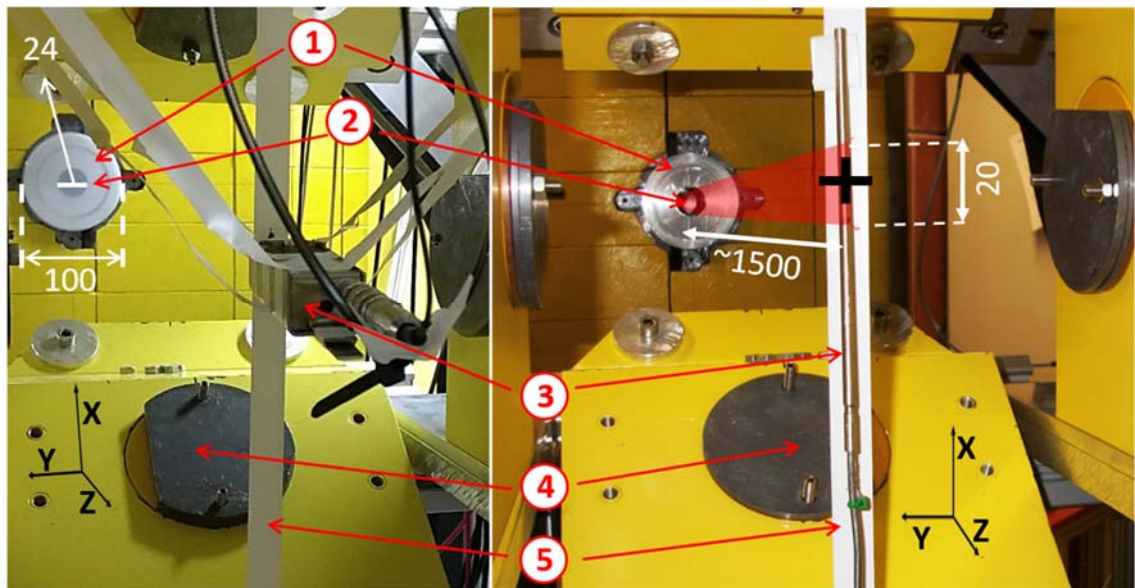
Figure 4-10: Labelled photographs of the experimental setup in GELBE cave. Some essential approximate dimensions (in mm) have been shown. Left shows an edition-2 flat SPD mounted while the right shows a cylindrical SPD. The wall on the back side is at the end of the Al-collimator. (1) shows the feedthrough with a (100 mm diameter) cylindrical Al vacuum chamber which holds the beam exit, which itself is shown by (2). (3) marks the two mounted SPDs, and (4) the auxiliary mounts for Ge detectors. The beam axis is along Z-axis and its centre is marked using a crosswire (shown in black plus sign on right figure) drawn on a long piece of cellophane tape (shown in (5)) stuck along X-axis. The position of SPD mounting is behind the regular target position (see Figure 4-8). A translucent red beam is sketched out in the right figure to visualize the position of the SPD in the photon beam.

The vertical level of the center of the beam in GELBE cave can be obtained using a position-calibrated laser beam installed on the beam dump side. For ease of alignment of the SPDs, a piece of cellophane tape (5 in Figure 4-10) has been stuck vertically and a cross-wire has been drawn at the beam-center found using the laser. For testing them, the test SPDs, cylindrical or flat have been stuck using tapes to float in an in-the-beam orientation (3 in Figure 4-10). A rough augmented image (in translucent red) on the right photograph in Figure 4-10 shows the beam emanating out of the beam exit and illuminating the cylindrical SPD.

A second test position has been used for some photon tests of SPDs in this work, which is at the high-density graphite-made dump of electron beam, *ELBE-BD,* as shown in (5) in Figure 4-9. The method of characterisation of this setup is similar to that of GELBE cave, so, it is not described in detail here.

4.3.2 Flux Calculations and Measurements

The photon flux-spectra in GELBE cannot be measured by directly putting a photon spectrometer in the beam. It is done by measuring photons scattered from chosen targets, in the high-efficiency low-background germanium detector system(s). Experimental measurements are utilized to confirm the Monte-Carlo models, which are used for descriptive analyses. For photon tests of SPDs, a Monte-Carlo simulation of the GELBE facility in the FLUKA code [67] has been provided by the HZDR for the pre-analyses. This model defines the facility in a similar fashion as drawn in Figure 4-9 (see Appendix 4 for a rendition of the model geometry). The spectrum is calculated for several electron beam energies, and at the two available positions in the GELBE cave: at the beam exit (12 in Figure 4-9) and the SPD mounting position (15 in Figure 4-9). The spectrum of bremsstrahlung photons is a continuous distribution in energy, ending at the energy of the impinging electron beam (E_{beam}). The flux density is directly proportional to the beam current (I_{beam}) for a given E_{beam}. In Table 4-2, the range of photon fluxes calculated for various beam conditions at the SPD position are shown.

Table 4-2: The applied electron beam energies and currents, and the corresponding calculated photon fluxes in GELBE tests.

Beam Energy	12 MeV	13.5 MeV	15 MeV
Employed Beam Currents	350 µA to 600 µA	350 µA to 600 µA	350 µA to 600 µA
Estimated Photon Flux	1.8×10^9 cm^{-2} s^{-1} to 3.1×10^9 cm^{-2} s^{-1}	2.3×10^9 cm^{-2} s^{-1} to 3.9×10^9 cm^{-2} s^{-1}	2.9×10^9 cm^{-2} s^{-1} to 4.9×10^9 cm^{-2} s^{-1}

An important aspect for SPDs' testing at GELBE is to compare the normalized spectrum of photons at this position with the one in TUD-NG. In Figure 4-11, such a comparison for (E_{beam} = 13.5 MeV at I_{beam} = 500 µA) is shown. This beam provides photons with energy over the whole requisite range. TUD-NG spectrum is the one of Figure 4-8. Agreement between the spectral shapes seems acceptable and the photon sensitivities in the two cases can be compared for a broad idea of the SPD's photon

response. Therefore, a 13.5 MeV electron beam on Nb radiator foil has been used for measurement of photon sensitivities of SPDs in this work.

An experiment to measure the photon flux at the experimental position has also been performed prior to the irradiation tests of SPD, by the HZDR GELBE team, for the standard beam used (E_{beam} = 13.5 MeV, I_{beam} = 500 μA). The result has been used to compare the newly implemented FLUKA model of the GELBE cave. The experiment is based on a measurement of photons scattered from a thin [11]B-target [68]. Around the transition energies of the target isotope, one can obtain the information on the incident photon fluxes. For extrapolation beyond the measured energies, analytical Schiff's formula [69] for bremsstrahlung spectrum is applied.
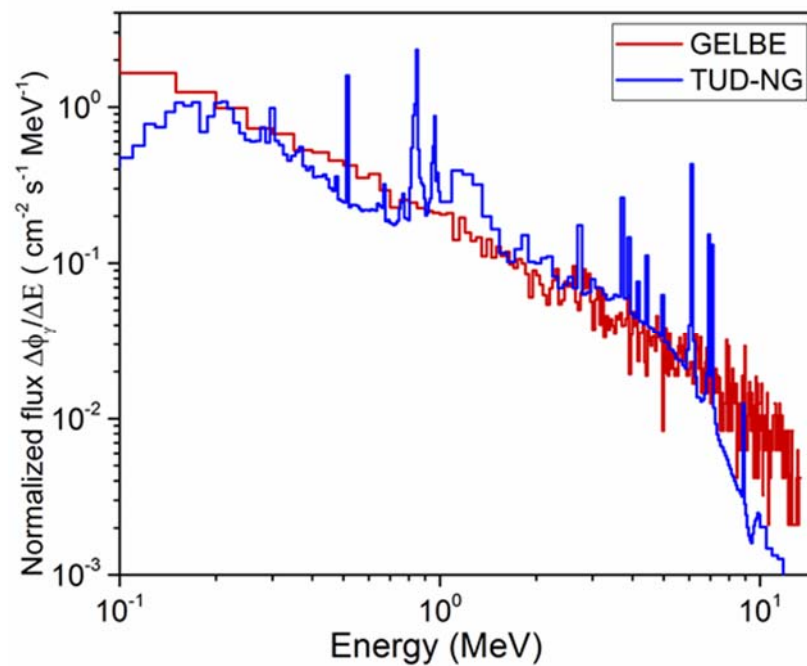
Figure 4-11: Comparison of FLUKA-calculated normalized photon-spectrum at the experimental position in GELBE (red curve) with the normalized MCNP-calculated photon spectrum at the test position in TUD-NG (blue curve). For GELBE, electron beam with E_{beam} = 13.5 MeV, I_{beam} = 500 μA and Nb radiator foil have been taken. For TUD-NG, this is same as in Figure 4-8, with [2]D beam of current around 1 mA, providing monitor count rate of approx. 2000 s^{-1}. For spectral comparison, the group fluxes have been normalized and are shown as flux per unit of the energy-bin size ($\Delta\phi_\gamma/\Delta E$).

In Figure 4-12, the experimental photon-flux measurements, the extrapolated photon spectrum and the FLUKA-calculated spectrum are compared. Schiff's interpolation below approx. 4 MeV is generally known to over-estimate the experimental values in such a measurement. Thus, the higher energy part of the spectrum has been compared with the calculations. For this energy-range, the total photon flux density measured in the experiment (E) is 4.2×10^8 cm^{-2} s^{-1}, while that in the calculation (C) is approx. 4.5×10^8 cm^{-2} s^{-1}. The C/E ratio of 1.09 is considered to be acceptable.

The flux calculations in FLUKA have about 1% statistical uncertainties. Apart from that the only known source of error is the extension of the tested detector outside of the beam area. This has been an issue observed in case of the test of flat sandwich-type SPD (edition-2). Lateral dimensions of the SPD layers (foils) is 2.5 cm × 2.5 cm, because of which a part of the area is outside the beam, which itself is uniformly distributed over a circle of 2 cm diameter. The flux drops sharply outside of the beam zone, which has been corrected for when analysing and comparing the experimental results. Due to missing information on the modelling issues, only the mentioned sources of uncertainties have been accounted for in SPDs' analyses.
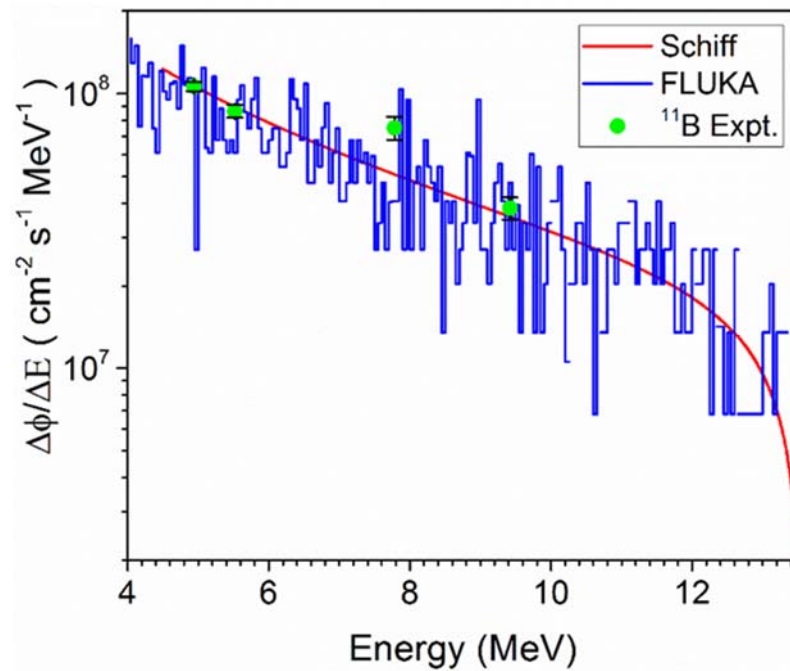
Figure 4-12: Comparison between the measured photon flux-spectrum at the SPD irradiation position (red curve) in GELBE with the calculated flux-spectrum from the corresponding FLUKA simulation (blue curve). The red-curve is obtained through a Schiff's extrapolation applied to the data points (shown in green) from the [11]B scattering experiment.

5. Experimental Tests and Assessment of the Reference SPDs

To draw conclusions on the feasibility of the use of SPDs in TBMs, it is necessary to check their nuclear performance under representative radiation conditions. While it is also essential to understand the difference in SPDs' behavior with change of important properties like the detector's geometry, its layers' dimensions, materials, overall design etc., all detector-variants need not be tested experimentally. For brevity, two test SPDs have been chosen for reference assessments and comparisons: one in cylindrical geometry for which the V-SPND is used (denoted as *CYL* henceforth) and the other in flat design, for which an edition-2 of sandwich-like SPD is used (called as *FLT* henceforth). The *reference SPDs* are irradiated in different experimental setups explained in Chapter 4. An SPD's signal results from aggregate of time-dependent charge-deposition processes in its different layers. In the upcoming sections, the signals of the FLT SPD are presented and explained first, showing the performance of the newer detector under different setups. Its various sensitivities are analysed and its neutron-photon discrimination in fusion-neutron field is checked. The FLT SPD is also compared with the CYL SPD, by comparing their signals and sensitivities in each setup.

5.1 Why Vanadium as Reference Emitter Material?

The CYL and FLT reference SPDs have different geometrical designs, but same layer-materials combinations, i.e. vanadium emitter, Al_2O_3 insulator and Inconel-600 collector. Overall dimensions of the active detectors and layer thicknesses are comparable, ignoring the aluminum shield in FLT SPD (also called as *V-SPD*). In Table 5-1, these properties of CYL and FLT detectors are highlighted.

Table 5-1: Essential properties of CYL and FLT vanadium detectors; *R* denotes radius and *T*, thickness

CYL			FLT		
Cylindrical V-SPND from market			Sandwich-type design Edition 2 (V-SPD)		
Emitter Volume = 0.706 cm³			Emitter Volume = 0.625 cm³		
Emitter	**Insulator**	**Collector**	**Emitter**	**Insulator**	**Collector**
Vanadium	Al₂O₃	Inconel-600	Vanadium	Al₂O₃	Inconel-600
R = 0.15 cm	T = 0.05 cm	R = 0.26 cm	T = 0.10 cm	T = 0.05 cm	T = 0.10 cm

There are three main reasons for the use of vanadium as the reference emitter material. Firstly, it is widely used as an emitter in fission reactor delayed SPNDs. Its response mechanism is simple and is well-understood for the case of thermal reactor application, related to which there are ample experimental and computational data available in the literature. This provides a solid base for study and comparison of the behavior of newly designed flat SPD. Secondly, vanadium is a candidate emitter material for fast neutron SPNDs. In the TBMs, V-SPND signal would have a notable contribution from the thermal neutrons also. Information on thermal neutron flux in the TBM is also valuable. The thermal neutrons are responsible for a major share of tritium breeding, due to the high cross-section of the breeding reaction in ^{6}Li nuclei with the slower neutrons (Eq. 1.2). For application in TBM, it is essential to acquire a good understanding of the behavior of vanadium as an emitter. And finally, vanadium is inexpensive and relatively easier material to handle in laboratories for numerous experiments. For test as emitter, in contrast to vanadium, beryllium is highly toxic, chromium is brittle and silver oxidizes quickly under laboratory conditions

5.2 Thermal Neutron Response

The FLT sandwich-type V-SPD with PTW Low-Noise cable has been mounted on a plastic frame, positioned inside the central channel of TRIGA GTC and irradiated at a constant flux (100 kW reactor power). Figure 5-1 shows the signal obtained with irradiation for 20 min, which is more than five times the half-life of ^{52}V (3.74 min), the expected radionuclide behind delayed response of a V-SPD in thermal neutron field.

The signal rises rapidly in the first two minutes of irradiation, approaching about 67% of the total saturation current. During this time, the reactor power is increased sharply and the detector sees a rapid variation of photon and neutron fluxes. The high prompt response is due to the reactor photon field and photons produced in the detector components including its aluminum electromagnetic case. In this time, and in the rest of the irradiation period, an approach to equilibrium current has been observed. In vanadium SPD, this is anticipated from built-up and decay of the main beta emitter ^{52}V. The signal enters the saturation regime with a current around (492 ± 0.14) pA in this test. On immediate shutdown of the reactor, the FLT SPD current drops to 75% of its value in less than three seconds. The portion of the electrical signal associated with the prompt photons from the surrounding and those induced in detector materials disappears with the neutrons. An exponential decay of the remaining current is observed afterwards.
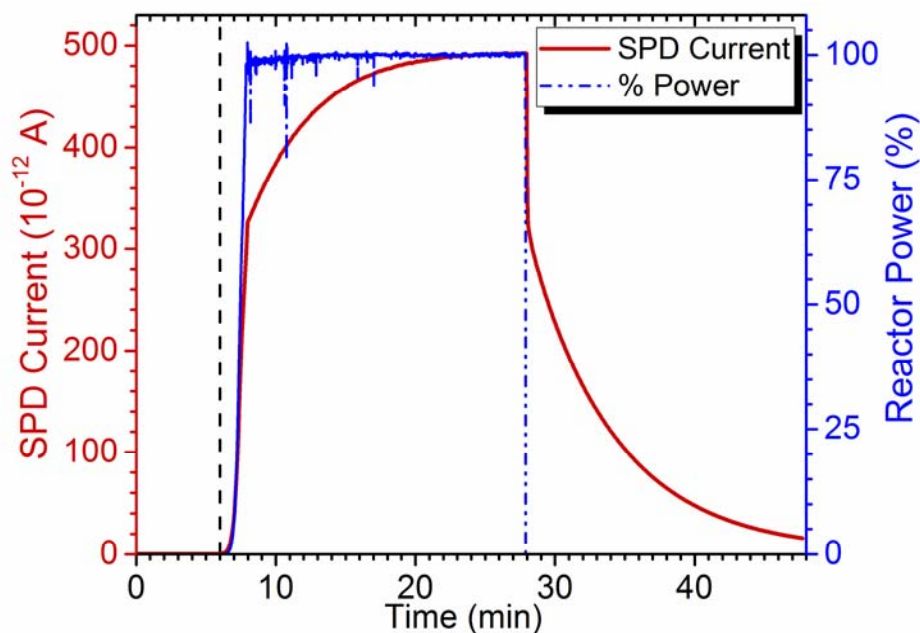
Figure 5-1: Measured thermal neutron signal (red curve) of the FLT V-SPD in the TRIGA GTC (maximum power = 100 kW) and the normalized % power (blue curve) from the reactor feedback system plotted as a function of time. The start of irradiation is depicted by a dotted vertical line at Time ≈ 6 min.

In Figure 5-2, the decaying part of the signal (after Time ≈ 28 min in Figure 5-1) has been shown. The SPD-current signal is originally sampled at the speed of one value per 2.44 s. For ease, the acquired data has been smoothed using time-averaging to reduce the sampling rate, resulting into a *reduced curve.* Then, an exponential curve has been fitted to it. Points of averaged values (reduced curve) and the exponential fit are also shown in the figure. A half-life of around 248.5 s has been determined from this, which is about 10.7% higher than 224.4 s (i.e. 3.74 min), the half-life of ^{52}V.

The deviation from the expected half-life, a frequent occurrence for SPDs, results due to other smaller signal components from reactions in SPD's vicinity which release electrons with delay. Candidates are, for example, capture reactions on materials like Al in the insulator and the EM shield, and Ni and Cr in the collector. The delayed photons, either emitted in the detector or outside, also contribute. The signal originating from non-emitter parts of the detector can be positive, negative or zero, depending on where the emitted charge stops in the detector. The capture cross-sections of other materials are much lower in comparison to that of the main reaction, ^{51}V (n, γ) ^{52}V. If one takes the ^{27}Al (n, γ) ^{28}Al reaction as an example, because aluminum is present in the largest quantity in the detector, its thermal neutron cross-section is of the order of 0.25 b which is only about 0.05 times the cross-section of the ^{51}V (n, γ) ^{52}V reaction under the same conditions. The aggregated effect on the saturated signal due to such processes would amount to a few percent only. For all of them to saturate (and/or decay), several hours of constant flux conditions are required, which is beyond the scope of this study. But, it is clear that they make it challenging to finely resolve all components of the signal. Nevertheless, the overall signal of FLT V-SPD shows a time-dependent behavior expected from a typical SPD, including prompt and delayed parts. This establishes a proof-of-principle of the newly designed flat sandwich-type SPDs.
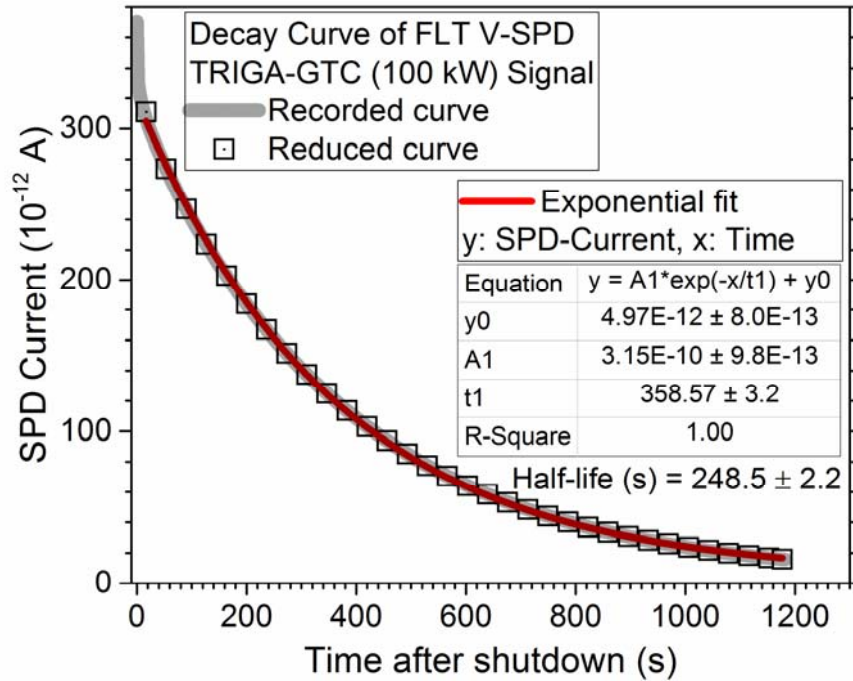
Figure 5-2: Time- dependent decay curve obtained from the delayed component of the FLT V-SPD signal measured in TRIGA-GTC (20 min irradiation at power = 100 kW; see Figure 5-1). The plot shows the recorded current values (grey line), average current values (black squares) with reduced number of data-points and the exponential fitting (red line) with the corresponding parameters (Half-life = ln(2) × t1).

A comparable test of cylindrical CYL V-SPND has been conducted like the FLT SPD, in the central channel of TRIGA GTC. A constant flux irradiation at the highest power level (100 kW) is performed for a period of approx. 20 min and then the reactor is rapidly shut down. The signal is recorded from 5 min before the irradiation (zero current) to 20 min after the irradiation, capturing the signal rise, saturation and decay, as shown in Figure 5-3. The highest signal close to the saturation (after 20 min of irradiation) is measured to be about (153 ± 0.13) pA. The prompt current, which is the portion disappearing immediately after the reactor trip, is about 20 pA.

Backward extrapolation of the exponential decay curve of the CYL V-SPND delayed signal yields approx. (130 ± 1.53) pA as the signal component from ^{52}V. Here, the decay half-life observed is merely about 3% higher than the expected half-life of ^{52}V. This level of deviation is quite normal in reactor-based operation of delayed SPNDs, showing that the contribution of the decaying nuclides in the cable and those of activated materials in the collector, insulator and detector's surroundings are negligible. For complete saturation of smaller delayed factors, many hours of irradiation at constant flux is necessary, which has not been done here.

Magnitude of the SPD signal increases significantly, by about three times, on changing from CYL to FLT geometry for the similar quantity of emitter material. One reason for this is that the flat geometry enhances the probability of charge movement between layers. The physics of charge movement, which is assumed one-dimensional along radius in CYL SPDs, changes to some extent due to FLT geometry. Though it needs to be studied deeply, its effect on the SPD's sensitivity is positive (as intended).
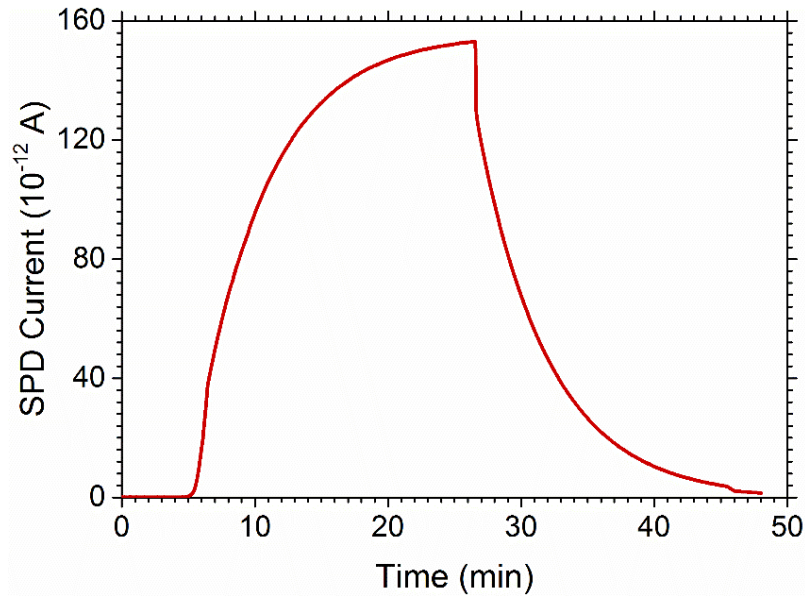
Figure 5-3: Measured thermal neutron signal of CYL V-SPND from irradiation at 100 kW power in TRIGA GTC as a function of time.

The FLT detector, in addition to being more sensitive, turns out to be not well optimized to have a pure delayed SPND. The ratio of prompt to delayed (*P/D*) current components increases by about two times on changing from CYL to FLT. For reliable application, it will be essential to either enlarge (to have a prompt SPND) or reduce (to have a delayed SPND) this ratio. This behaviour is largely attributed to the extended size of the FLT detector, the bulky aluminum shield, exposed sides of emitter foils and the FLT structure's higher susceptibility to stray sources of current in comparison to a more physically compact and shielded CYL design. Therefore, design optimization of FLT SPDs is required to solve these issues. Nonetheless, the signal increase is an important improvement, as the low magnitude of the signal is a big disadvantage of SPNDs, especially for use in low-flux locations.

5.3 Fast Neutron Response

Vanadium SPDs in fast neutron irradiation are expected to produce signals due to the ^{51}V (n, γ) ^{52}V reaction, the threshold reactions like ^{51}V (n, p) ^{51}Ti, and secondary electrons from photon scattering. The FLT and CYL vanadium reference detectors have been tested at TUD-NG for the comparison of their 14 MeV fast neutron responses. The irradiation of two detectors has been performed under similar conditions.

In Figure 5-4, the signal from FLT V-SPD is shown along with the count rate from TUD-NG monitor detector. In this case, the V-SPD signal rises and disappears almost instantaneously with the neutron flux. The saturated signal amplitude is approx. (34.8 ± 0.18) pA. The major, prompt signal component combines the effects of prompt photons from the detector and its surroundings. While the prompt current dominates, a small (approx. 6% of the total) delayed component is also present. It is a sum of the contributions from ^{51}Ti and ^{52}V beta electrons, betas from aluminum case, collector and insulator materials, and decay gamma from the activated detector and surroundings,

whose ratios are not possible to determine in this case due to severely small magnitude of the delayed signal. Due to technical reasons, the incident neutron flux is not stable and changes by 1% to 2% during the irradiation shown in this signal. This is visible in the flat part of the signal (1 min to 16 min).
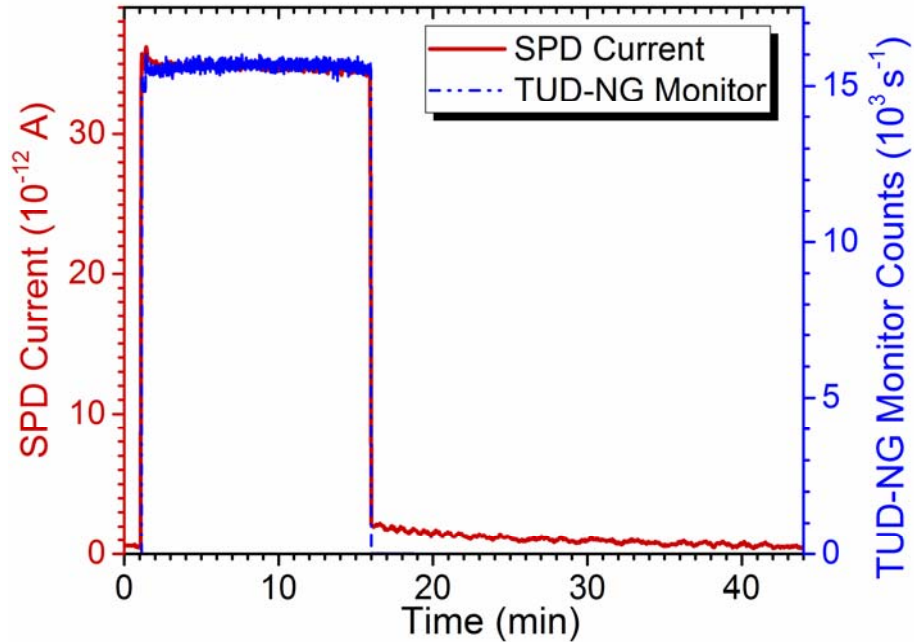
Figure 5-4: Measured fast neutron signal of the FLT V-SPD (red curve) and the corresponding count rates from the TUD-NG α-particle monitor (blue curve) as a function of time.

On careful analyses, some minor contributions from the radiation-induced electrical effects in the SPD, contacts and cables have also been found in the prompt signal. Experimental studies to resolve these are performed at TUD-NG, as shown in Chapter 7. These effects are not well-understood at this stage and are difficult to study due to small magnitudes of currents, but the FLT SPD is deemed susceptible to them.

In Figure 5-5, the signal of CYL SPD under TUD-NG field is shown. The current, almost completely prompt, lies close to the background, in the range of hundreds of fA. Its dependence on the incident flux is clearly visible. At the highest level, the measured current is approx. (0.14 ± 0.05) pA. On comparing with Figure 5-4, FLT SPD signal is found to be about hundred times higher than CYL SPD signal under similar flux conditions. Also, the RMS of fluctuations in CYL SPD is about 33% of the mean signal as compared to the 0.5% in case of the FLT SPD.

The arguments for the increase of the neutron signal magnitude on change of geometry are same as those mentioned in Section 5.2. This is, at first an effect of larger surface area of emission in flat geometry. The change of geometry also brings the active volume (i.e. sandwich) closer to the radiation source in a disc-like source, e.g. TUD-NG, which has been the main motivation behind design and construction of flat SPDs. While, a first order of reasoning of the benefits of flat geometry can be acquired by this, SPD

signal generation is a much more complicated phenomenon vis-à-vis the geometry changes. Also from TUD-NG based simulations in Chapter 6, one can observe that a stronger signal is expected of a FLT SPD in comparison to a CYL SPD. In addition, in Chapter 7, the dependence of signal magnitude on some of the geometrical characteristics of the FLT SPD are understood through experiments.
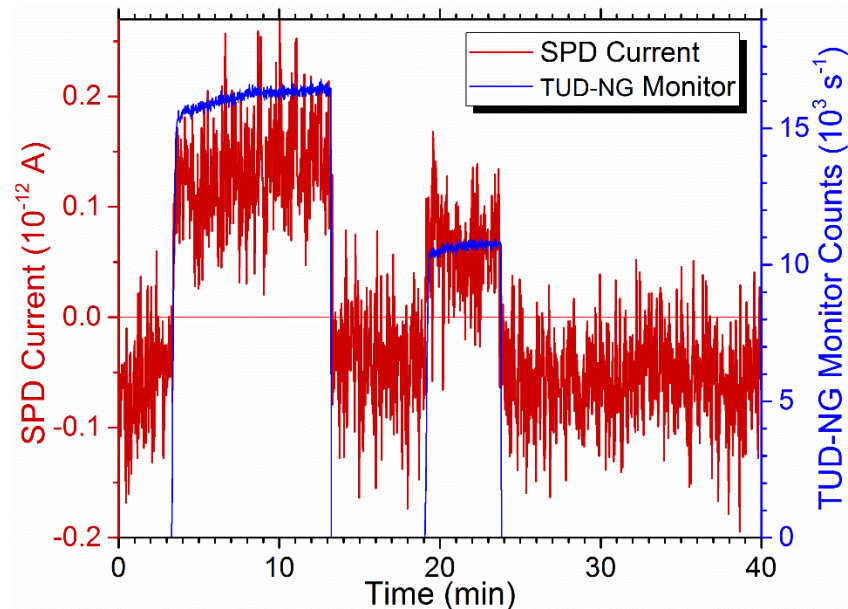
Figure 5-5: Signal of CYL V-SPND under fast neutron irradiation at TUD-NG. The signal is found to vary in proportion with incident neutron flux, but at very low-level currents with large fluctuations.

5.4 Response to High-Energy Photons

The prompt signal component which forms the major part of TUD-NG signals of SPDs contains contribution of external photons also. To discriminate the neutron and photon parts, and for understanding the behaviour of FLT SPD with changing photon field, irradiation tests have been conducted in the GELBE bremsstrahlung photon facility.

At first, the signal from FLT V-SPD measured at GELBE cave has been shown in Figure 5-6. The energy of electron-beam for this experiment is 13.5 MeV. The beam current (thereby the photon flux) is varied in steps and the signal is found to vary accordingly, showing that the detector has high sensitivity to photons. According to the (γ, e^-)-type reactions expected with photons, the signal is 100% prompt, showing approx. (145.6 ± 0.59) pA at the highest flux-level (beam with current = 550 μA).

The same test has been repeated for CYL V-SPND, whose signal is shown in Figure 5-7. The CYL signal also follows the change in the photon flux. In this test, the continuous measurement of beam current has not been possible due to technical reasons. The accelerator operators set the currents as demanded and gave the value of set current through telephone, which have been noted down and are shown through dotted blue lines in the figure. This detector is commercially designed for low gamma response, as evident

from its lower signals. The photon signal of FLT is hundred times higher than that of CYL, strengthening the observation of benefits of flat design for laboratory-based tests of the SPD technology.
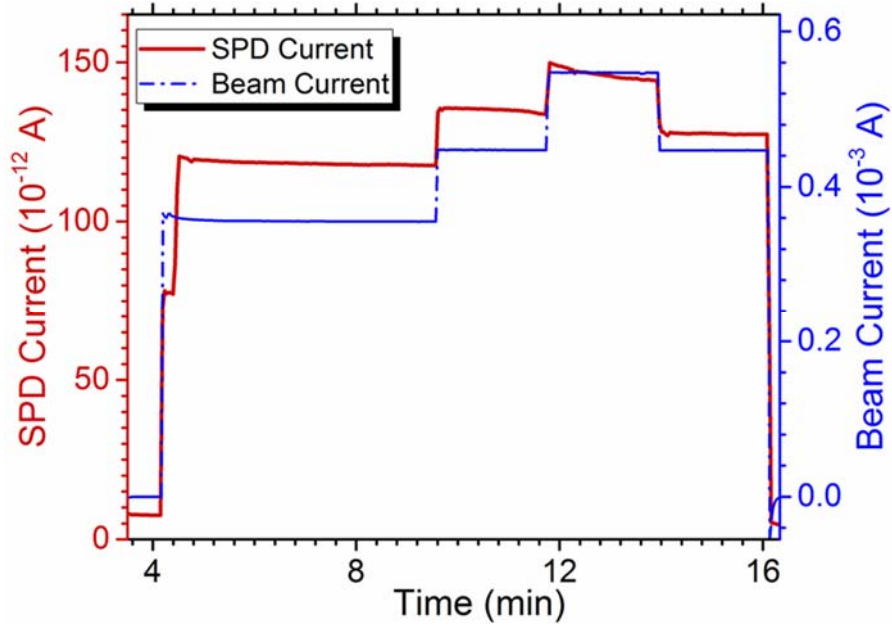
Figure 5-6: Measured high-energy photon signal from FLT V-SPD with GELBE electron beam of energy 13.5 MeV and various levels of beam current (blue), as a function of time.
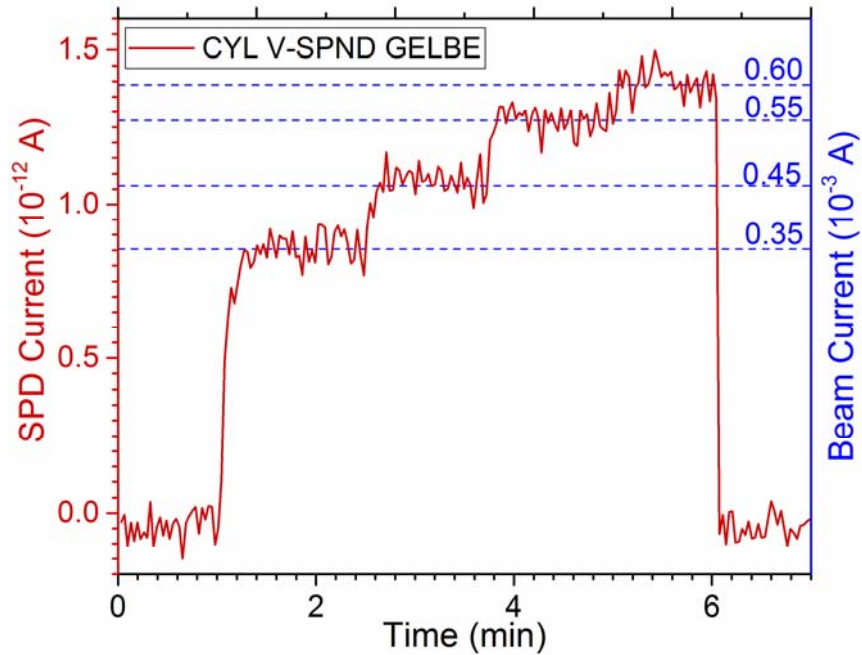
Figure 5-7: Measured high-energy photon signal from CYL SPD at various accelerator beam currents (shown in blue) in GELBE, as a function of time.

Due to a glitch during the experiment with FLT SPD, at two points with the same incident GELBE beam current (~450 µA), the recorded SPD-currents have different values (see current levels around Time = 10 min and 15 min in Figure 5-6). The FLT SPD was hanged using cellophane tapes, one of which came off during the measurement leading to a change in the cable background current (see the decline in red curve around 12 min in Figure 5-6). However, the deviation caused due to this has been less than 5% and the results are reproducible. This is also established in a separate discussion later. Slight overshoots of the FLT SPD signal observed sometimes on increasing the flux levels are artefacts of the manual setting of several operating parameters of the accelerator dictating the output beam current, to set a new flux level. This happens only at a transient, is not visible in beam monitor, but affects the first reading of SPD-current (an average value over 2.44 s). Because the sensitivity of CYL SPD is much lower, such artefacts do not have bigger effects on its signals.

In general, the measurements at GELBE are affected by much lower levels of fluctuations, compared to the tests at other facilities. For example, in Figure 5-6, the RMS of noise at beam current = 450 µA is only 0.05% of the mean signal of the FLT SPD at that level of photon flux. At the same level, for CYL SPD, the RMS of noise is about 3% of the mean signal.

5.5 Reproducibility and Stability of FLT V-SPD Signals

Due to the delayed signal components, the variation of an SPD's signal in a transient reactor condition is peculiar. A few examples of transient condition responses of FLT V-SPD are shown in this subsection, highlighting the need for a dynamic real-time signal processing for SPDs. Also, for a newly developed sensor, like the FLT V-SPD, it is essential to establish the reproducibility of its signal. The reproducibility of signals have been checked experimentally. An SPD is measured at the same flux level twice and the output signals are compared. This has been done for all three test setups exclusively, and some examples are shown here. The percent difference between the two measured values (at same flux-level) are reported for each case.

Besides the tests at constant fluxes in TRIGA GTC, irradiations with sequentially varying fluxes have also been performed, specifically to capture the dynamic characteristics of the signal. The reactor has been run for 20 min period (for saturation of ^{52}V delayed signal) at a constant flux at the power of 100 kW, followed by similar 20 min periods at powers of 50 kW and 25 kW. The signals for FLT and CYL SPDs are shown in Figure 5-8, in which vertical lines separate the constant flux regions (corresponding reactor powers are mentioned). The signals vary proportionate to the incident flux.

For a check of reproducibility, the saturated signals at 100 kW can be compared with the respective 100 kW measurements shown in Figure 5-1 (FLT) and Figure 5-3 (CYL). The difference of mean signals at 100 kW, from the mentioned individual measurements, are –2.4% for FLT SPD and +5.1% for CYL SPD. Such small differences signify that the signals in both the cases are reproducible. These small differences in signals can be caused by activation of cables and surroundings materials in any of the two measurements. For CYL SPD, the cable is an MI cable, capable of producing higher RIEMF, which is why it registers a bigger difference.
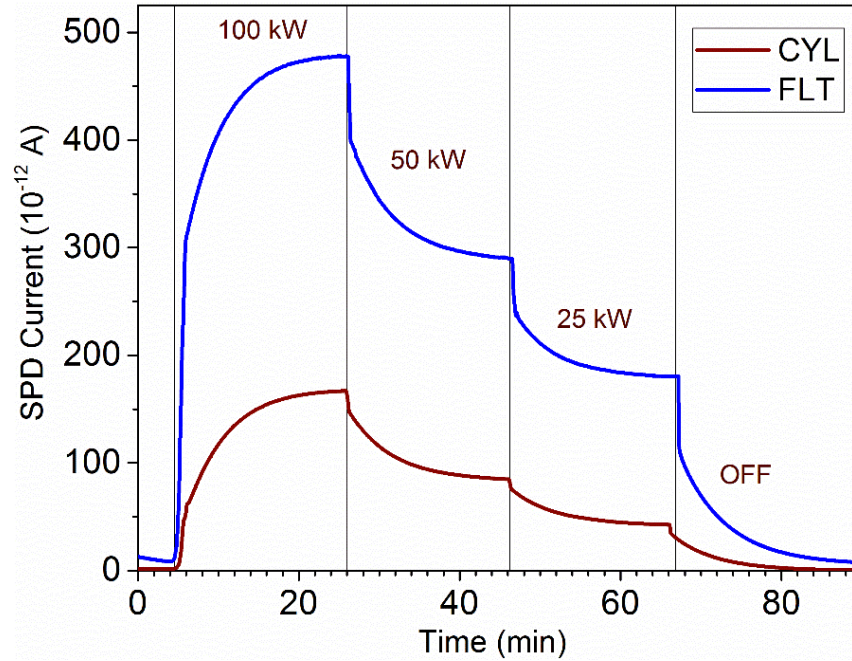
Figure 5-8: Comparison of measured thermal neutron signals of FLT and CYL in TRIGA GTC as a function of time, and their variations with a sequential change of power of the reactor showing the dependence of the signals on incident flux. Constant power (flux) regions are divided using vertical lines.

In the Figure 5-9, the dependence of the newly designed FLT SPD signal on the incident fast neutron fluxes from the tests made in TUD-NG is shown. First of all, this figure illustrates how well the signal follows the variations in the incident flux of fast neutrons. Secondly, the peak signal in this case (approx. 36 pA) is only +3.5% different from that in the measurement shown in Figure 5-4. This is a proof of reproducibility of FLT SPD signals in fast neutron case.

The measurement shown in Figure 5-9 can also be treated as a representative signal profile for understanding the FLT V-SPD performance in terms of signal-noise behaviour and signal-stability. There are four clearly visible levels of DC signals in this curve. The sensitivity of the SPD to slight changes in incident neutron flux is also impressed upon well.

Information on the time-lag in SPD's response is useful for its application as an active flux-monitor. Figure 5-9 provides a second proportional time-series signal, i.e. the TUD-NG monitor count rate, to highlight this. However, both the SPD current and TUD-NG monitor counts are positive DC-like signals. Major DC-offsets in the signals prohibit a meaningful use of the cross-correlation analysis, a common tool for this purpose. Moreover, the TUD-NG monitor is yet another nuclear detector, with its own independent noise, lags and stability performances. It cannot be employed as an absolute measure of the neutron source stability. Ultimately, one relies on visual inspection and coarse temporal comparison between the two channels. Such studies have led to conclude that the measured SPD-current signals are reliably stable and exhibit minimal lags.

Slight decay of SPD-currents have been observed at some of the levels in the Figure 5-9. The total drop of signal from start to end of the irradiation at any level in the

curve, roughly ranges between 0.20 pA and 0.55 pA. This is due to two reasons. Firstly, the flux level itself is not stable and changes by 1% to 5% during the course of a constant flux irradiation. It is common for the operation of the TUD-NG radiation source. Secondly, a small delayed component always gets added to the total signal of SPD in a neutron irradiation experiment, arising due to a previously conducted irradiation of the SPD in the same setting. Often very long cooling periods (few hours to days) are not practical for repeated measurements with SPDs. This particular signal has been acquired few hours after a series of irradiations performed with the same SPD at TUD-NG. Resultantly, a small decaying signal due to activated structures has been present.
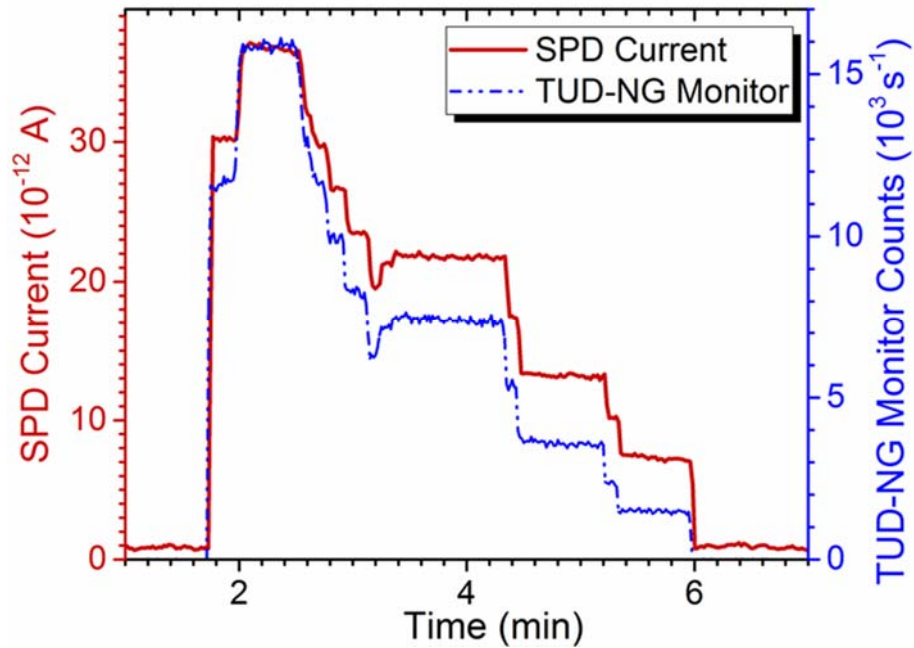
Figure 5-9: Measured dependence of FLT V-SPD signal at different incident fast neutron flux levels, as a function of time. The secondary Y-axis shows counts from the α-particle monitor of TUD-NG.

It is useful to study the SPD's performance with its *signal to noise ratio (SNR)* in decibel (dB) units, which is defined for the SPDs as,

$$SNR = 20 \times LOG_{10}\left[\frac{Mean\ amplitude\ of\ the\ DC\ signal}{RMS\ of\ the\ signal\ noise}\right] \qquad . \qquad \text{(Eq. 5.1)}$$

For the highest level of signal in Figure 5-9, the SNR is about 47.3 dB. This decreases at lower levels, going to 36.8 dB for the mean signal of (7.3 ± 0.1) pA measured at an incident neutron monitor count rate of approx. (1494 ± 41) s^{-1}. Such high SNRs are an advantage of SPDs and their direct measurement schemes. The SNR for the TUD-NG monitor, defined in the same way as above, ranges from 46.5 dB at highest flux-level to 31.3 dB at the lowest.

To complement the discussion on neutron signals, Figure 5-6 shows the signal dependence on photon flux variations. In that test, an experimental glitch led to a change in the background cable signal midway of the test. To suffice for the discussion here, a different signal from the same SPD's test at GELBE is shown in Figure 5-10. This measurement has been done in an across-the-beam orientation in GELBE, instead of the regular in-the-beam position. This makes both the total magnitude of signal and the background currents different from the other test. But here, signals at flux levels corresponding to beam currents 350 μA and 450 μA have been repeated. The signal-differences observed between repeated measurements are less than 1%, verifying the reproducibility of the signals.
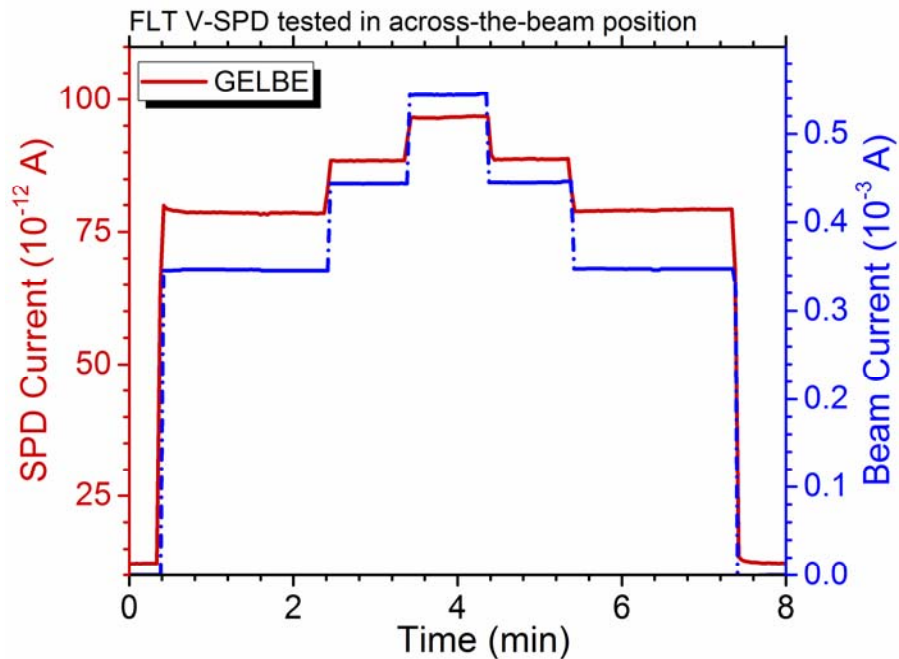
Figure 5-10: Measured photon signal of FLT SPD (red curve) and GELBE photon beam current (blue curve) as a function of time. The SPD is placed across-the-beam in this experiment.

5.6 Determination of Flat V-SPD Sensitivities

5.6.1 Method for sensitivity formulation in mixed fields

The linearity between the incident flux and the signal is a crucial factor in the application of SPDs. Ideally, the sensitivity, ratio of SPD current to the flux density should be constant for a well-calibrated SPD, if the energy-spectrum of the incident particles does not change. With a well-optimized design, the linearity is good for the dominating signal from one of the three current-creating processes: (n, β⁻), (n, γ, e⁻) or (γ, e⁻). In contrast, when the sensitivity is low in magnitude and the current-formation mechanism has several competing contributing processes, then the linearity may suffer. During irradiation tests, the SPDs have been irradiated at each constant flux-level for

sustained time-periods to obtain stable signals. For neutron measurements, more than 20 min have been given to ensure the saturation of ^{52}V induced delayed signals. For photons, where there are no delayed signals, few tens of seconds to several minutes have still been provided to obtain good statistics and stable signals.

In post-analyses, the mean (saturated and delayed) currents with uncertainties have been determined for each flux-level in the SPD signals, correcting for the background or zero currents in the detector setup (see next subsection). The sensitivity has been obtained as the slope of the best fit line between the incident flux density and the SPD current. The line, called as *sensitivity curve*, represents one of the common physical situations of calibration, where both the variables are met with measurement uncertainties. These arise from numerous sources of errors (see Figure 3-7) and noises. The two variables are assumed to be uncorrelated. The corresponding two quantities have been measured completely independently and are affected by physically separated systematic sources of errors. As done typically in linear regression for calibration, more weights have been given to points with smaller absolute uncertainties. A numerical method capable of consistently accounting for the uncertainties in both SPD-currents (Y-axis) and flux densities (X-axis) has been utilized here for the linear fitting.

Through estimation and comparison of the sensitivities to neutrons and photons, the possible modes of application of an SPD and essential modifications in the response mechanism(s) can be realized. Such a comparison has been performed for the TUD-NG fusion neutron tests of the newly designed FLT V-SPD. The response in the mixed neutron-photon field of TUD-NG is a sum of neutron and photon generated currents. The sensitivity curve for GELBE based photon measurements has been used to separate the two of them. It is assumed that the sensitivity to photons is not changing much between TUD-NG and GELBE, as the energy-spectra have been chosen to resemble in the two facilities. Certain aspects of this comparison, for example, effects in detector circuit at higher fluxes, effects of smaller changes in energies, etc., would demand more rigorous physics treatment. Although this is a simplification, this serves well for a first order analysis of the response in mixed fields. It provides a qualitative idea of the feasibility of neutron-photon discrimination using the SPD. Based on this method, the fast neutrons sensitivity ($S_{neutron}$) can be obtained using the following equations.

$$I_P = S_{photon} \times \varphi_{photon} \qquad . \qquad \text{(Eq. 5.2)}$$

$$I_N = I_{total} - I_P \qquad . \qquad \text{(Eq. 5.3)}$$

$$S_{neutron} = \frac{I_N}{\varphi_{neutron}} \qquad . \qquad \text{(Eq. 5.4)}$$

Here, the photon-induced current (I_P) comes as the product of pure photon sensitivity (S_{photon}) measured in GELBE facility and the photon flux (φ_{photon}) at the experimental position in TUD-NG. The neutron-induced current (I_N) is the difference between total measured current (I_{total}) at TUD-NG and the calculated I_p, which when divided by the neutron flux ($\varphi_{neutron}$), gives the neutron sensitivity of the SPD in TUD-

NG. The assumption is that the above simple relation is valid for the measurement regime followed in TUD-NG tests. Standard unit of currents is A, for flux densities $cm^{-2} s^{-1}$, and for sensitivities it is A cm^2 s.

5.6.2 Background currents in three setups

The background currents have been measured over sustained periods before each irradiation test. For this, the detector, cable and picoammeter are set in position and measurement is carried out from few minutes to few hours depending on the need. The background or the zero current, as defined in Chapter 3, appears mainly due to residual currents in the cables (e.g. Figure 3-9). Cables extended over lengths of 10 m in most of the tests, are turned at a few places and hanged from heights at some other places. The SPD's leakage currents and SPD's response to the longer-lived radioactive decay of structural components of the experimental setup are other main sources of background.

Table 5-2 reports the smallest and the largest background currents seen in the FLT V-SPD tests at three experimental setups. The shown uncertainties, between ±0.1% and ±19% of the means in these cases, are the RMS deviations of mean current values, bigger if the measured currents are of smaller magnitudes (order of 100 fA).

Table 5-2: Average of the smallest and largest background currents (in pA) with their standard deviations as measured in the three experimental setups with the FLT V-SPD

	TRIGA GTC	TUD-NG	GELBE
Smallest	0.34 ± 0.02	0.39 ± 0.06	0.52 ± 0.10
Largest	4.50 ± 0.36	0.53 ± 0.02	7.45 ± 0.01

In TRIGA, the highest background has been seen when the measurement is performed around 2–3 hours after a previous reactor run, essentially showing the signal due to long-term decay products from the core. In GELBE, a further higher background, around 7.5 pA has been observed, because the detector and cable had to be hanged using cellophane tapes to be aligned along the beamline, leading to a mechanical stress in the cable due to gravity. For the analyses of the sensitivities, it has been ensured in each case that the backgrounds are stable and as low as achievable. The background before a measurement is subtracted as a constant value from the total signal in the measurement.

5.6.3 Overall sensitivities in thermal neutrons case

As a first step to demonstrate the sensitivity analysis, separate irradiation tests at reactor powers 100 kW, 50 kW and 25 kW have been conducted at TRIGA for CYL and FLT SPDs. The scheme comprises of 20 min irradiations and subsequent decays. The delayed components of the signals are separated through exponential fitting of decay curves and their backwards extrapolation. The net currents (I_{Net}) and the ^{52}V-initiated delayed current ($I_{Delayed}$) components are then plotted for each level. In the Figure 5-11 and Figure 5-12, respectively, the net and delayed current sensitivity curves for CYL and FLT detectors are shown. The average fluxes on detectors' surfaces have been determined

through activation foil measurements (Figure 4-4), with relative uncertainties up to approx. ±17%, arising mainly from errors of averaging, those in time measurements, gamma detector efficiencies and effective cross-sections. The uncertainties in flux densities are also the main reasons for high uncertainties in the calculated slopes, i.e. the estimated SPD sensitivities.
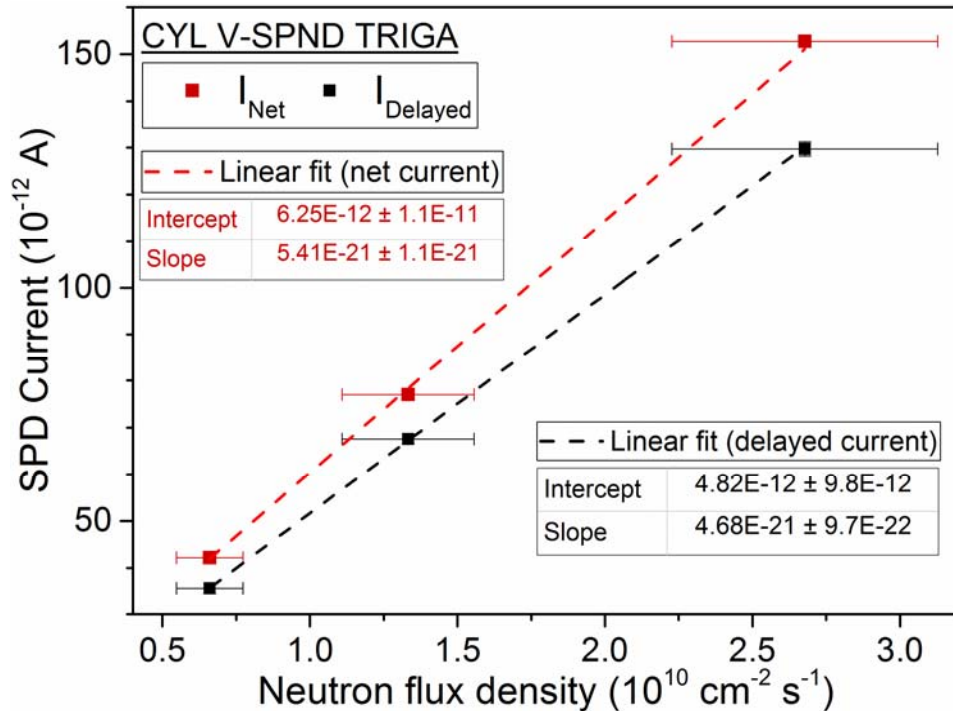
Figure 5-11: Measured net and delayed currents of the CYL V-SPND tested in TRIGA-GTC, plotted at different neutron flux densities. The linear sensitivity curves for net and delayed signals are shown.

For the CYL SPD, the signal-to-flux linearity in TRIGA-GTC is very good as it is a commercially manufactured delayed fission reactor SPND. The total sensitivity of the CYL V-SPND in TRIGA GTC is approx. 5.4×10^{-21} A cm^2 s with an uncertainty of ±20%, mainly incurred in the flux measurements. Of this sensitivity, about 86% is from the ^{52}V-induced delayed current. Net currents have been measured with low uncertainties (±0.1%) and the estimated delayed currents have up to ±3% relative uncertainties. The vertical error bars for the current values in Figure 5-11 are difficult to see due to small sizes. The uncertainties in delayed currents come mainly from the estimated deviations in the half-life using the exponential decay curves of the individual signals.

Similarly, for the FLT SPD in thermal neutron conditions, the total neutron sensitivity is approx. 1.3×10^{-20} A cm^2 s (Figure 5-12). The relative uncertainty of ±21% is largely due to the uncertainties in flux. The net currents, on the other hand, have standard deviations of ±3% to ±8%. The error bars on net currents are difficult to see on the graph. Like the case of CYL, the delayed currents of FLT have higher relative uncertainties (±14% to ±21%) due to larger discrepancies in the extraction of ^{52}V-induced components using the exponential decay curve fitting.
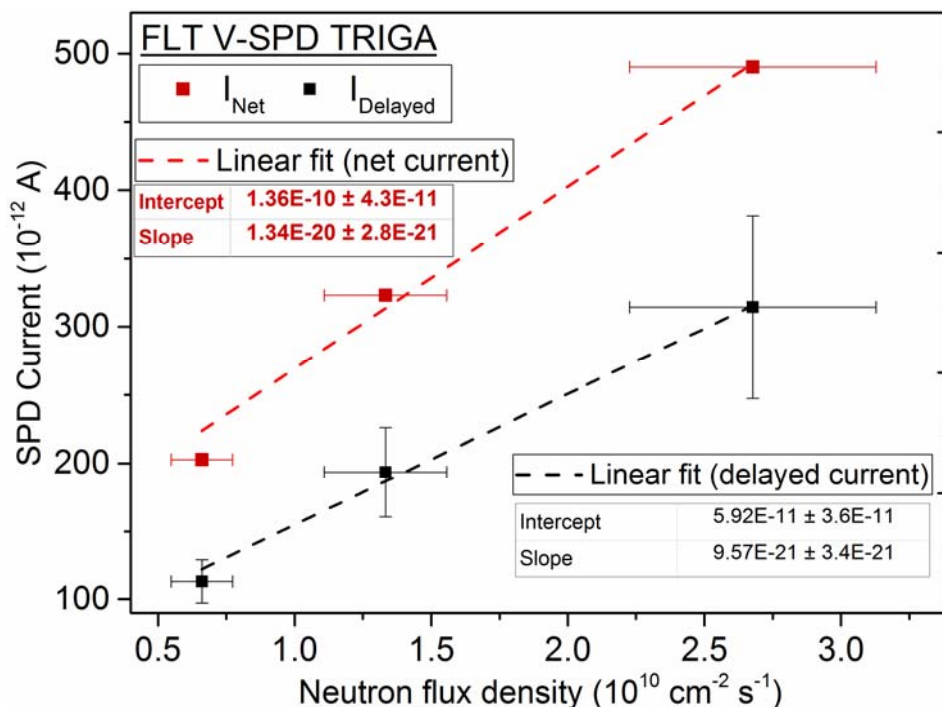
Figure 5-12: Measured net and delayed currents of the FLT V-SPD from TRIGA GTC tests at different incident neutron flux densities. Linear sensitivity curves for net and delayed signals are also shown.

Around 71% of the total sensitivity of FLT SPD has been formed due to the delayed current component, which signifies that the newly designed V-SPD is preferentially a delayed SPND under thermal neutron fields. But, it has an increased prompt response than the CYL SPD. This, as discussed earlier, is a matter of detector's overall design and geometry, and calls for careful optimization before application. The prompt signal does contain photon-induced current, however in view of a much larger proportion of delayed signal, it will not be detrimental to SPND's performance. This effect could not be studied deeply due to unavailability of a suitable pure photon source for this purpose, which could provide a comparable energy-spectrum with high-quality alternative flux measurements for sensitivity analyses. Also, as discussed previously, the sensitivity of FLT SPD has been found to be approx. 2.4 times that of the CYL SPD.

5.6.4 Fast neutron and photon sensitivities of FLT V-SPD

To separate the photon part of the prompt signal of FLT SPD in TUD-NG, first the photon sensitivity of the detector has been analyzed at GELBE. The sensitivity curve for this measurement is shown in Figure 5-13. The currents in GELBE exhibit excellent stability and the relative uncertainties in mean currents are lower than ±0.1%. The fluxes however, have been estimated with larger relative uncertainties, up to ±20%. This is almost solely due to the uncertainty in the position of the detector. The GELBE photon beam has a diameter of 2 cm (Figure 4-10) [65]. As a result, it does not expose the whole face of the detector (lateral size 2.5 cm). In contrast, the geometrical features of the radiation source at TUD-NG are different. Corrections have been made to the estimated flux density in GELBE so as to directly compare this response with the expected photon

response in TUD-NG. The linear fit gives an approx. photon sensitivity (S_{photon}) for the FLT V-SPD as 2.2×10^{-20} A cm^2 s ($\pm67\%$). The large uncertainties in fluxes at the three levels evidently lead to a large uncertainty in the sensitivity.
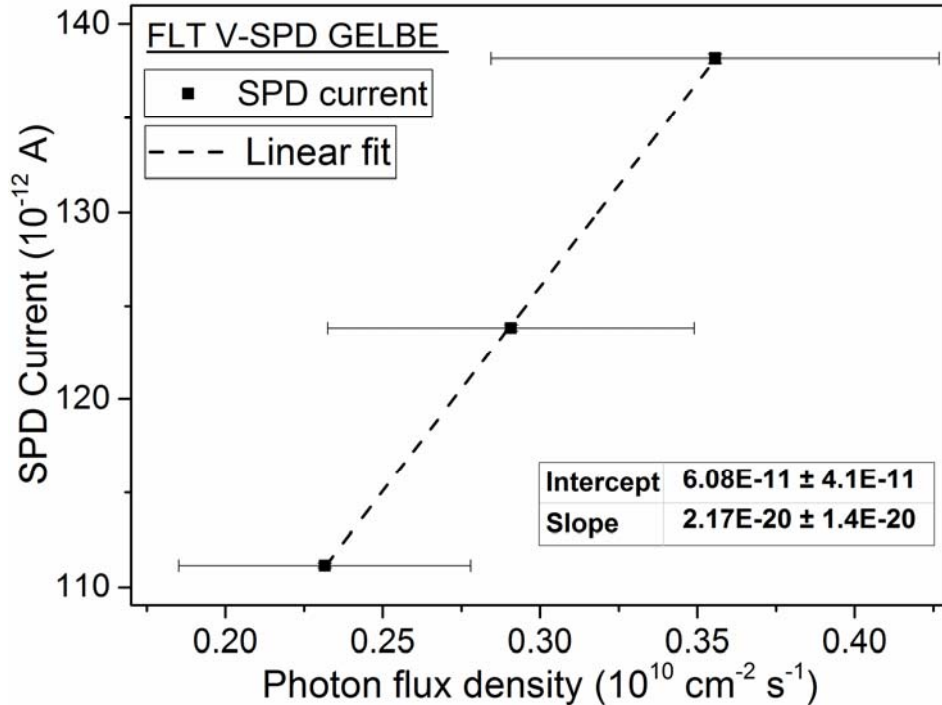
Figure 5-13: Measured currents of FLT V-SPD at different flux-levels of the high-energy photons, and the photon sensitivity curve of V-SPD, from the tests conducted at the GELBE facility.

Using the Monte-Carlo simulations corresponding to the experiments done in the TUD-NG facility, it has been found that the 17% of total particle flux density at the SPD test position is composed of the photons. This information has been used to obtain the photon flux density for each of the levels of TUD-NG operation in Figure 5-12. This factor is met with only statistical errors of the radiation transport calculations, below $\pm0.1\%$. Additionally, the larger relative uncertainties (around $\pm60\%$, see Subsection 4.2.2) of the neutron fluxes have been assumed. This has been then used in conjunction with the Eq. 5.4, to obtain neutron (I_N) and photon (I_P) current components, which are compared in the Figure 5-14. It can be seen that, on overall, the neutron component is around 4 times higher than the photon component for the measured SPD-currents.

The neutron-induced current components at each flux-level in TUD-NG are plotted against the corresponding neutron flux densities in Figure 5-15. This gives the fast neutron sensitivity of the FLT SPD as approx. 1.9×10^{-20} A cm^2 s ($\pm50\%$). Again, the large uncertainties encountered in neutron current component estimations (which includes the uncertainty of photon sensitivity) and flux values, give rather large uncertainty. The sensitivity value is around 12% lower than the high-energy photon sensitivity of the detector. This means that under the mixed field of TUD-NG, FLT V-SPD provides a highly mixed signal, preferentially working as an SP<u>G</u>D.
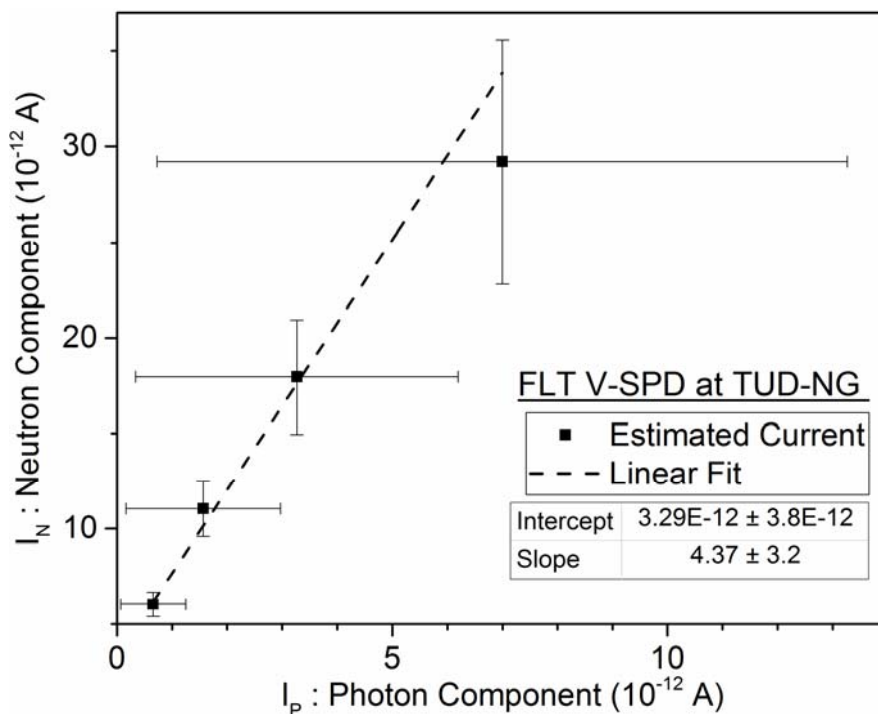
Figure 5-14: A plot of the experimentally obtained neutron (I_N) and photon (I_P) current components from the FLT V-SPD tests at TUD-NG. Four data points correspond to the four levels of fluxes at which the measurements are done. The photon sensitivity (Figure 5-13), in conjunction with the calculated photon fluxes has been used as per Eq. 5.4 to obtain the neutron signal components.
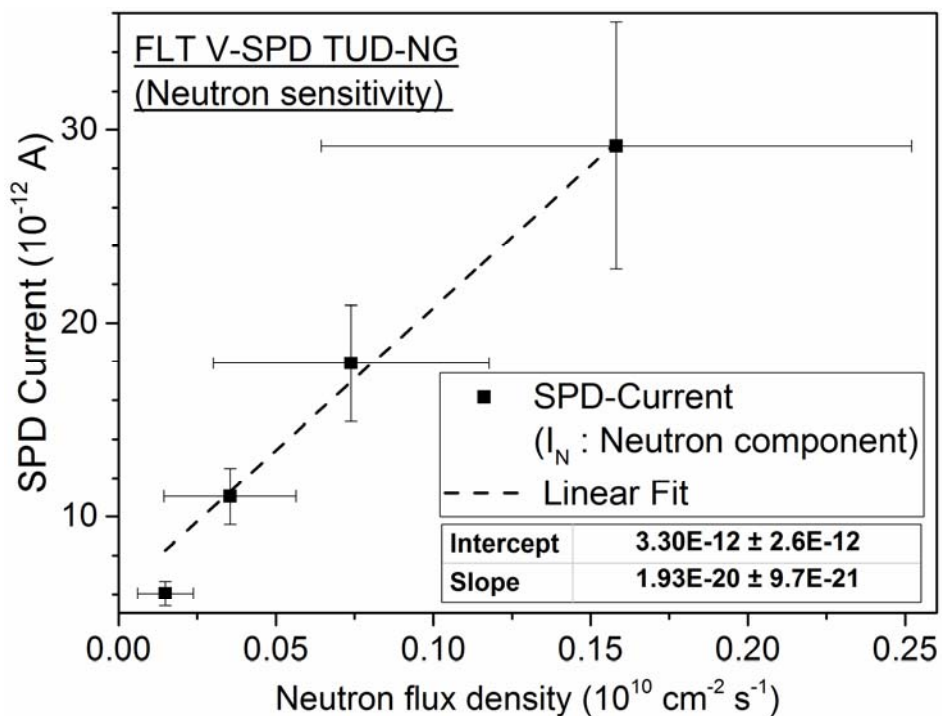
Figure 5-15: Measured neutron currents (I_N) of the FLT V-SPD from the TUD-NG measurements, plotted as a function of the incident neutron flux density. The line shows the sensitivity curve for the neutron component of the mixed-field signal of FLT V-SPD at TUD-NG.

5.7 Conclusions of the Reference Experimental Assessment

5.7.1 On applicability of SPDs in fusion environment

Extensive testing of the reference FLT SPD at 14 MeV D-T neutron based TUD-NG facility results in important conclusions related to the response anticipated from SPDs under fusion neutron conditions. The SPD currents are found to vary linearly with the variation of the incident flux densities. So, the SPDs can be used as flux monitors. Higher magnitude of signals have been obtained in flat geometry as compared to the cylindrical one. The total sensitivities of the FLT V-SPD towards thermal neutrons in TRIGA, high-energy photons at GELBE and fast 14 MeV neutrons at TUD-NG are shown in Table 5-3. For a comparison, the values for the CYL SPD are also presented.

Table 5-3: The estimated final sensitivities (in units of 10^{-20} A cm^2 s) for the CYL and FLT SPDs tested in TRIGA, GELBE and TUD-NG (only 14 MeV neutron sensitivities are shown).

	TRIGA	GELBE	TUD-NG (14 MeV)
CYL	0.54 ± 0.11	0.04 ± 0.01	–
FLT	1.34 ± 0.28	2.17 ± 1.45	1.93 ± 0.97

The photon sensitivity of the FLT SPD is found to be relatively higher than its sensitivity towards the fast neutrons. While the calibration procedure and operating conditions in TBM-like fusion reactor conditions are yet unknown, it appears that SP<u>G</u>D technology may be suitable for photon flux measurements with appropriate adjustments in the design. It is to be noted that, the detector alone provides no means of neutron-photon discrimination.

A major conclusion made related to SPDs is that the neutron signals in fusion environment will almost always be dominated by prompt components. Extraction of delayed signal due to threshold reactions representing fast neutron fluxes, which has been proposed earlier for TBMs [19], will be difficult and prone to devastatingly large uncertainties. Pure D-T neutron measurements using the present SPD designs may get adversely affected by photons from the surroundings. However, the spectrum of the neutrons in TBM is much wider than pure D-T spectrum and the neutron response in TBM of such an SPD will be higher. Therefore, neutron flux monitoring with SP<u>N</u>Ds are also found viable. It will be necessary to determine optimum SP<u>N</u>D geometrical design, layer arrangement with thicknesses, and also the combination of materials to reduce photon-induced signals. Some more detailed conclusions on SPDs under fusion conditions have been made through Monte-Carlo simulations under reactor-like radiation fields, as described in Chapter 8.

5.7.2 Discrepant sensitivity assessment and recommendations

Experimental testing of the SPDs and their calibrations involve reliable estimations of the sensitivity to the reactor radiation fields and their variations. Sensitivity

estimation, as demonstrated for the tests of FLT V-SPD at TUD-NG, is faced with multiple issues. Many factors make the signal-flux curve non-linear, including nuclear activation with various half-lives, decay photons, electronic effects etc., many of which vary with neutron flux themselves. In the early days of its implementation in the reactor, an SPD's sensitivity is measured systematically, by changing the positions and the reactor power, finally arriving at a mean value. This is a long-term task and is routinely done. But, for the feasibility tests like the ones presented here, such long-term comparisons are not possible. In mixed neutron-photon fields, a dynamic processing technique identifies the part of the signal which is linearly varying with the (neutron or photon) flux, through well-known cross-sections or accurately determined calibration factors. This part is suitably filtered out of the total and shown as the flux monitor signal for the operators. Power reactors typically use such methods.

The sensitivity estimation is also considerably affected by the need for a complementary flux measurement at the SPD's position. The flux density and energy-spectrum vary on small changes of positions, thereby leading to a difference in the sensitivity. This makes a huge difference on a comparison of experimental results with the calculations, which is important for several reasons (subject of the next chapter). This is a known problem for SPD users [70]. The computational models often rely on comparison of the sensitivities and not the SPD current directly. The latter can be measured with better confidence. The diversity of flux measurement methods in power reactors is exploited to get accurate estimates of fluxes for cross-calibration of SPDs. It can be thus concluded that, in the TBMs, it is advisable to integrate SPD-like devices closer to the irradiation ends of the neutron activation system, or to the position of the diamond neutron detectors, for a better quality of cross-calibration between two methods.

An additional note should be made of the systematic difficulty of one-to-one comparison of the sensitivities measured in two different facilities. The photon response of SPD-type detectors are known to have strong dependence on the energy-spectrum of the photons [35, 43]. So much so that, even the polarity of the net current changes on change of incident photon energies over 1 MeV. This poses a severe challenge in the study of gamma and prompt neutron SPDs, even in reactors where the induced currents are above μA-scales, six orders of magnitude higher than what have been measured here. Thus, the difference between the energy-spectra of photons at TUD-NG and that in facilities like GELBE would affect this kind of assessment. Therefore the results are only to qualitatively indicate that the photon sensitivity looks higher than the 14 MeV neutron sensitivity.

For accurate extrapolation of this knowledge to any other scenario, especially TBMs, more careful studies with alternative flux measurements and, extensive and accurate modelling of the facilities are demanded. Most of the test facilities, and those under design like the TBMs, are not well-characterized for such sensitive studies. Considerable help is possible in this through the Monte-Carlo simulations, for which an attempt has been made in this thesis.

5.7.3 Extended behaviour of the current flat sandwich-like design

The experimental tests in TRIGA GTC, TUD-NG and GELBE enunciate that a flat geometry SPD can be implemented for neutron and photon flux monitoring. The signals are stronger than a classical cylindrical detector, because of which it can be claimed to be comparatively better suited for laboratory-based tests and also application in reactors, in particular for the zones with lower flux densities. An adaptation of such a geometry should be preferred for prototypes of SPDs in TBMs. However, the present detector design responds to the electron-releasing processes in its vicinity also, leading to an extended active region. Parts of its signal depend on the prompt and decay photon fields up to a few cm away from the detector boundaries. The detailed nature of this behavior of FLT SPD is not clear at this stage. The design has been found vulnerable to complicated electronic effects also, pertaining to its open and flexible construction, exposed surfaces and electrical contacts. This affected the signal analyses, and therefore it is important to do deeper scrutiny of the design aspects through more experiments in better-characterized irradiation setups. In any case, the present SPD is only for the test-purposes and cannot be directly used in TBM. Better and optimized mechanical and electrical construction, and further tests, including tests for effects of high-temperature and electromagnetic fields on the SPD behavior are proposed for the future.

6. MONTE-CARLO MODEL-BASED EVALUATION OF THE TEST SPD RESPONSES

The designing of a radiation detector and analysis of its signals require analytical and computational modeling of the physical events in the detector. Models can be used to predict signals in planned irradiation experiments. In-depth interpretation of the aggregated signals from experiments is also possible with them, making models inevitable tools for calibration and operation of the detector. Computational studies further assist by reducing the experimental effort and expenditure in selecting the optimum design of the detector and the experimental setup. Sensitivity calculations for SPDs have been carried out since the time of their inception.

This chapter discusses the SPD modeling with its theoretical basis, computer tools and the complete recipe for its implementation as undertaken in this work. The consistency of the model has been checked and it has been extended for analysing the experimental tests reported in the previous chapter. Firstly, more insight about the response of SPDs, cylindrical and flat under different radiation fields is gathered through this, and secondly, the pros and cons of the models and the requisite improvements are established. Finally, it is verified for use in the computational prediction of SPD electrical signals under real TBM-like fields.

6.1 Warren's Model of SPD Sensitivity Analysis

H. D. Warren [71] formulated and demonstrated one of the first complete models of a delayed SPND analysis in thermal fission reactors. It is a consistent and universal model for calculation of the sensitivity, accounting for the effects of geometry, materials, and radiation, both incident and emitted. The obtained electrical current per unit length

of an SP<u>ND</u> with cylindrical symmetry, as per this model can be specified by the following formula (symbols explained in the following).

$$I_\beta = \frac{eV}{L} \int_0^{E_{max}} \Sigma(E_n)\, \varphi(E_n)\, f(E_n)\, dE_n$$
$$\times \int_{E_{MIN}}^{E_\beta} \left(\frac{-dE}{dx}\right)_E^{-1} dE \;\times \int_E^{E_\beta} N[R(E') - R(E)]\, B(E')\, dE' \;.$$

<div align="right">(Eq. 6.1)</div>

I_β – current per unit length (unit: A cm^{-1}),

e – electronic charge (= 1.6×10^{-19} C),

V – emitter volume (unit: cm^3),

L – detector length (unit: cm),

E_n – energy of incident neutron (unit: MeV),

$\Sigma(E_n)$ – macroscopic cross-section for capture reaction of interest at neutron energy E_n (unit: cm^{-1}),

$\varphi(E_n)$ – incident flux of neutrons with energy E_n (unit: cm^{-2} s^{-1}),

$f(E_n)$ – self-shielding factor of neutrons with energy E_n in emitter (unit-less),

E_{max} – maximum energy of incident neutrons (unit: MeV),

E – energy of emitted beta particle (electron) (unit: MeV),

E_β – beta end-point energy (unit: MeV),

E_{MIN} – minimum energy of electrons required to cross the insulator (unit: MeV),

$\left(\frac{-dE}{dx}\right)_E^{-1}$ – reciprocal of specific energy loss of electron with an energy E in the emitter (unit: cm MeV^{-1}),

$B(E')$ – normalized energy distribution of emitted beta particles (unit-less),

$R(E)$ – range of an electron with energy E in the emitter material (unit: Å),

$N(l)$ – probability per unit track length that a track of length l to the surface exists within the emitter (unit-less).

The first integral (over energy E_n) of the formula is the neutron capture rate in the emitter. Reaction rate is a multiple of the neutron flux ($\varphi(E_n)$) and the reaction macroscopic cross-section ($\Sigma(E_n)$). A fraction of the flux of neutrons incident on the reactant material from the outside is absorbed in the material itself, making the effective

flux lower. This is known as *self-shielding of neutrons*. A theoretical formula for self-shielding of neutrons in each material and geometry is used to obtain the factor *f(En)*.

The product of the second and the third integrals gives the number of current-creating electrons emitted out of the neutron-activated emitter. The latter considers the energy spectrum of the emitted beta particles and their probabilities of arriving at the surface of the emitter, thereby giving the number of emitted particles able to come out. The former includes the cutoff of slow energy electrons due to *space-charge effects* in the insulator. The space-charge effect is the phenomenon in which slower electrons are repelled back to the emitter zone due to the static charges absorbed in the interstitials of insulator material. This effect is expressed by determining a point of inversion of electric field along the insulator radius using governing electrostatic equation(s) and calculating the minimum energy of electron (E_{MIN}) required for crossing it.

Warren's model provides a rather simple formalism for calculation of a delayed SP<u>N</u>D's response. The results predicted by this model have been found to agree well with the experimental values in most of the reported thermal reactor cases. With small modifications in the formula, one can also formulate sensitivities for prompt SPDs. So, this model became the basis for all the future work carried out in the modeling of the response of all types of reactor SPDs: delayed and prompt [72] SP<u>N</u>D and SP<u>G</u>D [33].

With advent of the Monte-Carlo numerical methods, more input information, and also features missing from the original model like directional effects in radiation transport etc., can be included in calculations. It was first applied using a Monte-Carlo numerical method to calculate the sensitivity of self-powered detectors of delayed and prompt types by Goldstein et al [73]. In recent years, the model has been adapted using modern radiation transport computer codes to design and analyze SPDs [74, 75]. Apart from SP<u>N</u>D, the same method has been extended for calculating radiation-induced voltages in coaxial cables, which have similar geometry [76, 77].

6.2 Applied Monte-Carlo and Activation Codes and Nuclear Data

Nowadays, highly efficient computational tools like radiation transport and activation codes are available for simulations of nuclear detectors. Prime examples are the Monte-Carlo (MC) particle transport codes [78]. An MC method involves tracking of a particle's history from birth to death in the modeled geometry containing materials, while simulating the physical events like collision, absorption etc. By following many such particle-histories and tallying the events, one can estimate mean physical quantities like particle currents, fluxes, energy depositions etc. MC methods are commonly applied for the study of radiation detectors wherein the radiation source, detector and its surroundings are modeled and experiments are computationally simulated. There are numerous codes and tools for this, e.g. MCNP [79], GEANT [80], FLUKA [67], etc.

For radiation detectors, the irradiation of materials is also important to account for. Activation leads to the creation of unstable products which decay by the emission of γ, β, α and other charged particles. Especially for a neutron SPD, many effects which have a significant role in the detector's functioning depend on the irradiation history of the detector materials. Thus, activation calculations play a significant role in modelling

of SPDs also. The European Activation SYstem (EASY-2007) is a package of activation code(s) and nuclear data for such applications. The inventory code used in this package is called FISPACT-2007 which has also been applied to various calculations in this work. Starting with a user-defined radiation source (energy spectrum and flux) and material (mass, density, and isotopic composition), the code uses external cross-section and decay data libraries to calculate the effective reaction cross-sections, numbers and activities of various unstable nuclides, their creation and decay pathways, half-lives, radiation doses etc. The inventory can be calculated at a specified time during the irradiation or after a cooling period, in different combinations.

6.2.1 A brief on the essential terminology of MCNP

MCNP is an MC-based multi-purpose particle transport code from Los Alamos National Laboratory (LANL). A versatile code, MCNP has been extensively validated and verified by comparing with integral experiments, providing users a high-level of confidence in the performed calculations. Its versions 5 and 6 have been utilized in this work for SPD simulations, and this subsection introduces some basic terms from MCNP.

An MCNP calculation starts with an input file which has three sections, historically called as *cards:* cells, surfaces and data. The input file is run using the code executable in serial or parallel processor mode, depending on the time required for reaching acceptable statistical uncertainties in the results. Some important features of the input deck and the results are explained in the following without the syntax. The reader is referred to the user manual and primer [79, 81] for the details of MCNP usage.

1. MCNP has a robust geometry modeling and visualization tool. Three-dimensional entities from simple detectors to complex reactors can be modeled in the code. The geometry specification is contained of *surfaces* and *cells*. First and second-degree surfaces like cylinders, planes, spheres etc. can be defined. Cells are volumes bound by these surfaces. Cells represent the volumes or the solids of the real entity modeled, for which respective materials can be specified in the cell cards of the input. In some sections of the thesis, 2-D plots from MCNP's geometry plotter are used to present the modelled geometries.

2. The code offers flexibility in associating real materials to the geometry cells. Isotopic concentrations of the materials need to be provided. One can use any number of isotopes in arbitrary fractions as required for the case. Manufacturers' datasheets and available literature are used in defining the materials.

3. MCNP requires nuclear interaction probabilities in the form of cross-section data to simulate the physics. Cross-sections are experimentally determined [82] for a vast number of projectiles and energies for various nuclides. For each nuclide, theories and models of nuclear structure and interactions are implemented to fit the physical data to obtain energy-dependent cross-sections of various reactions, which are assembled into data files. This process is also called *evaluation* and the resulting evaluated data are published for different uses like MC simulations. There are multiple evaluations of cross-section data available for use with MCNP. For neutron reactions, ENDF/B-VII.1 [83], JEFF [46] and FENDL [84] data libraries are some examples. Data with appropriate format accepted by MCNP code is either provided in the code package or they need to be converted [85].

Latest libraries for gamma and electron transport are MCPLIB84p and MCPLIB03e, respectively, which are provided with the MCNP code package [79]. Cross-section data from various sources in user-intended combinations can be used in calculations.

4. The code can handle coupled transport of neutrons (N), photons (P) as well as charged particles (electrons (E), protons (H), heavy particles etc.). In the *mode* card, a part of data cards, one can specify the explicit particle(s) of interest in the problem: N, P, E, H etc., in any combination. When a particle is not mentioned in the mode, its transport is not modeled. The nomenclature of calculation steps in SPD simulations, as described later, uses this kind of mode specification.

5. The tool for source description (*SDEF* card in data cards) in MCNP is used to define the source of initial particles, with its shape or spatial distribution, directional and energy distributions etc. through various variables of the SDEF card. The variables can be defined as singular values, or as probability distributions, or can be interdependent (with some restrictions).

6. The code scores different physical events encountered during the transport of a particle (history) and the user can save them using the *tally* cards. Tallies can be attributed to different real-life nuclear quantities like fluxes, currents, energies etc. Tally multiplication (*FMn*) card can be used to calculate derived quantities, like doses, reaction rates etc. for which appropriate coefficients are required, e.g., to calculate reaction rate one requires the cross-section data as the multiplier. The tally energy (*En*) and directional cosine (*Cn*) cards are provided for obtaining the energy and direction dependent values of a parameter. Extensive choices of tallies exist for calculation of various physical parameters in the cells or on the surfaces of the modeled geometry. There are several methods of estimation used by MCNP for different tallies. A so-called surface-crossing tally is used to generate values for surface current (*F1 tally)* in units of particles, or average surface flux (*F2 tally*) in units of particles per cm^2. Track-length estimator is used to score the average cell flux (*F4 tally*) in units of particles per cm^2. The methods of estimating the total energy (*F8 tally*) and total charge (*+F8 tally*) deposited in a cell are like the track-length estimators.

6.3 Monte-Carlo Calculation Model for SPDs

A multi-step model has been developed in MCNP for calculation of SPD sensitivity based on Goldstein's adaptation of Warren's analytical model. This model presumes that the net charge deposited on the emitter, through combination of all kinds of nuclear and electrical processes in the detector, forms the major portion of the measured DC signal. The current measurements are performed between the emitter and the grounded collector electrodes. The first part of the modeling is the calculation of the emitter charges through particle transport simulations. In a separate calculation, the effect of insulator space-charge is unfolded. Finally, the emitter charge updated with the charges returning from the insulator is divided by the flux density on the surface of the detector to obtain sensitivity in units of A cm^2 s, a physically measurable quantity.

The detector geometry is accurately defined in MCNP (example in Figure 6-1), with material layers segmented into sub-cells. Segmentation of the layers is important for

transferring the information of spatial dependence of physical events in the detector, from one step to the other. For example, this is needed to store the distribution in space of the neutron reaction rates or electron charge creation rates. Too thick cells would not account for self-shielding of neutrons or emitted electrons, thereby not fulfilling the required purpose. On the other hand, too thin cells require longer calculation times as much larger number of histories are needed to have statistically viable results in each cell. Too many cells make the subsequent arithmetic of charge distributions cumbersome, specifically for flat SPDs. Taking these into account, preliminary simulations have been done to realize sufficient number of divisions of emitter or insulators in each case. Number of cells in each material layer has been decided specifically for each case under study. Often, for cylindrical SPDs, emitter has been divided into 10 equally thick cells and insulator into 25 cells, while for flat SPDs, 10 cells of both emitter and insulator have been selected.
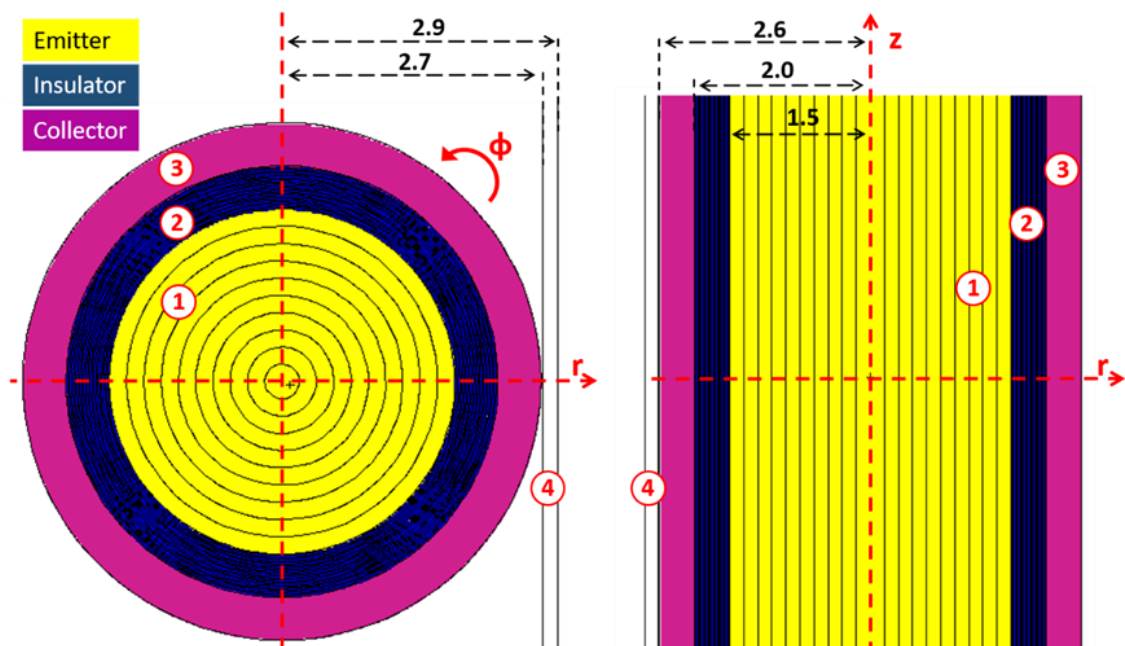
Figure 6-1: Detector and neutron source geometry definition in MCNP, an example of a cylindrical SPD and a rectangular surface source. The transversal (left) and longitudinal (right) cross-sections of the geometry are shown, with a representative coordinate system and major dimensions. Colours are used in MCNP plotter to show different materials in the regions. Figure presents the regions with (1) emitter, (2) insulator and (3) collector. The flat neutron source on the side of the detector is marked (4).

MCNP has a limited capacity to follow the unstable nuclei and their radioactive emissions, in the same step as the neutron transport. Thus, the problem of neutron-induced beta production, as needed for (n, β^-) processes, is divided into two steady state MCNP calculations, followed in a sequence. Direct results of the steps assume a state when the neutron reaction and beta decay processes are in equilibrium.

The MCNP model for SPD sensitivity calculations is divided into following steps. These are followed to obtain the charge deposition in SPD layers due to various processes, delayed as well as prompt. The neutron and photon spectra and their relative intensities are pre-requisites for these calculation steps.

1. Mode N: This step involves transport of neutrons. The detector can be integrated into the model of the irradiation setup, like the reactor, but that increases the complexity of the calculation. An acceptable compromise is made by defining a simplified point, surface or volume neutron source (with distributions of its positions of origin, energy, and direction) close to the detector. For this, it is necessary to obtain the nature of neutron field, mainly its energy-spectrum in the position of the SPD in the reactor. In this work, the source has been defined as a cell or a volume close to the detector, with a geometry closely simulating the real-life irradiation condition. The reactions of interest are chosen and corresponding tally multipliers (reaction cross-section data) are used with the cell flux (F4) tally to calculate the number of betas per source neutron (N_β), in different cells. This should be done for the emitter, collector, insulator and the surroundings, because beta emissions are possible in all those materials. As the emitter layer is segmented into thinner (sub-) cells, the spatial distribution of neutron reactions is also obtained. The incident neutron flux (φ) on the outermost surface or the front of the detector is also calculated in this step with the surface flux (F2) tally.

2. Mode E: This is an electron transport step to determine delayed component from (n, β^-) process. This step is required as the code has limited capacity to follow beta-decaying unstable nuclei and the emitted electrons in the same step as the neutron transport. For each capture reaction in the emitter, one beta emission is assumed, except in the cases of nuclei with less than 100% beta-emission probabilities, where one needs to multiply the branching ratios. The electron source is defined in the emitter cells based on the spatial distribution of neutron capture from Mode N calculation. The energy spectrum of source electrons is the beta spectrum of the product nucleus. Directionally, an isotropic emission is considered. Electron current using surface current (F1) tally is scored at various cell boundaries with directional cosine (Cn) card. Appropriate arithmetic of the directional electron currents gives the rates of charge deposition in the emitter (I_{eE}) and insulator (I_{iE}). Through finer cell definition in the insulator, the spatial charge distribution ($Q_{iE}(x)$), containing charges in C units in each insulator cell is also retained for integrating the equations of insulator space-charge effect.

3. Mode PE: This is a coupled photon-electron (PE) transport step to determine the prompt contribution from (γ, e^-) process. Like Mode N, a photon source is defined outside the detector and transport of photons and their secondary electrons are performed. Like Mode E, the total charge deposition rates in emitter (I_{ePE}) and insulator (I_{iPE}), and cell-wise charges in insulator ($Q_{iPE}(x)$) are calculated.

4. Mode NPEH: This is coupled neutron-photon-electron-proton (NPEH) transport calculation to determine the contribution from (n, γ, e^-) process. It is like the Mode PE calculation albeit it starts with the neutron source as in Mode N. Charge deposition rates in emitter (I_{eNPEH}), insulator (I_{iNPEH}) and insulator cell-wise charges ($Q_{iNPEH}(x)$) are obtained. It can ideally be combined with Mode N but it is done separately to simplify the analysis of the MCNP outputs.

In an electron transport simulation in MCNP, the number of electrons (per source particle) output on F1 tally, can be converted to standard charge units (C) by multiplying it with the electronic charge ($e = 1.6 \times 10^{-19}$ C). For calculation of charge deposition rate in a cell, two cosine groups are used for the surfaces enclosing the cell. One cosine bin gives the current along the surface normal, while the other gives that in the opposite direction. Sense of the cosine tally modification and partial and net currents along surfaces are shown for a simple MCNP geometry in the sketch in Figure 6-2. For the example in the figure, the net charge deposition rate (I) in cell C_2 is given by the following formula. The Mode E, PE and NPEH steps use this scheme.

$$I(C_2) = I_3 - I_2 = (I_3^+ - I_3^-) - (I_2^+ - I_2^-) \qquad . \qquad \text{(Eq. 6.2)}$$
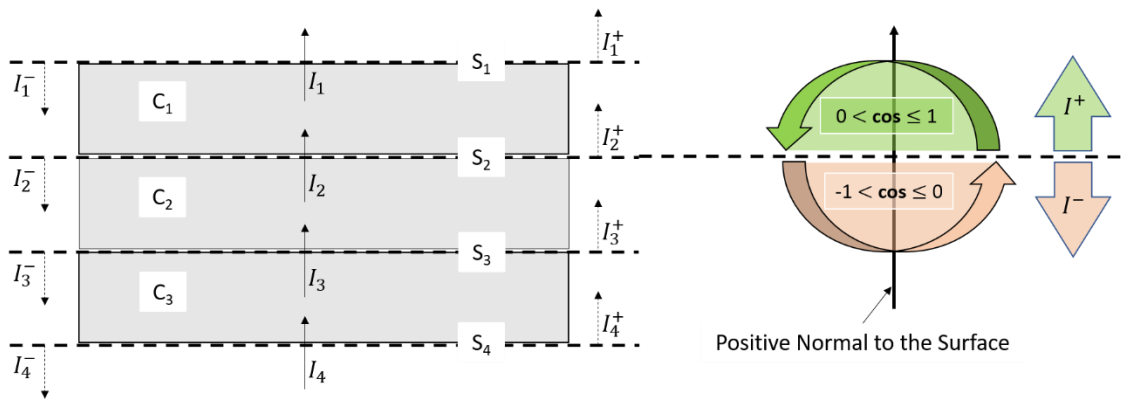
Figure 6-2: Description of methodology for calculating charge deposition rates in the cell in Mode E, PE and NPEH calculations. On the left, surfaces (S_1 to S_4) and cells (C_1 to C_3) of a simplified geometry are shown. The partial currents in the positive and the negative directions (I^+ and I^- respectively) and net currents in the positive direction (I) for each surface are shown. On the right, the sense of the cosine (cos) tally modification is shown: green part represents the current (I^+) in the direction of the surface normal, which is also considered the positive flow, while the orange part gives one in the opposite direction (I^-) and this flow is considered negative.

All the results obtained from MCNP simulations are normalized to the number of source particles in that particular step, a default output of MCNP, unless altered by a tally multiplication card. To obtain SPD sensitivity in correct units however, all physical quantities need to be normalized to the number of the same kind of source particles, primly the neutrons. To do this, currents from non-neutron simulation steps, Mode E and Mode PE, need to be multiplied by corresponding factors. For Mode E, this factor is simply the number of betas per neutron (N_β) obtained in Mode N calculation. For Mode PE, this is the ratio ($\varphi_{g/n}$) of flux of photons to that of neutrons on the detector surface.

The measurable current flowing through the SPD circuit depends on the total charge deposition rates in emitter and insulator from all calculation steps. These are obtained by combining the results of Mode E, PE, and NPEH, as per the equations 6.3 and 6.4. Also, the distribution of total charges deposited in insulator cells, used in space-charge effect calculation, is determined as per Eq. 6.5.

Emitter current: $I_{eTOT} = [N_\beta \times I_{eE}] + [\varphi_{g/n} \times I_{ePE}] + I_{eNPEH}$.   (Eq. 6.3)

Insulator current: $I_{iTOT} = [N_\beta \times I_{iE}] + [\varphi_{g/n} \times I_{iPE}] + I_{iNPEH}$.   (Eq. 6.4)

Charge in an insulator cell: $Q_{iTOT} = [N_\beta \times Q_{iE}] + [\varphi_{g/n} \times Q_{iPE}] + Q_{iNPEH}$. (Eq. 6.5)

In Mode N and Mode E, all the reactions in a complete detector which can make (n, β^-) type of contribution should be considered, including those in collector and insulator, and summed to obtain the total charges from the formula shown above.

6.3.1 Insulator Space-Charge Effect

Besides the particle transport simulations, a so-called *space-charge effect calculation* is done separately. At the onset of the movement of electrons from the emitter surface, first few of them fill up the interstitial sites in the insulator material. Stopping of the electrons in the interstitials creates an electrostatic field in their path. If the charge distribution in the insulator is close to uniform, like it is in most of the SPD simulations because the emitter electrons are fast, then the electric potential along the insulator thickness is parabolic in shape and the electric field crosses zero at the so-called *inversion point*. The sign-inversion of field in the insulator means that if the electron from the emitter crosses the inversion point then the induced field will push it away to the collector. If it stops before, due to its lower energy or more complex path, then it will be decelerated and pushed back to the emitter, nullifying its contribution to the signal.

To take the space-charge effect into account, the electric potential and field based on the electrostatic Poisson's equation is calculated. In all the charge deposition steps of Monte-Carlo simulations, average charge distribution in the insulator layer is also calculated. For each insulator cell, the charges per source neutron from various steps are added, and the resulting average charges, $Q_{iTOT}(x)$ are used in a discretized numerical integration method to solve the equation. This gives the inversion point, and thereby the so-called *returning fraction* (*F*). F is part of the total insulator charge which is reflected back to the emitter [29]. An example of a steady state electrostatic potential and corresponding field in a 0.5 mm thick Al$_2$O$_3$ insulator plate of the FLT V-SPD, in arbitrary units is shown in Figure 6-3. As these calculations are needed only to obtain the inversion point, the absolute units are not necessary. In the case of simulation of coaxial cylindrical SPDs, the discretized formula for the returning fraction F, as derived in the reference [80], has been frequently used.

The net current flowing out of the emitter (I$_e$), which represents the measurable detector current and the sensitivity (*S*) are given by the following formula. Finally one obtains S in the units of A cm^2 s, which can be compared with the experimental results.

$I_e = I_{eTOT} + F \times I_{iTOT}$.   (Eq. 6.6)

$S = \dfrac{I_e}{\varphi}$.   (Eq. 6.7)
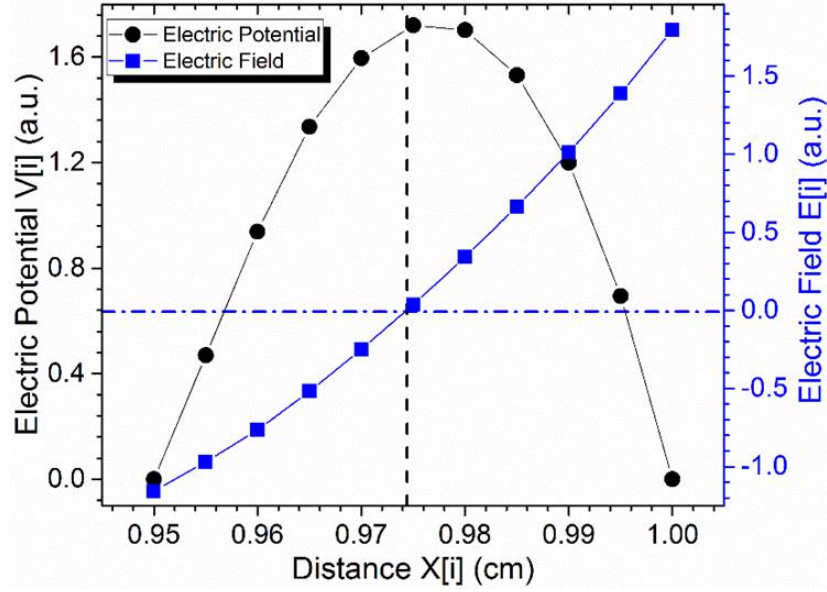
Figure 6-3: Calculated electric potential and field in arbitrary units (a.u.) along the thickness of insulator in a flat SPD. Electric field crosses zero at inversion point ≈ 0.975 cm in this example.

6.3.2 Non-saturated Currents

Some of the delayed currents in SPDs are away from saturation, as the underlying radioactive decay half-life is much longer than the irradiation period. Such cases require activation calculations to determine the fraction of saturation activity attained in the periods of irradiations and cooling which occurred in the experimental measurement. This fraction must be applied to the calculation of total charges because a saturation condition is assumed by default in this calculation method using MCNP.

If the scheme of irradiation is simple, so that a single constant flux irradiation is performed to measure the current, then this effect can be accounted for in a simple manner. For any such delayed process, tagged x, a partial sensitivity S_x is determined using the model. Its corrected contribution S_{xc}, to the total sensitivity (S) of the SPD is calculated using the following equation. Here, λ_x is the decay constant of the respective beta-emitter and T_{irr} is the time of irradiation.

$$S_{xc} = S_x \times (1 - \exp(-\lambda_x \times T_{irr})) \qquad . \qquad \text{(Eq. 6.8)}$$

The scheme of the complete sensitivity calculation model is summarized in the flowchart in Figure 6-4. The signals measured in reference experiments can be studied using the multi-step Monte-Carlo models, and through this, a validation can be performed for this method, as done in the next section. For this, the calculated values of sensitivities (S_C) and the ones experimentally estimated (S_E) have been compared, using the percentage deviation (Δ) of calculations from experiments, .i.e. [$\frac{S_C - S_E}{S_E}$].
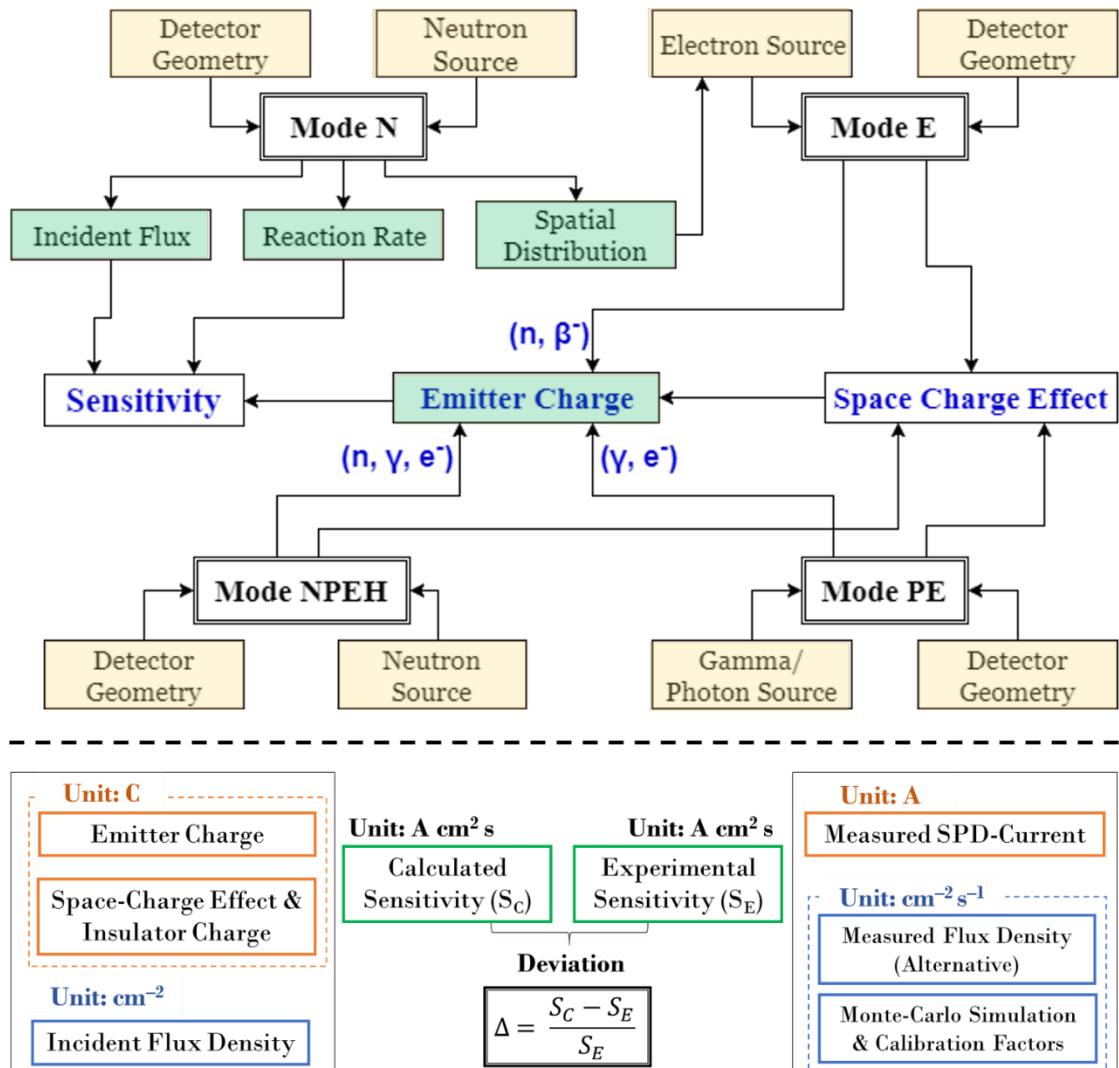
Figure 6-4: Upper half shows a schematic flowchart of the steps in MC calculation of SPD sensitivity as implemented in this thesis. The main steps are in double lined boxes, inputs are shown in yellow-shaded boxes and outputs in green-shaded boxes. Space charge effect calculation is a separate step using insulator charge output in three steps. Lower half of the figure shows the main results/parameters (with units) needed from the (left) calculation and (right) experimental sides in obtaining the deviation (Δ) between the experimental sensitivity (S_E) and the calculated one (S_C).

     The comparison between experiments and calculations is a tricky task in itself, shown in the lower half of Figure 6-4. It involves dealing with errors on both experimental (Chapter 5) and calculation sides. Units of parameters ascertained through calculation or experiment, on both the sides, are shown in the figure. The model essentially deals with static charges formed for each incident source neutron. This may not represent the dynamism of electrical fields in experiments, especially for small currents in the miniature geometries of SPDs. The physical formalisms for estimating the normalizing parameter, i.e. the neutron flux density, are also often different in calculation and experiment. As a cumulative result of such differences, the method of comparison, apart from the MCNP model, can lead to a crucial source of discrepancy. While retaining the simplicity of the model, some of these aspects have been taken care of in the simulations, and addressed in the concluding discussion of the chapter.

6.4 MCNP Modelling and Comparison with Experiments

Using the developed MCNP model for SPDs, the reference tests reported in Chapter 5 have been simulated for both test detectors, CYL and FLT.

6.4.1 Modelling for TRIGA-GTC Test of Reference SPDs

To correctly represent the irradiation setup in the MCNP geometry, two sets of calculations have been performed for the experiments in TRIGA. The models are based on the two available neutron and photon source definitions (Figure 4-3). First ("Model-1") defines the geometry of TRIGA GTC with the Blackner's source-plane. The geometry in this model includes available details on the lines of the sketch of GTC shown in the Figure 4-2. In second, a simplified model ("Model-2") with a flat surface source (with Wortmann spectra for neutron and photon, Figure 4-3) in front of the detector is used. Figure 6-5 shows the examples of the MCNP geometry plots from the two models.
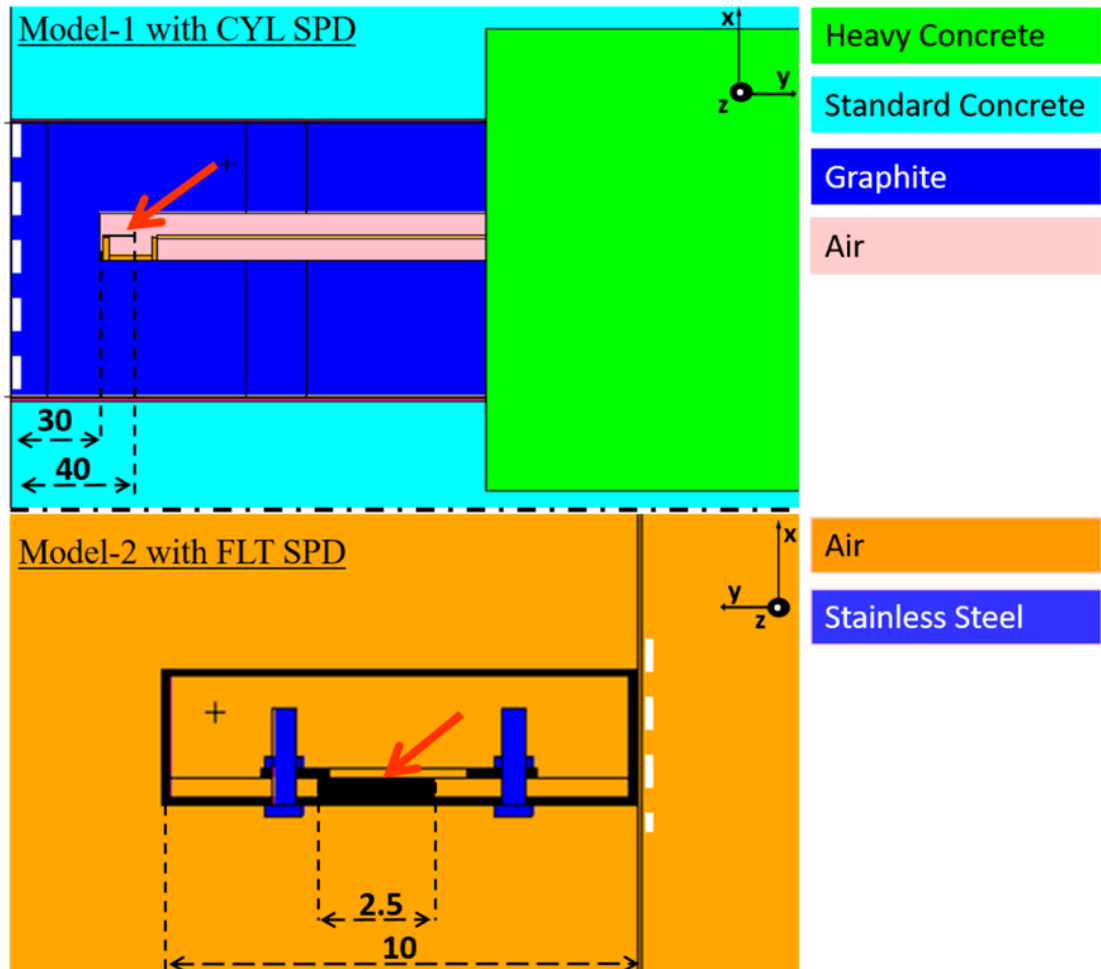
Figure 6-5: TRIGA GTC geometry models as implemented in SPD simulation model in MCNP. (Top) plot shows the Model-1 with simplified definition of GTC, Blaickner's source plane (dashed white line) and CYL SPD model (red arrow). (Bottom) plot shows Model-2 with the simplified flat surface source based on Wortmann's simulations (dashed white line) and FLT SPD (red arrow). Colour codes used in MCNP models to show different defined materials are presented and major distances (in cm) are shown.

Whereas both detectors have been simulated using both models of the geometry, totaling to four separate calculations, only two of them are shown in the figure. In these simulations, the delayed currents from ^{52}V in emitter, ^{28}Al in the insulator and EM shield of the flat detector, and ^{56}Mn and ^{65}Ni in the collector cells are calculated. The irradiation times (~20 min) are considered for their contributions to the total.

The results for both the detectors calculated using two models, are given in Table 6-1 and Table 6-2. The total sensitivity and the partial sensitivities due to ^{52}V induced (n, β⁻)-component are shown in the tables. Ratio of the (n, γ, e⁻)-type prompt component to the delayed (n, β⁻)-component, i.e. the *P/D ratio* and deviations of the calculations (S_{C1} for Model-1 and S_{C2} for Model-2) from experiments are also shown.

Table 6-1: MCNP-calculated results for irradiation of CYL V-SPND in TRIGA GTC; the total and ^{52}V-induced delayed (n, β⁻) sensitivities from the experiment (S_E) and two models' calculations (S_{C1}, S_{C2}), with the ratio of prompt to delayed components (P/D), and the deviations of the respective calculations (Δ_1 and Δ_2) from experimental values. The sensitivities are expressed in units of 10^{-20} A cm^2 s.

Total or Partial Sensitivity	Experiment	Model-1		Model-2	
	S_E	S_{C1}	Δ_1	S_{C2}	Δ_2
Total	0.54 ± 0.11	0.61	9.9 %	0.52	−5.7 %
^{52}V (n, β⁻)	0.47 ± 0.00	0.52	12.2 %	0.41	−12.1 %
P/D Ratio	0.19 ± 0.03	0.18	−7.1 %	0.29	52.2 %

The calculations for CYL V-SPND match with the experimental findings with small deviations. The total sensitivity is predicted within 10% difference of what is measured, which is within the experimental uncertainty. The model-2, the simplified model, systematically under-estimates the values, while model-2 over-estimates. Compared to model-2, model-1, which includes materials near the detector, accounting for phenomena like scattering etc., seems to perform better if the prompt to delayed (P/D) ratio is considered. In the composition of the CYL signal, around 77% of the charge is deposited due to ^{52}V-induced delayed contribution. Other delayed components are negligible and add up to 1% of the net signal. The calculated prompt neutron component is 15% and a prompt component due to reactor gammas is around 8%.

For the FLT V-SPD modelling in TRIGA GTC (Table 6-2) the calculated values are uniformly lower than the experimental ones. The detector has higher prompt current than the CYL SPD as can be seen in the reported value of P/D. The prompt contribution (due to photons from outside and inside of the detector) is under-predicted by 10 to 50 times in the models, which points at a discrepancy in the method for accurate modelling of the flat SPDs. Reproducing prompt components using steady-state model in MCNP is a challenging task, as briefly discussed in Section 6.5. Using Model-1, it has been determined that 88% of the signal is delayed, almost exclusively due to capture reaction on ^{51}V nuclei. On the other hand, 12% of the current is from prompt neutron processes in the detector. The current calculated for reactor gammas is negligible.

Table 6-2: MCNP-calculated results for irradiation of FLT V-SPND in TRIGA GTC; the total and ^{52}V-induced delayed (n, β⁻) sensitivities from the experiment (S_E) and two models' calculations (S_{C1}, S_{C2}), with the ratio of prompt to delayed components (P/D), and the deviations of the respective calculations (Δ) from experimental values. The sensitivities (S_E, S_{C1} and S_{C2}) are expressed in units of 10^{-20} A cm^2 s.

Total or Partial Sensitivity	Experiment	Model-1		Model-2	
	S_E	S_{C1}	Δ_1	S_{C2}	Δ_2
Total	1.34 ± 0.13	0.50	–62.9 %	0.45	–66.3 %
^{52}V (n, β⁻)	0.96 ± 0.06	0.45	–53.3 %	0.41	–57.6 %
P/D	0.40 ± 0.15	0.13	–66.8 %	0.12	–69.8 %

The models can predict the polarities of the current signals and their orders of magnitude well. The detailed model, model-1 has provided relatively better results overall. The divergence of calculations from experiments can be primarily attributed to a deficiency in the models to correctly model prompt processes, and the experimental discrepancies in sensitivity estimations, as discussed later in details.

6.4.2 Modelling for TUD-NG tests of reference SPDs

For the fast neutron test-setup at the TUD-NG, an MCNP geometry description is available, which has been relatively simple for integration of the tested SPDs. The two reference detectors' geometries have been defined in this model (Figure 6-6), and MCNP simulations have been performed to calculate their currents normalized to a total number of source neutrons in the problems. Neutron emission rate have been determined in the experiments using the calibrated neutron monitor of the TUD-NG (Chapter 5). This is multiplied with simulation results to obtain the absolute currents. The results for the CYL and FLT SPDs in TUD-NG are given in Table 6-3 along with their deviations (Δ) from the experimental results.

Table 6-3: The experimentally measured (I_E) and MCNP-calculated (I_C) values of the total current (in units of 10^{-12} A) and the ratio of prompt to delayed components (P/D) for CYL and FLT SPD irradiation tests in the TUD-NG, with the deviations (Δ) of I_C from I_E for each case.

Current	CYL			FLT		
	E	C	Δ	E	C	Δ
Total	0.17 ± 0.06	0.08	–55.0 %	30.8 ± 1.8	0.29	–99.1 %
P/D	--	–4.24	--	14.87	27.50	84.9 %

The MCNP model under-predicts the total CYL SPD current in TUD-NG by around 55%. The CYL detector resulted in very small signals, close to the background. The net current measurement have been difficult for these. Statistical deviation from the mean value of the current at the highest flux in this measurement is as high as 70%. The signal's delayed component could not be resolved, and therefore the whole signal is assumed to be prompt. Considering this, the experimental P/D ratio and its comparison

with the calculation are indeterminate in the table. It is worthwhile to note that these magnitudes of signals are negligible in case of thermal neutron application of SP<u>N</u>Ds. This, as it will be seen in the upcoming discussion, is true for flat SPD also.
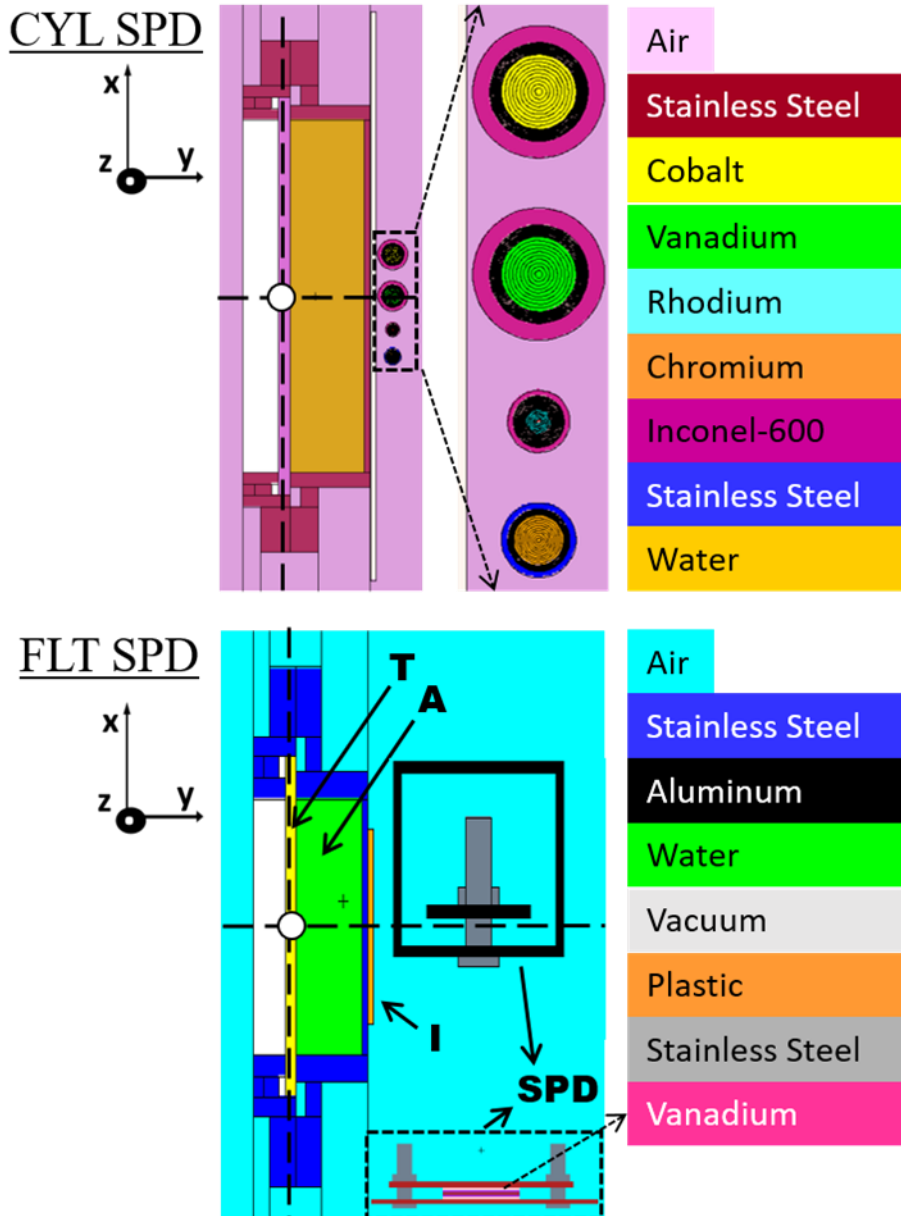
Figure 6-6: Geometry plots from the TUD-NG MCNP model. In the top figure, irradiation of four cylindrical SPDs is modelled. In the bottom is the plot of the setup with sandwich-type flat SPD (a different cross-section of the geometry is shown in inset). The model defines the Ti-^{3}T target (T), assembly (A) with steel frame, cooling water cap etc., and irradiation setup which contains a thin layer of insulator (I), usually plastic scotch-tape and the mounted SPD.

From the MCNP simulations, it has been observed that the magnitude of total positive polarity current of CYL SPD in TUD-NG test is three times that of the total negative current. It is reminded that a net negative component of signal occurs when the nuclear process ends in deposition of net negative charge in the emitter zone. This usually

happens in the electron-emission events taking place outside the emitter, i.e. in the insulator or the collector, or the objects in the detector's surroundings. Electrons from the collector do not contribute much, and more than 75% of the mentioned negative share comes from neutron interactions in the insulator. Around 50% of this is produced in the ^{16}O (n, p) ^{16}N reaction in the oxygen nuclides of Al_2O_3 due to a comparatively high cross-section of this reaction with 14 MeV neutrons. Of the total positive contribution, around 87% is prompt current. In the modelling of TUD-NG irradiation experiments, prompt components contain both (n, γ, e$^-$) and (γ, e$^-$)- types of events. Around 13% of the positive current is delayed, almost completely due to ^{51}V (n, p) ^{51}Ti reaction. Net delayed current is negative (insulator's effect), which makes the ratio of prompt-to-delayed (P/D) components negative.

For FLT SPD, the experimental measurements exhibit larger signal amplitudes compared to the CYL SPD. But, the MCNP model under-predicts the current by big margins, producing electrical signals lower than those measured by about 100 times. This, again, highlights a severe deficiency of the model in predicting fast neutron induced (prompt) currents. Only the net polarity of the current is predicted accurately, while the P/D ratio of the signal is also predicted relatively better.

Some more insight of the signal formation can be found by going into the components of FLT SPD net signal. Like CYL SPD, here also there are negative contributions. Total positive contribution is however more than 5 times the total negative contribution. Prompt current is clearly dominating the signal, with up to 96% of the total in this calculation.

Among the delayed components, there are both positive and negative currents with the sum of positives being only 17% larger than the other. While the reaction ^{51}V (n, p) ^{51}Ti forms 67% of the positive, around 29% of it comes from the ^{16}O (n, p) ^{16}N reaction in the insulator. Interestingly, the latter process had a negative signal in CYL case. This signifies a strong dependence of signal formation mechanism on the geometry of the detector. Around 65% of the negative contribution is due to the ^{52}Cr (n, p) ^{52}V reaction in the Inconel-600 collector. Such large effect of collector and insulator reactions shows that the detector is not optimum for delayed responses, at least for the 14 MeV fast neutron applications. The components of the delayed signal (for both SPDs) could not be resolved, as the magnitude of these signals are low and contained several components, lending the exponential decay curve fitting for each decaying nuclide highly inaccurate.

6.4.3 Modelling the GELBE tests of reference SPDs

For simulation of the reference detectors in the high-energy photon field, a simple model comparable to the model-2 of TRIGA GTC simulations has been implemented for the experiment performed in the GELBE cave. The detector is defined with a beam-like photon source a few cm away from it. The calculation is done in a single step with coupled Mode PE type run of MCNP. The subsequent steps give the sensitivities. The comparison of calculations with the experiments is shown for the two SPDs in Table 6-4. The current in both cases are prompt, as there are no neutron activation processes and photon activation is negligible.

Table 6-4: The experimental (S$_E$) and MCNP-calculated (S$_C$) sensitivities of the CYL and FLT SPDs (in units of 10^{-20} A cm^2 s) obtained in GELBE high-energy photon test facility, and the deviations (Δ) of the calculations from the respective experiments.

Sensitivity	CYL			FLT		
	S$_E$	S$_C$	Δ	S$_E$	S$_C$	Δ
Total	0.04 ± 0.01	0.09	138.7 %	2.17 ± 1.45	0.09	−96.0 %

The sign of the current has been predicted correctly for both the detectors. For CYL, the order of magnitude is also correct. The discrepancy encountered in FLT SPD simulation is similar to the one in the earlier case of the reported test, TUD-NG. It can be noted from the experimental assessment in TUD-NG measurement, that the photon sensitivities for SPDs are higher than the neutron sensitivities. It has been realized, over all, that the MCNP model(s) perform the worst for prediction of photon-induced signals, in comparison to the other two, in case of both the geometries.

6.5 Remarks on the Modelling of SPDs

Simulations of SPDs are considered very complex and the quality of results depends on many factors. It is affected by many systematic uncertainties which are difficult to quantify. Dedicated efforts to perform sensitivity studies for such calculations towards each of these possible sources of uncertainties have not been made in this work. The code used, MCNP is well validated for radiation transport but differences can arise due to insufficient details in elemental and isotopic compositions of materials and their chosen densities, quality of the cross-section data, and geometry and source definitions.

The material compositions have been obtained, as far as available, from the manufacturers' datasheets for the purchased detectors or the material foils. Radioactive decay in an activated material mixture, and so the delayed signal prediction can be affected by this. The V foil in FLT V-SPD, annotated as 99.9% pure V by the supplier, has been described as 100% pure V in the model in lack of the detailed composition. This is a part of the reason, although explaining only up to around ±1%, why larger deviation of the model from experiment has been seen for ^{52}V component in Table 6-2. The estimate of the effect of density is negligible for final results, also amounting to around ±1% in the worst observed case (alumina insulator density).

The cross-section data is a big source of uncertainties. No coherent method of propagation of the individual cross-section uncertainties to the integral results of this modelling is available in MCNP. But in the simplified activation calculations using FISPACT-2007, the uncertainties in effective cross-sections (similar to the ones reported in Table 2-1) can lie between ±10% to ±70%. The data sources also influence the results. For V-SPND, the final results have been found to be differing by up to around 10% on change of the source of neutron data files. To check this, separate calculations have been performed using different standard evaluated nuclear data libraries. For consistency, all the reported calculations in this thesis have been performed with the recommended ENDF-B/VII.1, MCPLIB84p and MCPLIB03e data libraries for neutrons, photons and electrons, respectively. Used cross-section files have been checked for availability of the

right data, especially of neutron interactions and photon productions. They are checked for quality by comparing with experimental cross-sections data.

In most cases, the geometry lacks accurate details of the surroundings. It is more economic to perform simplified modelling if the source (neutron/photon) is well-known. Knowledge of the source, and the assumptions made to define it in the model can make substantial differences. This difference is actually more pronounced in the calculation of incident flux in Mode N step. It did not seem to affect the results much in TRIGA GTC (compare Model-1 and Model-2) much. But, this systematic error can be exemplified in case of TUD-NG. There, if a 1 cm deviation in the ^{2}D beam spot on ^{3}T target in assumed, which is physically possible, then the flux estimate at the point of FLT V-SPD can be changed by roughly ±34%. This effect is somewhat eased by averaging over front SPD surfaces, like done here, but nevertheless it can explain a big share of observed deviations. A study of this problem in ref. [70] noted overall difference of 20% in calculated results, with much detailed models than those in this thesis. At the same time, the experimental estimation is also met with this issue, as discussed in Chapter 5. The fluxes could not be measured with enough rigor here, due to a lack of accurate characterization of the irradiation facilities, the time constraints, unavailability of the facilities or the appropriate measurement equipment. This is one of the main factors affecting the comparison (see the bottom part of Figure 6-4). For FLT SPD, this is a relatively bigger effect. It is natural, as the flat design has a larger lateral size than cylindrical one, and it can alter fluxes and spectra in its vicinity rather considerably.

There are many competing processes to account for SPDs when the signals are small. In earlier works, as many as 76 distinct mechanisms of current-creation have been identified for SPDs [39]. Computational tools cannot include these effects together, and even in advanced methods like the one used in this thesis, one needs to externally impose the crude knowledge of these processes through multiple sequential steps. For the (n, β$^-$) type events, where the major process has a very high cross-section, the theoretical idea works well, but for the prompt processes this has been traditionally found inapt. Deviation of calculations from experiments on the scale of ±10% are very common in literature. In one of the first implementations of this model [86], up to ±20% deviations have been noted. With powerful codes like MCNP also, ±35% is noted in ref. [87]. Similarly, for the prompt neutron and gamma-ray sensitivities, in a number of tests of SPD-like effects in coaxial cables, refs. [42, 76, 77] reported gross differences, even in the order of ±100% of the calculations from the measurements. Indeed the major discrepancies have been found for prompt signals in this thesis. Moreover, the signals are in pA-scale, several orders of magnitude lower than what can be measured in a typical reactor-based test. This is already a remarkable point to gather the difficulty of accurate simulations of SPD using simplistic models, to the extent that the authors in [42] have recommended usage of such a modelling of prompt processes for qualitative purposes only. In several cases among these, and in other available literature, the polarities of prompt signals are predicted wrongly also. The polarities have always been reproduced correctly in this thesis.

Instead of refining the model, which has a rather limited scope, it is a better idea to improve the detector design and experiment's quality, because if the signals remain smaller then in a reactor environment the parasitic effects will only increase, further complicating the modeling process.

The extension of the simplified model for the insulator leakage current to flat geometry is inefficient. The model for space-charge effect only includes the effect of deceleration of emitter electrons, giving a returning fraction of electrons. Through the ad-hoc numerical solutions for the space-charge effect in 1-D flat geometry, the returning fraction (F) has been found mostly around 40% to 50%. With several secondary currents in flat SPDs, this might not be enough. There are events which lead to a net positive charge deposition in insulator also, which has an accelerating effect. This has been seen in many cases of calculations done in this work, and partially accounted for as required. Furthermore, the insulators used in FLT SPD are not hermetically sealed. There must be increased leakage due to exposure of the ceramics to the moisture and subsequent degradation. In addition, the electronic effects are more consequential as a result of the flexible contacts, air gaps and supporting structures. All these are not possible to include in particle-transport simulations and require alternative ways of including the effect of external electric fields, metallic conduction of electric charges through extended structures like screws, nuts and wires, etc. Superposing of the theoretical ideas related to dielectric behaviour, e.g. on the lines of [88], upon the modelling approach can yield better results. A meaningful comparison would be that with a code capable of handling electric fields directly, e.g. GEANT [80].

Considering the inherent difficulty in the multi-physics simulations needed for SPD, and the re-normalization of calculated results to experimental parameters, the Monte-Carlo model developed in this thesis is concluded to give reasonable results for the purpose of qualitative studies. It produces correct polarities of various signal components. For cylindrical detector, it could also give correct order of magnitude of the currents. Similarly, for flat SPD, the calculations in thermal neutron field compares well with the experiments. Overall, this model can be considered as verified for the study of detector responses in complex irradiation scenarios, albeit some care must be taken in analyzing the sandwich-type flat SPDs. It is established as a highly useful tool in the prediction of SPD responses under known radiation fields for cylindrical designs of the detector, and it can be qualitatively used for feasibility studies of SPDs in TBMs and fusion reactors. With regard to flat SPDs, it is proposed that some of the issues related to secondary contributions be studied in models through other kinds of methods than particle transport, as well as other codes for nuclear detector modelling.

7. ANALYSIS OF THE SPD SIGNAL WITH VARIATION OF MAIN CHARACTERISTICS

In the experiments and calculations with SPDs, it has been established that several characteristics like the combination of materials used, their dimensions, the electronic circuit elements etc. can contribute to SPD's signal. These set the constraints for the designs and operable conditions for SPDs. Some important studies on this front are presented in this chapter. The openable flat SPD designs allow changing of the material foils. These have been used to prepare test SPDs with different combinations of foils and to study the operational behaviors on making such changes through fast neutron irradiations at TUD-NG. Different avaliable emitter (including Be, a proposed emitter for fast neutron SPND for ITER TBM) and collector materials have been compared and so are the layer thicknesses. A study of spurious signals due to circuit elements of an SPD has also been done. Most of the irradiations have been conducted at TUD-NG. For cases to be compared, the responses are measured under similar irradiation conditions. Overall, a broad perspective of the crucial design parameters and their levels of significance in finished test-SPDs has been obtained. The knowledge of the dependence of SPD signal on these properties is essential to limit the number of free parameters on which the detector needs to be optimized before applying it in a reactor.

Ideally, for the parametric studies of the kind shown here, precisely repeatable irradiation conditions are necessary. As it is clear from the discussion on radiation sources (Chapter 4), it is often difficult to obtain this. At TUD-NG, main bench for these tests, the exact incident beam position on the target is tough to achieve every time in such long series of runs. The aging of the tritium target and the altering quantity of deuterium ion source during the series of such tests also affect this. The longer constant-flux runs are more complicated, often resulting into unstable operations and change of maximum

achievable flux-level. For comparison of the results in two separate runs, the test SPDs have been positioned exactly the same, which fixes the neutron spectrum. For cases to be compared, wherever possible, the runs have been performed on the same day.

Apart from measuring SPD currents, the TUD-NG monitor counts have also been recorded in all the tests. For a given test position, within the uncertainty margins (Section 4.2), the neutron flux is only dependent on the monitor count rate. Flux-specific signals are therefore, used to compare the tests. *Specific signal* (unit: A s) is defined as the ratio of the mean SPD-current (unit: A) and mean TUD-NG monitor count rate (unit: s^{-1}). Measured in an analogous way, this quantity is directly proportional to the sensitivity of the tested SPD. In some situations, instead of the individual specific signals, corrected SPD-current (in A units) signals w.r.t. a constant monitor count rate (e.g. $2 \times 10^4 \, s^{-1}$) has been reported for a better representation.

7.1 Effect of Emitter Material

In a delayed-SP<u>N</u>D, the SPD-current's magnitude is related to the cross-section of the (n, β^-) process in the emitter, and the response time depends largely on its half-life. But for the prompt SP<u>N</u>D and SP<u>G</u>D signals, a major dependence is on the atomic number (Z) of the emitter. The electron production is through the interaction of photons, which is higher for higher Z. Here, in a given geometrical setting of the SPD, emitter materials have been changed and the currents measured in TUD-NG irradiation tests. V, Be and Ag emitters have been compared in the edition-1 of the flat sandwich-type SPD (details in Table A2-1 in Appendix 2, detectors: V-InC, Be-InC and Ag-InC). The Z varies from 4 for Be, 23 for V, to 47 for Ag. All of them contain Al_2O_3 insulator and Inconel-600 collector and they have been tested at the same distance from the target.

Figure 7-1 shows, in three parts, the signals from V, Be and Ag based flat SPDs, with the corresponding TUD-NG monitor count rates on right Y-axes. All the three signals are majorly prompt. The delayed components are less than a tenth of the totals. The half-lives of the major beta-emitters are considered for the lengths of the irradiation at constant flux. One may notice that the difference in the decay times of the delayed parts of V and Ag signals are small. For V and Ag, the delayed components can be compared in the insets of their respective graphs. Similar, long-term, small-magnitude delayed currents in SPDs with different emitter materials, signifies that the delayed currents are largely formed by the betas and photons from other layers, those from the EM shield, and the decay products from the surroundings, apart from the respective emitters' betas.

The saturated specific signals, i.e. the ratio of SPD current to the monitor counts (in units of pA s) from three detectors with same geometrical details are compared in the Table 7-1. The signal rises on increase of Z. With Z, the interactions of photons, from outside and those induced by neutron interactions in the detector materials, increase. For Be, the magnitude is about 5 times smaller than the others. Be emitter forms the subject of the next section. Ag-InC SPD has the highest response, with that of V-InC SPD nearly comparable, having specific signal around 30% lower than that of the Ag-InC SPD.
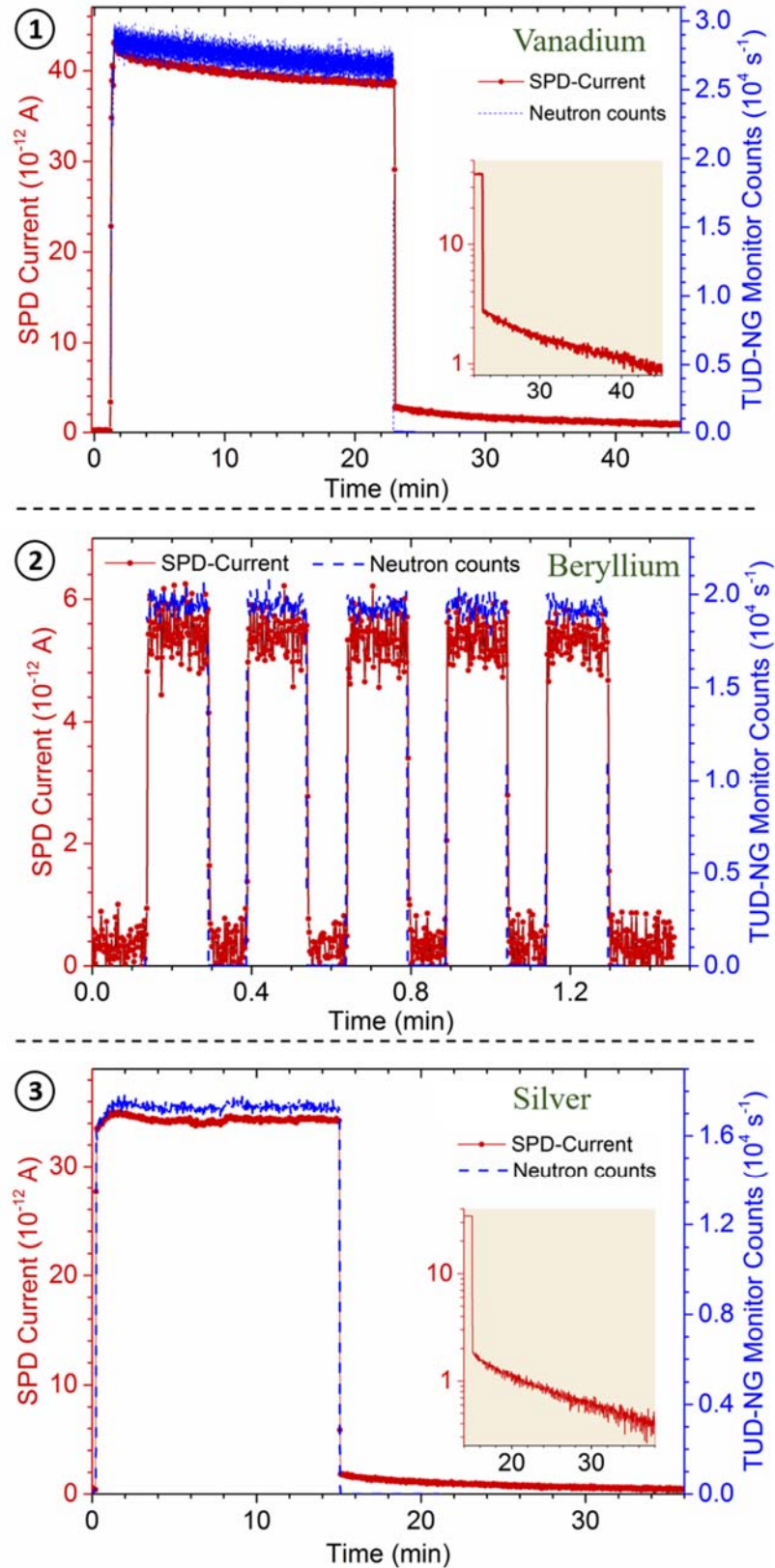
Figure 7-1: A comparison of the measured signals of (1) vanadium, (2) beryllium and (3) silver test-SPDs in edition-1 sandwich-type design, containing Al_2O_3 insulation and Inconel-600 collector. Red curve shows the SPD-current, and blue the corresponding measurement of TUD-NG monitor count rates. The insets in (1) and (3) show the delayed component of the signals on log-scale (see the resemblance). Time-averaged currents and count rates at high-level of flux in each case are used to get specific signals.

Table 7-1: Measured SPD currents, monitor count rates and specific signals from SPDs with different emitter-collector material combinations in the same flat sandwich-type (edition-1) design tested under similar conditions at TUD-NG. Specific signals can be compared for comparison of emitter materials.

Combination	SPD Current	Monitor Count Rate	Specific Signal
Be-Inconel 600	5.5 pA	1.9×10^4 s^{-1}	2.9×10^{-4} pA s
V-Inconel 600	40.7 pA	2.7×10^4 s^{-1}	1.5×10^{-3} pA s
Ag-Inconel 600	34.4 pA	1.7×10^4 s^{-1}	2.2×10^{-3} pA s

7.2 Beryllium as a Fast Neutron SPND Emitter

One of the tasks under the project of F4E for development of SPDs for EU ITER TBMs has been to construct and test Be SPD, which is accomplished in this work. Delayed SPND based on beryllium emitter was proposed for application in TBM in the first studies [19, 20] because there are no competing reactions in Be emitter, so fast neutron fluxes can be efficiently measured using (n, β^-) type process with ^{9}Be (n, α) ^{6}He reaction. The half-life of the generated ^{6}He is 0.81 s, which means the response would practically be instantaneous. It is, however, to be reminded that, the claim regarding the feasibility of a reliable delayed SPND for ITER TBM has been disproved in this thesis. The measured signals in various fast neutron and photon tests are mostly prompt. The prompt-to-delayed signal ratios are very high. The prompt signal needs to be subtracted from the total to extract delayed signal and the associated information on fast neutron flux (similar to what is done for thermal neutron signals in Chapter 5). This process with SPNDs in 14 MeV neutron cases, if possible, incurs very high uncertainties.

The Be emitter has been combined with different collectors in edition-1 of sandwich-type SPD and tested under TUD-NG neutron field. The corresponding details of test SPDs are available in Table A2-1 of Appendix 2. The results are shown in the Table 7-2. It has been experimentally shown that the Be delayed current value is not clearly measurable (Figure 7-1 (2)). So, it should be compared with other emitter choices for prompt response. The specific signals from Be based SPDs, as seen in Table 7-2, are one or two orders of magnitude smaller than other emitters (see Table 7-1). Thus, it can be regarded as a poorer choice.

Table 7-2: Measured SPD currents, monitor count rates and specific signals from tests at TUD-NG, under similar conditions, for SPDs with Be emitter combined with different collector materials.

Combination	SPD Current	Monitor Count Rate	Specific Signal
Be-Inconel 600	5.5 pA	1.9×10^4 s^{-1}	2.9×10^{-4} pA s
Be-Nb	5.5 pA	2.6×10^4 s^{-1}	2.1×10^{-4} pA s
Be-Graphite	–2.1 pA	2.5×10^4 s^{-1}	-8.5×10^{-5} pA s
Be-Be	15.5 pA	2.4×10^4 s^{-1}	6.6×10^{-4} pA s

With low neutron reaction cross-sections, and a low Z, the probabilities of delayed as well as prompt interactions in Be are low. The signals are small, and get largely affected by the collector material. Non-neutronic effects tend to play a major role in such a case also. While a detailed discussion on effect of collector materials is postponed for later, interestingly, a combination with Be as collector seems to perform better than others (Table 7-2). Other tested collectors have Z much higher than that of Be, leading to lower currents. The negative net current in case of Be-graphite combination is a replication of the lower density of graphite. This allows more outside electrons from the box, fixtures etc. to enter the emitter and create negative signals.

The edition-1 flat test-SPD could not be checked for photon sensitivity in ELBE. Due to its bigger size and weight, it did not fit into the experimental position. However, positive and higher signals with the edition-2 Be-Inconel-600 SPD have been measured with photons at the experimental facility in ELBE beam dump. The details of this test SPD is given under the name Be-SPD in Table A2-1 of Appendix 2. Background current of around −1 pA has been measured in this detector, unlike the cases of V-SPD or Ag-SPD in the same geometry. The signal measured at ELBE-BD is shown in Figure 7-2.
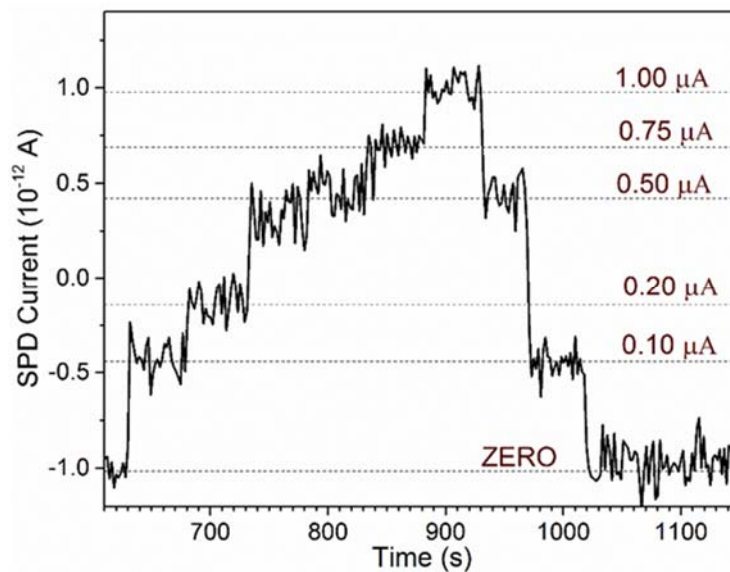
Figure 7-2: Measured signal of edition-2 flat Be-Inconel-600 SPD at ELBE beam dump. The levels show different photon fluxes set in the test, with the approx. electron beam current achieved on the level.

The same Be-Inconel-600 SPD, in edition-2 sandwich-like design, on the irradiation with TUD-NG neutrons, has yielded negative currents (Figure 7-3). It is realized that the emission from the collector generated a prominent effect when the neutron source is on. On switching off the neutron source, the positive signal (delayed) due to Be activation is seen. The edition-2 SPD is more compact than the edition-1 and the geometrical difference affects the smaller magnitude signals quite a lot. However, it could be concluded that the signal due to photons is positive and higher, while that from the fast 14 MeV neutrons is smaller and negative.
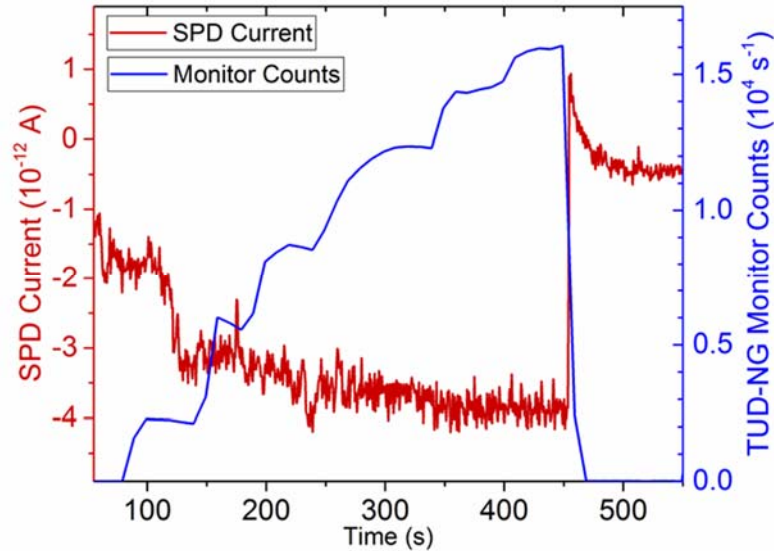
Figure 7-3: (Red) measured signal of edition-2 Be-SPD at TUD-NG, showing the absolute current and corresponding NG monitor counts (blue). The signal, when neutrons are switched on, is negative.

Given the overall experience of testing Be based SPDs, it is not advisable to use Be as an emitter for it will produce sensitivity far lower than other choices, and will be more prone to spurious effects. Also, it does not suffice for the proposed measurement of fast neutron fluxes through (n, α) reaction based (n, β⁻) process.

7.3 Contributions from Detector Assembly Components

It has been realized in earlier experiments that some portions of the SPD-current arise due to the presence of several physical components apart from the main detector sandwich, specifically the fixture units, electrical contact etc. A set of experiments has been performed here to find how sensitive the measured SPD current signals are to these components. This gives an idea of the lower limits on the "sensible" signals. But, it is understood that these components constitute the detector and are not independent, and it is essential to eliminate or reduce them through better practices while designing the prototype SPDs.

The sandwich of the SPD whose signal is shown in Figure 7-1 (1), has been completely disassembled, the copper wire for contacting emitter with the lead cable removed, and merely the aluminum EM shield with the cable attached to it is retained. It has been tested under high flux conditions at TUD-NG. After this, the detector sandwich has been assembled sequentially, starting by attaching a new connector with copper wire extension to the box. Then, the sandwich fixtures, the insulation and collector in the correct order and copper wire pressed in the center have been added in steps. Finally, the emitter has been introduced, giving the complete assembly back. At each stage, fast neutron irradiation has been performed, under similar conditions (less than 5% average difference between fluxes in different tests). To reduce the occupational radio-exposure from the irradiated units, several hours or days of waiting times are needed between two such irradiations. The saturation signals (almost instantaneously achieved, as the signals are prompt) and decay on switching off the neutrons are shown in Figure 7-4.

With only the shield, a current of around 6 pA is measured. A possible reason behind this is the SPD-like effects in the multi-layered structure of the cable and connectors attached to the shield. With copper wire soldered to the conductor of the connector, it produces around 11 pA. This, on the addition of sandwich layers around the copper wire reduces by about 2 pA. This is explainable, because the wire is now shielded. On putting the emitter, i.e. with the full V-InC SPD, the current is around 39 pA, a reproduction of the previously shown V-InC SPD signal. The delayed signal is almost purely due to the emitter. For this SPD about 25% of the signal can be attributed to nuclear interactions and electrical effects in the circuit components. These effects are not independent in a fully assembled SPD. The final contributions of any such assembly will not necessarily be like what is seen in this experiment. These effects could be detrimental when the signals are small, depending on factors such as the layer materials.
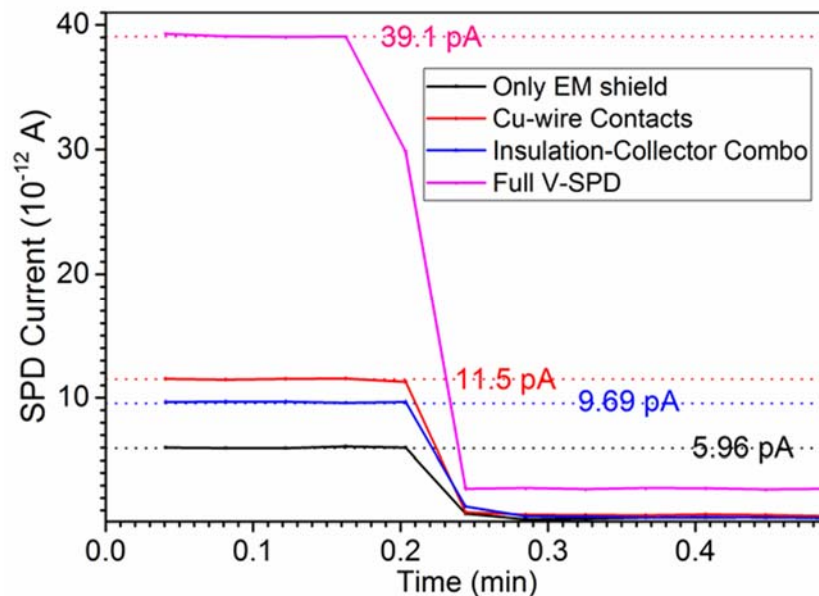
Figure 7-4: Experimentally measured breakup of flat V-SPD signal at the highest level of flux as tested in TUD-NG, showing independent contributions from different components of the detector.

Many electrical nuisances, like the effects of the surface characteristics of the emitter, emitter-cable junction, quality of contact with the cable, layer resistivity etc., and their dependences on the nuclear properties of the materials are not well-understood. In an open detector design, like the flat SPDs, this is highly consequential. Some of practical experiences from re-designing of an SPD-type detector are exemplified below.

With the flat sandwich-type Ag-InC SPD, changes in SPD current have been observed on use of a new silver foil as compared to a foil which has been already used two months earlier, having same physical dimensions. Due to fast corrosion on staying in ambient atmosphere during this time, the electrical contact on the silver surface gets affected. However, if the sandwich is not opened then the contact does not change. The copper wire used for contacting is securely pressed between the emitter and the insulator foil. And, the signal is found to be same within experimental errors.

Similarly, some metals are soft, in which the pressure type contact can create dents and give rise to complicated leakage effects. In some of the tests with Pb, Bi and Cr emitter foils, large fluctuations in the background current have been found on testing under same conditions but shaking or spatially shifting the detector(s). Due to the physical quality of the materials and their surfaces, the contacts get altered, leading to such a behavior. These are not reported in details here, and merely highlighted for discussion.

A striking example of such issues with SPDs has been found with the cylindrical SPD with Cr emitter, the Cr-SPD. It has not been possible to test it due to sustained, high and variable background current. Two measured Cr-SPD signals, with neutrons and photons irradiations are shown in Figure 7-5. The background current drift is devastatingly large for any meaningful extraction of SPD signal(s). The junction between cable conductor and emitter is suspected be loosened due to fragility of chromium metal over the cycles of mechanical and thermal stresses that the detector underwent in previous tests and during several transportations. The exact reason and its resolution requires dismantling of the SPD, however, long durations of stabilization of decaying background signals, from several hours to few days could help in these measurements. Such long-term and repetitive measurements have been done elsewhere to successfully determine Cr-SPND signals under fusion conditions [24].
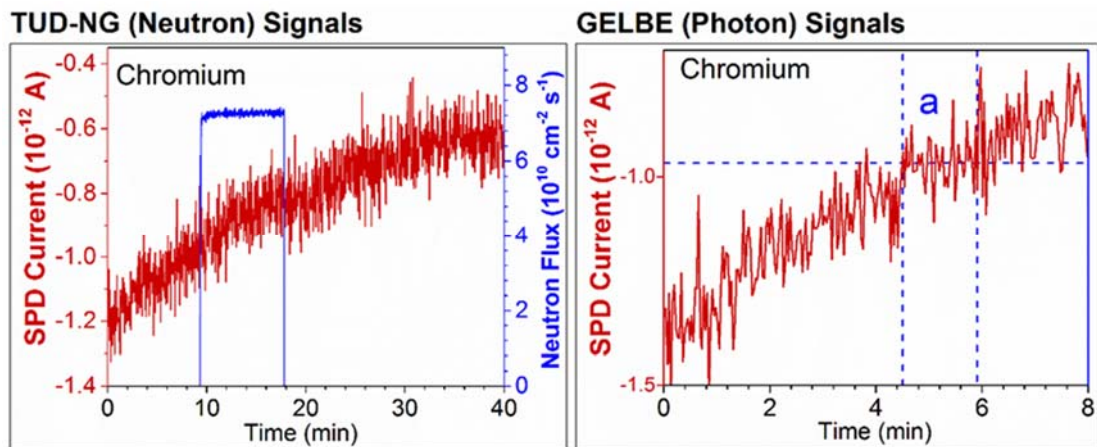
Figure 7-5: Signals from (left) TUD-NG neutron irradiation test and (right) GELBE high-energy photon test of the chromium SPD. The corresponding neutron flux is shown in blue on left curve, and the region of high photon flux in right curve ("a" indicates electron beam current = 600 µA) is shown through dotted lines. It is indicate that a negative and continuously decreasing zero current was present in the SPD, which made flux measurement impossible.

Repeatability of the results have been ensured by performing tests with well-chosen materials and accepting only those materials for which these effects could be minimized below the experimental errors. The signal contribution of such effects in fast neutron fields are difficult to eliminate. Fortunately, for a traditional reactor SPD, the signals are much stronger and the imperfections of the circuit can be neglected. But in the present openable design, the fixtures, contacts etc. are changed multiple times during the tests and the signals are smaller in amplitude. It is worthwhile to note that the Be-SPD,

for its smaller signals, must be greatly affected by such phenomena. Deep reasoning of all these effects is difficult and expensive, especially so in the irradiation experiments. Comparisons of different materials to obtain the best-performing ones is recommended. More detailed examinations of these signals shares and many stages of refining of the detector design will be needed to reliably accept these effects in practice.

7.4 Effect of Collector Materials

The collector material can affect the SPD signal by the emission of beta particles in the direction of the emitter. Secondly, collectors contribute by large photon production, larger in comparison to the emitter, and therefore producing larger currents due to processes of (n, γ, e^-)-type. They can also stop external photons to create charges through (γ, e^-) type interactions. The photon production from fast neutron inelastic collision and threshold reactions has a higher probability for materials with higher Z. From the investigation of the cross-section files from ENDF-B/VII.1 for ^{NAT}C and ^{93}Nb nuclides, the total gamma production cross-section in graphite is found less than about a tenth of that in Nb, at around 14 MeV neutron energy. Furthermore, the electron emission due to photon interactions depends on Z also, being higher for higher Z material [51]. Compton interaction probability has a direct dependence on Z and density of the material. Also, the photo-electric absorption depends on Z^n (n between 3 and 5) and pair-production on Z^2.

Often, the net signal share of collector elements is negative, however, a process of the (n, γ, e^-)-type where photon-production occurs in the collector but electron emission in emitter, can give positive share also.

For a survey, three conducting materials have been chosen to test for compatibility with the emitters of interest for TBM SPDs: C, for which graphite foils have been acquired, Inconel-600 and Nb. The Z differs from 6 for graphite, 24 for Cr and 28 for Ni (Inconel-600), to 41 for Nb. With enlisted emitters: Be, V, and Ag, this yields nine material-combinations. To recognize the trend of signals with the Z of the collector element, the *effective Z* (Z_{eff}) of Inconel-600 has been calculated using analytical methods. It employs a standard formula with the weight fractions of major elements and their gamma attenuation coefficients, to obtain approx. 26.9 for Z_{eff} of Inconel-600. The edition-2 of sandwich-type SPD has been used and tests have been conducted at TUD-NG for all combinations (see Be-1/2/3, V-1/2/3 and Ag-1/2/3 in Table A2-1 in Appendix 2), under similar test conditions. The resulting specific signals are multiplied with a constant monitor count rate and a so-called saturated *average SPD-current* is obtained for each combination, which can be compared directly as shown in Figure 7-6.

Overall, the observed tendency for the dependence of SPD current on Z of the collector is not monotonous. The graphite collector, keeping in view its lower Z, should show the highest signals, but it does not. It can be explained through the relatively lower density of graphite. As it is known from the extended behavior of flat designs, the influence of charges produced outside of detector sandwich, specifically the Al EM shield and TUD-NG target metals also add to the measured signal. This is limited to some extent due to the stopping of outside electrons in the collector and the insulator layers. The electron-stopping capacity of graphite is lower than other two collector materials, which means it allows more outside electrons to enter the SPD core and finally leads to relatively

lower signals. The signals are strongest with the Inconel-600 collector. The currents for Be SPD are negative and low, and so a Be detector is more prone to bigger changes due to changes in the geometry or material of the detector.
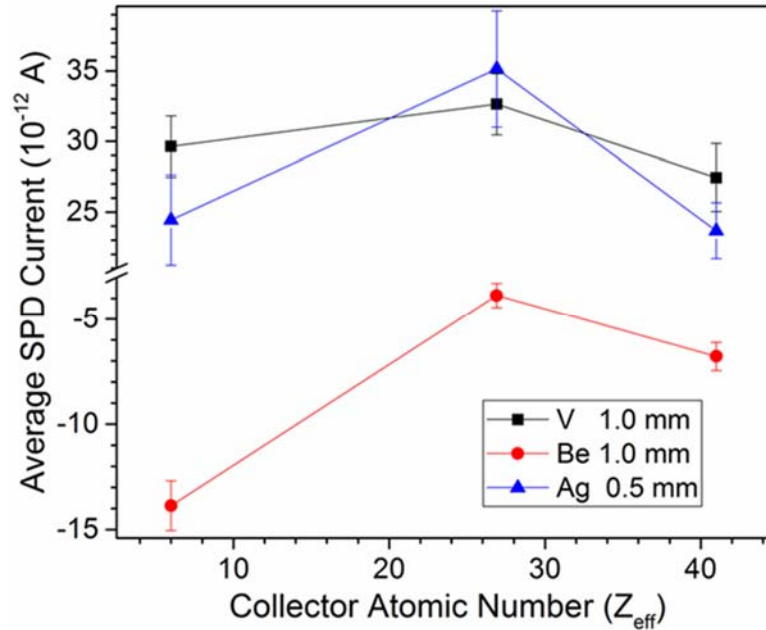
Figure 7-6: Dependence of the measured SPD current on the effective atomic number (Z_{eff}) of collector materials- graphite (Z=6), Inconel-600 (Z_{Ni}=28, Z_{Cr}=24) and niobium (Z=41), for three emitter materials- V (1 mm foil), Ag (0.5 mm foil), and Be (1 mm foil). All collector layers were 1 mm thick and insulator was 0.5 mm foil of Al_2O_3 in all cases. Error bars show the standard deviations of the average SPD currents, which are normalized with respect to a given flux value for direct comparison of the cases.

For clarity of signals in delayed SPDs, it is advisable to have difference of Z between emitter and collector small, effectively cancelling other important effects than the beta emission cross-section. But in the case of fusion neutrons, the main competition between the two layers is not due to the difference of cross-sections. The signals, much smaller, are from the prompt processes, which do not necessarily cancel out even if same material is placed in the emitter and collector. Only first step of (n, γ, e⁻) process is cross-section dependent. Smaller asymmetries in the geometry and shape can still produce charge separation. So, even with a symmetric emitter-collector combination, substantial signals can be expected. For prompt SP<u>N</u>Ds and to reduce SPD-like effects in mineral cables, such a method has been implemented in previous works also [32]. Table 7-2 has such a combination with Be. Other combinations (see Be-Be, Nb-Nb, Gr.-Gr. and InC-InC test SPDs in Table A2-1 of Appendix 2) have also been tested, as reported in Table 7-3. The normalized signal for Inconel-Inconel SPD is found to be higher than others by a large margin. It can be concluded that this combination has higher response and should also be paid attention to. Also, the Be-Be combination has a sensitivity higher than the other combinations of Be emitter (see Table 7-2).

Table 7-3: Measured SPD currents, monitor counts and normalized signals for different materials making the emitter and collector in symmetric combination SPDs.

Material	SPD Current	Monitor Counts	Specific Signal
Beryllium	15.5 pA	2.4×10^4 s^{-1}	6.6×10^{-4} pA s
Niobium	25.6 pA	2.8×10^4 s^{-1}	9.3×10^{-4} pA s
Graphite	23.0 pA	2.4×10^4 s^{-1}	9.8×10^{-5} pA s
Inconel 600	18.6 pA	1.8×10^4 s^{-1}	1.1×10^{-3} pA s

7.5 Effect of Thicknesses of Material Layers

Geometry of an SPD is defined by the lateral dimensions of the sandwich (or the length of a cylindrical design) as well as the thickness of the layers. Naturally, a thicker layer contains more material, equating to higher reaction volume. But, thickness is also the reason behind self-shielding of neutrons, photons and electrons. It is expected that the signal either increases or decreases monotonously, on change of a layer's thickness. However, there is a *local optimum* (maximum or minimum) of the thickness around which the behaviour either saturates or changes, for each layer in each material-combination. This depends on the material properties, and on the penetration power of incident neutrons and photons and that of the emitted photons and electrons.

A set of irradiation tests have been conducted at TUD-NG, keeping the materials fixed while varying the thicknesses of different layers and measuring the signals under similar conditions. Resulting average currents (defined in the same way as in Figure 7-6) are compared in Figure 7-7. To test the dependence on the thickness of one layer, other two are kept constant. These tests have been done with Ag emitter and graphite (C) collector (test SPDs Ag-a/b/c in Table A2-1 of Appendix 2). However, the behaviour with respect to the thickness of layers will remain largely the same with other collectors and emitters also.

It is imperative that the increase of the volume and emission surface (the outer surface) of the emitter layer through an increase in its thickness should lead to increase in the signal. While an opposing effect of doing this is stopping of more of the electrons from insulator, collector and outside, leading to negative currents. In the measurements with Ag SPD, shown in Figure 7-7, the SPD-current increases initially. After increasing to a given thickness, close to 1.5 mm here, the self-attenuation of the electrons (and also incident photons) becomes more prominent. A big part of the emitted electrons move inwards in the emitter (ultimately stopping there), and at the same time those emitted in the inner regions of the emitter find it difficult to penetrate through its thickness. Therefore, at this juncture, the latter of the effects of increasing emitter thickness can overpower and that should explain the small reduction of the net signal.

The main function of the insulator is to slow down the electrons and electrically isolate the conductors. But insulator also has its own electron emission effects and leakage effects associated with the space-charge field from accumulated charges. They can lead to positive or negative contribution(s) to the SPD-current. However, the effect

of the change of insulator thickness is not as critical as that of the other layers. The change in insulator thickness is not drastically changing the produced SPD signals, as seen in Figure 7-7. The signal rises with increasing thickness, and there is a zone more akin to saturation observed at the thickness of around 1.5 mm.
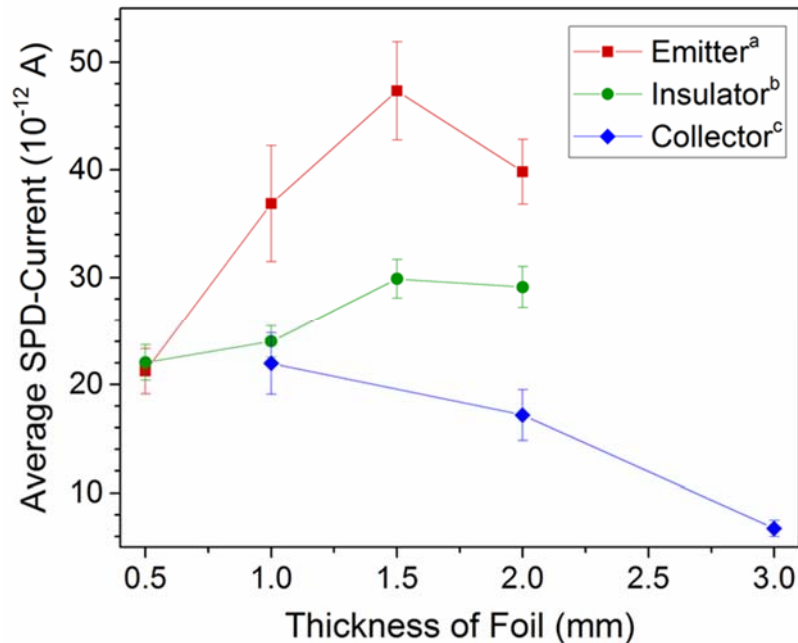
Figure 7-7: Variation of the measured SPD current with variation of layer thicknesses. Here, an Ag-Al$_2$O$_3$-Inconel-600 SPD is tested under similar conditions by changing the thickness of layer: a. emitter (insulator 0.5 mm, collector 1.0 mm), b. insulator (emitter 0.5 mm, collector 1.0 mm) and c. collector (emitter 0.5 mm, insulator 0.5 mm). Error bars show the standard deviations of average signals, which are normalized to a given flux value for comparison.

The collector element produces electrons through prompt interactions with the photons from inside and outside the detector, which contribute negatively to the SPD current and lead to a monotonous decrease of the SPD current with an increase of the thickness of the collector. Another important phenomenon in the collector is the shielding of photons, the major projectile for electron-ejection processes, from the emitter. This effect is smaller in case of the graphite collector for its relatively smaller density and smaller Z, as illustrated earlier.

Broadly speaking, it has been found that for Ag-SPD in edition-2 of flat sandwich-type design, the emitter should be between 1 to 2 mm thick, the collector should be thinner than 1 mm, and insulator around 1.5 mm thick. It is important to choose optima of thicknesses of different material layers. Overall, the choice of materials, quality of the design of the electrical circuitry and the construction parameters like geometrical shape and layer thickness, have been found to affect the signals considerably. It is often difficult to find a clear physical trend with respect to these features, especially with the small-scale signals in 14 MeV neutron fields. Extensive parametric studies would be required to acquire optimum performance in any such device.

8. COMPUTATIONAL STUDIES OF NEUTRON AND PHOTON SPDS FOR ITER TBMS

As the currently available radiation sources cannot produce fields like those expected in fusion reactors (characterized by wide energy-spectra and high flux densities), it becomes necessary to utilize the computational studies to decide on detectors applicable for nuclear measurements. For the SPDs, the Monte-Carlo calculation scheme which has been developed for electrical sensitivity predictions, can be applied to study the SPDs under ITER TBM conditions. To demonstrate this, a set of survey calculations has been conducted with two representative SPD variants.

The signal of an SPD has several components and the delayed part has a peculiar time-dependence. The aim of this chapter is to provide a first view of the signal profiles possible from SPDs in ITER. To this end, reference locations in the two European TBMs have been selected and the radiation fields have been calculated there through coupled radiation transport simulations. Then, the sensitivities and signal amplitudes are calculated for the chosen SPDs. Their time-dependencies under a typical plasma pulse of ITER have been predicted also, to get a more intuitive idea of the operation of SPDs in ITER. The results have been used to make conclusions on the SPDs' possible modes of operations and their applications in ITER TBMs and future fusion reactors.

8.1 Neutron and Photon Fluxes and Spectra in Fusion Blankets

The study of an SPD under representative fusion reactor conditions begins with identification and estimation of various nuclear interactions in the SPD materials at the position of its integration. For this work, only the nuclear response of SPDs is of interest.

Many other integrational aspects of an SPD in a reactor, the effect of electromagnetic fields, high temperatures etc. are not dealt with.

At first, a radiation transport modeling of the reactor under investigation is performed. ITER is a complex machine, and computational models with sumptuous details are difficult to come by. For nuclear analyses, simplified models of reactors can give sufficient insight for designers and engineers [89]. Therefore, for particle transport simulations with codes like MCNP, scaled-down models are used, which have only necessary details of component geometries and materials, but are adequate for neutronics studies. ITER and its parties have been developing these models and prescribing them for use in computations related to the reactor. Here, an adaptation of the previous reference MCNP model of ITER, the *A-lite model* with EU HCLL and HCPB TBM systems defined in their designated positions, has been used in the feasibility study on SPDs [89, 90]. Some essential details of the A-lite model with the TBMs are provided in Appendix 5.

The neutron and photon spectra in TBMs may vary substantially with change in the position of measurement. As partially discussed in Chapter 1, the number of accessible positions for nuclear detectors is restricted because of the close-packed mechanical design of TBM, thermal-hydraulic constraints (e.g. temperature hot-spots) and limited routes for inserting signal cables. Whereas, for a reasonably complete flux map in the TBM during ITER runs, it will be interesting to have flux monitors strategically positioned at multiple points. For SPDs, necessary and suitable positions need to be selected through careful examination of various possibilities, including the consideration of the engineering challenges for integration of the SPDs. Taking the generic considerations however, there is more interest in installing SPDs close to the plasma-facing front walls of the TBMs. The signal amplitude of an SPD is directly proportional to the incident neutron or photon particle density. Around a location near the front-wall of TBM, the neutron and photon flux intensities are the highest, which would ensure higher responses and lower secondary contributions for the SPD. Secondly, an SPD is cross-calibrated w.r.t. other types of neutron detectors, e.g. neutron activation system and the fission chambers. These sensors would provide measurements close to the front wall, which makes it logical to place the SPDs also nearby.

Central positions on the front walls of the two TBMs, designated as *A5* in HCLL and *B5* in HCPB, have been selected in the A-lite model. For brevity of description here, the discussion on these positions are placed in the Appendix 5. It is to be noted that these are not necessarily the points of measurements in the real TBMs but have been implemented only for reference feasibility study of SPDs. Neutron and photon flux-spectra have been calculated using MCNP simulations at these positions in the ITER model. Superimposed cuboidal meshes of size $(5 \text{ cm})^3$ have been employed to score cell fluxes. An energy mesh with 175 groups has been used to evaluate the neutron flux-spectra as well as for the photon spectra. The MCNP output cell fluxes (in units of cm^{-2} per source neutron) are multiplied with a normalization factor, w.r.t. 500 MW fusion power to get results in the units of $\text{cm}^{-2} \text{ s}^{-1}$. The statistical uncertainty in the calculated fluxes is low, with the maximum going to 5% in only a few (low statistics) energy groups.

The calculated neutron and photon flux-spectra at A5 and B5 are compared in Figure 8-1. The total neutron flux intensities are: $2.0 \times 10^{14} \text{ cm}^{-2} \text{ s}^{-1}$ at A5 in HCLL TBM

and 1.9×10^{14} cm^{-2} s^{-1} at B5 in HCPB TBM. The total photon fluxes in the two TBMs are 3.3×10^{13} cm^{-2} s^{-1} at A5 and 7.2×10^{13} cm^{-2} s^{-1} at B5.
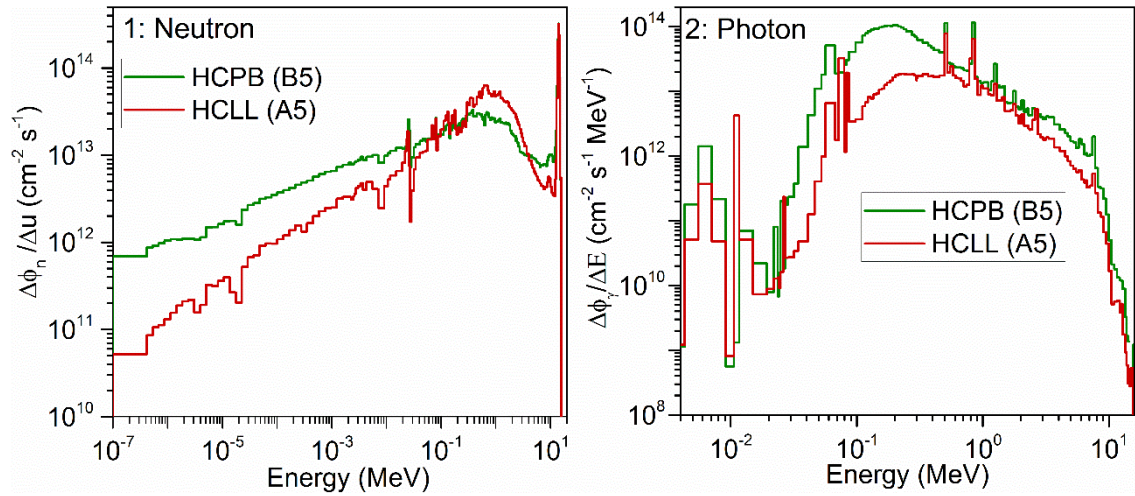
Figure 8-1: (Left) calculated neutron spectra at B5 in HCPB and A5 in HCLL TBMs, and (Right) calculated photon spectra at the same positions in two TBMs. Ordinates show group neutron fluxes ($\Delta\varphi_n$) per unit lethargy (Δu) for neutrons, and group fluxes ($\Delta\varphi_\gamma$) per unit of energy bin size (ΔE) for photons.

With higher concentration of lead, a photon absorbing material, in HCLL, the photon flux is lower than that in HCPB. Salient differences can be observed in the signals of SPDs due to the changes in the spectral shapes between the two TBMs. Small difference due to pronounced thermal energy region of neutrons in HCPB is probable, while relatively lower photon fluxes in HCLL can also lead to different photon signals. In the next stage of prediction of SPD signals, these spectra and integrated fluxes are used as input for the calculations of sensitivities and signal amplitudes.

8.2 Signal Characteristics and Adaptability of SPDs in Reactors

8.2.1 Choice of SPDs and Method of Sensitivity Analyses

In the second part of the study, the Monte-Carlo modeling of SPD-variants have been performed with MCNP. For completeness, two representative detectors are chosen.

1. Vanadium emitter: vanadium has functioned as the reference emitter material for most of the experimental tests in this thesis. It is a candidate emitter for TBM SP<u>N</u>D and is a common commercial SPND emitter. Moreover, V has been found to be one of the better performing emitters in TBM-like fast neutron field.
2. Bismuth emitter: while the choice of V is primarily expected to serve as neutron detector, it is also worthwhile to estimate the response of an SPD primarily anticipated to be a photon detector. Bismuth, a common SP<u>G</u>D emitter, has been selected for this purpose. The delayed contributions in Bi-emitter are negligible due to small cross-sections of threshold reactions, and large half-lives of the decay products (^{209}Pb and ^{206}Tl).

Only cylindrical SPDs have been selected for this assessment because the MCNP model for SPDs has been found to lack essential details for calculation of sensitivities of flat SPDs (Chapter 6). The demonstration is nevertheless complete, and remarkable conclusions can be made on the basis of its results, as shown in the forthcoming.

Both the candidate SPDs for the simulations and analyses have been assumed to have same lateral dimensions (see V-SPND in Table 3-1). Commercial standards have been adopted to provide results possible to extrapolate to other SPDs available in the market. The diameter of emitter layers in both SPDs are taken as 3 mm. While the thickness of insulation layer is 0.53 mm and outer diameter of the collector is 5.3 mm, for both. The length of the studied SPDs has been set at 100 cm. Both V- and Bi-SPDs have been modelled with Al_2O_3 insulation and Inconel-600 collector. The layer materials encountered and their isotopic compositions are given in Table 8-1.

Table 8-1: List of materials and their isotopes with respective percent weight compositions (in parentheses) in different layers of the SPDs studied under TBM conditions.

Layer material	Isotope and weight percentage
Vanadium	^{51}V (99.75), ^{50}V (0.25)
Bismuth	^{209}Bi (100.0)
Inconel-600	^{58}Ni (49.8), ^{60}Ni (19.2), ^{52}Cr (13.6), ^{56}Fe (8.6), ^{62}Ni (2.7), ^{53}Cr (1.5)
Alumina (Al_2O_3)	^{27}Al (52.9), ^{16}O (47.1)

For each detector, there are multiple steps in order to ultimately calculate neutron induced delayed and prompt currents, and photon-induced prompt currents. In each case, for calculating sensitivity of an SPD at one position, there are one of each Mode-N, Mode-NPEH and Mode-PE steps (see Chapter 6 for details of the steps). The neutron or photon source has been defined as surface (or thin cell) source near the detector. Energy distribution is given by the calculated neutron or photon spectrum at the position of calculation, A5 or B5. The angular distribution is given by the cosine of the emission angle, which is a typical choice in the DIR parameter of the MCNP SDEF card.

Table 8-2 shows the delayed contributions, i.e. the (n, β^-) processes in different detector layer materials, along with the decay characteristics of the beta-emitters. These contributions have been calculated through combination of Mode-N and several, between 12 and 15 for each case, Mode-E steps with the MCNP model(s).

The coupled neutron-photon-electron-proton transport, Mode-NPEH calculation gives the charge contributions from (n, γ, e^-)-type processes due to neutron-induced photons in the detector materials. In Mode-PE step, the (γ, e^-) effect is simulated in a coupled gamma-electron transport. Space charge returning fraction is calculated using the analytical method, combining insulator charges from all steps involving electron transport.

In ITER tokamak, the normal operation regime has a 450 s full power (500 MW fusion power) pulse. Ramp up (from zero power) and ramp down (to zero power) times

are estimated to be 60 s and 200 s, respectively. Dwell times of 1600 s to 4000 s are to be expected. In advanced scenarios [91], aimed to be explored during ITER runs, up to 3000 s pulses, at reduced powers will be considered. The two pulse scenarios are as following.

- Pulse-1: 500 MW operation with 450 s long flat-top pulses
- Pulse-2: 350 MW operation with 3000 s long flat-top pulses

Table 8-2: List of (n, β⁻)-type processes in the materials of the simulated SPDs; showing the reaction, product half-life ($T_{1/2}$), the mean beta energy of the emitter nuclide (E_β, in MeV units) and an effective cross-section of the reaction under HCPB TBM conditions (Eff. σ, in b units) as calculated using FISPACT-2007. The units of $T_{1/2}$ (s, m, h) stands for standard units of sec, min and hr.

(n, β⁻) Process	$T_{1/2}$	E_β	Eff. σ	(n, β⁻) Process	$T_{1/2}$	E_β	Eff. σ
	s, m, h	MeV	b		s, m, h	MeV	b
Vanadium				**Bismuth**			
^{51}V (n, γ) ^{52}V	3.74 m	1.07	3.16E-02	^{209}Bi (n, p) ^{209}Pb	3.23 h	0.20	2.46E-04
^{51}V (n, p) ^{51}Ti	5.76 m	0.87	4.55E-03	^{209}Bi (n, α) ^{206}Tl	4.20 m	0.53	1.14E-04
Alumina				**Inconel-600**			
^{27}Al (n, γ) ^{28}Al	2.24 m	1.24	3.71E-03	^{56}Fe (n, p) ^{56}Mn	2.58 h	0.79	1.69E-02
^{27}Al (n, p) ^{27}Mg	9.46 m	0.70	1.26E-02	^{52}Cr (n, p) ^{52}V	3.74 m	1.07	1.16E-02
^{27}Al (n, α) ^{24}Na	15.0 h	0.55	1.24E-02	^{53}Cr (n, p) ^{53}V	1.54 m	1.01	6.22E-03
^{16}O (n, p) ^{16}N	7.13 s	2.68	5.94E-03	^{62}Ni (n, p) ^{62}Co	1.54 m	1.59	2.55E-03
				^{62}Ni (n, p) ^{62m}Co	13.9 m	1.09	2.17E-03

Waiting periods of approx. 20 min are enough to remove the majority of the important delayed signal components in case of 450 s irradiations. In case of 3000 s irradiations, small delayed contributions may remain for longer periods and affect the signal generated in the subsequent pulses. In the study of SPDs, signal profiles under single pulses of both kinds have been studied. The ramp up, down and dwell times have been ignored, which is a reasonable simplification.

The sensitivity (S) is calculated using the formulas from Chapter 5. Towards each of the considered processes, a *partial sensitivity (S_p)* has been calculated, leading to the *partial saturated current (I_{psat})*. The partial current (I_p) due to a delayed process has a time-profile depending on the decay constant (λ_p) of the radioactive process. The partial current during and after a pulse of length *pulse*, at the time *t,* is given by the equations 8-1 and 8-2, respectively.

$$I_p\,(t) = \ I_{psat}\ \times \left(1 - \exp\!\left(-\lambda_p \times t\right)\right). \qquad\qquad \text{(Eq. 8-1)}$$

$$I_p\,(t) = \ I_{psat}\ \times \left(1 - \exp\!\left(-\lambda_p \times t_{pulse}\right)\right) \times \left(exp\left(-\lambda_p \times \left(t - t_{pulse}\right)\right)\right). \quad \text{(Eq. 8-2)}$$

8.2.2 Signal Details at Reference Positions in the two TBMs

The analyses of predicted responses for SPDs involves comparison of the sensitivities and the SPD-currents of both the detectors, between the front-central positions of calculations in HCLL and HCPB TBMs, i.e. A5 and B5. This has been done in Figure 8-2, where the left graph shows sensitivities and the right one shows currents. The sensitivities are compared for unit-size SPDs (active length = 1 cm), expressed in units A cm s, while the SPD-currents are shown in A cm^{-1}. The latter is obtained by multiplying the sensitivities' values with calculated neutron fluxes (at nominal 500 MW operation of ITER) at the respective positions in the TBMs. The total sensitivity is comprised three main processes, (n, β^-), (n, γ, e^-) and (γ, e^-), which are also reported. In presenting the delayed, (n, β^-) signal components, saturation states have been taken for all delayed processes.
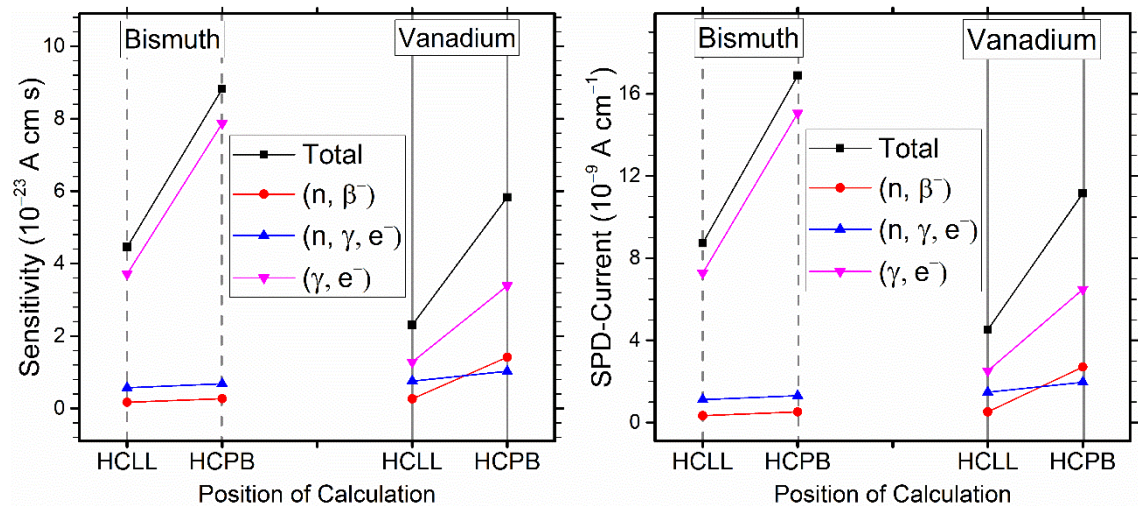
Figure 8-2: Calculated (left) unit sensitivities and (right) unit SPD-Currents w.r.t. 500 MW steady state operation of ITER, for the Bi and V SPDs at the front central positions in the HCLL (A5) and HCPB (B5) TBMs of ITER A-lite model. The three main components of the signal have been also provided.

The total unit sensitivities in the HCLL and HCPB TBMs for Bi-SPD are of the orders of 4.4×10^{-23} A cm s and 8.8×10^{-23} A cm s, respectively. While for the V-SPD, these are 2.3×10^{-23} A cm s and 5.8×10^{-23} A cm s. For 10 cm units of these SPDs, which is a commonly used active length in fission reactors, the net currents in ITER TBMs can range roughly between 30 nA and 170 nA.

For both SPDs, the position in HCPB TBM is relatively more sensitive. It provides approx. 2 times higher magnitude of response than the position in the HCLL TBM for Bi-SPD, and about 2.5 times for V-SPD. The primary reason for this is the presence of a more intense photon field in the HCPB TBM. It turns out, as explained below in detail, the strongest component of signals in both SPDs is from the photons, the (γ, e^-) type response. Given this, as Bi is a photon absorbing material, Bi-SPD is evidently more sensitive than the V-SPD, even though they both have same geometrical properties. The overall sensitivity of Bi-SPD is 1.9 times that of V-SPD in HCLL, and 1.51 times that of

V-SPD is HCPB. Also, as the difference in the total neutron fluxes between the two TBM positions is negligible (< 3%), the SPD-currents (right graph, Figure 8-6) compare in a similar way as the corresponding sensitivities do, between the two positions.

The Bi-SPD is primarily expected to be a photon detector due to its higher Z. This has been observed clearly in all the four analysed cases in Figure 8-2. In HCLL TBM, 83% of the total signal is due to external photons. The same share in HCPB TBM is 89%. Of the very small neutron shares in Bi-SPD signals, around 70% to 75% is prompt, which is natural as the cross-sections for (n, β^-)-type processes in Bi are negligible. It allows to conclude that Bi-SPD is indeed majorly working as an SP<u>G</u>D in the ITER TBMs, with a small prompt-type neutron contribution.

The V-SPD, in contrast to Bi-SPD, has a more mixed signal. The V is a medium Z element and its neutron interaction cross-sections are relatively higher than Bi. But still, like Bi-SPD, a bigger fraction of V-SPD signal is photon-induced. The neutron and photon signal shares are respectively, about 44% and 56% for HCLL, and 42% and 58% for HCPB. In such a situation, a geometrical optimization can provide for enhancement of the neutron shares in V-SPD, giving a reasonable scope of making an SP<u>N</u>D.

In the neutron shares of the V-SPD signals under a saturation state, about 74% of it is prompt neutron signal in HCLL, while it is only 42% prompt in HCPB. The delayed neutron share in HCPB is larger as there are higher fluxes of thermal neutrons in it as compared to HCLL. Thermal and epithermal thermal neutrons have the highest cross-sections for (n, β^-)-type processes. This comparable mixing of delayed and prompt neutron signals in SPD can complicate the signal interpretation.

Regarding the delayed (n, β^-)-type neutron signal components in both detectors, several nuclides (Table 8-2) from capture and threshold reactions in all layers contribute. For the V-SPD, in all cases this is almost solely due to production of ^{52}V in emitter, a thermal neutron reaction. Its extraction from the net signal can be used to find thermal neutron flux, the major contributor to tritium breeding reactions in TBMs. Although the possibility of extracting this signal share in real-life application remains a difficult and error-prone task, this can serve for an indirect way of tritium measurement. More details on the delayed signal components of the two SPDs have been provided in Appendix 6.

Because ITER will not provide continuous neutron or photon fields for the delayed signals to fully saturate, the time-behaviour of the signals becomes interesting to look at. For the two aforementioned typical pulse scenarios of ITER's operation, the time-profiles of the signals for two SPDs in the two TBMs have been shown in Figure 8-3. From these, the Bi-SPD signal can be assumed to be prompt in all situations. Also, the presence of delayed signals is more critical for V-SPD, especially so in the HCPB TBM. With 3.74 min half-life of major beta-emitter ^{52}V, the delayed signal is well saturated by the end of Pulse-2 (almost 13 half-lives), but not with Pulse-1 (around 2 half-lives).
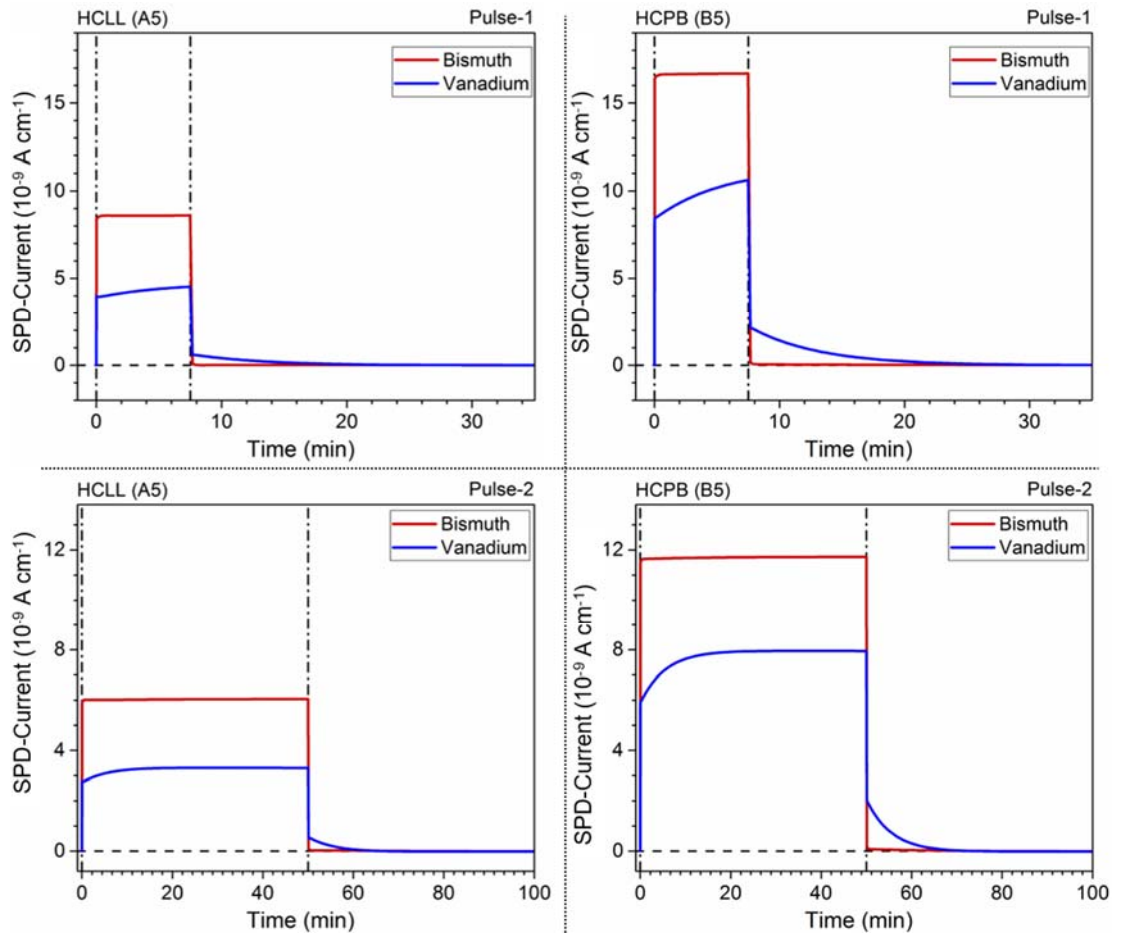
Figure 8-3: Calculated time-dependent signal profiles of the unit Bi- and V-SPDs under (left) HCLL and (right) HCPB TBM radiation conditions, for one flat-top pulse of type (top) pulse-1 and (bottom) pulse-2. The signals show total currents per unit of emitter length. The starting and ending point of the pulses are depicted using dashed black vertical lines, to assist observing the decays of the delayed signal components.

8.3 Adaptability and Modes of Operation of SPDs in ITER TBMs

Starting with the comparison of neutron reaction cross-sections between thermal and fast neutron energy-ranges for the emitter materials in Chapter 3, to the detailed experimental assessment performed in Chapter 5, MCNP model-based evaluation of the tested SPDs in Chapter 6, parametric studies in Chapter 7 and the computational analyses of two representative variants of SPDs under realistic reactor radiation conditions, one can make conclusions on the matter of SPDs' applicability in the ITER TBMs and the future fusion reactors. Comparing with fission reactors, common place for SPD applications, the cross-section of neutron reactions in fusion reactors is low and SPD's response is easily overshadowed by photon-induced effects. Nevertheless, the SPD technology is, in principle, adaptable to ITER TBMs' conditions. Computational analyses show that currents in the range of nA to mA can be expected with minimal time-delay for SPDs. This is a well-transmittable and measurable amplitude of DC signal. And with optimization of design and selection of more sensitive locations, much higher signals can be achieved.

A photon detector (SPGD) with a heavy element like Bi in emitter layer is expected to be highly suitable for photon flux monitoring in TBMs. Experiments have shown quite high amplitudes and stable performances of SPDs with high-energy photon tests, and computations show that the major fractions of signals in both Bi- and V-SPDs are due to photons. Therefore, SPDs for photons can be realized relatively easily.

Neutron detection seems tricky, but it is possible through indirect prompt-type SPNDs. A delayed SPND, originally proposed for TBMs, is expected to have numerous competing reactions. Higher fluxes of thermal neutrons in HCPB TBM means that delayed responses can be enhanced, but it remains to be ascertained how difficult it is to separate them in pulsed operation of the tokamak. In TUD-NG testing of SPDs, delayed signals have been found to be negligible and resolution of their components is rendered impossible. The cylindrical V-SPD also ends up with a mixed neutron-photon response as well as a mixed delayed-prompt neutron responses in the computations under TBM conditions. On the other hand however, optimization of the geometry and dimensions can provide for increasing prompt to delayed ratio, and having prompt SPNDs for the actual application in the TBM. Medium to medium-high weight materials like V, Ag, Inconel-600 are more suited for neutron applications. A commercial cylindrical SPD with V emitter will provide tens to hundreds of nA in total, which can be increased by one or two orders of magnitude on changing to flat geometry.

As an alternative proposal, a photon signal can be utilized as a measure for neutron flux as well, because majority of the photons produced in TBM-like environment result directly from prompt neutron interactions, the cross-sections for which are known with high confidence. The decay photons in pulsed devices like ITER make a smaller fraction. This kind of application needs study of the dependence of the photon signal on the neutron flux, through extensive radiation transport simulations at the detectors' positions and the surroundings in the reactor. A similar conclusion has been made in recent studies conducted with prompt SPNDs for application in fast fission reactors [92, 93]. The signal due to gamma background from fission products is considered as an indirect measure of neutron flux. For such an SPND, it will also be necessary to achieve a good understanding of the flux dependence of other effects, including electronic ones, which contribute to the signals. Finally, a robust method of calibration will need to be established, in which validated computational models for SPDs will be required. While the neutronic performances of detectors have been studied in this thesis, it is important to note that many other critical effects need to be subsequently accounted for, like electromagnetic fields, high temperature, mechanical vibrations, radiation damage (burnup) etc.

9. SUMMARY AND OUTLOOK

9.1 Summary of the Studies on SPD for Fusion Applications

Online monitoring of the neutron and photon fluxes in the fusion reactors will serve for the direct and indirect measurements of its critical operating parameters. The instrumentation for this purpose should provide low measurement uncertainties, and needs to face the harsh fusion environment with high fluxes of energetic particles, intense electromagnetic fields and high temperatures. This thesis presents a nuclear performance study for the self-powered detectors (SPD) for monitoring the neutron and photon fields in fusion reactors, specifically in the test blanket modules (TBM) of ITER.

An SPD is an electrical device having two electrode layers insulated by a layer of ceramic. Nuclear processes initiated by the incident particles lead to separation of charges between its central electrode, emitter, and the outer electrode, collector. This produces a DC signal varying linearly with the incident fluxes. By the right choice of layer materials and geometry, this detector-type can be optimized to perform either neutron detection (delayed or prompt SPND) or photon detection (SPGD).

The aim of the thesis is to verify the adaptability of SPDs to a fusion environment and elaborate upon the challenges in the construction, application and the signal-analyses for this detector-type. The commercial SPDs are tailored to the needs of fission reactors, with elongated cylindrical geometry and layer materials specially chosen for thermal neutron energies. An openable flat sandwich-like SPD design, providing higher signals at laboratory-based sources and allowing testing of multiple material combinations has been conceptualized and developed in this work. Several emitter materials, V, Be, Ag and Cr, and also collector materials, Inconel-600, Nb and graphite, in various combinations have been experimentally analysed. In the absence of a consistent fusion reactor-like irradiation source, the detectors have been tested with a thermal neutron source, a 14 MeV D-T neutron source and a high-energy bremsstrahlung photon source. The tested SPDs have been concluded to show strong linearity with the incident fluxes as essential for a flux monitor.

A proof-of-principle of the flat SPD design has been achieved through comparison with a standard off-the-shelf cylindrical SPD under thermal neutron field. The test SPDs in flat and cylindrical geometries both have V emitters, a common choice for fission reactor and a candidate for fusion reactor SPNDs. The flat design has been found to produce a signal with a portfolio expected from a delayed SPND. Delayed signal is mainly due to ^{52}V beta-emissions in the emitter. Substantial improvement has been observed in the signal strength on geometry-change. Thermal neutron sensitivities for these SPDs are in the orders of 10^{-20} A cm^2 s. Both SPDs exhibited majorly prompt signals with 14 MeV neutrons and high-energy photons. The less than 10% delayed components in fast neutron tests can be attributed to the small quantities of betas and photons from the activated SPD and the test setup. For the 14 MeV neutrons and high-energy photons, the cylindrical SPD has very low sensitivities. Whereas, for flat SPD, it is of the order of 10^{-20} A cm^2 s.

In a reference assessment, the photon sensitivity of the SPD has been found slightly higher than the neutron sensitivity in the fusion-relevant mixed neutron-photon field. While this indicates the feasibility of an effective SPGD in TBMs, a neutron-photon discrimination with the detector alone is challenging. The energy spectrum of neutrons in a reactor is much wider than the one in the 14 MeV neutron test setup, suggesting a reasonable scope for the increase of SPD's neutron sensitivity. There are slower neutrons producing capture reactions, as well as intermediate energy neutrons having high probabilities of photon production which can lead to prompt neutron signal. The currents produced in fast neutron field due to the prompt routes have been proven to dominate the signals, and hence, it can only be applied as prompt SPND. The use of delayed processes is realized to be inefficient because the signal due to a threshold reaction has to be subtracted from the major prompt component, which is both difficult and error-prone. The delayed SPND with emitters of Be and Cr for fusion represent even poorer choices.

A generic property of the SPDs is that the geometric design and material choices can affect the signal magnitude and the neutron-to-photon sensitivity ratio. So, with careful optimization of the design, a prompt SPND can be realized. In the experiments, Ag and V emitters with Inconel-600 collector have shown the best performance while symmetrical emitter-collector combination with Inconel-600 is an alternative choice. A high-Z emitter like Bi should be considered for SPGDs. The thickness of the collector should be low, as it has a big negative impact on the signal. The thickness of emitter needs optimization; thicker emitters yield higher prompt signal amplitudes but a reduction of signal is seen with increasing thickness after a certain value. As the photon flux in a fusion reactor varies linearly with the neutron flux, a photon signal can also be utilized for an *indirect* SPND, for which a robust calibration methodology needs to be formulized.

To complement the detector development and tests, a computational method using a sequence of coupled Monte-Carlo particle transport simulations has been developed for calculation of the SPD sensitivities. The polarities and the orders of magnitude of the simulated sensitivities have compared well with the corresponding measurements, especially for the cylindrical SPDs. For flat detectors, and in fast neutron and photon fields, the calculated results have been 50 to 100 times lower than the experiments, pointing at a deficiency in the model which calls for deeper theoretical scrutiny. Considering the complexity of the current formation in an SPD (especially for

fields providing low sensitivities), the difficulty in comparison with the experiments, large systematic uncertainties, the limited capacity of the Monte-Carlo techniques for describing all small-scale physical events etc., the model is deemed to be reasonably good for studies, albeit some care is needed in analysing the flat SPD designs. It has been implemented for a demonstrative analysis of the integration of commercial cylindrical SPDs in the European ITER TBM. Locations close to the front plates of the TBMs have been chosen and the electrical signals and their time-profiles under typical ITER pulses have been predicted for two main cylindrical SPDs with V and Bi emitters. Signals, with the state-of-the-art SPDs in the TBMs are shown to range from nA to mA, which can be reliably measured in tokamaks, and also enhanced further with optimized SPD geometry.

It is ultimately concluded from this thesis that with right geometry and materials, the SPDs can be utilized as photon as well as (prompt) neutron flux monitors in the TBMs of ITER, and future fusion reactors.

9.2 Recommendations for Future Developments of SPDs

On the basis of the new information obtained in this work, SPDs are deemed reasonable choices to monitor neutron and photon fluxes in a fusion reactor. This allows to propose further designing and testing of prototype SPDs. Because the computational model developed here performs well with the cylindrical detectors, and preliminary simulations have shown promising outputs with this geometry per se, the starting point can be extensive parametric analyses through Monte-Carlo modeling to establish best thicknesses of materials layers and best material combinations for both neutron and photon measurements. Several elements and alloys should be checked for emitters and collectors. Medium Z for SPNDs to have low photon effects while enhanced performance compared to smaller Z materials, and high Z for SPGDs are basic guidelines to reduce the parameter space. More compact SPDs, for example in a coaxial chip-like geometry can be reliably studied through the model also, provided that the test detector is constructed in the same way as the traditional ones. Deeper theoretical investigations and application of Monte-Carlo codes capable of directly simulating electrodymanic effects are recomennded for the improvement of the modelling methodology, so as to have it as a strong tool for further development and calibration of SPD.

Prototype SPDs should be designed and professionally constructed with pure materials and under inert conditions. For a prototypical TBM SPD, it will be important to avoid openable and flexible designs as they lead to unstable parasitic effects. It is required to invent efficient techniques of electrical contact between the emitter and the signal cable. The extra fixtures and elements need to be eliminated, as the detector has an extended behavior, and each new kind of material introduces new signal component, small or big, which depends on its nuclear and electrical properties. It should be completely packaged, preferably with collector encapsulating the emitter in a compact and rugged design. For the irradiation tests, it is recommended to employ well-characterized experiments setups. Time and resources should be dedicated to achieve high quality alternative flux measurements, precise estimation of source-detector distances and detailed (validated) Monte-Carlo modelling of the setup.

REFERENCES

[1] P.J. Gertler et al, *The Demand for Energy-Using Assets among the World's Rising Middle Classes*, American Economic Review. 106 (2016) 1366–1401. DOI:10.1257/aer.20131455

[2] M.M. Abu-khader, *Recent advances in nuclear power : A review*, Progress in Nuclear Energy. 51 (2009) 225–235. DOI:10.1016/j.pnucene.2008.05.001

[3] H.A. Bethe, *Energy Production in Stars*, Physical Review. 55 (1939) 434. DOI:10.1103/PhysRev.55.434

[4] S. Nakai, H. Takabe, *Principles of inertial confinement fusion—physics of implosion and the concept of inertial fusion energy*, Reports on Progress of Physics. 59 (1996) 1071–1131. DOI:10.1088/0034-4885/59/9/002

[5] **(Book)** W.M. Stacey, *Fusion: An introduction to the physics and technology of magnetic confinement fusion*, Second Edition, Wiley-VCH Verlag GmbH & Co. KGaA, Weinheim (2010). ISBN: 9783527629312, DOI:10.1002/9783527629312

[6] **(Book)** P.K. Kaw et al, *The Case for Fusion*, in: M. Kikuchi et al, *Fusion Physics*, IAEA Publications-International Atomic Energy Agency (IAEA), Vienna (2012). ISBN:978-92-0-130410-0

[7] **(Book)** J. Wesson, D.J. Campbell, *Tokamaks*, Fourth Edition, Oxford University Press, Oxford (2011). ISBN:9780199592234

[8] **(Webpage)** *ITER Organization: Homepage*, (2018). https://www.iter.org/ (accessed April 14, 2018).

[9] A.M. Bradshaw et al, *Is nuclear fusion a sustainable energy form?*, Fusion Engineering and Design. 86 (2011) 2770–2773. DOI:10.1016/j.fusengdes.2010.11.040

[10] T. Ihli et al, *Review of blanket designs for advanced fusion reactors*, Fusion Engineering and Design. 83 (2008) 912–919. DOI:10.1016/j.fusengdes.2008.07.039

[11] F. Romanelli et al, *A roadmap to the realization of fusion energy*, EFDA Publications- European Fusion Development Agreement (EFDA), Munich (2012). Available online at: https://tinyurl.com/y6koc72z (accessed July 26, 2019).

[12] V.A. Chuyanov et al, *TBM Program implementation in ITER*, Fusion Engineering and Design. 85 (2010) 2005–2011. DOI:10.1016/j.fusengdes.2010.07.005

[13] **(Webpage)** *Fusion For Energy - Bringing the power of the sun to earth*, (2017). http://fusionforenergy.europa.eu/ (accessed October 12, 2017).

[14] F. Hernández et al, *Thermo-mechanical analyses and assessment with respect to the design codes and standards of the HCPB-TBM Breeder Unit*, Fusion Engineering and Design. 87 (2012) 1111–1117. DOI:10.1016/j.fusengdes.2012.02.088

[15] U. Fischer et al, *Comparison of nuclear irradiation parameters of fusion breeder materials in high flux fission test reactors and a fusion power*

demonstration reactor, Journal of Nuclear Materials. 280 (2) (2000) 151-161.
DOI:10.1016/S0022-3115(00)00049-0

[16] P. Calderoni, *Status of the HCLL and HCPB Test Blanket System instrumentation development*, 21st Topical Meeting on the Technology of Fusion Energy (TOFE) (2014), Anaheim, USA. Available online at:
https://tinyurl.com/y69kygod (accessed July 26, 2019).

[17] D. Leichtle et al, *The F4E programme on nuclear data validation and nuclear instrumentation techniques for TBM in ITER*, Fusion Engineering and Design. 89 (2014) 2169–2173. DOI:10.1016/j.fusengdes.2014.02.056

[18] **(Book)** G.F. Knoll, *Radiation Detection and Measurement,* Fourth Edition, John Wiley & Sons, Inc., New York (2010). ISBN:9780470131480

[19] M. Angelone et al, *Development of self-powered neutron detectors for neutron flux monitoring in HCLL and HCPB ITER-TBM*, Fusion Engineering and Design. 89 (2014) 2194–2198. DOI:10.1016/j.fusengdes.2014.01.077

[20] P. Raj et al, *Self-powered detectors for test blanket modules in ITER*, Conference Record of 2016 IEEE Nuclear Science Symposium, Medical Imaging Conference and Room-Temperature Semiconductor Detector Workshop (IEEE NSS/MIC) (2017), Strasbourg, France. DOI:10.1109/NSSMIC.2016.8069908

[21] P. Raj, A. Klix, *Irradiation Tests of a Flat Vanadium Self-Powered Detector with 14 MeV Neutrons*, Proceedings of 48. Jahrestagung Kerntechnik / 48th Annual Meeting on Nuclear Technology (AMNT) (2017), Berlin. Invited reprint in Atw. Internationale Zeitschrift fuer Kernenergie. 63 (4) (2018) 246–249. ISSN:14315254

[22] P. Raj et al, *Experimental Assessment of a Flat Sandwich-like Self-Powered Detector for Nuclear Measurements in ITER Test Blanket Modules*, IEEE Transactions on Nuclear Science. 65 (2018) 2385–2391. DOI:10.1109/TNS.2018.2844554

[23] P. Raj et al, *Computational study of a chromium self-powered detector for neutron flux monitoring in the test blanket module of ITER*, Nuclear Instruments and Methods in Physics Research, Section A: Accelerators, Spectrometers, Detectors and Associated Equipment. 908 (2018) 10–17. DOI:10.1016/j.nima.2018.08.020

[24] M. Angelone et al, *Performance test of radiation detectors developed for ITER-TBM*, Fusion Engineering and Design. 136 B (2018) 1386–1390. DOI:10.1016/J.FUSENGDES.2018.05.018

[25] J.B. Kramer, *A New Electronic Battery*, The Electrician. 93 (1924) 497.

[26] M.G. Mitel'man et al, *Transformation of the Energy of Short-lived Radioactive Isotopes*, Atomnaya Energiya. 10.1 (1961) 70–71. DOI:10.1007/BF01483413

[27] J.W. Hilborn, *Self-Powered Neutron Detectors for Reactor Flux Monitoring*, Nucleonics. 22 (1964) 69–74.

REFERENCES

[28]   N.P. Goldstein, W.H. Todt, *A Survey of Self-Powered Detector - Present and Future*, IEEE Transactions on Nuclear Science. 26 (1979) 916–923. DOI:10.1109/TNS.1979.4329746

[29]   R.B. Shields, *Self-Powered Flux Detectors: A Bibliography with Summaries*, (1983). Available online at: https://tinyurl.com/yytctnmt (accessed July 26, 2019).

[30]   G. Ramirez, L. David, *A Study of Self-Powered Detectors for Mixed Neutron-Gamma Fields*, Nuclear Instruments and Methods 85 (1970) 279–283. DOI:10.1016/0029-554X(70)90249-1

[31]   M.A. Lone et al, *Sensitivity of self-powered detector probes to electron and gamma-ray fields*, Nuclear Instruments and Methods in Physics Research, Section A: Accelerators, Spectrometers, Detectors and Associated Equipment. 349 (1994) 563–576. DOI:10.1016/0168-9002(94)91228-9

[32]   M. Alex, M.D. Ghodgaonkar, *Development of an inconel self powered neutron detector for in-core reactor monitoring*, Nuclear Instruments and Methods in Physics Research, Section A: Accelerators, Spectrometers, Detectors and Associated Equipment. 574 (2007) 127–132. DOI:10.1016/j.nima.2007.01.084

[33]   M. Alex et al, *Development of bismuth self-powered detector*, Nuclear Instruments and Methods in Physics Research, Section A: Accelerators, Spectrometers, Detectors and Associated Equipment. 523 (2004) 163–166. DOI:10.1016/j.nima.2003.12.030

[34]   L. Vermeeren et al, *Irradiation tests of prototype self-powered gamma and neutron detectors*, Proceedings of International Conference on Advancements in Nuclear Instrumentation, Measurement Methods and their Applications (ANIMMA) (2011), Ghent, Belgium. DOI:10.1109/ANIMMA.2011.6172889

[35]   A.K. Mahant et al, *A theoretical study of a nickel SPND using Warren's model*, Nuclear Instruments and Methods in Physics Research, Section A: Accelerators, Spectrometers, Detectors and Associated Equipment. 406 (1998) 117–126. DOI:10.1016/S0168-9002(97)01214-X

[36]   M.E. Miller et al, *Implantable self-powered detector for on-line determination of neutron flux in patients during NCT treatment*, Applied Radiation and Isotopes. 61 (2004) 1033–1037. DOI:10.1016/j.apradiso.2004.05.041

[37]   M. Grin, *Collectrons, Self-Powered Neutron Flux Detectors- Part I: Theoretical Considerations*, EUR 4775 e, Joint Nuclear Research Centre, Ispra, Italy. (1972). Available online at: https://tinyurl.com/y4exwmhw (accessed July 26, 2019).

[38]   **(Book)** *Low Level Measurements Handbook: Precision DC Current, Voltage, and Resistance Measurements*, Seventh Edition, Tektronix (2016). Available online at: https://tinyurl.com/y58jrxp5 (accessed July 26, 2019).

[39]   G.F. Lynch, *Some Theoretical Aspects of Self-Powered Detectors,* Proceedings of the Specialists' Meeting on In-core Instrumentation and Failed Fuel Detection and Location (1974), Mississauga, Canada. Paper no. 1.8, AECL-5124 (1975) 97–110. Available online at: https://tinyurl.com/y2xrv23o (accessed July 26, 2019).

[40] R. Van Nieuwenhove, *Effect of fission betas, activated structures and hydrogen on self powered neutron detectors*, IEEE Transactions on Nuclear Science. 61 (2014) 2006–2010. DOI:10.1109/TNS.2014.2304563

[41] C.J. Allan, G.F. Lynch, *Radiation Induced Currents in Mineral Insulated Cables,* IEEE Transactions on Nuclear Science. NS-27 (1980) 764–768. DOI:10.1109/TNS.1980.4330924

[42] R. Van Nieuwenhove, L. Vermeeren, *Experimental study of radiation induced electromotive force effects on mineral insulated cables*, Review of Scientific Instruments. 74 (2003) 4675–4682. DOI:10.1063/1.1622977

[43] R. Van Nieuwenhove, *Improved cable compensation technique for self powered neutron detectors*, Nuclear Instruments and Methods in Physics Research, Section A: Accelerators, Spectrometers, Detectors and Associated Equipment. 373 (1996) 202–205. DOI:10.1016/0168-9002(95)01440-3

[44] S.O. Yusuf, D.K. Wehe, *Analog and Digital Dynamic Compensation Techniques for Delayed Self-Powered Neutron Detectors*, Nuclear Science and Engineering. 106 (1990) 399–408. DOI:10.13182/NSE90-A23765

[45] **(Webpage)** *JANIS 4.0 - OECD Nuclear Energy Agency*, (2017). https://www.oecd-nea.org/janis/ (accessed August 9, 2017).

[46] **(Webpage)** OECD Nuclear Energy Agency: JEFF and EFF Projects, (2017). http://www.oecd-nea.org/dbforms/data/eva/evatapes/jeff_32/ (accessed July 29, 2017).

[47] **(User Manual)** R.A. Forrest, *FISPACT-2007 : User manual*, UKAEA FUS 534. (2007). Available online at: https://tinyurl.com/y65we85j (accessed July 26, 2019).

[48] Materion Brush Inc., *Material Safety Data Sheet- No. M10 Beryllium Solid*, (2017). Available online at: https://tinyurl.com/y4nt8ve4 (accessed July 26, 2019).

[49] J.W. Upton et al, *In-Core, Self-Powered Fast Neutron Flux Monitors*, American Nuclear Society Power Depletion Topical Meeting, (1970), Williamsburg, USA. Available online at: https://tinyurl.com/y4dyzz5u (accessed July 26, 2019).

[50] **(Patent)** I.L. Mcintyre, C.J. Allan, *Self-powered neutron flux detector assembly*, Canadian patent no. CA1084176A (1980).

[51] **(Book)** W.R. Leo, *Techniques For Nuclear And Particle Physics Experiments: A How-To Approach,* Second Edition, Springer-Verlag Berlin Heidelberg GmbH, (1994). ISBN: 9783540572800

[52] K. Noda et al, *Electrical resistivity of ceramic insulators under irradiation using 14 Me V neutrons*, Journal of Nuclear Materials. 233–237 (2) (1996) 1289–1293. DOI:10.1016/S0022-3115(96)00251-6

[53] F.E. Levert et al, *Analysis of Self-Powered Gamma Ray Detector with Directional Discrimination*, Nuclear Instruments and Methods. 160 (1979) 61–72. DOI:10.1016/0029-554X(79)90166-6

REFERENCES

[54]   **(Webpage)** *Belden 9222 Triax- 50 Ohm Triax*, (2017). http://www.belden.com/techdatas/english/9222.pdf (accessed Aug 22, 2017).

[55]   **(Webpage)** *PTW Detector Extension Cable- T26059-20 - BNC Low-Noise Extension Cable*, (2017). https://tinyurl.com/yc5fjm4k (accessed Dec 15 2018)

[56]   **(Webpage)** *Thermocoax: signals transmission*, (2017). https://www.thermocoax.com/signals-transmission/ (accessed October 15, 2017)

[57]   **(User Manual)** *Model 6485 Picoammeter Instruction Manual*, Keithley Series 6400 Picoammeteres, Part Number: 6485-901-01A, (2015). Available online at: https://download.tek.com/manual/6485-901-01(A-Nov2001)(Instruction).pdf (accessed July 26, 2019).

[58]   **(Webpage)** *National Instruments: A Global Leader in Automated Test and Automated Measurement Systems*, (2017). http://www.ni.com/en-us.html (accessed August 3, 2017).

[59]   K. Eberhardt et al, *The research reactor TRIGA Mainz- A neutron source for versatile applications in research and education*, Kerntechnik. 65 (5) (2000) 269–274.

[60]   A. Klix et al, *The intensive DT neutron generator of TU Dresden*, EPJ Web of Conferences. 170 (2018) 02004. DOI:10.1051/epjconf/201817002004

[61]   R. Schwengner et al, *The photon-scattering facility at the superconducting electron accelerator ELBE*, Nuclear Instruments and Methods in Physics Research, Section A: Accelerators, Spectrometers, Detectors and Associated Equipment. 555 (2005) 211–219. DOI:10.1016/j.nima.2005.09.024

[62]   M. Blaickner et al, *Dosimetric feasibility study for an extracorporeal BNCT application on liver metastases at the TRIGA Mainz*, Applied Radiation and Isotopes. 70 (2012) 139–143. DOI:10.1016/j.apradiso.2011.08.008

[63]   **(Doctoral Thesis)** B. Wortmann, *Auslegung und Optimierung einer Bestrahlungseinrichtung fuer die Bor-Neutroneneinfangtherapie an autotransplantierten Organen*, Mechanical Engineering Faculty, Technical University of Dresden, (2008). Available online at: http://nbn-resolving.de/urn:nbn:de:bsz:14-qucosa-231889 (accessed July 26, 2019).

[64]   **(Doctoral Thesis)** D. Szalkai, *Experimental investigations for development of an innovative SiC sensor for spectrometry of neutrons under harsh environmental conditions*, Department of Mechanical Engineering, Karlsruhe Institute of Technology (KIT), (2018). (Thesis in press)

[65]   F. Gabriel et al, *The Rossendorf radiation source ELBE and its FEL projects*, Nuclear Instruments and Methods in Physics Research Section B: Beam Interactions with Materials and Atoms. 161–163 (2000) 1143–1147. DOI:10.1016/S0168-583X(99)00909-X

[66]   **(Doctoral Thesis)** G. Rusev, *Dipole-strength distributions below the giant dipole resonance*, Faculty of Physics, Technical University of Dresden, 2006.

[67]   A. Ferrari et al, *FLUKA: A Multi-Particle Transport Code*, CERN, (2005). Available online at: https://tinyurl.com/yxqlegrh (accessed July 26, 2019).

[68]   C. Nair et al, *Photoactivation experiment on Au 197 and its implications for the dipole strength in heavy nuclei*, Physical Review C. 78 (2008) 055802. DOI:10.1103/PhysRevC.78.055802

[69]   L.I. Schiff, *Energy-Angle Distribution of Thin Target Bremsstrahlung*, Physical Review. 83 (1951) 252–253. DOI:10.1103/PhysRev.83.252

[70]   V. Radulović et al, *Multi-step Monte Carlo calculations applied to nuclear reactor instrumentation - Source definition and renormalization to physical values*, Proceedings of International Conference on Advancements in Nuclear Instrumentation Measurement Methods and their Applications (ANIMMA) (2015), Lisbon, Portugal. DOI:10.1109/ANIMMA.2015.7465522

[71]   H.D. Warren, *Calculational model for self-powered neutron detector*, Nuclear Science and Engineering. 48 (1972) 331–42. DOI:10.13182/NSE72-A22491

[72]   W. Jaschik, W. Seifritz, *Model for Calculating Prompt-Response Self-Powered Neutron Detectors*, Nuclear Science and Engineering. 53 (1974) 61–78. DOI:10.13182/NSE74-A23330

[73]   N.P. Goldstein, *A Monte-Carlo Calculation of the Neutron Sensitivity of Self-Powered Detectors*, IEEE Transactions on Nuclear Science. 20 (1973) 549–556. DOI:10.1109/TNS.1973.4326961

[74]   L. Vermeeren, *Neutron and gamma sensitivities of self-powered detectors: Monte Carlo modelling,* Proceedings of International Conference on Advancements in Nuclear Instrumentation Measurement Methods and their Applications (ANIMMA) (2015), Lisbon, Portugal. DOI:10.1109/ANIMMA.2015.7465531

[75]   W. Lee et al, *A study on the sensitivity of self-powered neutron detectors (SPNDs)*, IEEE Transactions on Nuclear Science. 48 (2001) 1587–1591. DOI:10.1109/23.958400

[76]   L. Vermeeren et al, *Radiation induced currents in mineral- insulated cables and in pick-up coils : model calculations and experimental verification in the BR1 reactor*, EPJ Web of Conferences. 170 (2018). DOI:10.1051/epjconf/201817002008

[77]   L. Vermeeren, R. Van Nieuwenhove, *Theoretical study of radiation induced electromotive force effects on mineral insulated cables*, Review of Scientific Instruments. 74 (2003) 4667–4674. DOI:10.1063/1.1622977

[78]   F.B. Brown, *Fundamentals of Monte Carlo particle transport*, Los Alamos National Laboratory, (2005). Available online at: https://tinyurl.com/yazopq8z (accessed July 26, 2019).

[79]   **(Webpage)** *A General Monte Carlo N-Particle (MCNP) Transport Code*, (2017). https://mcnp.lanl.gov/ (accessed July 29, 2017).

[80]   **(Webpage)** *Geant4 Home*, (2017). http://geant4.cern.ch/ (accessed Jan 1, 2017).

[81]   **(User Manual)** J.K. Shultis, R.E. Faw, *An MCNP primer*, (2017). Available online at: https://www.mne.k-state.edu/~jks/MCNPprmr.pdf (accessed July 26, 2019).

[82]   N. Otuka et al, *Towards a More Complete and Accurate Experimental Nuclear Reaction Data Library (EXFOR): International Collaboration Between Nuclear Reaction Data Centres (NRDC)*, Nuclear Data Sheets. 120 (2014) 272–276. DOI:10.1016/j.nds.2014.07.065

[83]   M.B. Chadwick et al, *ENDF/B-VII.1 nuclear data for science and technology: Cross sections, covariances, fission product yields and decay data*, Nuclear Data Sheets. 112 (2011) 2887–2996. DOI:10.1016/j.nds.2011.11.002

[84]   **(Webpage)** *FENDL-3.1b: Fusion Evaluated Nuclear Data Library Ver.3.1b,* (2017). https://www-nds.iaea.org/fendl/ (accessed Jul 29, 2017).

[85]   **(Webpage)** *KAERI Nuclear Data Validation Group*, South Korea, (2017). http://atom.kaeri.re.kr/NDVG/ (accessed Jul 29, 2017).

[86]   D.P. Mcallindon, *Comparison of Measured and Predicted Sensitivities of In-Core Flux Detectors*, Chalk River Laboratories Report. (1996). Available online at: https://tinyurl.com/yy42crya (accessed July 26, 2019).

[87]   J. Kohpazi et al, *Measuring Delayed Part of the Current of a Self Powered Neutron Detector and Comparison With Calculations*, Proceedings of International Conference on Nuclear Energy in Central Europe (2001) 1–8, Portoroz, Slovenia. Available online at: http://www.djs.si/proc/port2001/pdf/603.pdf (accessed July 26, 2019).

[88]   A.R. Frederickson, *Charge Deposition, Photoconduction, and Replacement Current in Irradiated Multilayer Structures*, IEEE Transactions on Nuclear Science. NS-22 (1975) 2556–2561. DOI:10.1109/TNS.1975.4328167

[89]   M.J. Loughlin et al, *ITER Nuclear Analysis Strategy and Requirements*, Fusion Science and Technology. 56 (2009) 566–572. DOI:10.13182/FST56-566

[90]   P. Pereslavtsev et al, *Neutronic analysis of the HCPB TBM in ITER utilizing an advanced integral approach*, Fusion Engineering and Design. 85 (2010) 1653–1658. DOI:10.1016/j.fusengdes.2010.05.008

[91]   A.C.C. Sips et al, *Progress in preparing scenarios for operation of the International Thermonuclear Experimental Reactor*, Physics of Plasmas. 22 (2015). DOI:10.1063/1.4904015

[92]   V. Verma et al, *Self powered neutron detectors as in-core detectors for Sodium-cooled Fast Reactors*, Nuclear Instruments and Methods in Physics Research, Section A: Accelerators, Spectrometers, Detectors and Associated Equipment. 860 (2017) 6–12. DOI:10.1016/j.nima.2017.04.011

[93]   L. Lepore, R. Remetti, *Application of Prompt Self-Powered Neutron Detectors to the Lead-Cooled Fast Reactor Demonstrator ALFRED: Validation of the Monte Carlo Model for Selected SPNDs*, Journal of Nuclear Engineering and Radiation Science. 3 (2017) 041018. DOI:10.1115/1.4037262

APPENDIX 1 : List of Emitter Materials for Fast Neutrons SPDs

Target	Product from (n,γ) reaction					Product from (n,p) reaction					Product from (n,α) reaction					Product from (n,2n) reaction				
	Product	$T_{1/2}$ (s)	E_β (MeV)	σ_{14MeV} (b)	σ_{HCPB} (b)	Product	$T_{1/2}$ (s)	E_β (MeV)	σ_{14MeV} (b)	σ_{HCPB} (b)	Product	$T_{1/2}$ (s)	E_β (MeV)	σ_{14MeV} (b)	σ_{HCPB} (b)	Product	$T_{1/2}$ (s)	E_β (MeV)	σ_{14MeV} (b)	σ_{HCPB} (b)
^{9}Be	^{10}Be	4.73E+13	0.20	9.10E-07	2.18E-05	^{9}Li	1.78E-01	4.82	2.78E-04	9.05E-07	^{6}He	8.07E-01	1.57	8.99E-03	8.45E-03	^{8}Be	x	x	x	x
^{23}Na	$^{24g/m/n}$Na	5.40E+04	0.56	(g) 2.50E-04 (m) 8.26E-05	(g) 1.04E-03 (m) 2.46E-03	^{23}Ne	3.72E+01	1.89	3.74E-02	8.20E-03	^{20}F	1.11E+01	2.48	1.50E-01	2.19E-02	^{22}Na	x	x	x	x
^{27}Al	^{28}Al	1.35E+02	1.24	6.00E-04	2.39E-03	^{27}Mg	9.46E+00	0.70	6.51E-02	1.26E-02	$^{24g/m/n}$Na	5.40E+04	0.55	(g) 7.54E-02 (m) 3.39E-02	(g) 1.22E-02 (m) 5.47E-03	^{26}Al	x	x	x	x
^{51}V	^{52}V	2.25E+02	1.06	6.01E-04	3.16E-02	^{51}Ti	3.46E+02	0.87	2.94E-02	4.55E-03	^{48}Sc	1.57E+05	0.22	1.75E-02	1.94E-03	^{50}V	x	x	x	x
^{52}Cr	^{53}Cr	x	x	x	x	^{52}V	2.25E+02	1.06	7.38E-02	1.14E-02	^{49}Ti	x	x	x	x	^{51}Cr	x	x	x	x
^{55}Mn	^{56}Mn	9.28E+03	0.80	6.54E-04	1.54E-01	^{55}Cr	2.10E+02	1.10	3.41E-02	5.50E-03	^{52}V	2.25E+02	1.07	2.38E-02	2.99E-03	^{54}Mn	x	x	x	x
^{56}Fe	^{57}Fe	x	x	x	x	^{56}Mn	9.28E+03	0.79	1.03E-01	1.65E-02	^{53}Cr	x	x	x	x	^{55}Fe	x	x	x	x
^{63}Cu	^{64}Cu	4.57E+04	0.19	2.61E-03	1.12E-01	^{63}Ni	3.19E+09	0.02	5.27E-03	1.51E-02	$^{60g/m}$Co	1.66E+08	0.10	(g) 3.30E-02 (m) 1.01E-02	(g) 5.23E-03 (m) 1.75E-03	^{62}Cu	x	x	x	x
^{65}Cu	^{66}Cu	3.07E+02	1.07	4.56E-04	4.74E-02	^{65}Ni	9.06E+03	0.59	2.23E-02	3.23E-03	$^{62g/m}$Co	9.24E+01	1.54	(g) 6.45E-03 (m) 7.65E-03	(g) 7.42E-04 (m) 8.80E-04	^{64}Cu	4.57E+04	0.19	9.76E-01	1.10E-01

$T_{1/2}$: half-life, E_β: mean energy of beta particles, σ: effective cross-section.

Target	(n,γ) Product	(n,γ) T₁/₂ (s)	(n,γ) Eβ (MeV)	(n,γ) σ₁₄MeV (b)	(n,γ) σHCPB (b)	(n,p) Product	(n,p) T₁/₂ (s)	(n,p) Eβ (MeV)	(n,p) σ₁₄MeV (b)	(n,p) σHCPB (b)	(n,α) Product	(n,α) T₁/₂ (s)	(n,α) Eβ (MeV)	(n,α) σ₁₄MeV (b)	(n,α) σHCPB (b)	(n,2n) Product	(n,2n) T₁/₂ (s)	(n,2n) Eβ (MeV)	(n,2n) σ₁₄MeV (b)	(n,2n) σHCPB (b)
^{64}Zn	^{65}Zn	x	x	x	x	^{64}Cu	4.57E+04	0.19	1.44E-01	3.71E-02	^{61}Ni	x	x	x	x	^{63}Zn	x	x	x	x
^{66}Zn	^{67}Zn	x	x	x	x	^{66}Cu	3.07E+02	1.07	7.21E-02	1.11E-02	^{63}Ni	3.15E+09	0.02	2.94E-02	5.39E-03	^{65}Zn	x	x	x	x
^{68}Zn	$^{69g/m}$Zn	3.38E+03	0.32	(g) 2.81E-04 (m) 4.16E-04	(g) 6.09E-03 (m) 5.59E-03	$^{68g/m}$Cu	3.09E+01	1.20	(g) 9.24E-03 (m) 6.43E-03	1.11E-03	^{65}Ni	9.06E+03	0.59	1.22E-02	1.59E-03	^{67}Zn	x	x	x	x
^{103}Rh	$^{104g/m}$Rh	4.23E+01	0.98	(g) 4.11E-04 (m) 4.41E-04	(g) 1.831 (m) 1.52e-1	^{103}Ru	3.39E+06	0.59	2.21E-02	2.86E-03	^{100}Tc	1.55E+01	1.26	1.01E-02	1.00E-03	$^{102g/m}$Rh	x	x	x	x
^{107}Ag	$^{108g/m}$Ag	1.43E+02	0.60	(g) 5.42E-04 (m) 3.32E-04	(g) 1.133 (m) 1.31E-02	^{107m}Pd	x	x	x	x	$^{104g/m}$Rh	4.23E+01	0.98	(g) 5.93E-03 (m) 6.83E-03	(g) 6.65E-04 (m) 6.59E-04	$^{106g/m}$Ag	x	x	x	x
^{109}Ag	$^{110g/m}$Ag	2.46E+01	1.14	(g) 5.46E-04 (m) 3.35E-04	(g) 3.175 (m) 1.54E-01	$^{109g/m}$Pd	4.93E+04	0.36	(g) 1.24E-02 (m) 6.12E-03	(g) 1.53E-03 (m) 6.39E-04	^{106m}Rh	3.01E+01	1.28	3.58E-03	3.02E-04	$^{108g/m}$Ag	1.43E+02	0.59	(g) 7.43E-02 (m) 7.19E-01	(g) 9.97E-02 (m) 8.42E-02
^{115}In	$^{116g/m/n}$In	1.41E+01	1.36	(g) 2.00E-04 (m) 5.39E-04	(g) 7.89E-01 (m) 1.431 (n) 1.534	$^{115g/m}$Cd	1.92E+05	0.31	(g) 5.38E-03 (m) 5.67E-03	(g) 5.73E-04 (m) 6.03E-04	^{112}Ag	1.13E+04	1.20	3.12E-03	2.40E-04	$^{114g/m/n}$In	7.19E-01	0.77	(g) 2.70E-01 (m) 1.33	(g) 1.65E-01 (m) 3.36E-02
^{28}Si	^{29}Si	x	x	x	x	^{28}Al	1.35E+02	1.24	2.28E-01	4.19E-02	^{25}Mg	x	x	x	x	^{27}Si	x	x	x	x

$T_{1/2}$: half-life, $E_β$: mean energy of beta particles, $σ$: effective cross-section.

APPENDIX 2: Details of Various Test SPDs in Flat Geometry

Table A2-1: Exhaustive list of all the utilized flat SPDs in the thesis, with the chapter number (*Ch.*) where they have been used, the edition (*Ed.*) of the flat sandwich-type SPD design, and materials and dimensions of the layers. The dimensions (in mm) are as length × breadth × thickness of the layer (foil). Some short forms are used for materials: InC stands for Inconel-600 and Graph. for graphite (^{NAT}C).

Ch.	Name	Ed.	Emitter	Insulator	Collector
5 & 6	FLT V-SPD	2	V (25 × 25 × 1)	Al$_2$O$_3$ (25 × 25 × 0.5)	InC (25 × 25 × 1)
7	V-InC	1	V (25 × 25 × 1)	Al$_2$O$_3$ (25 × 25 × 0.5)	InC (25 × 25 × 1)
	Be-InC	1	Be (25 × 25 × 1)	Al$_2$O$_3$ (25 × 25 × 0.5)	InC (25 × 25 × 1)
	Ag-InC	1	Ag (25 × 25 × 1)	Al$_2$O$_3$ (25 × 25 × 0.5)	InC (25 × 25 × 1)
	Be-Nb	1	Be (25 × 25 × 1)	Al$_2$O$_3$ (25 × 25 × 0.5)	Nb (25 × 25 × 1)
	Be-Graph.	1	Be (25 × 25 × 1)	Al$_2$O$_3$ (25 × 25 × 0.5)	Graph. (25 × 25 × 1)
	Be-Be	1	Be (25 × 25 × 1)	Al$_2$O$_3$ (25 × 25 × 0.5)	Be (25 × 25 × 1)
	Be-SPD	2	Be (25 × 25 × 1)	Al$_2$O$_3$ (25 × 25 × 0.5)	InC (25 × 25 × 1)
	Be-1	2	Be (25 × 25 × 1)	Al$_2$O$_3$ (25 × 25 × 0.5)	Graph. (25 × 25 × 1)
	Be-2	2	Be (25 × 25 × 1)	Al$_2$O$_3$ (25 × 25 × 0.5)	InC (25 × 25 × 1)
	Be-3	2	Be (25 × 25 × 1)	Al$_2$O$_3$ (25 × 25 × 0.5)	Nb (25 × 25 × 1)
	V-1	2	V (25 × 25 × 1)	Al$_2$O$_3$ (25 × 25 × 0.5)	Graph. (25 × 25 × 1)
	V-2	2	V (25 × 25 × 1)	Al$_2$O$_3$ (25 × 25 × 0.5)	InC (25 × 25 × 1)
	V-3	2	V (25 × 25 × 1)	Al$_2$O$_3$ (25 × 25 × 0.5)	Nb (25 × 25 × 1)
	Ag-1	2	Ag (25 × 25 × 0.5)	Al$_2$O$_3$ (25 × 25 × 0.5)	Graph. (25 × 25 × 1)
	Ag-2	2	Ag (25 × 25 × 0.5)	Al$_2$O$_3$ (25 × 25 × 0.5)	InC (25 × 25 × 1)
	Ag-3	2	Ag (25 × 25 × 0.5)	Al$_2$O$_3$ (25 × 25 × 0.5)	Nb (25 × 25 × 1)
	Nb-Nb	1	Nb (25 × 25 × 1)	Al$_2$O$_3$ (25 × 25 × 0.5)	Nb (25 × 25 × 1)
	Gr.-Gr.	1	Graph. (25 × 25 × 1)	Al$_2$O$_3$ (25 × 25 × 0.5)	Graph. (25 × 25 × 1)
	InC-InC	1	InC (25 × 25 × 1)	Al$_2$O$_3$ (25 × 25 × 0.5)	InC (25 × 25 × 1)
	Ag-a	2	Ag (25 × 25 × 0.5) Ag (25 × 25 × 1.0) Ag (25 × 25 × 1.5) Ag (25 × 25 × 2.0)	Al$_2$O$_3$ (25 × 25 × 0.5)	Graph. (25 × 25 × 1)
	Ag-b	2	Ag (25 × 25 × 0.5)	Al$_2$O$_3$ (25 × 25 × 0.5) Al$_2$O$_3$ (25 × 25 × 0.5) Al$_2$O$_3$ (25 × 25 × 0.5) Al$_2$O$_3$ (25 × 25 × 0.5)	Graph. (25 × 25 × 1)
	Ag-c	2	Ag (25 × 25 × 0.5)	Al$_2$O$_3$ (25 × 25 × 0.5)	Graph. (25 × 25 × 1) Graph. (25 × 25 × 2) Graph. (25 × 25 × 3)

APPENDIX 3: Neutron Activation Analysis in TRIGA

For neutron flux measurements in TRIGA GTC, Au and Zn wires have been placed at three positions along the SPD length and irradiated under constant flux conditions. The activated wires are then assayed for gamma-rays of interest using HPGe detectors. The count rate of relevant gamma-lines are used to determine the flux of incident neutrons using the following formula.

$$\varphi = \frac{\lambda\, M\, C}{\sigma\, \varepsilon\, I_\gamma\, m\, N_a \left(e^{-\lambda t_{cool}}\right) \left(1 - e^{-\lambda t_{irr}}\right) \left(1 - e^{-\lambda t_{meas}}\right)} \quad . \qquad \text{(Eq. A3.1)}$$

The symbols represent,

φ: neutron flux (unit: cm^{-2} s^{-1}),

σ: effective neutron cross-section under the given energy-spectrum (unit: b),

ε: HPGe detection efficiency, defined as number of gamma-rays recorded by the detector per number of gamma-rays emitted by the nuclide,

I_γ: probability of decay by emission of the gamma-ray γ,

m: mass of the target nuclides in the activated sample (unit: g),

N_a: Avagadro's number = 6.022×10^{23},

M: molar mass of the target nuclide isotope (unit: g),

C: measured count-rate of the gamma-ray in the HPGe detector (unit: s^{-1}),

λ: radioactive decay constant of the nuclide in question (unit: s^{-1}),

t_{irr}: time-period of irradiation of the sample (unit: s),

t_{cool}: time-period required to cool the radioactive sample before spectrometry (unit: s),

t_{meas}: time-period of gamma-ray spectrometry of the activated sample (unit: s).

Among these quantities, ε, the HPGe efficiency is measured using a calibration radio-isotope source. While several other characteristics quantities related to the nuclides and gamma-decays are obtained from trusted nuclear data files, the count-rate (C), isotope mass (m) and various time-periods (t_{irr}, t_{cool} and t_{meas}) are measured in the experiments. The quadratic propagation of uncertainties from all the parameters in the equation lead to the total uncertainty in a measured neutron flux value.
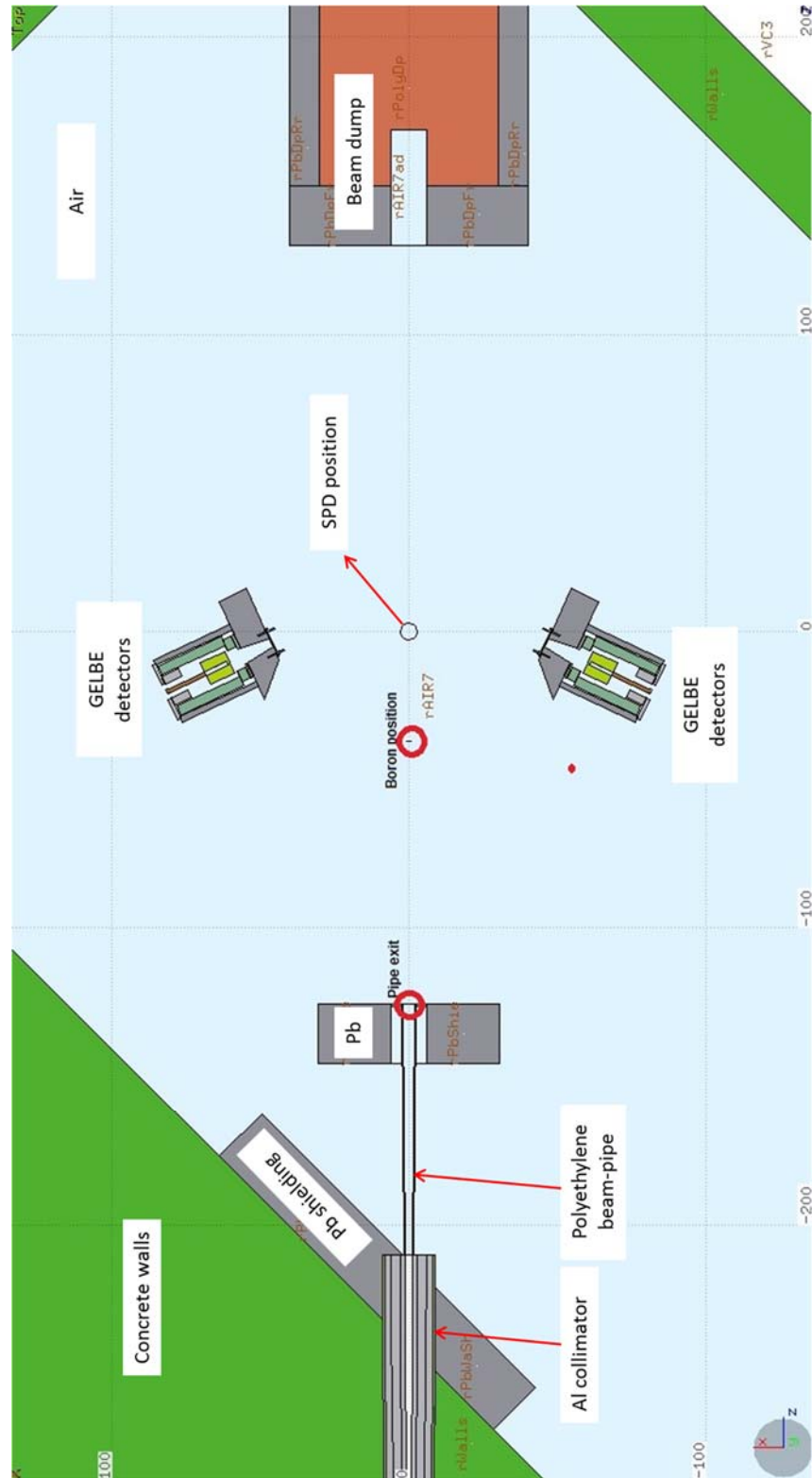
APPENDIX 4: FLUKA Model for the GELBE Cave

Figure A4-1: Rendition of the geometry of the GELBE cave as modelled in the FLUKA calculation for characterization of the photon source for SPD tests, showing the SPD position in the cave. This calculation has been performed at HZDR and has only been reproduced here for reference. Courtesy: Anna Ferrari (Helmholtz-Zentrum Dresden-Rossendorf).

APPENDIX 5: ITER A-lite Model and Positions in TBMs

The *ITER A-lite* is a previous reference MCNP model of ITER, defining a 40° sector of the tokamak [89]. This model has been developed as a collaborative effort between the FDS team of ASIPP China, ENEA Frascati, JAEA Naka, and the ITER Organization. The A-lite model comes with an SDEF card for neutron source definition in the input file, with distribution for the D-T neutrons in the plasma of ITER. Although more recent models of ITER exist, the A-lite is sufficiently detailed for detector feasibility studies, while also being relatively easier to handle and computationally more economic. Figure A5-1 shows images of the ITER and the TBM geometries as defined in the A-lite model. The plasma region, part of the torus between components on the inboard and the outboard sides, is defined as vacuum. The neutron source is defined in this region as an isotropic volume or cell source. This has been marked as "Neutron/plasma" in the left image in the figure. Other components of the ITER structure are defined to scale in the model and represented using different colors in the figure. Even though MCNP geometry description follows a default Cartesian coordinate system, typical toroidal (r, ϕ, z) coordinates are shown in the figure for consistency of discussions. The top-view, or the poloidal view (part-2 of the figure) shows the cross-section of the HCLL and HCPB TBMs better, which are further zoomed-into in part-3.
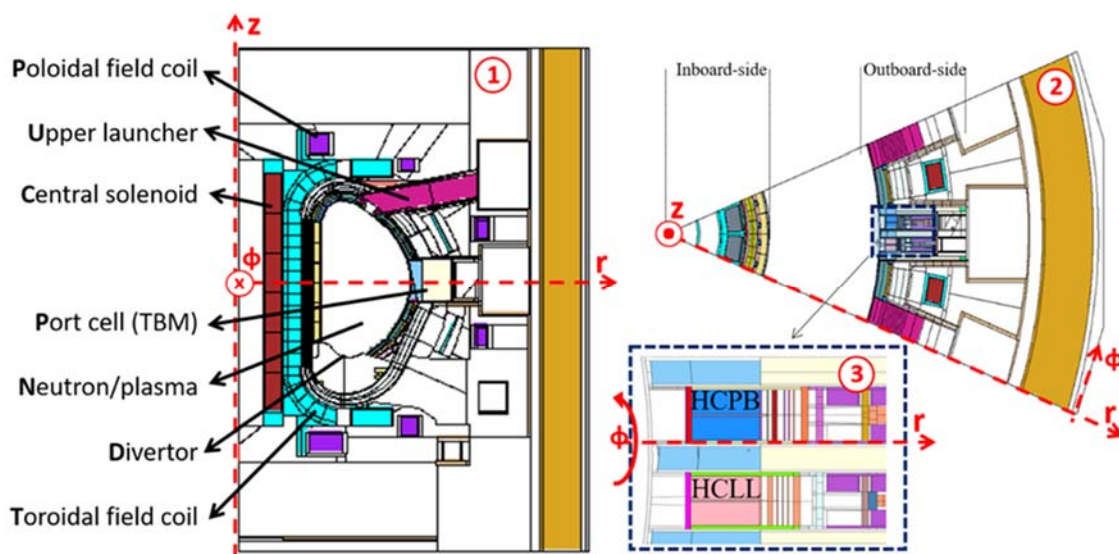

Figure A5-1: ITER A-lite MCNP model geometry showing (1) side view of the tokamak, (2) top view (octant of the tokamak), and (3) an expanded view of the integrated EU TBM units: HCPB and HCLL. Different colours represent different materials defined in the MCNP geometry model [89]. The typical tokamak (r, φ, z) coordinate system has been shown. Important components of the tokamak assembly, including the port-cell containing TBMs have been marked in (1).

Neutronic simulations with A-lite model and its successors are frequently done for design and analyses of radiation and associated effects in the ITER components.

Typically, parallel runs of MCNP code in coupled neutron-photon mode are undertaken to perform such calculations. In this thesis, this model has been utilized to obtain position-dependent distribution of fluxes and energy-spectra of neutrons and photons in the two EU TBMs, HCLL and HCPB. For this, a validated adaptation of A-lite model with HCLL and HCPB TBM systems defined in their designated positions has been used. In Figure A5-2, the cross-sectional plots of the two TBMs, extracted out of the ITER model, have been shown. Each part shows two renditions of the TBM geometries.

In HCPB (Figure A5-2, left), the TBM frame is shown in red colour. Be multiplier zone is in blue, Li-containing pebble beds in beige and stiffening rods of stainless steel in navy blue. In HCLL (Figure A5-2, right), the magenta coloured components show the TBM frame, and in pink are the lines for Pb-Li flow. In both, the He-coolant flow lines, side-caps, back-plates and auxiliary components are also modelled. For details of the models, the reader is referred to ref. [89, 90].
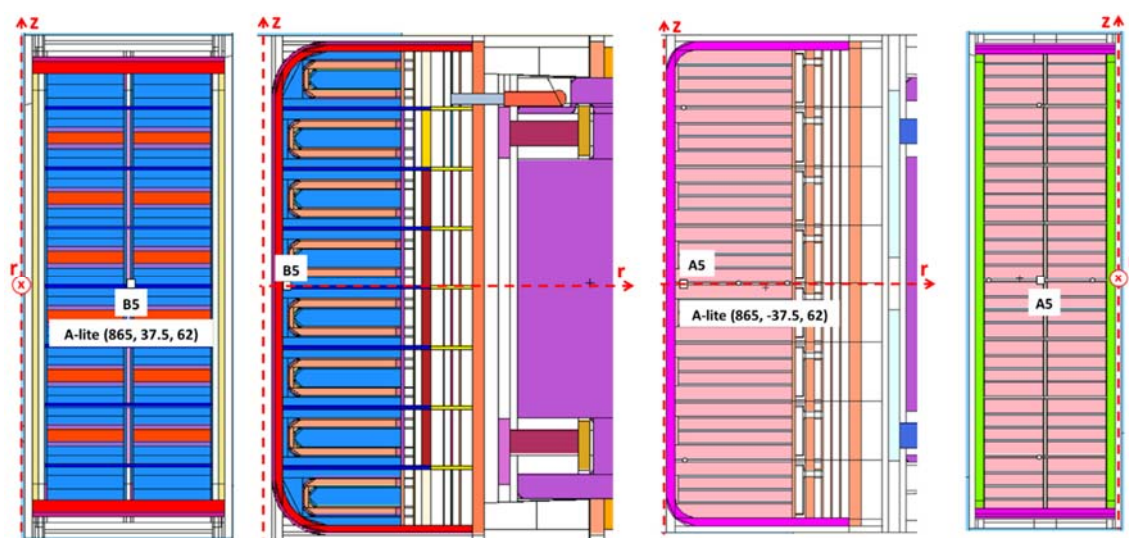

Figure A5-2: (Top) cross-sectional views of the (left) HCPB and (right) HCLL TBMs as defined in the A-lite MCNP model. For each TBM, the left section shows radial (r) and right section the toroidal views of the geometry. The positions of radiation field calculations have been shown using white squares in both TBMs. On the bottom the plot of HCPB TBM has been expanded. B5 is the reference position for calculations, close to the front wall. Other locations, two along each of the principal axes, are as: (poloidal) B1, B3, (toroidal) B2, B4, (radial) B6 and B7. The approximate distances between the positions of calculations (in mm units) have been noted.

For feasibility studies of SPDs, locations on the front walls of two TBMs have been chosen. Five locations on the walls, strategically chosen along the three principal axes have been studied in preliminary stages. Finally, the central locations B5 in HCPB and A5 in HCLL have been selected for SPD simulations. These positions are indicated on the TBM models in Figure A5-2, along with the coordinates in the A-lite MCNO model Cartesian coordinate system. The results of SPD simulations in Chapter-8 are for these two positions.

APPENDIX 6: Delayed Signals in Bi- and V-SPDs

For a completely saturated state of the delayed, (n, β⁻)-type signal components of the simulated SPDs with Bi and V emitters, the breakup of delayed components of the sensitivities in two TBMs is given in more details in Figure A6-1. Unit sensitivities due to various beta-emitting nuclides formed in different layers (*E*: emitter, *I*: insulator and *C*: collector) of the SPDs have been compared here. For the list of beta-emitting nuclides, one may see Table 8-2.
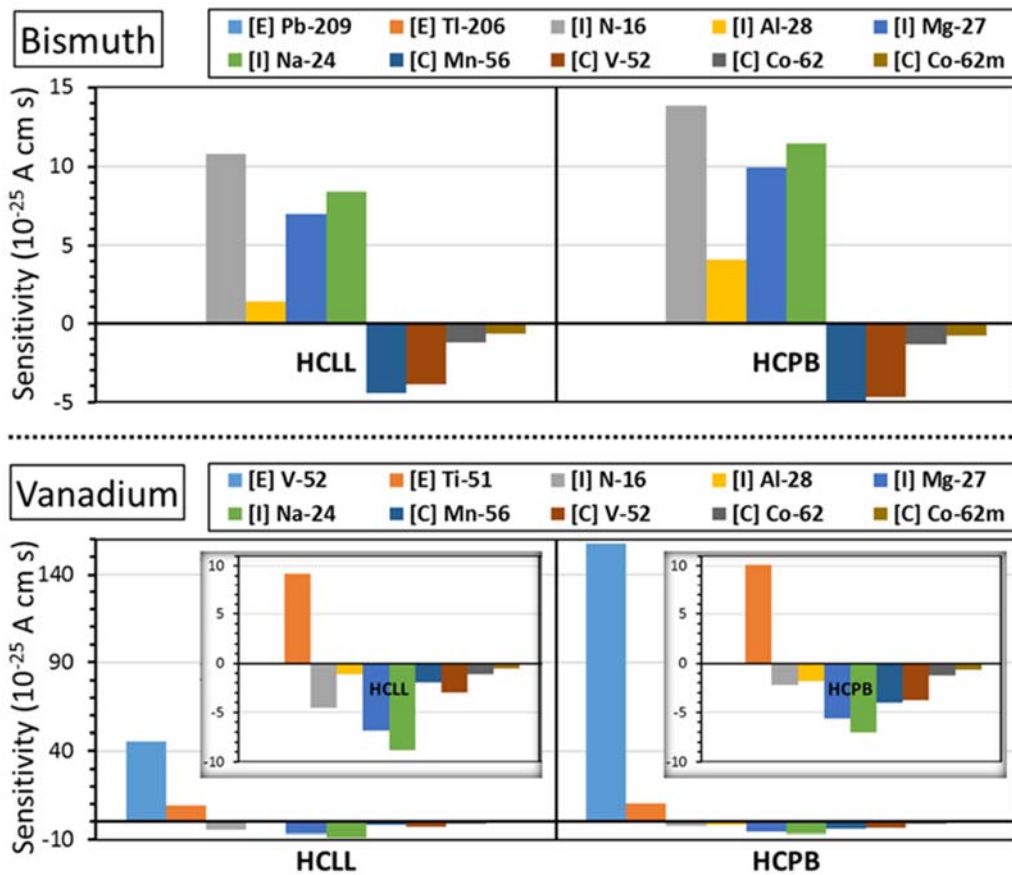

Figure A6-1: Saturated delayed signal components of (top) Bi and (bottom) V SPDs at the front central positions in (left) HCLL and (right) HCPB TBMs. The components arise due to the given nuclides generated in different layers of the SPD: [E] emitter, [I] insulator and [C] collector. For V-SPD, majority of the signal is due ^{52}V in emitter layer. To show the other, relatively smaller components, the insets have been provided on the bottom graph.

Naturally, the Bi-SPD has ten times lower delayed signals than V-SPD, due to its much lower neutron interaction cross-sections. The thermal neutron reaction on ^{51}V leading to production of ^{52}V is almost solely responsible for the delayed signals in V-SPD. This component is almost four times higher in HCPB than in HCLL, as thermal neutron share in the former is much higher. To show the other beta emitters in V-SPD, insets with changed abscissae are given on both graphs. Apart from ^{52}V in emitter,

there are positive as well as negative signals from beta emission reactions in insulator and collector, viz. [16]N, [56]Mn, [52]V etc. Depending on the position (in one of the three layers of the SPD or outside) of the stopping of beta of a particular kind, its signal share can be of positive or negative polarity. This is dependent not only on the energy-spectrum of the betas from the nuclide, but also on the electron interaction probabilities of the materials of the layers. For example, the signal due to [16]N, produced in the insulation, has a positive sign in Bi-SPD but negative sign in V-SPD.

Under a transient condition, the delayed signals change considerably. In the Figure A6-2, the detailed breakup of V-SPD delayed signal components under the two ITER pulse-types and in two TBMs are shown. These correspond to the blue curves in Figure 8-3. In general, the amplitudes of the signals in Pulse-2 are lower due to its low-power operation regime (350 MW instead of 500 MW for Pulse-1). As already pointed out, [52]V is the main reason for delayed signals in V-SPD. Other components are rather small and difficult to segregate, but nonetheless they are shown in the figure. It is evident that this reaction can serve as a good way to measure thermal neutron fluxes if an accurate method to extract it from the total signal is established.
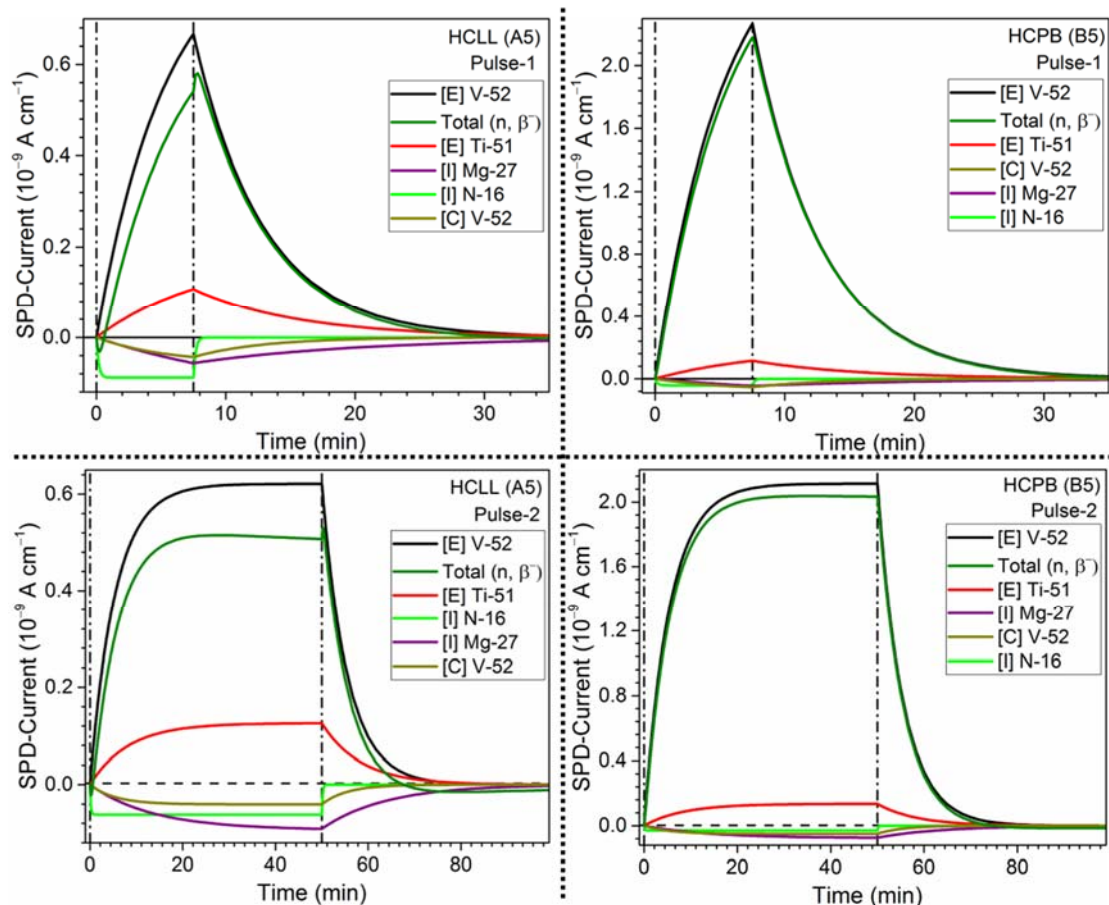

Figure A6-2: Calculated delayed signal shares in the signals of a unit SPD with V emitter under radiation conditions in (left) HCLL and (right) HCPB TBMs, and pulse regimes of type (top) pulse-1 and (bottom) pulse-2. The delayed components are identified using the nuclides emitting the betas, in different layers of the SPD: [E] emitter and [I] insulator, [C] collector. Major component is due to [52]V in emitter. One can notice fast neutron-induced [51]Ti, [16]N and [27]Mg, while the other nuclides are barely identifiable.